

**Microscopic disorder, finite temperatures and spin waves in
domain-wall driven exchange bias**

Joo-Von Kim

Bachelor of Science (Honours), UWA

This dissertation is presented for the degree of

Doctor of Philosophy

of the University of Western Australia

School of Physics

2002

Abstract

Microscopic disorder, finite temperatures and spin waves in domain-wall driven exchange bias

Exchange bias is an interface effect that results from the exchange interaction between a ferromagnet in contact with an antiferromagnet layer. The existence of bias depends on the magnetic order in the antiferromagnet and the effect is commonly characterized by a hysteresis loop displacement along the field axis and enhancements to the coercivity in the ferromagnet. These features are sensitive to the details of the physical and chemical structure of the ferromagnet/antiferromagnet interface. Although exchange bias was discovered over forty years ago, there still remains a host of unanswered questions and contradictions between experimental observations and theoretical predictions. The problem poses many challenges to test our current understanding of interfacial magnetism and frustrated spin systems.

A theoretical study of exchange bias in bilayer systems, based on partial domain wall formation near the interface in the antiferromagnet, is presented in this dissertation. A continuum theory developed for mixed interfaces demonstrates a link between microscopic spin order and phenomenological bilinear and biquadratic terms coupling the two magnetic layers. Particular attention is given to the role of impurities, such as interface roughness in the form of geometrical imperfections and magnetic defects within the film layers. Results from numerical calculations show that dramatic modifications to the hysteresis can occur with the presence of such impurities, and some effort is made at providing clues to help identify defect types in experiment. Periodic imperfections at the interface are shown to modify the angular dependence of the bias and the behaviour can be understood in terms of changes in the natural orientation of the ferromagnet magnetization. Local spatial variations in the magnetic constants result in domain wall pinning effects and are shown to give rise to coercivity enhancement. The effects of finite temperatures are studied with a local mean-field theory and the results demonstrate the importance of thermally-driven wall pinning processes in the antiferromagnet. Suggestions for alternative means of characterizing antiferromagnetic order are made in light of studies of the magnetic heat capacity. Finally, the behaviour of long-wavelength spin excitations in the bilayer is examined. Changes to the ferromagnet spin wave spectra due to the interlayer coupling are studied in detail and some estimates are given for frequency shifts and linewidth variations resulting from interfacial inhomogeneities.

Contents

List of Figures	ix
1 Introduction	1
1.1 Exchange bias: Overview of experimental results	3
1.1.1 Phenomenology	3
1.1.2 Hysteresis and magnetization reversal	5
1.1.3 Thermal properties and time-dependent phenomena	6
1.1.4 Dynamic measurements	8
1.1.5 Role of microstructure and geometry	9
1.2 Basic mechanisms	12
1.2.1 Coherent rotation	12
1.2.2 Antiferromagnet domains	14
1.2.3 Partial wall formation	17
1.3 Microscopic disorder, finite temperatures and spin waves	20
2 Partial wall theory of exchange bias	23
2.1 Effective Hamiltonian and bilayer geometry	23
2.2 Continuum theory of uncompensated interfaces	26
2.3 Bias field and magnetization curves	30
2.4 Angular dependence of the bias field	31
2.5 Continuum theory of compensated and mixed interfaces	35
2.6 Bilinear and biquadratic coupling	41
2.7 Numerical integration of equations of motion	43
2.8 Antiferromagnet film thickness dependence	47
2.9 Ferromagnet film thickness dependence	49
2.10 Stability of spin-flop coupling	55
3 Interface roughness	59
3.1 Periodic defects	61
3.2 Variations in the natural angle	63
3.3 Angular dependence of exchange bias	66
3.4 Random defects	73
4 Defect-induced domain wall pinning	77
4.1 Model for domain wall pinning	77
4.2 Bias field reduction and coercivity enhancement	82
4.3 Asymmetric hysteresis	88
4.4 Angular dependence of exchange bias	91
4.5 Spin dilution and site anisotropy variations	95

5	Finite temperature effects	103
5.1	Local mean-field approach	103
5.2	Thermal domain wall profiles	105
5.3	Hysteresis	107
5.4	Temperature induced domain wall pinning	110
5.5	Angular dependence of exchange bias	113
5.6	Thermal-enhanced impurity pinning	115
5.7	Heat capacity as probe of antiferromagnetic order	118
6	Long-wavelength spin dynamics	127
6.1	Linear spin wave theory	127
6.2	Spin waves in non-uniform ground states	129
6.3	Antiferromagnetic spin-flop	131
6.4	Ferromagnetic hysteresis	136
6.5	Excitation profiles	141
6.6	Angular dependence of resonance frequency	146
6.7	Linewidth enhancement	148
7	Concluding remarks and outlook	155
7.1	Overview of results	155
7.2	Criticisms and limitations of the partial wall model	160
7.2.1	Critique of model Hamiltonian and geometry	160
7.2.2	Limitations of present theory	163
7.3	Suggestions for new experiments	165
7.4	Future work	168
A	Numerical time-integration model	171
A.1	Algorithm	171
A.2	Convergence tests	173
A.3	Hysteresis curves	178
A.4	Partial wall profile	179
B	Rapidly converging dipole sums	181
C	Construction of dynamical matrix	187
D	Derivation of antiferromagnet critical fields	191
	References	195
	Bibliography	223
	Selected Publications	225

List of Figures

1.1	Exchange biased hysteresis	3
1.2	Schematic of biased hysteresis loop	4
1.3	Coherent rotation model of exchange bias	12
1.4	Kouvel's domain model for disordered Cu-Mn alloys	15
1.5	Partial wall model of exchange bias	17
2.1	Geometry of ferromagnet/antiferromagnet bilayer	25
2.2	Geometry of the partial wall model for perfect uncompensated interfaces .	28
2.3	Magnetization curves from analytical model for uncompensated interfaces	31
2.4	Predicted angular dependence of the bias field from partial wall model . .	33
2.5	Geometry for the two-sublattice model	37
2.6	Schematic profile of spin-flop and partial Bloch walls in the antiferromagnet	39
2.7	Geometry for the discrete numerical model	44
2.8	Antiferromagnet energy as a function of twist angle	48
2.9	Bias field and coercivity variations with film thickness of antiferromagnet	49
2.10	Bias field variations with film thickness of an isotropic ferromagnet	50
2.11	Magnetization profile of ferromagnet partial wall	51
2.12	Bias field variations with film thickness of an anisotropic ferromagnet . .	54
2.13	Stability of spin-flop coupling at compensated interfaces	56
3.1	Frustrated spins at a rough interface	60
3.2	Geometry for interface roughness in the numerical model	61
3.3	Bias field variation with line defect period	62
3.4	Natural angle variations for line defects	64
3.5	Natural angle variations for step defects	66
3.6	Angular dependence of bias with line defects	68
3.7	Irreversible behaviour at rough interfaces	69
3.8	Sense of rotation of magnetization	70
3.9	Fourier analysis of angular dependence - line defects	71
3.10	Angular dependence of bias with step defects	72
3.11	Variation in natural angle with bump defects	74
3.12	Bias field and coercivity changes due to bump defects	75
4.1	Partial wall energy with the presence of impurities	79
4.2	Partial wall formation viewed as soliton propagation	80
4.3	Geometry for reduced exchange and anisotropy defects	82
4.4	Bias field and coercivity variations for reduced-exchange defects	84
4.5	Bias field and coercivity variations for reduced-anisotropy defects	85
4.6	Variation in the position of partial wall centre with magnetic defects . . .	87
4.7	Defect-induced asymmetric hysteresis loops	88
4.8	Variation in extent of partial twist with defects	90

4.9	Defect-modified angular dependence of exchange bias	92
4.10	Model of rotational hysteresis	93
4.11	Defect-modified reversible and irreversible rotations	95
4.12	Modified exchange bias through spin dilution - uncompensated interfaces	97
4.13	Modified exchange bias through spin dilution - compensated interfaces . .	98
4.14	Modified exchange bias through local site anisotropy enhancements	100
5.1	Thermally averaged spin profile for antiferromagnetic domain wall	106
5.2	Variation in antiferromagnetic domain wall width with temperature. . . .	108
5.3	Thermal dependence of exchange bias	109
5.4	Thermal spin profile of an exchange coupled ferromagnet/antiferromagnet bilayer	111
5.5	Variation of partial wall centre with temperature	112
5.6	Angular dependence of exchange bias at finite temperatures	114
5.7	Defect enhanced thermal pinning of domain wall	116
5.8	Asymmetric hysteresis due to thermally enhanced impurity domain wall pinning	117
5.9	Magnetic heat capacity for uncompensated interfaces with large J_{f-af} . . .	120
5.10	Magnetic heat capacity for varying ferromagnet film thickness	121
5.11	Heat capacity of an antiferromagnetic twist	122
5.12	Magnetic heat capacity for uncompensated interfaces with small J_{f-af} . . .	124
5.13	Magnetic heat capacity for compensated interfaces	125
6.1	Schematic diagram of a spin wave	128
6.2	Spin waves in a canted antiferromagnet	132
6.3	Spin structure of canted antiferromagnet coupled to a ferromagnet film . .	133
6.4	Spin waves in a canted antiferromagnet coupled to a ferromagnet film . .	135
6.5	Hysteresis curves for limiting cases of partial wall formation.	137
6.6	Spin waves in a ferromagnet/antiferromagnet bilayer - I	138
6.7	Spin waves in a ferromagnet/antiferromagnet bilayer - II	139
6.8	Spin waves in a ferromagnet/antiferromagnet bilayer - III	140
6.9	Mode profiles in a ferromagnet/antiferromagnet bilayer - I	142
6.10	Mode profiles in a ferromagnet/antiferromagnet bilayer - II	143
6.11	Mode profiles in a ferromagnet/antiferromagnet bilayer - III	144
6.12	Angular dependence of the bilayer resonance mode	147
6.13	Bilayer resonance mode frequency for varying interlayer coupling	149
6.14	Bilayer resonance mode frequency for varying applied field orientation . .	150
6.15	Bilayer resonance mode frequency with reduced exchange defects	151
A.1	Convergence of numerical model from random initial state	174
A.2	Convergence of numerical model from saturated initial state	176
A.3	Algorithm performance for hysteresis loop calculation	177
A.4	Comparison of analytical and numerical magnetization curves	178
A.5	Comparison of analytical and numerical wall profiles	179
D.1	Antiferromagnetic spin-flop transition	192

Chapter 1

Introduction

The study of interface phenomena related to layered magnetic materials has grown rapidly over the past few decades. An impetus for such developments has been the vast improvement in the technical ability to fabricate readily thin films and multilayered materials in the laboratory. These low dimensional systems have proven to be a source of interesting physics for basic research, which in turn has led to practical applications for magnetic recording technology and magneto-electronics.ⁱ Despite this flurry of activity there still remains a large number of unanswered questions and outstanding problems in thin film magnetism. A challenge in resolving many of these issues is the same as that faced by the wider condensed matter physics community, namely, to provide quantitative theories for complex many-body problems.

Surface and interface phenomena arise as a matter of scale. To illustrate, consider a finite-sized sample of a homogeneous material. As the dimensions of this object are reduced a point is reached where the dominant properties of the material are governed by the behaviour of the surface, because a significant proportion of the material is now comprised of surface atoms. The surface environment is markedly different to the bulk, where, for example, there are fewer nearest neighbours at the surface and these conditions can give rise to modified physical properties. Interfaces between two media exhibit

ⁱA general overview has been given by Prinz [1].

similar effects, as atoms at the interface layer of one material have neighbours from both species. Thin films and multilayers can be anywhere between one and 100 atomic layers in thickness, and as such, the surfaces and interfaces can dominate the physics governing magnetic order at these dimensions.ⁱⁱ

An interface effect that has sparked much interest over the last 40 years is exchange bias, which is caused by interactions between a ferromagnetic film and a neighbouring antiferromagnetic layer in contact. The bias effect results from competing energies at the ferromagnet/antiferromagnet interface and exhibits the complexity seen in frustrated spin systems. As such, these materials have proven to be fruitful for basic scientific research and have provided many challenges to understand the associated time- and history-dependent phenomena. Bias systems have found many practical uses in modern magnetoresistive field sensor technology, where the biasing effect is exploited as a pinning mechanism for spin-valve structures that operate using giant magnetoresistance [3–8].

The underlying physics of exchange bias is still not well understood. The difficulties in constructing meaningful quantitative theories may be due to the sensitivity of the effect on the details of the ferromagnet/antiferromagnet interface, which forms part of the motivation for this thesis. Information about the spin structure and the magnetic properties at the interface are hard to obtain experimentally, making an additional handicap for testing theoretical predictions. Nevertheless, insight into the essential physics, accounting for the general features observed in experiment, can be obtained through the use of relative simple models.

This thesis aims to extend the domain-wall theory of exchange bias, in which a partial twist in the spin structure is supposed to form in the antiferromagnet near the interface. The primary goal of this work is to examine how this magnetic inhomogeneity responds to the presence of impurities, finite temperatures and periodic temporal fluctuations in the magnetization in the form of linear excitations.

ⁱⁱA recent review of layered magnetic structures is given by Grünberg [2].

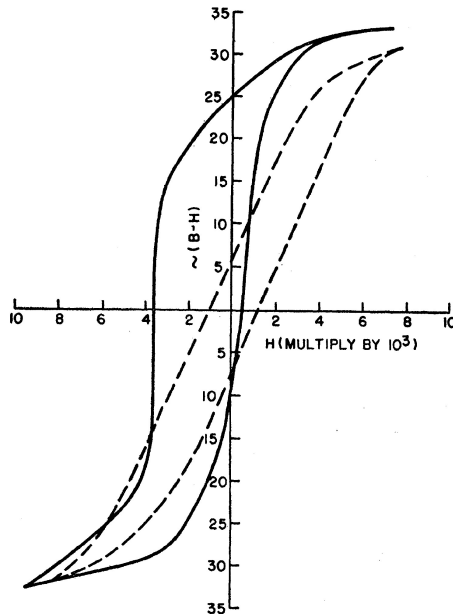


Figure 1.1: Exchange biased hysteresis. The shifted hysteresis loop originally obtained by Meiklejohn and Bean with oxidized Co particles. From Ref. [9].

In this chapter, the reader is introduced to the main features of exchange bias. A brief overview of experimental observations is given in the first section and is followed by an introduction to the main theoretical descriptions, with particular emphasis on the partial wall model and its relevance to existing experimental data. Finally, a summary of the work presented in this dissertation is given in the third section.

1.1 Exchange bias: Overview of experimental results

1.1.1 Phenomenology

Exchange bias was discovered in 1956 by W. H. Meiklejohn and C. P. Bean and was observed in experiments with fine Co particles [9, 10]. They noticed that upon cooling their specimens in an applied field a displacement in the hysteresis loop was obtained (Fig. 1.1). This behaviour was attributed to the presence of a thin oxidized layer of CoO that had formed on the surface of the particles and the effect was termed “exchange anisotropy”. The origin of this anisotropy has subsequently been traced to the exchange coupling between the ferromagnetic Co and the antiferromagnetic CoO, and

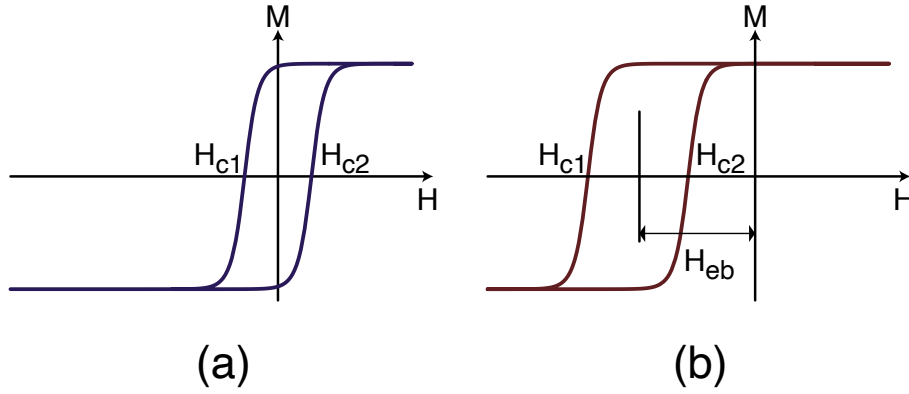


Figure 1.2: Schematic diagram illustrating the exchange bias effect on ferromagnetic hysteresis. (a) An unbiased ferromagnetic hysteresis loop, with two coercive fields H_{c1} and H_{c2} of equal magnitude. (b) Biased hysteresis loop displaced from the origin along the field axis by $H_{eb} \equiv \frac{1}{2}(H_{c1} + H_{c2})$.

since this discovery, a multitude of related phenomena accompanying the hysteresis loop displacement has been observedⁱⁱⁱ [15–281].

Antiferromagnetic order is crucial to the existence of exchange bias and is evidenced by the disappearance of the loop shift above the Néel temperature (T_N) [6, 7, 10, 15, 19–21, 23, 31–33, 35–39, 42, 45, 48, 52, 56, 63, 65, 68, 70, 72, 80–82, 85, 89, 95, 96, 107–110, 117, 125, 136, 137, 139, 141, 144, 148, 152, 153, 155, 156, 158, 160, 163, 165, 166, 169, 177, 181, 185, 192, 194, 195, 200, 202, 209–211, 213, 215, 232, 235, 237, 240, 242, 245–247, 250, 252, 255, 256, 261, 264, 271, 272, 274, 279]. The direction of the bias can be set in two ways. In the first, the system is heated above T_N and then subsequently cooled through this ordering temperature in the presence of a large external field. Above the Néel temperature the ferromagnet magnetization is aligned parallel to the field and experiences no effects of the neighbouring antiferromagnet.^{iv} Upon cooling through T_N the interfacial antiferromagnet spins order according to the orientation of the neighbouring ferromagnet, and this order is transmitted into the antiferromagnet bulk as the temperature is further reduced. In the second, the antiferromagnet film is grown on the ferromagnet in an external field below the Néel temperature and order is established as each successive layer deposited orients

ⁱⁱⁱFor some recent reviews, the reader is referred to references [11–14].

^{iv}In most experimental systems, the Curie temperature of the ferromagnetic material is larger than the Néel temperature, so it is safe to assume that the ferromagnetic moments are ordered for temperatures slightly above T_N .

accordingly to the interactions across the interface.

1.1.2 Hysteresis and magnetization reversal

The hysteresis loop displacement is the most characteristic feature of exchange bias. The magnitude of this displacement is called the bias field, H_{eb} , because the shift can be described by assuming the presence of an additional fictitious field of the same magnitude acting on the ferromagnet. Predicting the bias shift magnitude is the primary challenge and is difficult because of the uncertainty surrounding the magnetic properties at the interface. Nevertheless, measurable shifts can be engineered in experiment without a complete understanding of the bias mechanisms.

An enhancement to the coercivity accompanying the loop shift is reported in certain systems [59, 95, 97, 103, 110, 117, 135, 160, 163, 212, 252, 279]. In Figure 1.2, the enhancement corresponds to the quantity $|H_{c1} - H_{c2}|$ being larger for the biased curve. A good example of coercivity enhancement was demonstrated by Wu et al. in experiments with amorphous ferromagnets [61]. The coercivity of an as-deposited $\text{Co}_{65}\text{Mo}_2\text{B}_3$ amorphous alloy was observed to be approximately 1 Oe, which is characteristic for soft magnetic materials. However, the same material grown on antiferromagnetic CoO exhibited an increased coercivity by two orders of magnitude after field cooling, where the width was observed to be 120 Oe accompanying a shift of 76 Oe. Although such changes are not as dramatic for all ferromagnets, the example serves to illustrate the influence of the antiferromagnetic layer on ferromagnetic hysteresis.

Magnetization reversal in the ferromagnet is also modified by the coupling across the interface [73, 89, 113, 127, 133, 137, 142, 143, 164, 166, 170, 172, 195, 196, 203, 206, 209, 211, 216, 217, 220, 221, 225, 239, 244, 258, 266, 275, 280], where such changes can appear as asymmetric hysteresis loops in which the magnetization undergoes different switching mechanisms during reversal and remagnetization [59, 113, 118, 137, 164, 166, 195, 216, 217,

220, 258, 266]. For Fe coupled to twinned FeF_2 and MnF_2 structures, experiments with polarized neutron reflectometry have revealed that reversal can take place via coherent rotation with domain wall propagation dominating during the remagnetization process, where the asymmetry is dependent on the relative orientation of the applied field and the anisotropy axes in the antiferromagnet [118]. Double-shifted magnetization curves are another example of reversal anomalies and are argued to arise from an induced biquadratic coupling at the ferromagnet/antiferromagnet interface [191], consistent with the higher-order exchange interactions used to account for bias at compensated interfaces. This will be revisited in more detail in later chapters.

The hysteresis loop displacement can actually occur as a positive shift under certain conditions, i.e. in a direction opposite to that depicted in Figure 1.2. This phenomenon is observed after field cooling in a large external field [44, 112, 249, 255], and experiments show a transition from negative to positive bias can be controlled by tuning the magnitude of the cooling field [44]. It is argued that this can be explained if the exchange coupling between the ferromagnet and antiferromagnet layers is antiferromagnetic, whereby a sufficiently large cooling field aligns the interface spins in parallel during ordering and results in the high energy metastable state attained at reverse field for negative bias [44].

1.1.3 Thermal properties and time-dependent phenomena

The bias field disappears at a blocking temperature T_B that may not coincide with the Néel temperature, and the differences between T_N and T_B have been studied in detail by several groups [33, 41, 136]. Interestingly for the $\text{Fe}_3\text{O}_4/\text{CoO}$ system, finite-size effects are not responsible for variations in the blocking temperature with antiferromagnet (CoO) film thickness, where an increase in T_N is accompanied by a decrease in T_B for thinner films [136]. The enhancement of the ordering temperature is attributed to the

close proximity of the magnetic Fe_3O_4 layer. Variations in the T_B have also been reported for diluted antiferromagnets [202], where interesting diamagnetic effects from introduced impurities are shown to enhance the blocking temperature.

In most cases the Curie temperature (T_C) of the ferromagnet is much higher than T_N , which is useful for the preparation of bias because the ferromagnetic order can be transmitted to the antiferromagnet upon cooling. However, interesting effects appear when the Néel and Curie temperatures are comparable because of the competing temperature dependencies in the two layers. Novel features in the thermal dependence of the bias field and coercivity have been observed in experiments with the $(\text{Fe}_x\text{Ni}_{1-x})_{80}\text{B}_{20}/\text{CoO}$ system, which are attributed to large changes in the intensity of magnetization M_f of the ferromagnet [68].

It is important to point out that exchange bias represents a form of dynamic hysteresis^v because the coercive fields depend strongly on the rate at which the measuring field is varied [7,126,169]. Magnetic viscosity experiments have shown the amount of time spent “waiting” at maximum reverse field is important, and for sufficiently long waits, the unidirectional anisotropy is suppressed completely [7,126,127,164,242]. Thermal activation and non-equilibrium processes during reversal in exchange bias systems have been studied by several groups [7,21,56,64,104,169,206,219,274].

The magnetization history of the sample is also important in determining the hysteresis properties. Training effects, where repeated measurements of the hysteresis loops yield different coercive fields, have been reported for many systems [18–20,178,229]. This behaviour is characteristic of a frustrated spin system, such as a spin-glass, where the energy landscape over which the ferromagnet magnetization traverses is complex and populated with many metastable states. The reversal of the magnetization can follow a complicated path along this landscape that is unlikely to be retraced. Of course, transitions between metastable states are aided by thermal fluctuations, as discussed above.

^vFor a general review on dynamic hysteresis, the reader is referred to Ref. [282].

Other related phenomena, such as rotational hysteresis [17–19, 120, 128, 178, 183, 199] and memory effects [96, 125], have prompted suggestions likening the interface to a kind of spin-glass state.

1.1.4 Dynamic measurements

The magnitude of exchange bias observed is sensitive to the particular measurement technique employed. Marked differences in estimates of the effective unidirectional field can depend on whether a reversible or an irreversible measurement is used [82, 122, 182], but this is not true for all exchange bias systems [189]. A non-intrusive way to study the magnetic properties is to examine the linear response of the system. Small fluctuations in the magnetization orientation, called spin waves, can give much information about the magnetic properties of buried interfaces because the excitation frequencies are sensitive to the material constants.

Brillouin light scattering (BLS) and ferromagnetic resonance (FMR) experiments probe the linear dynamics of the ferromagnet, where information about the effective fields can be obtained from the spin wave frequencies. In BLS, the surface spin waves are probed by incoming electromagnetic radiation, where for sufficiently thin films, the interface can be studied by examining how the spin wave behaviour changes with the presence of an antiferromagnet in contact. Experiments have shown that the interlayer coupling can produce measurable shifts in the frequencies [58, 77, 144, 167], and angular dependence measurements have revealed induced higher-order anisotropies in the ferromagnet [146]. The response of the entire film is probed in FMR experiments, in which accurate measurements of additional effective fields (due to the interlayer coupling, for example) can be obtained [24, 27, 29, 95, 109, 119, 125, 155, 167, 177, 211, 213, 237, 255, 261, 263, 283]. The presence of a “rotatable anisotropy” term has also been revealed in FMR experiments [125, 283], and some preliminary work has been performed to address this issue [284].

The linewidths in the excitation spectra provide information about damping processes in the material. Relaxation processes are sensitive to the interactions in the system and in some cases provide a way to identify inhomogeneities that may be present at the ferromagnet/antiferromagnet interface. Several groups have reported linewidth broadening in exchange bias systems [29, 58, 77, 167, 255, 283], where some contributions to the broadening have been attributed to two-magnon scattering processes mediated by variations in the exchange coupling at the interface [58, 167, 283].

Measurements of the ac-susceptibility of exchange biased films have raised questions about the correspondence between the shift field H_{eb} and an equivalent Stoner-Wohlfarth unidirectional anisotropy^{vi} used to describe the effect [48, 82, 105, 122]. In this method small rotations of the magnetization are measured at an angle from the field-cooled direction. The results indicate that the unidirectional energy can be inconsistent with magnetometry measurements by up to a factor of three.

The relaxational dynamics at the ferromagnet/antiferromagnet interface have also been probed with other dynamical techniques. Modulation of the exchange coupling has been demonstrated in experiments with laser pulses applied to the interface region [71, 93, 138]. The spins are photoexcited on a femtosecond timescale and measurements of the transient magneto-optical response of the ferromagnet show that this modulation occurs within a picosecond regime. Frequency-dependent susceptibility measurements have also demonstrated the importance of magnon scattering events at the interface [259].

1.1.5 Role of microstructure and geometry

The interfacial structure is important in governing the observed exchange bias properties. In particular, aspects of the film preparation pertinent to interface quality such as material composition [40, 62, 65, 161, 176, 210, 214, 234, 245, 249, 250], growth techniques

^{vi}The unidirectional anisotropy can be expressed as $\mathcal{E}_{ud} = K_{ud} \cos \theta$ for a Stoner-Wohlfarth particle, where θ denotes the orientation of the magnetization relative to the anisotropy axis.

and conditions [22, 76, 89, 139, 149, 168, 171, 187, 188, 197, 215, 218, 230, 236, 238, 240, 241, 254, 267, 278, 281] have been studied in great detail. The role of the external cooling field has also been given some attention by several groups [66, 99, 102, 115, 186, 213, 249].

The sign and magnitude of the interlayer coupling are difficult to determine, in practice, because they strongly depend on the chemical and physical structure at the interface. Although much effort to obtain quantitative measures of J_{f-af} [95, 111, 112, 176, 181] has been made, it is generally believed the coupling should be similar to the antiferromagnet exchange. To illustrate, consider a common experimental scenario where the Curie temperature (and hence the exchange coupling in the ferromagnet) is much larger than the Néel temperature. For a ferromagnetic $J_{f-af} \approx J_f$, one would expect any interface spins to be rigidly aligned with the ferromagnetic layer, leaving the antiferromagnet coupling between the next layer forming the effective interface. Exchange bias is observed to be sensitive to roughness of the ferromagnet/antiferromagnet interface [37, 43, 49, 51, 60, 74, 80, 102, 107, 117, 130, 131, 165, 195, 208, 233, 242], although there are contradicting views on whether bias is improved or degraded by such imperfections.

Little information is available on the interfacial spin structure in bias systems. Experimental proof of uncompensated spins was presented for NiFe/CoO systems from measurements of the thermoremanent magnetization [52]. Other studies have suggested good correlation of exchange bias with interfacial spin structure [84, 98, 134, 140, 145, 162, 165, 179, 190, 201, 253]. Spin-flop or perpendicular coupling, where the ferromagnet magnetization orients perpendicular to the antiferromagnet easy axis, is reported in a number of systems [55, 57, 67, 88, 115, 123, 151, 194, 222]. This suggests a competition between the spins at the interface, which may arise from both antiferromagnet sublattices being in contact with the ferromagnet.

The nature of the interlayer coupling can be inferred from ferromagnetic domain structure [86, 140, 205, 221, 224, 226, 239, 251, 260]. The evolution of domains during

reversal can give much insight into the magnetization processes. Correlations between ferromagnetic and antiferromagnetic domains have been observed in some experiments [223], thus providing a means of characterizing antiferromagnetic order usually inaccessible via conventional magnetometry techniques.

Further complexity arises in polycrystalline materials [69], where an ensemble of interacting grains may be present at the interface of both ferromagnet and antiferromagnet layers. Grain size effects [120, 152, 153] and other microstructural properties [25, 31, 45, 53, 79, 171, 173, 175, 203, 207, 210, 215, 222, 228, 232, 243, 247, 254, 265] have been examined in detail by several groups. The introduction of impurities [83], through non-magnetic substitution (spin dilution) [132, 202, 250, 257], for example, can modify the bias properties significantly. Changes to the bias can also be effected with ion-irradiation [114, 157, 227, 280], although the origins of these effects are still largely contested.

Exchange bias has also been reported in other geometries. Oscillatory bias [124, 158, 181, 193, 204] is reported in trilayer structures where the ferromagnet and antiferromagnet layers are separated by an intervening spacer material (reminiscent of traditional GMR “sandwiches”) [54, 235, 262]. This behaviour is explained by the oscillatory exchange coupling that accompanies ferromagnet/spacer/ferromagnet structures. In other multilayered materials, superlattices with artificial antiferromagnets constructed from Fe/Cr multilayers also exhibit exchange bias. In a sense, these materials represent idealized systems because the difficulties involving the interfacial structure do not apply; the sign and magnitude of the exchange coupling can be controlled by varying the thickness of the spacer layer. Superlattices consisting of engineered ferromagnetic and antiferromagnetic layers have also been studied [106, 116, 141, 192, 204, 253]. Exchange bias has also been observed in patterned and nanostructured films [90, 150, 156, 180, 200, 280] and small particles [198, 246].

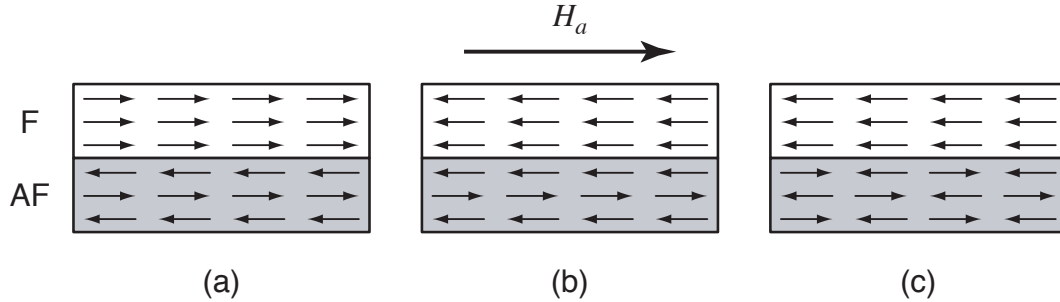


Figure 1.3: Coherent rotation model of exchange bias. The uniaxial anisotropy in the antiferromagnet is sufficiently large to render the spins rigid to the rotation of the ferromagnet. (a) At forward fields and reverse fields $H_a > H_{eb}$ the ferromagnet layer is pinned in the forward direction due to the exchange coupling to the antiferromagnet. (b) For $H_a < H_{eb}$ the ferromagnet switches into the reverse field direction. (c) For compensated interfaces there are equal populations of the two sublattice spins and no bias is predicted with this model.

1.2 Basic mechanisms

The variety of the experimental findings presented provides many challenges to the understanding of the physics of exchange bias, which consequently has motivated much theoretical study in this subject [142,248,285–358]. In this section, some of the main theories of exchange bias are presented. The discussion begins with a review of Meiklejohn and Bean’s original model and explores the development of more sophisticated models. Particular attention is given to the partial wall mechanism, which is the central topic of this dissertation. The relevance of this approach to experimental observations and other theories is discussed towards the end of the chapter.

1.2.1 Coherent rotation

Meiklejohn and Bean [9,10] proposed a simple model to explain the loop shift. The description involves a ferromagnetic Stoner-Wohlfarth particle subject to a unidirectional field, which represents the exchange coupling to a rigid antiferromagnet. Consider a single spherical particle in a single-domain state, with uniaxial anisotropy $-K_{ua} \cos^2(\theta)$ where θ is the angle between the magnetization M_f and the anisotropy axis. An external field H_a is applied collinear with the anisotropy axis. Neglecting thermal effects, the energy of this particle when the field is oriented opposite to the direction of the magneti-

zation is

$$\mathcal{E} = H_a M_f \cos(\theta) - K_{ua} \cos^2(\theta). \quad (1.1)$$

The switching field, H_s , is derived by considering the stability of the initial state at $\theta = 0^\circ$,

$$H_s = \frac{2K_f}{M_f}. \quad (1.2)$$

Suppose a unidirectional anisotropy of the form $-K_{ud} \cos(\theta)$ is introduced,

$$\mathcal{E} = H_a M_f \cos(\theta) - K_{ua} \cos^2(\theta) - K_{ud} \cos(\theta). \quad (1.3)$$

The solution to the switching field is identical to the previous case if the following substitution is made,

$$H'_a = H_a - \frac{K_{ud}}{M_f}. \quad (1.4)$$

Thus, the original hysteresis loop is displaced along the field axis by an amount K_{ud}/M_f .

A unidirectional anisotropy in the ferromagnet can arise from coupling to an antiferromagnetic layer. This is easy to see with an *uncompensated* interface, where only one sublattice species is present at the interface to give a net moment. Suppose that the ferromagnet/antiferromagnet couple is cooled in a field aligned parallel to the axis of uniaxial anisotropy in the antiferromagnet. The spin configuration at low temperatures is depicted in Fig. 1.3a, where it is assumed the magnetization within each layer is uniform. This alignment persists as the field is lowered to zero and reversed, provided the magnitude of the reversed field is not too large. The energy of this configuration in reverse field is

$$\mathcal{E} = H_a M_f t_f \cos(\theta) - K_f \cos^2(\theta) - J_{f-af} \cos(\theta). \quad (1.5)$$

The extrema of this energy are $\theta = 0, \pi$ for $H_a M_f t_f - J_{f-af} \geq 2K_f$, corresponding to the configuration at positive and negative saturation, and $\theta = \cos^{-1}(\frac{H_a M_f t_f - J_{f-af}}{2K_f})$ for $H_a M_f t_f - J_{f-af} \leq 2K_f$, which corresponds to the solution during rotation of the magnetization. The switching fields (forward and reverse) are calculated from the stability of the states at $\theta = 0, \pi$, which are

$$H_{c1} = -\frac{2K_f + J_{f-af}}{M_f t_f}, \quad (1.6)$$

and

$$H_{c2} = \frac{2K_f - J_{f\text{-af}}}{M_f t_f}. \quad (1.7)$$

The two switching fields are no longer equal due to the additional contribution from the interface coupling, so a hysteresis loop displaced by an amount $\frac{1}{2}(H_{c1} + H_{c2})$ is obtained,

$$H_{\text{eb}} \equiv \frac{1}{2}(H_{c1} + H_{c2}) = -\frac{J_{f\text{-af}}}{M_f t_f}. \quad (1.8)$$

The coercivity is due to the uniaxial anisotropy term in the ferromagnet,

$$H_c \equiv \frac{1}{2}|H_{c1} - H_{c2}| = \frac{2K_f}{M_f t_f}. \quad (1.9)$$

The $1/t_f$ film thickness dependence of the bias field underlines the interfacial origins of the effect, which has been verified extensively in experiment [22, 26, 30, 34, 35, 38, 70, 72, 73, 97, 107, 146, 154, 160, 170, 200, 208, 212, 236, 237, 264, 270, 278, 279]. More recently, the coherent-rotation model has been generalized to include explicit dependencies on the film thickness of the magnetic layers and the antiferromagnet magnetization [346].

Bias field estimates based on Eq. 1.8 are up to two orders of magnitude larger than experimental values. For the $\text{Ni}_{0.8}\text{Fe}_{0.2}/\text{FeMn}$ system reasonable estimates of the interlayer coupling, based on the interactions within the NiFe and FeMn layers, give $J_{f\text{-af}} 10^{-14}$ erg [22]. The bias field estimated from this figure is approximately 5 kOe, compared to the observed value of 50 Oe [22, 23]. Furthermore, the model fails to explain exchange bias in systems with *compensated* interfaces, where both antiferromagnet sublattices are exposed to the ferromagnet (Fig. 1.3c).

1.2.2 Antiferromagnet domains

It was recognized early on that the presence of an ensemble of domains at the ferromagnet/antiferromagnet interface can produce a loop shift, where an imbalance in the domain orientations occurs such that a net magnetization is generated at the antiferromagnet interface.

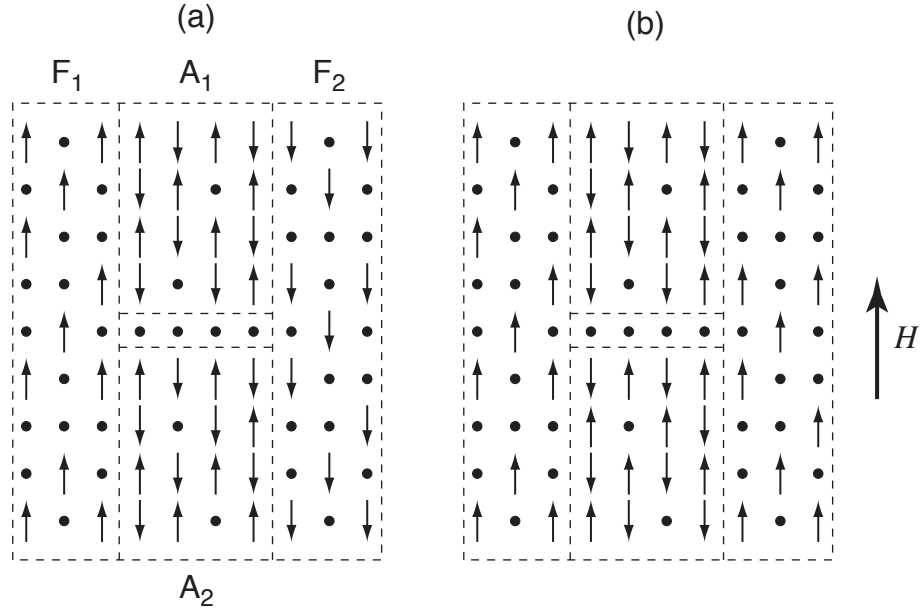


Figure 1.4: Kouvel's domain model for disordered Cu-Mn alloys. The magnetic configurations of a schematic ensemble of antiferromagnetic (A_1, A_2) and ferromagnetic (F_1, F_2) domains are shown, where it is assumed that only A and F domains with an antiferromagnetic coupling. The magnetic Mn atoms are indicated by the arrows. (a) In the ground state the net magnetization is zero in the absence of a magnetic field. (b) Field-cooling results in a net magnetization in zero field due to the configuration of the antiferromagnetic domains. After Kouvel [285].

In his study of disordered Cu-Mn systems, Kouvel showed that the presence of mutually interacting ferromagnetic and antiferromagnet domains can give rise to a shifted hysteresis curve [285]. In this picture, it is supposed the ground state of the disordered alloy can be described by a unit cell consisting of two ferromagnetic and two antiferromagnet domains, which are equal in size and oriented such that the net magnetization of the system is vanishing. An example is illustrated in Figure 1.4a. This configuration can occur with the oscillatory RKKY interaction between nearest and next-nearest neighbour spins. When the system is field cooled the second ferromagnet domain (F_2) orients with the applied field direction, causing a reorientation of the second antiferromagnetic domain (A_2) in order to satisfy the coupling (assumed to be antiferromagnetic here) between the two. The field cooled state is prevented from relaxing to the ground state, when the external field is removed, by the large uniaxial anisotropy assumed in the antiferromagnet. Thus, a unidirectional anisotropy occurs from the domain configuration set during field cooling.

Néel also recognized the possibility of obtaining exchange bias with interfacial domain structures in the antiferromagnet [286]. It was pointed out that domain wall pinning effects from such structures could lead to magnetic training effects, in the same way that domains behave in ferromagnets to give history-dependent phenomena. His work represents the first real treatment of domain-wall driven processes in the antiferromagnet to account for exchange bias. More recent treatments have examined the effects of interfacial steps [303, 313, 326, 344, 355].

Although the emerging picture of interface domains could describe the general features of exchange bias, it was difficult, from the treatments of Kouvel and Néel, to obtain estimates for domain sizes and the bias field. A novel mechanism was proposed by Malozemoff to address this issue, where it was supposed that roughness or chemical inhomogeneities at the interface result in a random exchange field between the two layers [291–293]. Following an argument by Imry and Ma [359], Malozemoff argued that the antiferromagnet should break up into domains due to the random fields in order to minimize the energy. Estimates of the bias field show an explicit link between the bias field and the domain wall energy in the antiferromagnet ($\sigma_{\text{af}} = 4\sqrt{AK_{\text{af}}}$ for a 180° Bloch wall),

$$H_{\text{eb}} = \frac{2z\sqrt{AK_{\text{af}}}}{\pi^2 M_{\text{f}} t_{\text{f}}}, \quad (1.10)$$

where A is the exchange stiffness, K_{af} is the uniaxial anisotropy constant and z is a measure of the number of unfavourable bonds across the interface.

Recent experiments have prompted a re-evaluation of Kouvel’s model to describe experimental observations of dilute antiferromagnets [132, 202, 250, 257]. In the domain-state model [333, 352, 353], the volume part of the antiferromagnet is supposed to be responsible for the bias. This can occur through the pinning of domain walls at magnetic vacancies, which form the boundaries for domain structures set during field cooling. Monte Carlo simulations show the bias can be enhanced by spin dilution in the antiferromagnet

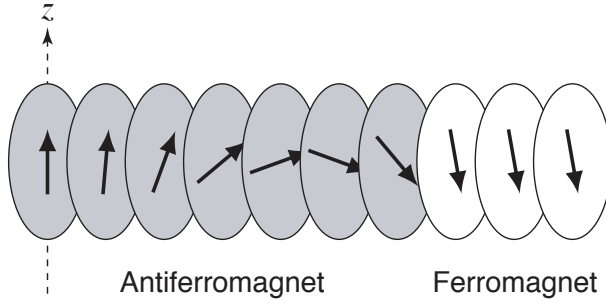


Figure 1.5: Partial wall model of exchange bias. A schematic of the magnetization profile in the ferromagnet/antiferromagnet bilayer is shown, where it is assumed that the magnetization is uniform within a layer. A twist forms in the antiferromagnet during the rotation of the ferromagnet layer. The direction of uniaxial anisotropy in the antiferromagnet is along the z -axis. Only one sublattice of the antiferromagnet is shown.

bulk, which is supported by experimental observations in CoO systems with non-magnetic Mg impurities [132, 250, 257].

1.2.3 Partial wall formation

Reasonable estimates for the bias field magnitude can be obtained, if the assumption of a rigid antiferromagnet in Meiklejohn and Bean’s treatment is relaxed, by allowing a partial domain wall to form in the antiferromagnet as the ferromagnet rotates (Figure 1.5). The partial wall provides an energy barrier that can be a factor of 10^2 smaller than the interlayer coupling $J_{\text{f-af}}$. Mauri et al. derived the following expression for the bias field assuming the formation of a 180° Bloch wall in the antiferromagnet [290],

$$H_{\text{eb}} = -\frac{2\sqrt{AK_{\text{af}}}}{M_{\text{f}}t_{\text{f}}}, \quad (1.11)$$

which underlines the dependence on the domain wall energy and is, to a large extent, independent of the interlayer coupling.^{vii} While this approach is consistent with the idea of Néel, the partial wall here is formed perpendicular to the interface (i.e. perpendicular to the film plane), which imposes a constraint on the thickness of the antiferromagnetic film. A detailed study following the work of Mauri et al. has been undertaken by Geshkev [324], and the thickness dependence of bias and trilayer structures have also been

^{vii}This is only true in the limit of large interlayer coupling, i.e. if $J_{\text{f-af}} \approx J_{\text{af}}$. This point is discussed in more detail in the following chapter.

investigated within this framework [314,323]. A partial wall energy based on Eq. 1.11 has been incorporated into more sophisticated phenomenological models for polycrystalline materials [120,304,309,330] and magnetic viscosity [320].

Extensions to the partial wall description have been made to describe compensated interfaces. Koon tackled this problem with numerical simulation and obtained bias through domain wall formation for a perpendicular alignment of the ferromagnet relative to the easy axis of the antiferromagnet [297]. The result is a 90° spin-flop coupling between the magnetization and the sublattice spins of the antiferromagnet, arising from an appreciable degree of spin-canting ($\sim 5\%$) at the interface. Schulthess and Butler showed that this partial wall is unstable to spin fluctuations out of the film plane [302]. When the assumption of planar rotation is relaxed, a centred hysteresis loop is obtained with a large coercivity. Thus, coercivity enhancement is possible from the partial wall model but at the expense of the displacement. Further work by the same authors shows that compensated interfaces can produce bias provided there are atomic dislocations at the interface [306]. The stability of the spin-flop coupling with respect to the planar anisotropy has been investigated by Wee et al. [325].

The partial wall mechanism is consistent with the requirement of antiferromagnetic order below the Néel temperature [6, 7, 10, 15, 19–21, 23, 31–33, 35–39, 42, 45, 48, 52, 56, 63, 65, 68, 70, 72, 80–82, 85, 89, 95, 96, 107–110, 117, 125, 136, 137, 139, 141, 144, 148, 152, 153, 155, 156, 158, 160, 163, 165, 166, 169, 177, 181, 185, 192, 194, 195, 200, 202, 209–211, 213, 215, 232, 235, 237, 240, 242, 245–247, 250, 252, 255, 256, 261, 264, 271, 272, 274, 279]. Experimental observations, primarily from Mn based antiferromagnets such as FeMn, indicate that there exists a critical film thickness above which bias exists that correlates well with the theoretical domain wall width in the antiferromagnet layer [32, 34, 38, 85, 119, 120, 145, 203, 256, 279]. Moreover, Yang and Chien presented evidence of a spiralling spin structure in the FeMn layer of a NiFe/FeMn/NiFe sandwich [145], where the onset of bias was close to the the-

oretical domain wall width in FeMn. Measurements performed for different orientations of the external field have revealed deviations from the simple sinusoidal dependence of the bias field as predicted by coherent rotation models [50, 61, 72, 91, 92, 100, 101, 188]. This discrepancy can be resolved with the partial wall model, as shown in Chapter Two. Observations of a preferred perpendicular alignment between the ferromagnet and antiferromagnet layers are consistent with spin-flop coupling [55, 57, 67, 88, 115, 123, 151, 194, 222].

Deformations in the magnetic structure are not restricted to the antiferromagnet layer. M. Kiwi et al. proposed the formation of a ferromagnetic partial wall to account for exchange bias at compensated interfaces [310, 311, 356]. Upon field cooling the interface antiferromagnet spins are argued to “freeze” into a spin-canted state, providing a net magnetic moment with which the ferromagnet can interact. The reversal of the magnetization causes a deformation in the ferromagnet spin profile. Numerical simulations show that the magnitude of the bias field can be accounted for by the partial ferromagnet twist, but does not predict the $1/t_f$ thickness dependence observed in experiment [22, 26, 30, 34, 35, 38, 70, 72, 73, 97, 107, 146, 154, 160, 170, 200, 208, 212, 236, 237, 264, 270, 278, 279].

The partial wall model in its present state leaves some important points undressed. The most notable failure of the model is the inability to explain a simultaneous coercivity enhancement with the bias. In fact, the theory predicts a reversible magnetization curve for an isotropic ferromagnet. It is also unclear how interface roughness and impurities would influence the process of partial wall formation, and it would be desirable to make a connection with domain formation models on this point. Finite temperatures need to be incorporated to describe realistic experimental systems and a description of the spin wave behaviour would be useful to explain data from FMR and BLS experiments.

1.3 Microscopic disorder, finite temperatures and spin waves

The complexity of exchange bias is a challenging problem. It is desirable to construct a theory that explains current observations and provides quantitative predictions for new experiments. The aim of this thesis is to develop the partial domain wall theory in order to address some of the problems and questions raised in the previous section.

A partial wall theory for perfect interfaces is developed in Chapter Two. Following the work of Mauri et al. [290], uncompensated interfaces are treated with a one-dimensional chain using a continuum approach and closed form solutions are derived in limiting cases for the bias field, including its dependence on the applied field orientation and the strength of the interlayer coupling, and the magnetization curve. A theory for compensated interfaces is developed to treat the two sublattices of the antiferromagnet explicitly. The calculated spin profile shows the existence of two intertwined walls localized to the interface in the antiferromagnet, from which a connection can be made between phenomenological bilinear and biquadratic exchange coupling terms and the microscopic spin configuration. Some attention is given to the film thickness dependence of bias, where the analytical work is supplemented by numerical simulation. Deviations from the $1/t_f$ dependence are predicted for thick ferromagnet films coupled to a rigid antiferromagnet. The stability of the spin-flop coupling at compensated interfaces to variations in the interlayer coupling is also examined.

The role of interface roughness, in the form of geometrical imperfections at the interface, is explored in Chapter Three. The imperfections are modelled by atomic steps and protrusions and the results from numerical simulations of periodic defects show drastic modifications to the angular dependence of exchange bias can occur. In particular, the period of the imperfections is shown to shift the angular positions at which the bias field attains a maximum and a minimum, which also results in the appearance of new local extrema. This behaviour is understood by a bifurcation of a natural equilibrium

orientation of the ferromagnet magnetization in the absence of an external field. Some attempt is also made to study the effects of uncorrelated roughness.

A treatment of bulk magnetic defects in the antiferromagnet follows in Chapter Four. Following the work of Braun et al. [360] the reduction in exchange or anisotropy at a local site, due to lattice strains or the presence of impurities, for example, is shown to generate an attractive potential for the partial wall that can lead to simultaneous coercivity enhancement and bias field reduction, consistent with some observations from experiments with ion-irradiation and non-magnetic impurity implantation. These changes result from a depinning of the partial wall from the interface and lead to asymmetric hysteresis loops. The angular dependence is also modified, where the pinning effects can only be seen within a certain angular range about the easy axis. This suggests an explanation of rotational hysteresis in terms of irreversible transitions effected by pinning effects. For sufficiently strong defects, the chirality of the pinned domain wall is important for governing the sense of rotation of the ferromagnet.

A discussion of some finite temperature effects forms the the topic of Chapter Five. Equilibrium thermal effects are included using a local mean-field theory. Salient features of the bias temperature dependence, such as the disappearance of the bias field and coercivity peaks at the blocking temperature, can be reproduced using the partial wall model. The study also reveals the importance of thermal domain-wall pinning processes on hysteresis, which leads to modifications at elevated temperatures in the angular dependence that should be detectable in experiment. The magnetic heat capacity is proposed as a useful probe for detecting the presence of the antiferromagnetic domain wall.

The linear excitations are examined at zero temperature in Chapter Six, with particular attention given to the properties of long-wavelength spin waves suitable for light scattering and ferromagnetic resonance experiments. Frequency shifts arising from the interlayer coupling are shown to be strongly correlated with the magnetic parameters and

spin configuration of the antiferromagnet. Crude estimates of the linewidth broadening due to interface grains and roughness are given.

In Chapter Seven, a critique of the partial wall theory and suggestions for improvements in future work are given.

Chapter 2

Partial wall theory of exchange bias

A partial wall theory of exchange bias is developed in this chapter. This approach is based on a semi-classical localized spin model and follows from the work of Néel [286] and Mauri et al. [290]. In the first half, a continuum approach is used to describe the spatial variation in the spin structure of the bilayer. For compensated interfaces the continuum approach is extended to include coupling of both sublattices to the ferromagnet explicitly, where the spin structure and energies at the interface are shown to give rise to an effective biquadratic interlayer coupling term. The analytical work is supported by a numerical model, where the ground state of the atomistic system is calculated by time-integration of the Landau-Lifshitz equation of motion for each spin. This method is applied to study the dependence of the bias on film thickness for both ferromagnet and antiferromagnet layers. Some attention is also given to the stability of the spin-flop coupling at compensated interfaces.

2.1 Effective Hamiltonian and bilayer geometry

A localized-moment Heisenberg model is used. Each magnetic layer in the bilayer film is taken to consist of interacting localized spins on a crystal lattice. The semi-classical limit is taken and each spin is represented by a vector \vec{S}_i , of constant length S , that may rotate freely in space. The Heisenberg hamiltonian with Zeeman, exchange and anisotropy

interactions for a particular spin at site i may be written in this approximation as

$$\mathcal{H}_i = -g\mu_B \vec{H}_a \cdot \vec{S}_i - \sum_j J_{ij} \vec{S}_i \cdot \vec{S}_j - K_i (\vec{S}_i \cdot \vec{n}_i)^2. \quad (2.1)$$

The first term is the Zeeman term, where H_a is the external applied field, g is the gyromagnetic ratio and μ_B is the Bohr magneton. The second term describes the exchange interaction between neighbouring spins. The summation index j represents a sum over nearest-neighbour sites and the exchange constant J_{ij} takes on one of the constant values J_f , J_{af} or J_{f-af} , which represents the coupling within the ferromagnet, within the antiferromagnet or across the interface, respectively. The exchange constants are assumed to be uniform in magnitude over the region in which they are applicable unless stated otherwise. The third term is the uniaxial crystalline anisotropy term, where the strength of the uniaxial anisotropy in the two layers are denoted by K_f and K_{af} . Similarly, these anisotropy constants are taken to be spatially uniform in the region in which they are valid. The vector \vec{n}_i represents the direction of uniaxial anisotropy at site i .

An illustration of the bilayer geometry is shown in Figure 2.1. It is assumed that the crystal structure of both films is simple cubic with a lattice constant δ and that the crystal axes are collinear with the (x, y, z) coordinate axes. The ferromagnet occupies the region $0 \leq x \leq t_f$ and is exchange coupled to an antiferromagnet layer in the region $-t_{af} \leq x < 0$. The direction of uniaxial anisotropy is parallel to the z axis in both materials. Two distinct magnetic symmetries are treated here: the uncompensated and compensated interface. Only one of the antiferromagnet sublattice species is present at the uncompensated interface (Fig. 2.1a). In a simple cubic lattice this means that all spins within a single $[010]$ (or yz -) plane are of the same species. This magnetic order can be replicated by assuming an antiferromagnetic coupling between successive layers and an effective ferromagnetic coupling between spins within a layer.¹ In contrast, there are equal numbers of spins from opposing sublattices present at the compensated interface

¹In fact, artificial antiferromagnets made from Fe/Cr superlattices, for example, are model systems for this type of magnetic symmetry.

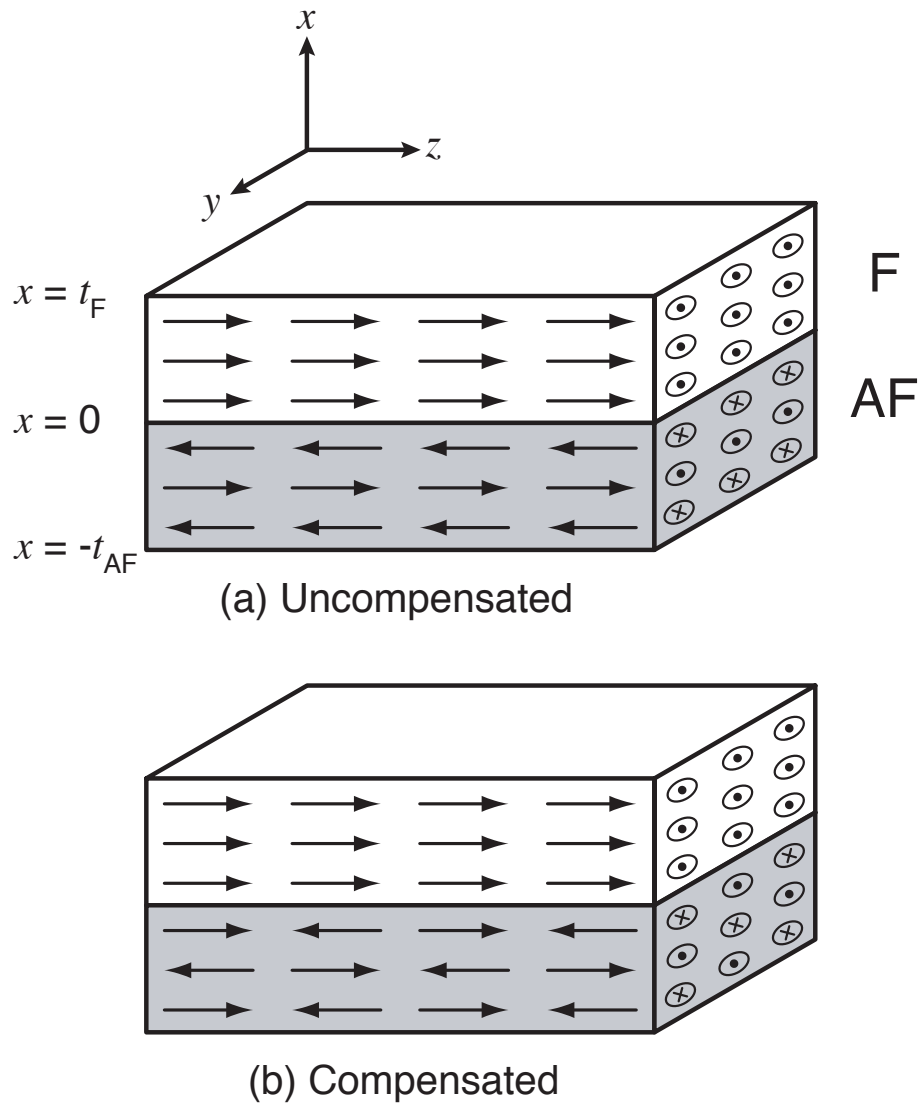


Figure 2.1: Geometry of the ferromagnet/antiferromagnet bilayer used in the continuum theory, for (a) uncompensated and (b) compensated interfaces. The thicknesses of the ferromagnet and antiferromagnet layers are designated by t_f and t_{af} , respectively. The direction of uniaxial anisotropy in the antiferromagnet is taken to lie along the z axis.

(Fig. 2.1b).

2.2 Continuum theory of uncompensated interfaces

The presence of only one antiferromagnet sublattice at the uncompensated interface allows for simple functional forms for the energies to be obtained. The total energy of the system can be represented by three components,

$$\mathcal{E}_{\text{tot}} = \mathcal{E}_{\text{f}} + \mathcal{E}_{\text{af}} + \mathcal{E}_{\text{f-af}}, \quad (2.2)$$

which describe the contributions from the ferromagnet, antiferromagnet and interface, respectively. Explicitly, these are

$$\mathcal{E}_{\text{f}} = - \sum_i g\mu_B \vec{H}_a \cdot \vec{S}_i^{\text{f}} - \sum_{\langle i,j \rangle} J_{\text{f}} \vec{S}_i^{\text{f}} \cdot \vec{S}_j^{\text{f}}, \quad (2.3)$$

$$\mathcal{E}_{\text{af}} = - \sum_{\langle i,j \rangle} J_{\text{af}} \vec{S}_i^{\text{af}} \cdot \vec{S}_j^{\text{af}} - \sum_i K_{\text{af}} (\vec{n}_{\text{af}} \cdot \vec{S}_i^{\text{af}})^2, \quad (2.4)$$

$$\mathcal{E}_{\text{f-af}} = - \sum_{\langle i,j \rangle} J_{\text{f-af}} \vec{S}_i^{\text{f}} \cdot \vec{S}_j^{\text{af}}. \quad (2.5)$$

The Zeeman energy of the antiferromagnet cancels to zero on average because of the antiparallel configuration and contributions from the magnetocrystalline anisotropy are usually much more dominant. As such, the influence of the external magnetic field on the antiferromagnet spins is neglected. The ferromagnet anisotropy is also neglected for the moment.

The problem of finding the ground state from the Hamiltonian defined in Eq. 2.1 requires solving a large set of coupled non-linear equations, however, analytical solutions can be obtained by with the aid of a few approximations. First, the spatial variations in the spin orientation in the yz plane are neglected, which allows for each magnetic layer to be described by a single vector of constant magnitude. Second, if the spatial variations along the film thickness are slow compared to the lattice constant, the magnetization can be taken to be a continuous function in x . In the ferromagnet, the orientation of the spin

at a neighbouring site $i \pm \delta$ can be written as a Taylor expansion about i ,

$$\vec{f}_{i\pm\delta} \simeq \vec{f}_i \pm \delta \frac{\partial \vec{f}_i}{\partial x} + \frac{1}{2} \delta^2 \frac{\partial^2 \vec{f}_i}{\partial x^2}, \quad (2.6)$$

where for convenience the notation $\vec{f}_i \equiv \vec{S}_i^f$ is used. The summation over all nearest-neighbour contributions gives the total exchange energy at site i ,

$$\mathcal{E}_{f,\text{ex}}^i = -J_f (\vec{f}_i \cdot \vec{f}_{i+\delta} + \vec{f}_i \cdot \vec{f}_{i-\delta}). \quad (2.7)$$

Substitution of the Taylor expansion (Eq. 2.6) into the equation above gives

$$\mathcal{E}_{f,\text{ex}}^i = -z J_f \vec{f}_i \cdot \vec{f}_i + D_f \vec{f}_i \cdot \frac{\partial^2 \vec{f}_i}{\partial x^2}, \quad (2.8)$$

where $z = 6$ is the coordination number of the crystal and $D_f \equiv \frac{1}{2} z \delta^2 J_f$ is the exchange stiffness. A similar expansion can be made for the antiferromagnet if a staggered magnetization is used for the region $-t_{\text{af}} \leq x < 0$ [361],

$$\vec{a}_i = (-1)^i \vec{S}_i^{\text{af}}. \quad (2.9)$$

To ensure the original energy (Eq. 2.1) remains invariant, the sign of the antiferromagnet exchange constant must change in this representation, i.e. $J_{\text{af}} \rightarrow -J_{\text{af}}$, such that the corresponding exchange stiffness $D_{\text{af}} \equiv -\frac{1}{2} z \delta^2 J_{\text{af}}$ is always positive. Because the lengths of the magnetization vectors are taken to be constant, the profile can be parametrized by a set of position dependent angles to specify the spin orientation at any point. Let $\phi(x), \varphi(x)$ and θ_{H} represent the angles (measured from the z axis) corresponding to the vectors $\vec{f}(x), \vec{a}(x)$ and \vec{H}_{a} , respectively. The terms in Eq. 2.2 can be converted into the following integral forms using these definitions,

$$\mathcal{E}_f[\phi(x), \varphi(x)] = \int_0^{t_f} dx \left[D_f \left(\frac{\partial \phi}{\partial x} \right)^2 - H_{\text{a}} \cos(\phi - \theta_{\text{H}}) \right], \quad (2.10)$$

$$\mathcal{E}_{\text{af}}[\phi(x), \varphi(x)] = \int_{-t_{\text{af}}}^0 dx \left[D_{\text{af}} \left(\frac{\partial \varphi}{\partial x} \right)^2 + K_{\text{af}} \sin^2(\varphi) \right], \quad (2.11)$$

with the interfacial exchange energy being

$$\mathcal{E}_{f\text{-af}} = -J_{f\text{-af}} \cos(\phi_0 - \varphi_0), \quad (2.12)$$

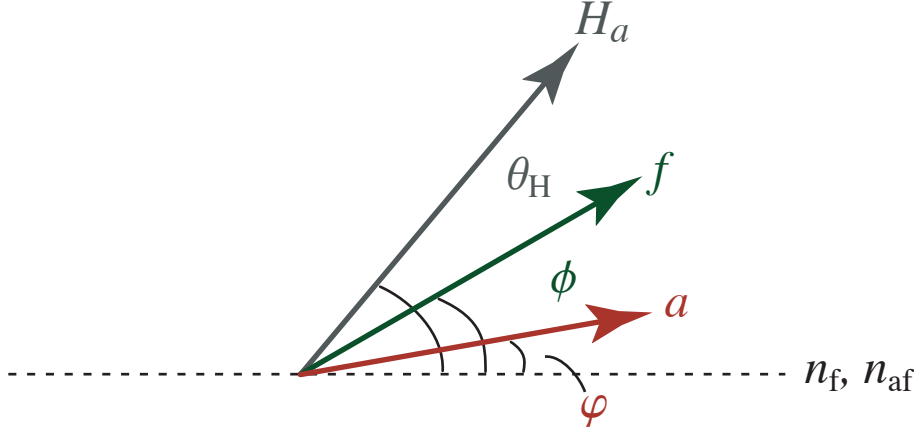


Figure 2.2: Geometry of the partial wall model for perfect uncompensated interfaces. The orientation of the antiferromagnet (\vec{a}), ferromagnet (\vec{f}) and applied field vectors (\vec{H}_a) are parametrized by the angles φ , ϕ , and θ_H , respectively. n_{af} refers to the axis of anisotropy in the antiferromagnet.

where $\phi_0 \equiv \phi(x=0)$ and $\varphi_0 \equiv \varphi(x=0)$ specify the angles of the interfacial ferromagnet and antiferromagnet spins, respectively.

To determine the equilibrium spin profile, a variational technique is used to calculate the functions $\phi(x)$ and $\varphi(x)$ that minimize the energies given in Eqs. 2.10 and 2.11. By assuming a small function $\eta(x)$ that deviates slightly from the minimum energy solution,

$$\mathcal{E}_{\text{tot}}[\phi(x) + \eta(x), \varphi(x)] = \mathcal{E}_{\text{tot}}[\phi(x), \varphi(x)] + \int_{-\infty}^{\infty} dx \eta(x) \frac{\delta \mathcal{E}}{\delta \phi} + O(\eta^2), \quad (2.13)$$

the following Euler-Lagrange equation is obtained by setting the $\frac{\delta \mathcal{E}}{\delta \phi}$ term equal to zero,

$$D_f \frac{\partial^2 \phi}{\partial x^2} - H_a M_f \cos(\phi(x) - \theta_H) = 0. \quad (2.14)$$

This has the corresponding boundary condition,

$$2D_f \left(\frac{\partial \phi}{\partial x} \right)_{x=0} = -J_{f\text{-af}} \sin(\phi_0 - \varphi_0). \quad (2.15)$$

Similarly, the functional derivative of the energy with respect to $\varphi(x)$ yields the following Euler-Lagrange equation,

$$D_f \frac{\partial^2 \varphi}{\partial x^2} - \frac{1}{2} K_{\text{af}} \sin(2\varphi(x)) = 0, \quad (2.16)$$

and gives a derivative-matching boundary condition for the functions at the interface,

$$D_f \left(\frac{\partial \phi}{\partial x} \right)_{x=0} = D_{\text{af}} \left(\frac{\partial \varphi}{\partial x} \right)_{x=0}. \quad (2.17)$$

The Euler-Lagrange equation for $\phi(x)$ (Eq. 2.14) is integrated once to give

$$\left(\frac{\partial\phi}{\partial x}\right)^2 + \frac{2}{\delta_f^2} \cos(\phi(x) - \theta_H) = C, \quad (2.18)$$

where a characteristic length of the ferromagnet is defined as

$$\delta_f^2 \equiv \frac{D_f}{H_a M_f}. \quad (2.19)$$

It is assumed that the gradient in the spin profile vanishes at $x = -t_f$ and that the orientation of the ferromagnet is parallel to the external field, so the first order equation can be integrated to give

$$\phi(x, \theta_H) = 4 \tan^{-1} \left[\exp\left(\frac{x - x_f}{\delta_f}\right) \right] + \theta_H. \quad (2.20)$$

For the antiferromagnet the same procedure gives a partial Bloch wall solution for the spin profile,

$$\varphi(x) = 2 \tan^{-1} \left[\exp\left(\frac{x - x_{af}}{\lambda_{af}}\right) \right], \quad (2.21)$$

where the characteristic length of the antiferromagnet is

$$\delta_{af}^2 \equiv \frac{D_{af}}{K_{af}}. \quad (2.22)$$

The shift constants x_f and x_{af} are determined by the boundary conditions.

The energies of the two layers are found by substituting the calculated profiles into Eqs. 2.10 and 2.11, giving

$$\mathcal{E}_{\text{tot}}(\phi_0, \varphi_0, \theta_H) = \frac{1}{4} \sigma_f \sin^4\left(\frac{\phi_0 - \theta_H}{2}\right) + \frac{1}{2} \sigma_{af} (1 - \cos(\varphi_0)) - J_{f-af} \cos(\phi_0 - \varphi_0), \quad (2.23)$$

where the first two terms represent the partial wall energies in the ferromagnet and antiferromagnet layers, respectively, with the scale of the wall energies defined as $\sigma_f \equiv 12\sqrt{D_f H_a M_f}$ and $\sigma_{af} \equiv 4\sqrt{D_{af} K_{af}}$. The equilibrium wall profile is found by minimizing the energy in Eq. 2.23 with respect to the two interface angles, giving the conditions

$$\frac{1}{4} \sigma_f \sin\left(\frac{\phi_0 - \theta_H}{2}\right) = -J_{f-af} \sin(\phi_0 - \varphi_0); \quad (2.24)$$

$$\tan(\varphi_0) = \frac{\sigma_{af}}{J_{f-af}} \sec(\phi_0) + \tan(\phi_0). \quad (2.25)$$

With the energy given by Eq. 2.23 and the minimization conditions the spin profile is completely specified for any arbitrary value of the magnetic constants, provided the continuum approximation still applies.

2.3 Bias field and magnetization curves

The magnetization curve can be derived from the total energy (Eq. 2.23) in the limit of large interlayer coupling. For simplicity the ferromagnet is taken to be uniform and reversal takes place via coherent rotation. The interlayer coupling is assumed to be sufficiently large such that the interfacial ferromagnet and antiferromagnet spins are effectively “locked” together, reducing the total energy to a sum of the field and antiferromagnet partial wall contributions,

$$\mathcal{E}_{\text{tot}} = -H_a M_f t_f \cos(\phi_0 - \theta_H) + \frac{1}{2} \sigma_{\text{af}} (1 - \cos(\phi_0)). \quad (2.26)$$

The equilibrium ferromagnet orientation, for a given value of the external field, is found by setting the derivative of the energy with respect to ϕ_0 to zero,

$$\frac{\partial \mathcal{E}_{\text{tot}}}{\partial \phi_0} = 0, \quad (2.27)$$

which yields the condition

$$\tan(\phi_0) = \frac{h \sin(\theta_H)}{1 + h \cos(\theta_H)}. \quad (2.28)$$

h is a dimensionless field variable defined as

$$h \equiv \frac{2H_a M_f t_f}{\sigma_{\text{af}}}. \quad (2.29)$$

The component of the magnetization along the field direction, M/M_s , is $\cos(\theta_H - \phi_0)$,

$$\frac{M}{M_s} \equiv \cos(\theta_H - \phi_0) = \frac{h + \cos(\theta_H)}{\sqrt{h^2 + 2h \cos(\theta_H) + 1}}, \quad (2.30)$$

which is obtained after substitution of Eq. 2.28 into $\cos(\theta_H - \phi_0)$. Some examples of hysteresis curves calculated using Eq. 2.30 are shown in Figure 2.3 for several field orientations. The sharpest transitions occur when the applied field is directed collinear to

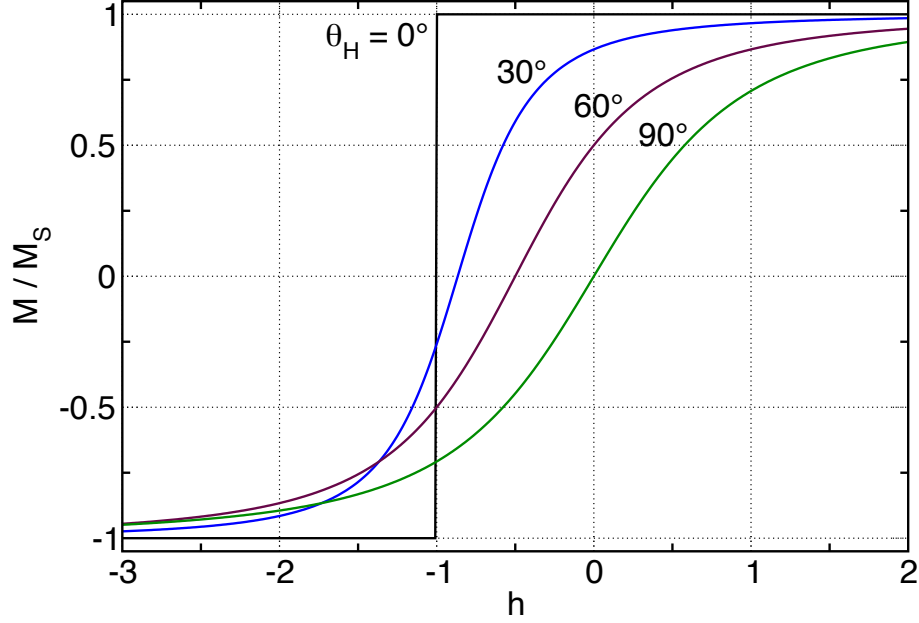


Figure 2.3: Magnetization curves from analytical model for uncompensated interfaces for several field orientations. The ferromagnet is taken to be uniform and the interfacial spins are rigidly coupled. The component of ferromagnet magnetization along the field direction M/M_s is shown as a function of a dimensionless field variable $h \equiv 2H_a M_f t_f / \sigma_{af}$.

the easy axis of the antiferromagnet ($\theta_H = 0^\circ$). The magnetization curves get gradually smoother as the field is rotated away from the easy axis, with the bias shift vanishing when the field is applied perpendicular to the easy axis. Because the magnetization curves are reversible in the absence of ferromagnet anisotropy an expression for the bias field can be obtained simply by setting the numerator of Eq. 2.30 to zero,

$$\text{i.e. } h + \cos(\theta_H) = 0,$$

$$H_{eb} = \frac{\sigma_{af} \cos(\theta_H)}{2M_f t_f}. \quad (2.31)$$

Thus, the expression derived by Mauri et al. [290] is obtained with the addition of an angular dependence in the applied field orientation.

2.4 Angular dependence of the bias field

A more realistic angular dependence of the bias field can be obtained by relaxing the assumption of locked interface spins. The total energy becomes

$$\mathcal{E}_{\text{tot}} = -H_a M_f t_f \cos(\phi_0 - \theta_H) - J_{f\text{-af}} \cos(\phi_0 - \varphi_0) + \frac{1}{2} \sigma_{af} (1 - \cos(\varphi_0)), \quad (2.32)$$

where an additional degree of freedom is included by allowing the relative orientation between the interface spins to vary. To obtain the bias field, the equilibrium spin profile is calculated first by minimizing the energy with respect to the ferromagnet angle ϕ_0 ,

$$\tan(\phi_0) = \frac{J_{\text{f-af}} \sin(\varphi_0) + H_{\text{a}} M_{\text{f}} t_{\text{f}} \sin(\theta_{\text{H}})}{J_{\text{f-af}} \cos(\varphi_0) + H_{\text{a}} M_{\text{f}} t_{\text{f}} \cos(\theta_{\text{H}})}, \quad (2.33)$$

and with respect to the antiferromagnet angle φ_0 ,

$$\tan(\varphi_0) = \frac{J_{\text{f-af}} \sin(\phi_0)}{\frac{1}{2} \sigma_{\text{af}} + J_{\text{f-af}} \cos(\phi_0)}, \quad (2.34)$$

giving two conditions for the interface angles. The bias field is defined as the zero-crossing of the magnetization curve, or equivalently, the point at which the magnetization is perpendicular to the applied field direction.ⁱⁱ As such, the ferromagnet orientation at $H = -H_{\text{eb}}$ is $\phi_0 = \frac{\pi}{2} - \theta_{\text{H}}$, which upon substitution into the second condition above gives

$$\tan(\varphi_0) = \frac{J_{\text{f-af}} \cos(\theta_{\text{H}})}{\frac{1}{2} \sigma_{\text{af}} + J_{\text{f-af}} \sin(\theta_{\text{H}})}, \quad (2.35)$$

In turn, this equation is substituted into the first condition to give an expression for the bias field ($0 \leq \theta_{\text{H}} \leq 180^\circ$),

$$H_{\text{eb}} = \frac{J_{\text{f-af}}}{M_{\text{f}} t_{\text{f}}} \frac{\cos(\theta_{\text{H}})}{\sqrt{\mathcal{J}_1^2 + 2\mathcal{J}_1 \sin(\theta_{\text{H}}) + 1}}, \quad (2.36)$$

where \mathcal{J}_1 is a constant that measures the strength of the interlayer exchange relative to the antiferromagnet partial wall energy,

$$\mathcal{J}_1 \equiv \frac{2J_{\text{f-af}}}{\sigma_{\text{af}}}. \quad (2.37)$$

The angular dependence of the bias field is shown in Figure 2.4 for three values of \mathcal{J}_1 of different orders of magnitude. For small values of the interlayer coupling ($\mathcal{J}_1 = 0.01$) the denominator approaches unity, so the angular variation of H_{eb} is close to a simple cosine dependence. In fact, the bilinear constant \mathcal{J}_1 vanishes in the limit that the interlayer

ⁱⁱThis is true for coherent rotation of an isotropic ferromagnet. The calculation considered here does not apply to reversal processes that take place through domain wall propagation.

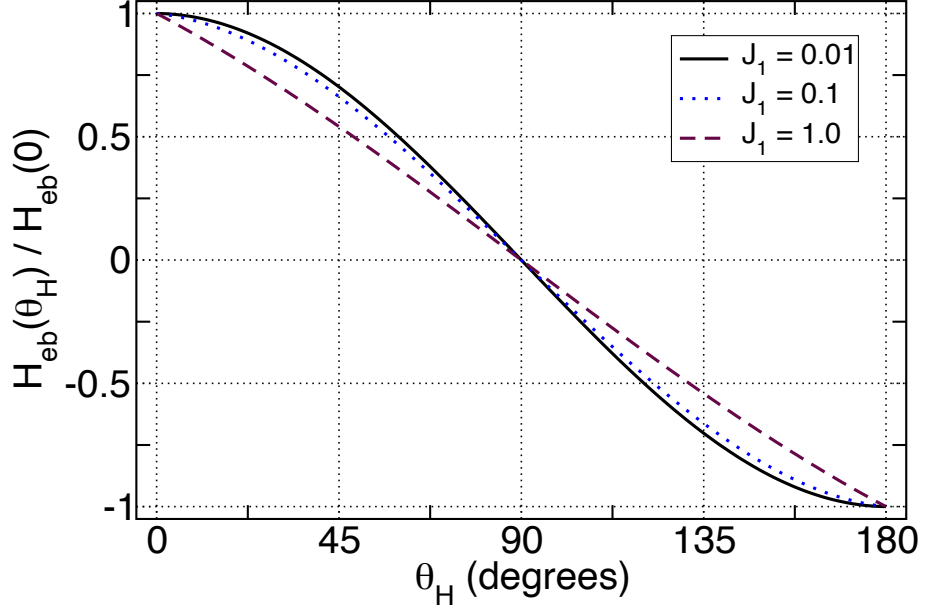


Figure 2.4: Predicted angular dependence of the bias field from the partial wall model. The bias field is normalized to the value at $\theta_H = 0$ and is shown for three values of the scaled interlayer coupling constant $\mathcal{J}_1 \equiv 2J_{f-af}/\sigma_{af}$.

coupling is much smaller than the domain wall energy in the antiferromagnet, $J_{f-af} \ll \sigma_{af}$ and Meiklejohn and Bean's result is recovered,

$$H_{eb} = \frac{J_{f-af} \cos(\theta_H)}{M_f t_f}, \quad (2.38)$$

which states that the bias field is proportional to J_{f-af} . In the opposite limit of large interlayer coupling, $J_{f-af} \gg \sigma_{af}$, the interface spins are effectively locked together and the bias field is proportional to the wall energy,

$$H_{eb} = \frac{\sigma_{af} \cos(\theta_H)}{2M_f t_f}, \quad (2.39)$$

which is equivalent to the expression derived by Mauri et al. [290] with the inclusion of an angular dependence shown earlier (Eq. 2.31). In this limit the angular variation of H_{eb} again takes a simple cosine form.

Deviations from the simple cosine dependence are due to changes in the angle between the interface spins ($\phi_0 - \varphi_0$) during reversal. For the limit $J_{f-af} \ll \sigma_{af}$, the antiferromagnet spins do not deviate from the easy axis so the angle between the interface moments is always the same as the ferromagnet angle ϕ_0 . In the opposite limit $J_{f-af} \gg \sigma_{af}$,

	$\mathcal{J}_1 = 0.01$	$\mathcal{J}_1 = 0.1$	$\mathcal{J}_1 = 1$
a_1	1	1	1
a_3	0.002520	0.022884	0.085714
a_5	0.000609	0.006165	0.030303
a_7	0.000284	0.002902	0.015385
a_9	0.000166	0.001699	0.009288

Table 2.1: Cosine series coefficients a_n for three different coupling constants \mathcal{J}_1 , normalized to the lowest order term a_1 .

the interface spins are always locked together so there are no deviations in the relative orientation $\phi_0 - \varphi_0$. A simple cosine dependence is obtained in both limiting cases because the quantity $\phi_0 - \varphi_0$ is proportional to the ferromagnet orientation ϕ_0 . Departures from this behaviour result when the rate at which $\phi_0 - \varphi_0$ varies changes as the ferromagnet rotates. This is demonstrated in Fig. 2.4 when \mathcal{J}_1 is comparable to unity, where a “sharp” variation in H_{eb} is seen as a function of θ_{H} .

The departure from a simple cosine variation may be quantified by expanding Eq. 2.36 in a cosine series,

$$H_{\text{eb}}(\theta_{\text{H}}) = \frac{J_{\text{f-af}}}{M_{\text{f}} t_{\text{f}}} \sum_{n=0}^{\infty} a_n \cos(n\theta_{\text{H}}), \quad (2.40)$$

where the coefficients are determined by the inner product

$$a_n = \frac{2}{\pi} \int_{-\frac{\pi}{2}}^{\frac{\pi}{2}} \frac{\cos(\theta_{\text{H}}) \cos(n\theta_{\text{H}})}{\sqrt{\mathcal{J}_1^2 + 2\mathcal{J}_1 \sin(\theta_{\text{H}}) + 1}} d\theta_{\text{H}}. \quad (2.41)$$

All terms with even n vanish because of the unidirectional anisotropy. The cosine series coefficients for the cases considered in Fig. 2.4 are shown in Table 2.1.

The angular dependence of exchange bias was first addressed in experiments with NiFe/CoO bilayers [50], where it was recognized that the simple $\cos(\theta_{\text{H}})$ dependence predicted from coherent rotation models was inadequate to describe experimental observations. With a Fourier analysis of the experimental data, it was found that contributions

from higher order terms can be as large as 21% as the $\cos(\theta_H)$ term. Subsequent experiments with amorphous $\text{Co}_{65}\text{Mo}_2\text{B}_{33}$ ferromagnets showed a simpler angular dependence with the absence of any ferromagnet anisotropy, where the largest higher order contribution (from $\cos(3\theta_H)$) amounts to $\sim 2\%$ [61]. This is in good agreement with the angular dependence derived with the partial wall model for interlayer coupling constants in the range $0.1 \leq \mathcal{J}_1 \leq 1.0$.

2.5 Continuum theory of compensated and mixed interfaces

Both sublattices of the antiferromagnet are in contact with the ferromagnet layer at compensated interfaces. In the absence of interface roughness or impurities there are, in principle, equal populations of a and b sublattice spins. At first glance it appears the exchange coupling between the two layers is independent of the ferromagnet orientation because of the zero net antiferromagnet moment at the interface. Koon showed that a perpendicular coupling between the two magnetic layers can occur due to spin canting of the antiferromagnet spins [297], analogous to the spin-flop state. This canting generates a small net moment to which the ferromagnet can couple, which allows for bias through the formation of a partial twist in the compensated structure.

The continuum treatment is extended in this section to include explicitly the two sublattice species in the antiferromagnet.ⁱⁱⁱ The antiferromagnet energy and the interfacial coupling are modified to include the extra terms associated with the second sublattice, represented by \vec{b}_i ,

$$\mathcal{E}_{\text{af}} = \sum_{\langle i,j \rangle} |J_{\text{af}}| \vec{a}_i \cdot \vec{b}_j + \frac{1}{2} \sum_i K_{\text{af}} ((\vec{n}_{\text{af}} \cdot \vec{a}_i)^2 + (\vec{n}_{\text{af}} \cdot \vec{b}_i)^2), \quad (2.42)$$

$$\mathcal{E}_{\text{f-af}} = \frac{1}{2} \sum_{\langle i,j \rangle} (J_{\text{a}} \vec{f}_i \cdot \vec{a}_j + J_{\text{b}} \vec{f}_i \cdot \vec{b}_j). \quad (2.43)$$

The sublattice spins are allowed to couple to the ferromagnet with different strengths J_{a}

ⁱⁱⁱThis approach differs from previous work based on a disordered uncompensated interface [13].

and J_b , and the effect of the external field on the antiferromagnet is neglected.

To apply the continuum approach it is necessary to make expansions based on the staggered magnetization for both sublattices. It is assumed that the magnetization for each sublattice is uniform in each magnetic layer. Let \vec{S}_i^a and \vec{S}_i^b represent the sublattice vectors for a given layer i . The staggered magnetizations \vec{a} and \vec{b} are defined as

$$\{\vec{a}_i\} = \{\cdots, \vec{S}_{i-2}^a, -\vec{S}_{i-1}^b, \vec{S}_i^a, -\vec{S}_{i+1}^b, \vec{S}_{i+2}^a, \cdots\}, \quad (2.44)$$

$$\{\vec{b}_i\} = \{\cdots, \vec{S}_{i-2}^b, -\vec{S}_{i-1}^a, \vec{S}_i^b, -\vec{S}_{i+1}^a, \vec{S}_{i+2}^b, \cdots\}, \quad (2.45)$$

which can be expanded in a Taylor series in the usual way,

$$\vec{a}_{i\pm 1} \simeq \vec{a}_i \pm \delta \frac{\partial}{\partial x} \vec{a}_i + \frac{1}{2} \delta^2 \frac{\partial^2}{\partial x^2} \vec{a}_i. \quad (2.46)$$

Next, a transformation using longitudinal and transverse vectors is made to describe the spin-canting in the antiferromagnet,

$$\vec{l}_i \equiv \frac{1}{\sqrt{2}}(\vec{a}_i - \vec{b}_i), \quad (2.47)$$

$$\vec{t}_i \equiv \frac{1}{\sqrt{2}}(\vec{a}_i + \vec{b}_i), \quad (2.48)$$

The longitudinal and transverse vectors are parametrized by the angles λ_i and τ_i , respectively, measured from the anisotropy axis. These definitions are illustrated in Figure 2.5. The vectors \vec{l}_i and \vec{t}_i are always perpendicular to each other in a given layer and represent an orthogonal basis for the orientation of the two sublattice spins. It is therefore unnecessary to keep track of both angles λ_i and τ_i . Instead, the angle α_i measured between the \vec{a}_i and \vec{t}_i vectors is used. Thus, the orientation of the two sublattice spins for each layer can be completely specified by two angles λ_i and α_i , where the latter enters as a vector magnitude,

$$l_i \equiv |\vec{l}_i| = \sqrt{2} \sin(\alpha_i), \quad (2.49)$$

$$t_i \equiv |\vec{t}_i| = \sqrt{2} \cos(\alpha_i), \quad (2.50)$$

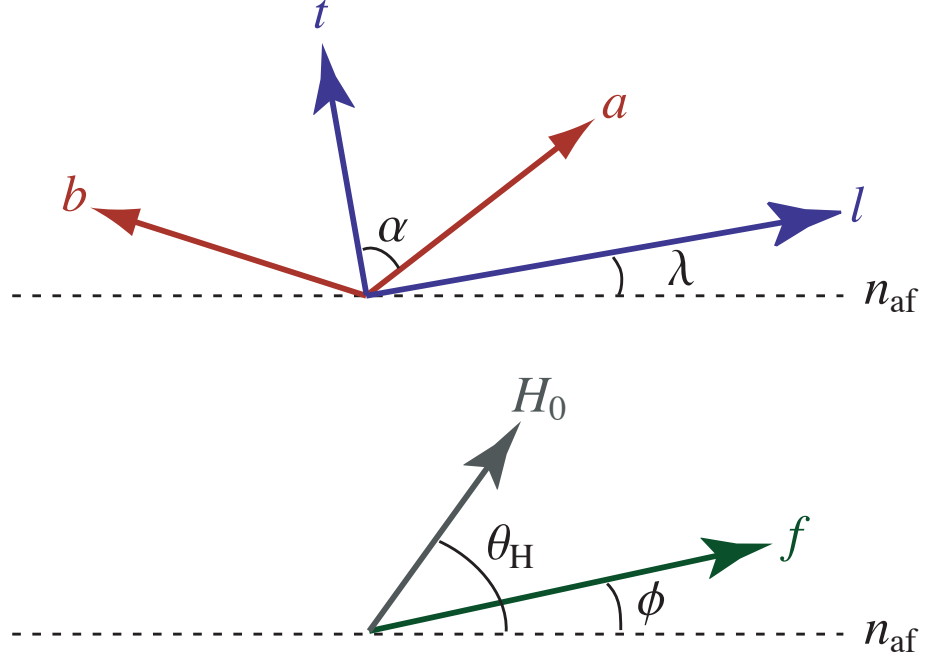


Figure 2.5: Geometry for the two-sublattice model. The sublattices vectors, \vec{a} and \vec{b} , are redefined in terms of a longitudinal and transverse vectors, \vec{l} and \vec{t} , which are in turn parametrized by the angles λ and α . The lower panel illustrates the convention used to parametrize the external field (\vec{H}_0) and ferromagnet orientation (\vec{f}) with θ_H and ϕ , respectively. n_{af} refers to the axis of anisotropy in the antiferromagnet.

With these definitions the antiferromagnet and interface exchange coupling energies in the continuum approximation can be written as

$$\mathcal{E}_{af}[\lambda(x), \alpha(x)] = \int_{-t_{af}}^0 dx \left\{ |D_{af}| \left[\left(\frac{\partial \alpha(x)}{\partial x} \right)^2 + \left(\frac{\partial \lambda(x)}{\partial x} \right)^2 \right] + \zeta |J_{af}| \cos[2\alpha(x)] + \frac{1}{2} K_{af} \cos[2\alpha(x)] \cos[2\lambda(x)] \right\}, \quad (2.51)$$

$$\mathcal{E}_{f-af}(\phi_0, \lambda_0, \alpha_0) = J_+ \cos(\alpha_0) \sin(\phi_0 - \lambda_0) + J_- \sin(\alpha_0) \sin(\phi_0 - \lambda_0), \quad (2.52)$$

where $\zeta = 4$ represents the number of nearest-neighbour spins in the yz -plane and the interfacial exchange constants are defined as $J_{\pm} \equiv \frac{1}{2}(J_a \pm J_b)$.

The equilibrium spin profiles for $\vec{l}(x)$ and $\vec{t}(x)$ are obtained by varying the total energy with respect to the three angles $\phi(x)$, $\lambda(x)$ and $\alpha(x)$,

$$\frac{\delta \mathcal{E}_{tot}}{\delta \phi} = \frac{\delta \mathcal{E}_{tot}}{\delta \lambda} = \frac{\delta \mathcal{E}_{tot}}{\delta \alpha} = 0. \quad (2.53)$$

The total energy, $\mathcal{E}_{tot} = \mathcal{E}_f + \mathcal{E}_{af} + \mathcal{E}_{f-af}$, comprises the terms given by Eqs. 2.10, 2.51 and 2.52. The Euler-Lagrange equations for $\lambda(x)$ and $\alpha(x)$ are obtained from setting the

appropriate functional derivatives to zero,

$$\frac{\partial^2 \lambda}{\partial x^2} + \frac{K_{\text{af}} \cos(\alpha)}{2|D_{\text{af}}|} \sin(2\lambda) = 0, \quad (2.54)$$

$$\frac{\partial^2 \alpha}{\partial x^2} + \frac{2\zeta|J_{\text{af}}| + K_{\text{af}} \cos(2\lambda)}{2|D_{\text{af}}|} \sin(2\alpha) = 0, \quad (2.55)$$

with the corresponding boundary conditions,

$$D_{\text{f}} \left(\frac{\partial \phi}{\partial x} \right)_{x=0} = |D_{\text{af}}| \left(\frac{\partial \lambda}{\partial x} \right)_{x=0}, \quad (2.56)$$

$$-2|D_{\text{af}}| \left(\frac{\partial \lambda}{\partial x} \right)_{x=0} = J_+ \cos(\alpha_0) \cos(\phi_0 - \lambda_0) - J_- \sin(\alpha_0) \sin(\phi_0 - \lambda_0), \quad (2.57)$$

$$-2D_{\text{af}} \left(\frac{\partial \alpha}{\partial x} \right)_{x=0} = J_+ \sin(\alpha_0) \sin(\phi_0 - \lambda_0) - J_- \cos(\alpha_0) \cos(\phi_0 - \lambda_0), \quad (2.58)$$

$$\left(\frac{\partial \phi}{\partial x} \right)_{x=t_{\text{f}}} = \left(\frac{\partial \lambda}{\partial x} \right)_{x=-t_{\text{af}}} = \left(\frac{\partial \alpha}{\partial x} \right)_{x=-t_{\text{af}}} = 0. \quad (2.59)$$

The Euler-Lagrange equations for $\lambda(x)$ and $\alpha(x)$ are similar to the form for a Bloch wall, where the correspondence can be seen upon comparison of Eqs. 2.54 and 2.55 with Eq. 2.16. This suggests that the spin profile in the antiferromagnet is a combination of two Bloch wall profiles, one in the longitudinal component of the spins that is analogous to the partial wall profile in the uncompensated case, and a second intertwined wall in the angle $\alpha(x)$, representing a partial wall in the spin-flop profile. Schematic representations of these profiles are shown in Figure 2.6. The equations are coupled through the prefactor representing the domain wall width, which suggests that the effective wall widths are angular dependent.

Closed-form solutions to these coupled equations can be obtained if the length scales of the two wall structures are very different. In the limit of weak anisotropy in the antiferromagnet, $J_{\text{af}} \gg K_{\text{af}}$, the $\lambda(x)$ wall is much larger than spatial variations in $\alpha(x)$. Based on the spin-flop picture proposed by Koon, one expects the largest variation in α to occur at the interface [297]. The spin-flop profile decays very rapidly from the interface to a bulk value of $\frac{\pi}{2}$. The Euler-Lagrange equations can be decoupled by assuming that this decay occurs over a region $-\delta_{\text{sf}} < x < 0$ near the interface in which the magnitude of

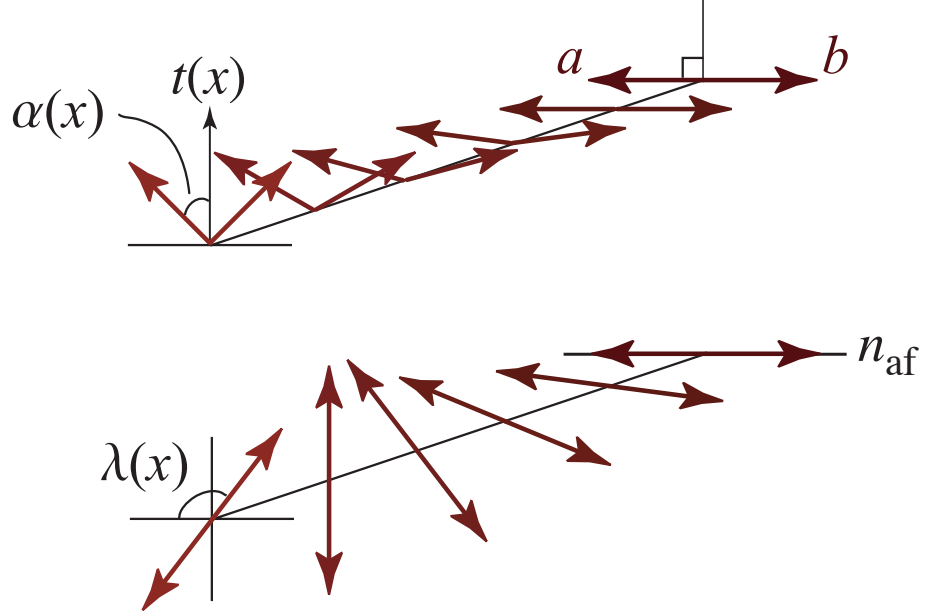


Figure 2.6: Schematic spin profile illustrating the two intertwined domain walls in the antiferromagnet. (a) The spin-flop wall extends from the interface with a decay length δ_{sf} and is parametrized by the angle α , which is measured from the direction of the local vector \vec{t} . (b) The partial Bloch wall profile, with characteristic width δ_{af} , is formed by the rotation of the ferromagnet layer and is parametrized by the angle λ , which is measured from the direction of uniaxial anisotropy in the antiferromagnet.

$\lambda(x)$ is constant in magnitude, i.e. $\delta_{sf} \ll \delta_{af}$. In this approximation the antiferromagnet energy can be decomposed into a spin-flop energy (\mathcal{E}_{sf}) and a partial Bloch wall energy (\mathcal{E}_{bw}),

$$\begin{aligned} \mathcal{E}_{af} = \mathcal{E}_{sf} + \mathcal{E}_{bw} &= \int_{-\delta_{sf}}^0 f_{sf}(x) dx + \int_{-t_{af}}^{-\delta_{sf}} f_{bw}(x) dx, \\ &\simeq \int_{-t_{af}}^0 f_{sf}(x) dx + \int_{-t_{af}}^0 f_{bw}(x) dx, \end{aligned} \quad (2.60)$$

where

$$\begin{aligned} f_{sf}(x) &= |D_{af}| \left(\frac{\partial \alpha}{\partial x} \right)^2 + \zeta |J_{af}| \cos(2\alpha) + \frac{1}{2} K_{af} \cos(2\alpha) \cos(2\lambda_0), \\ &= |D_{af}| \left[\left(\frac{\partial \alpha}{\partial x} \right)^2 + \frac{1}{2\delta_{sf}^2} \cos(2\alpha) \right]; \end{aligned} \quad (2.61)$$

$$\begin{aligned} f_{bw}(x) &= |D_{af}| \left(\frac{\partial \lambda}{\partial x} \right)^2 - \frac{1}{2} K_{af} \cos(2\lambda), \\ &= |D_{af}| \left[\left(\frac{\partial \lambda}{\partial x} \right)^2 - \frac{1}{2\delta_{af}^2} \cos(2\lambda) \right]. \end{aligned} \quad (2.62)$$

The variations in $\alpha(x)$ occur over a constant background λ_0 , corresponding to the angle of the longitudinal vector at the interface. The characteristic length for the spin flop decay,

δ_{sf} , is governed by the interfacial angle λ_0 ,

$$\delta_{\text{sf}}^2 \equiv \frac{|D_{\text{af}}|}{2\zeta J_{\text{af}} + K_{\text{af}} \cos(2\lambda_0)}. \quad (2.63)$$

This approximation decouples the two Euler-Lagrange equations and allows each to be solved independently. The first integral of Eq. 2.55 gives

$$\left(\frac{\partial\alpha(x)}{\partial x}\right)^2 - \frac{1}{\delta_{\text{sf}}^2} \cos^2(\alpha(x)) = C. \quad (2.64)$$

At the antiferromagnet film surface ($x = -t_{\text{af}}$) the gradient in the magnetization is assumed to vanish and the untwisted bulk value of $\alpha(x) = \frac{\pi}{2}$ is attained. The integration constant C vanishes when these boundary conditions are applied. The solution has the partial Bloch wall form,

$$\alpha(x) = 2 \tan^{-1} \exp\left(-\frac{x - x_{\text{sf}}}{\delta_{\text{sf}}}\right) - \frac{\pi}{2}, \quad (2.65)$$

where the shift constant x_{sf} , determined by the boundary conditions, is related to the interface angle α_0 by

$$x_{\text{sf}} = \delta_{\text{sf}} \ln \tan\left(\frac{\alpha_0}{2} + \frac{\pi}{4}\right). \quad (2.66)$$

To calculate the profile for $\lambda(x)$ under the weak anisotropy approximation, α is assumed to be equal to $\frac{\pi}{2}$ over the thickness of the antiferromagnet film. This defines a length scale for the variation in $\lambda(x)$ characteristic for a 180° Bloch wall,

$$\delta_{\text{af}}^2 \equiv \frac{|D_{\text{af}}|}{K_{\text{af}}}. \quad (2.67)$$

The first integral of Eq. 2.54 is

$$\left(\frac{\partial\lambda}{\partial x}\right)^2 - \frac{1}{\delta_{\text{af}}^2} \sin^2(\lambda) = C'. \quad (2.68)$$

Again, the constant C' vanishes after the boundary conditions are applied and the following spatial profile for the longitudinal vector of the antiferromagnet is obtained,

$$\lambda(x) = 2 \tan^{-1} \exp\left(\frac{x - x_{\text{af}}}{\delta_{\text{af}}}\right). \quad (2.69)$$

The shift constant x_{af} is related to the interface angle λ_0 by

$$x_{\text{af}} = \delta_{\text{af}} \ln \tan\left(\frac{\lambda_0}{2}\right), \quad (2.70)$$

and is a useful measure of the extent of the partial antiferromagnet twist formed.

The partial wall energies are computed by substituting the calculated profiles into the decoupled energy terms. The energy of the spin-flop structure is

$$\mathcal{E}_{\text{sf}} = \sigma_{\text{sf}} (1 - \sin(\alpha_0)), \quad (2.71)$$

where σ_{sf} represents the energy of a 90° spin-flop wall and is equal to $2|D_{\text{af}}|/\delta_{\text{sf}}$. The energy of the partial Bloch wall structure is parametrized by the interface angle λ_0 ,

$$\mathcal{E}_{\text{af}} = \frac{1}{2} \sigma_{\text{af}} (1 - \cos(\lambda_0)), \quad (2.72)$$

where as usual $\sigma_{\text{af}} \equiv 4|D_{\text{af}}|/\delta_{\text{af}}$ represents the energy of a 180° Bloch wall.

2.6 Bilinear and biquadratic coupling

A mixed interface can be studied by allowing different exchange constants between the two sublattices and the ferromagnet, i.e. $J_{\text{a}} \neq J_{\text{b}} \Rightarrow J_+, J_- \neq 0$. Using the expression for $\alpha(x)$ derived in the previous section, the corresponding boundary condition can be written as

$$\begin{aligned} \frac{2|D_{\text{af}}|}{\delta_{\text{sf}}} \cos(\alpha_0) &= J_+ \sin(\alpha_0) \sin(\phi_0 - \lambda_0) - J_- \cos(\alpha_0) \cos(\phi_0 - \lambda_0), \\ \text{i.e. } \tan(\alpha_0) &= \frac{\kappa_c \left(\frac{\sigma_{\text{sf}}}{J_-} + \cos(\phi_0 - \lambda_0) \right)}{\sin(\phi_0 - \lambda_0)}, \end{aligned} \quad (2.73)$$

where κ_c is a measure of the degree of compensation,

$$\kappa_c \equiv \frac{J_-}{J_+} = \frac{J_{\text{a}} - J_{\text{b}}}{J_{\text{a}} + J_{\text{b}}}. \quad (2.74)$$

A manipulation of the condition in Eq. 2.73 gives

$$\begin{aligned} \cos(\alpha_0) &= \frac{\kappa_c}{\gamma} \left(\frac{\sigma_{\text{sf}}}{J_-} + \cos(\phi_0 - \lambda_0) \right), \\ \sin(\alpha_0) &= \frac{1}{\gamma} \sin(\phi_0 - \lambda_0), \end{aligned}$$

where γ is defined as

$$\gamma \equiv \kappa_c^2 \left(\frac{\sigma_{\text{sf}}}{J_-} + \cos(\phi_0 - \lambda_0) \right)^2 + \sin^2(\phi_0 - \lambda_0). \quad (2.75)$$

The dependence of the interlayer coupling energy on α_0 can be eliminated with the boundary condition above,

$$\mathcal{E}_{\text{f-af}} = -\frac{\kappa_c \sigma_{\text{sf}}}{\gamma} \cos(\phi_0 - \lambda_0) - \frac{J_+(1 - \kappa_c^2)}{\gamma} \sin^2(\phi_0 - \lambda_0). \quad (2.76)$$

This form shows two contributions with distinctly different symmetries. The first term represents a bilinear exchange interaction between the two magnetic layers and is associated with the ferromagnet coupling to the net moment of uncompensated spins. The bilinear term prefers a collinear alignment between the interface moments \vec{f}_0 and \vec{l}_0 , and the sign of the coupling depends on the difference between the constants J_a and J_b . The second term represents a biquadratic interaction between the ferromagnet and the interface longitudinal component of the antiferromagnet. This coupling favours a perpendicular alignment between \vec{f}_0 and \vec{l}_0 and is reminiscent of the interaction proposed by Slonczewski to account for the behaviour in coupled magnetic films [362].

The bilinear term is largest when κ_c is unity, which is only possible when one of the sublattice constants J_a or J_b vanishes, and corresponds to the limit of a fully *uncompensated* interface. Notice that the second term vanishes in this limit, which leaves a pure bilinear exchange coupling. Taking $J_b = 0$,

$$\gamma^2 = 1 + 2 \left(\frac{2\sigma_{\text{sf}}}{J_a} \right) \cos(\phi_0 - \lambda_0) + \left(\frac{2\sigma_{\text{sf}}}{J_a} \right)^2,$$

a similar form of the interlayer coupling for uncompensated interfaces derived in Section 2.4 is recovered,

$$\mathcal{E}_{\text{f-af}} = -\frac{J_a \cos(\phi_0 - \lambda_0)}{2\sqrt{1 + 2\left(\frac{J_a}{2\sigma_{\text{sf}}}\right) \cos(\phi_0 - \lambda_0) + \left(\frac{J_a}{2\sigma_{\text{sf}}}\right)^2}}. \quad (2.77)$$

κ_c vanishes in the limit of a fully *compensated* interface ($J_a = J_b$). The factor γ becomes

$$\gamma^2 = \frac{\sigma_{\text{sf}}}{\mathcal{J}_2} \left(1 + \frac{\mathcal{J}_2}{\sigma_{\text{sf}}} \sin^2(\phi_0 - \lambda_0) \right), \quad (2.78)$$

where a biquadratic coupling constant \mathcal{J}_2 is defined as

$$\mathcal{J}_2 \equiv \frac{J_+^2}{\sigma_{\text{sf}}}. \quad (2.79)$$

The interlayer coupling energy in this limit is

$$\mathcal{E}_{\text{f-af}} = -\mathcal{J}_2 \sin^2(\phi_0 - \lambda_0) \left(1 + \frac{\mathcal{J}_2}{\sigma_{\text{sf}}} \sin^2(\phi_0 - \lambda_0) \right)^{-\frac{1}{2}}. \quad (2.80)$$

For a mixed interface the exchange coupling between the two layers can be described as a combination of bilinear and biquadratic interactions. This description is appropriate for partial compensated interfaces, where there may be a mixture of uncompensated and compensated regions in contact with the ferromagnet. Several authors have used the idea of competing bilinear and biquadratic terms in some phenomenological models of exchange bias [304,309,320,330]. Hence, the work here establishes a direct connection between the microscopic Hamiltonian and the phenomenological coupling terms and so justifies their use to treat partial compensation.

2.7 Numerical integration of equations of motion

To treat systems with arbitrary values of the magnetic parameters, it is necessary to solve the original Hamiltonian (Eq.2.1) directly because the approximations used to justify the continuum approach are not always valid. In antiferromagnets with large anisotropy, for example, variations in the spin orientations within a domain wall can occur over a few atomic sites. A numerical technique for calculating the equilibrium configuration is outlined in this section.

A schematic diagram illustrating the geometry of the numerical model is shown in Figure 2.7. Following the formulation earlier, the bilayer is taken to consist of sheets of spins with a simple cubic structure, oriented parallel to the surface of the film. The ferromagnet and antiferromagnet layers have the same lattice constant to give a perfect

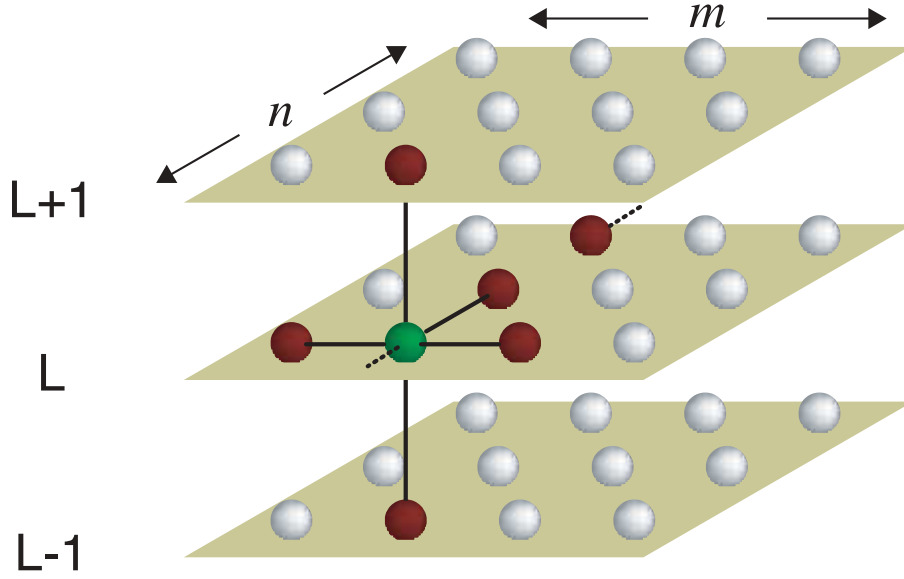


Figure 2.7: Geometry for the discrete numerical model. The bilayer is taken to consist of sheets of spins with a simple-cubic structure. Each layer L is represented by a unit cell $m \times n$ atoms in size and periodic boundary conditions are applied to the cell edges. The solid lines indicate exchange bonds within the unit cell and the broken lines indicate the mapping across the cell edges.

lattice-matched bilayer structure. A unit cell of spins is used to represent the magnetization distribution within each layer, where the cell is taken to be $m \times n$ atoms in size and periodic boundary conditions are applied to the unit cell edges in the plane of the film. The bilayer has a finite thickness, with t_f denoting the number of layers in the ferromagnet and t_{af} the number of layers in the antiferromagnet.

The dynamics associated with each spin is described by the equation of motion derived from commuting the local spin operator with the Hamiltonian given by Eq. 2.1,

$$-i\hbar \frac{\partial \vec{S}_n}{\partial t} = [\vec{S}_n, \mathcal{H}_n], \quad (2.81)$$

which, after application of the usual commutation relations, gives the precessional motion of the spin about its local effective field direction,^{iv}

$$\frac{\partial \vec{S}_n}{\partial t} = \gamma \vec{S}_n \times \vec{H}_n^{\text{eff}}. \quad (2.82)$$

γ is a gyromagnetic constant and the effective field \vec{H}_n^{eff} is equivalent to the gradient in

^{iv}A derivation is given by Herring and Kittel [363].

the local energy with respect to the spin variables,

$$\begin{aligned}\vec{H}_i^{\text{eff}} &= -\frac{1}{g\mu_B}\nabla_{\vec{S}_i}\mathcal{E}, \\ &= \vec{H}_a + \frac{1}{g\mu_B}\left(\sum_j J_{ij}\vec{S}_j + 2K_i(\vec{S}_i \cdot \vec{z})\vec{z}\right).\end{aligned}\quad (2.83)$$

The gyromagnetic constant is defined by

$$\gamma \equiv \frac{ge\mu_0}{2m_0},$$

where g is the gyromagnetic ratio, e is the electron charge, μ_0 is the permeability of free space and m_0 refers to the mass of the magnetic moment.

The dynamics governed by Eq. 2.82 does not include dissipation, which means that it cannot describe the change in the static orientation that takes place during magnetization processes. Relaxation can be included with a phenomenological damping term of the form

$$\frac{\partial \vec{S}_i}{\partial t} = \gamma \vec{S}_i \times \vec{H}_i^{\text{eff}} - \alpha \vec{S}_i \times \dot{\vec{S}}_i \times \vec{H}_i^{\text{eff}}, \quad (2.84)$$

first introduced by Landau and Lifshitz. The damping term represents a motion perpendicular to both \vec{S}_n and the force $\vec{S}_n \times \vec{H}_n^{\text{eff}}$ that acts on the precessional motion. The coefficient α is related to a relaxation frequency and is a measure of the degree of damping of the precession. This quantity can only be determined from experiment. Other forms of damping are also possible, such as the Gilbert and Bloch-Bloembergen equations, but the important feature of the Landau-Lifshitz forms is that the magnitude of the spin vectors is always conserved.^v

The ground state is found by integrating the coupled set of non-linear differential equations described by Eq. 2.84. Although the dynamical equation describes the motion of a spin about its local field axis, complexity arises because this local field is constantly changing due to the motion of all the other spins. Any solution must therefore be obtained

^vAn excellent discussion of relaxation in ferromagnetic materials is given by Sparks [364].

	J (meV)	T_{crit} (K)	K (meV/spin)	t_{film} (ML)
Ferromagnet (f)	45.0	1043	0	20
Antiferromagnet (af)	-3.40	79	0.34	20
	$J_{\text{f-af}}$ (meV)	θ_{H}	T (K)	
	-3.40	10°	0	

Table 2.2: Magnetic parameters for the numerical model. These are the numerical values used unless specified otherwise.

through some self-consistent means, where at equilibrium all spins are aligned parallel to their local fields.

A combination of single step and multistep time integration methods are used to calculate the equilibrium configuration in this dissertation. For details concerning the numerical model, the reader is referred to Appendix A. The magnetic parameters for the model are chosen be representative of typical exchange bias systems, where the Curie temperature is roughly an order of magnitude larger than the Néel temperature. The mean-field exchange constants are chosen to give ordering temperatures appropriate for a Fe/FeF₂ system. The ferromagnet and antiferromagnet layers are taken to consist of 20 monolayers (ML) each. The interlayer exchange constant is identical in sign and magnitude as the antiferromagnet exchange. The magnitude of the uniaxial anisotropy is an order of magnitude smaller than the antiferromagnetic exchange, such that the spatial extent of the partial wall formed is contained within the antiferromagnet film. The external field is applied at an angle of $\theta_{\text{H}} = 10^\circ$ from the easy axis^{vi} and the calculations are performed at zero temperature. It is convenient to express all field quantities H in terms of a reduced unit based on the ferromagnet film thickness t_{f} and the energy of a

^{vi}This is a nominal value of the field orientation. Angular dependence studies of the bias field and coercivity are undertaken throughout this dissertation.

180° Bloch wall in the antiferromagnet σ_{af} ,

$$h = \frac{2H M_{\text{f}} t_{\text{f}}}{\sigma_{\text{af}}}. \quad (2.85)$$

Unless specified otherwise, the magnetic parameters used in all calculations presented in this dissertation are listed in Table 2.2.

2.8 Antiferromagnet film thickness dependence

The dependence of exchange bias on the antiferromagnet film thickness is studied in this section with the numerical model. This is a non-trivial calculation because finite-size effects should become important when the antiferromagnet is sufficiently thin. In particular, the size of t_{af} is important for determining the existence of a partial wall.

An underlying assumption of the continuum formulation is that the antiferromagnetic film is sufficiently thick to support a twist. For film thicknesses below the domain wall width, one would expect partial wall driven bias to vanish. To explore this idea, the numerical simulation is used to probe a range of thicknesses of the antiferromagnet. Following Koon [297], the antiferromagnet energy is examined as a function of twist angle for a series of film thicknesses. The results for uncompensated interfaces are shown in Figure 2.8. The antiferromagnet is initially aligned along the easy axis direction (φ_0). The interface spin is then rotated by a small amount and the system is allowed to relax to equilibrium. The energy of the antiferromagnet is computed and the configuration serves as the initial state for the next angle. For thin films ($t_{\text{af}} = 2, 4$ ML) the rotation of the interface spin is a reversible process. The energy curves possess a mirror symmetry about $\varphi_0 = 0$ and $\varphi_0 = \pm 90^\circ$, which indicates that the entire antiferromagnet layer follows the rotation of the interface spin coherently. The symmetry is consistent with the two-fold symmetry of a uniaxial anisotropy. For thicker films ($t_{\text{af}} = 8 - 20$ ML) the mirror symmetry about $\varphi_0 = \pm 90^\circ$ disappears. As the interface moment rotates the energy increases on a path that approaches σ_{af} as $\varphi_0 \rightarrow \pm 180^\circ$, but makes a sudden transition to a lower

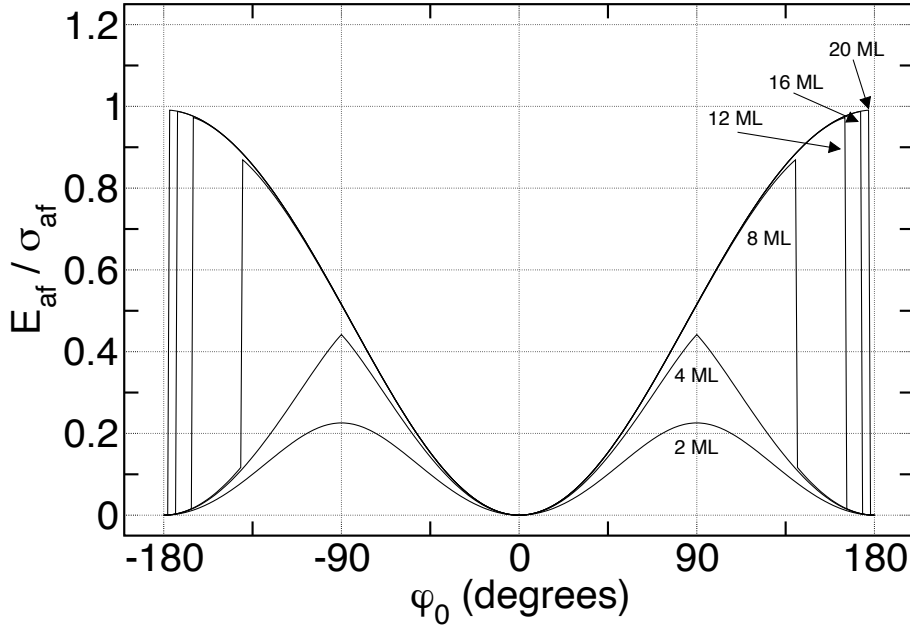


Figure 2.8: The antiferromagnet energy \mathcal{E}_{af} , normalized to the domain wall energy σ_{af} , is shown as a function of the antiferromagnet interface spin angle φ_0 for a series of film thickness t_{af} .

energy configuration when the extent of the partial wall form exceeds the film thickness.

This transition is an irreversible process.

In light of these results, one expects, for a given field orientation, that there should be a transition between irreversible and reversible rotations of the antiferromagnet as the film thickness t_{af} is increased. In Figure 2.9, the bias field and coercivity is shown as a function of t_{af} . The graph shows that there is indeed a sharp transition between a state with no bias and a state with a finite loop shift, indicated by the sharp jump from $h_{\text{eb}} = 0$ to $h_{\text{eb}} \simeq 0.85$ at approximately $t_{\text{af}} = 10$ ML. The critical thickness here is less than the domain wall width, but with the particular field orientation at $\theta_{\text{H}} = 10^\circ$ used, it turns out that the extent of the partial wall formed corresponds to roughly 75% of a 180° wall. These results are consistent with the experimental observation that the bias vanishes below a critical antiferromagnet film thickness that correlates well with the theoretical domain wall width of the material [32, 34, 38, 85, 119, 120, 145, 203, 279].

The coercivity for films below the critical thickness is due to the effective anisotropy introduced into the ferromagnet, resulting from the irreversible rotations of the antiferromagnet spins as seen in Fig. 2.8. In this regime, H_c increases with increasing film

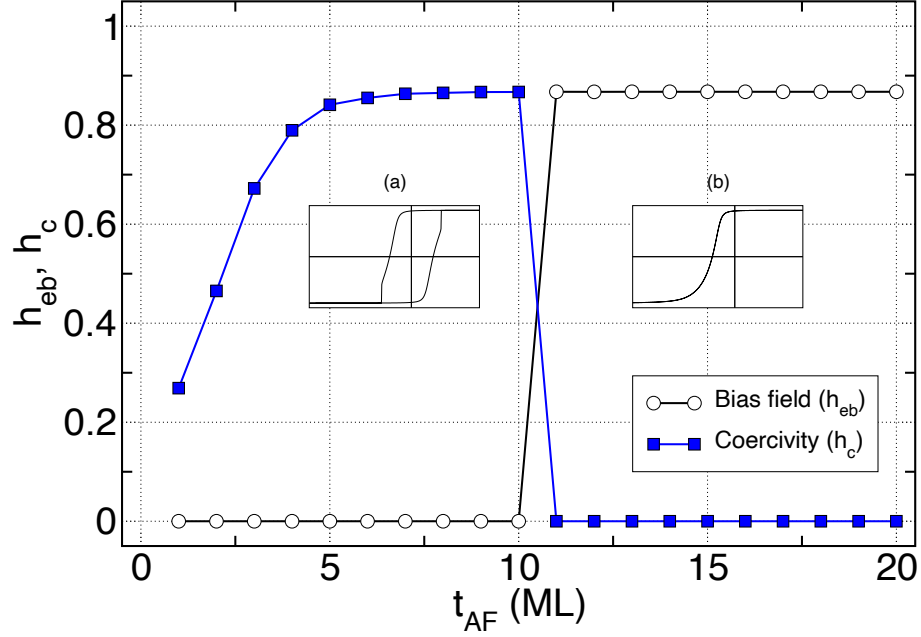


Figure 2.9: Bias field and coercivity variations with film thickness of the antiferromagnet film t_{af} . All fields are expressed in reduced units of $h = 2H_a M_f t_f / \sigma_{af}$. The insets shown the schematic magnetization curves for (a) $t_{af} = 5$ ML and (b) $t_{af} = 15$ ML.

thickness t_{af} because of the increase in antiferromagnet volume (and therefore the total anisotropy energy). Above the critical thickness, the rotation of the antiferromagnet spins is reversible and results in a shifted magnetization curve with no coercivity. Increases in film thickness above the critical value do not affect the hysteresis properties because the partial twist is localized to the interface; no deformations farther away into the antiferromagnet bulk are incurred. Similar results have been obtained by Xi and White [314], who showed using energy minimization techniques that such irreversible processes occur for antiferromagnet film thicknesses below a certain critical value.

2.9 Ferromagnet film thickness dependence

Partial wall formation in the ferromagnet layer may also occur. Kiwi et al. argued that deformations in the ferromagnet spins can take place if the interface antiferromagnet spins adopt a “frozen” configuration after field cooling [310, 311, 328, 356]. Such a state can be realized in the numerical simulation by using a large anisotropy constant in the antiferromagnet, taken to be $K_{af} = 6.8$ meV/spin for this calculation. All other

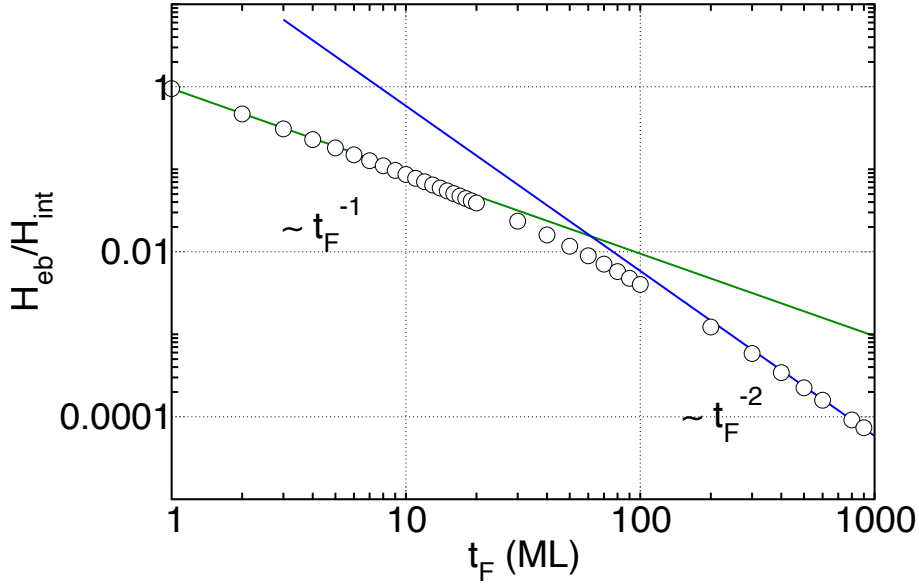


Figure 2.10: Bias field variations with film thickness of an isotropic ferromagnet t_f . The bias field given is normalized to the effective field generated by the interlayer exchange coupling, $H_{\text{int}} = J_{\text{f-af}}/g\mu_B$.

parameters are unchanged and the results are shown in Figure 2.10. The bias fields are normalized to the magnitude of the effective field due to the interlayer exchange.

From continuum theory, the bias field is predicted to be inversely proportional to the ferromagnet film thickness. This is obtained under the assumption that the magnetization rotates uniformly. This assumption is valid for thin films because deformations in the spin structure incur a high energy cost. However, this cost is reduced for thicker films and deviations from a $1/t_f$ dependence appear between $t_f = 10$ and 100 ML. Some examples of the ferromagnet spin profile are given in Figure 2.11, where the spatial variation in the magnetization is shown at maximum reverse field. For progressively thicker films the spatial extent of the twist structure formed increases. Because the exchange fields are much larger than the typical applied field values used to measure a hysteresis loop, it is preferable to minimize the exchange energy by spreading the twist over a large region. However, the Zeeman energy counterbalances this spread by preferring all spins to be aligned parallel to the field, and the result is a field-dependent wall width.

The departure from the $1/t_f$ dependence can be obtained from the continuum treatment presented in Section 2.2 by allowing the partial wall to form in the ferromagnet.

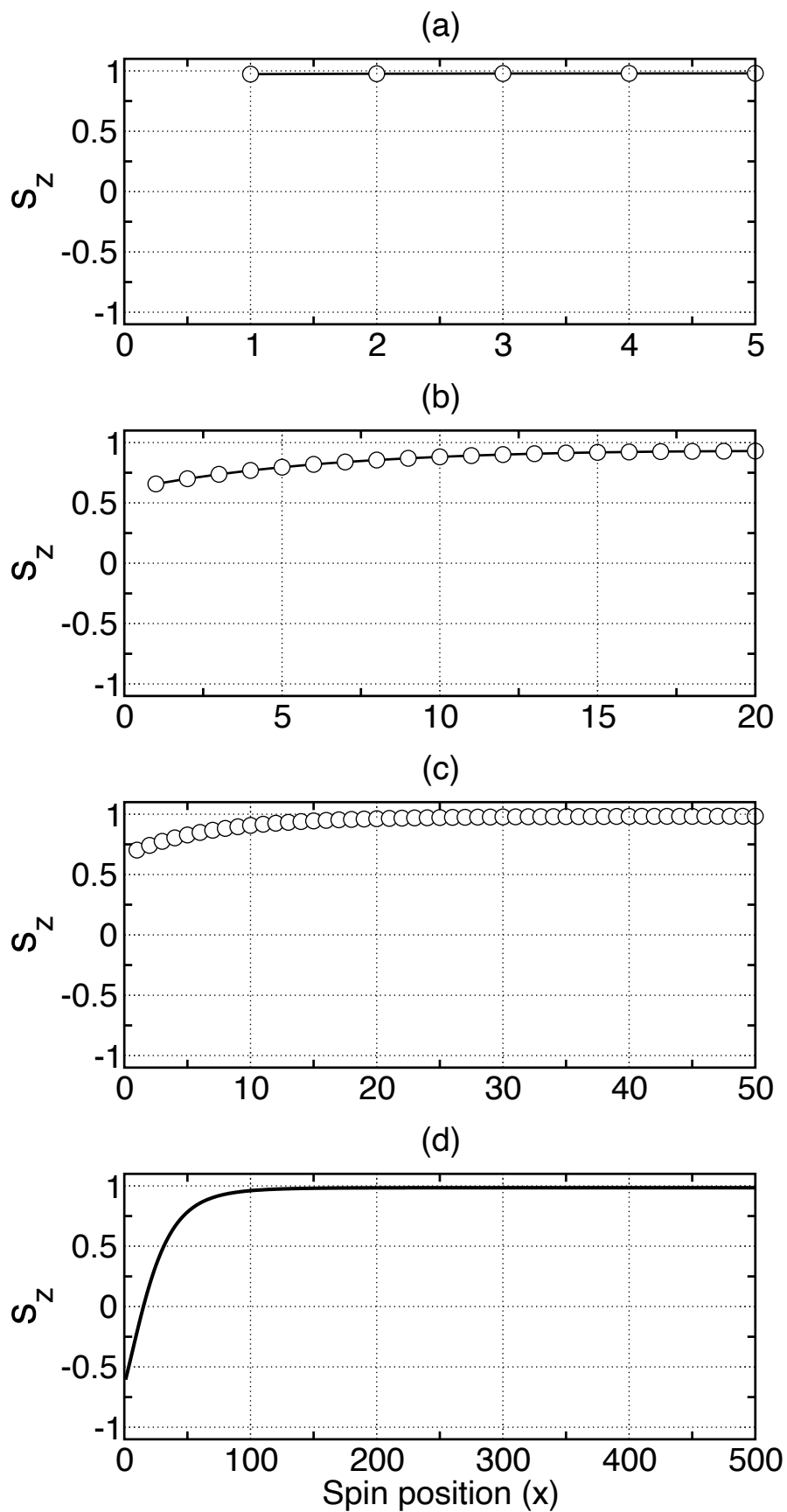


Figure 2.11: Magnetization profile of ferromagnet partial wall. The spatial profile of the spins at maximum reverse field is given for a series of ferromagnet film thicknesses: (a) 5 ML, (b) 20 ML, (c) 50 ML and (d) 500 ML. $x = 1$ is the interface layer of the ferromagnet. Note that the ferromagnet layer is isotropic.

Recall that the energy of this partial wall was obtained by substituting the wall profile given by Eq. 2.20 into Eq. 2.10, giving

$$\mathcal{E}_f = \sigma_f \sin^2\left(\frac{\theta_H - \phi_0}{4}\right), \quad (2.86)$$

where the characteristic wall energy scale is $\sigma_f = 12\sqrt{D_f H_a M_f}$. Notice that the energy and width of the partial wall are field dependent quantities. An expression for the bias field is obtained by comparing the energy of the forward and reverse field configurations of the system. At small negative fields $H_a < H_{eb}$ the ferromagnet magnetization remains saturated in the positive field direction and is held in place by the interlayer exchange coupling. The energy of this configuration is

$$\mathcal{E}_+ = H_a M_f t_f - J_{f-af}. \quad (2.87)$$

At sufficiently large negative fields, the reversal of the magnetization causes a partial twist to form in the ferromagnet. Neglecting any deviations in the antiferromagnet spins, the energy of the reverse field configuration is

$$\mathcal{E}_- = -H_a M_f t_f - J_{f-af} \cos(\phi_0) + \sigma_f \sin^2\left(\frac{\phi_0}{4}\right). \quad (2.88)$$

The energies \mathcal{E}_+ and \mathcal{E}_- are identical at the bias field. Equating these two expressions for $H_a = H_{eb}$ gives a quadratic equation for $\sqrt{H_{eb}}$,

$$H_{eb} - b\sqrt{H_{eb}} - c = 0, \quad (2.89)$$

where

$$b = \frac{6}{t_f} \sqrt{\frac{D_f}{M_f}} \sin^2\left(\frac{\phi_0}{4}\right), \quad (2.90)$$

$$c = \frac{J_{f-af}}{M_f t_f} (1 - \cos(\phi_0)). \quad (2.91)$$

Solving for H_{eb} ,

$$H_{eb} = \frac{b^2}{2} \pm \frac{b}{2} \sqrt{b^2 + 4c} + c. \quad (2.92)$$

The expression above shows a more complicated dependence of the bias field on the ferromagnet film thickness, where H_{eb} contains terms proportional to both $1/t_f$ and $1/t_f^2$. This is in agreement with the numerically determined results in Fig. 2.10, where the $1/t_f$ form at small t_f evolves into a $1/t_f^2$ dependence for thick films.

The inclusion of a small non-zero uniaxial anisotropy in the ferromagnet results in a Bloch wall profile for the partial twist. By analogy with the results for the antiferromagnet, a critical thickness for the ferromagnet is anticipated for the formation of a domain wall. The bias field and coercivity as a function of t_f are shown in Figure 2.12 for $K_f = 0.009$ meV/spin. A deviation from a $H_{\text{eb}} \propto 1/t_f$ behaviour is again observed at thick films, where the bias is accompanied by a non-zero coercivity above $t_f = 70$ ML. The inclusion of the ferromagnet uniaxial anisotropy allows for reversal via domain wall propagation perpendicular to the interface. This is the mechanism for thick films ($t_f > 200$ ML) where the bias field and coercivity are observed to be largely independent of film thickness, because the reversal fields in this regime only depend on the energy required for wall nucleation. An asymmetry between forward and reverse paths exists because of the coupling to the antiferromagnet, but this difference is small as the loop shift is approximately three orders of magnitude smaller than the interface field.

A similar crossover behaviour from $H_{\text{eb}} \propto 1/t_f$ to $H_{\text{eb}} \propto 1/t_f^2$ was obtained recently by Méjia-López et al. based on a discrete spin model [356]. It was found from numerical simulations that the bias field should approach a $t_f^{-1.9}$ dependence for thicker films. The results from the continuum theory above are in agreement with this finding, although experimental evidence for this behaviour is still lacking. For thicker films, one would expect that domain wall propagation processes along the thickness of the film to be important. A distinction between partial wall formation and wall propagation in the ferromagnet could be made in experiment by measuring the dependence of the bias field for thick films.

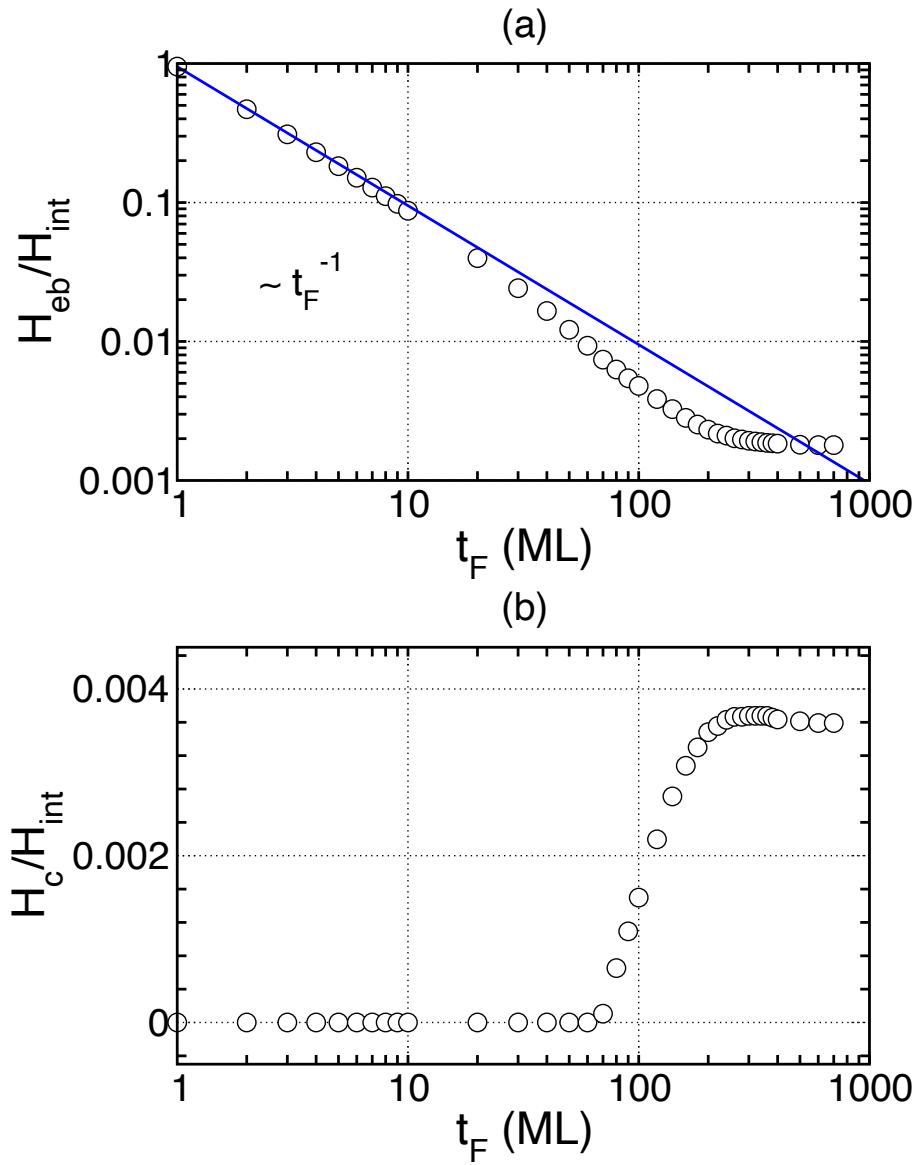


Figure 2.12: Bias field variations with film thickness of an anisotropic ferromagnet t_f . The bias field given is normalized to the effective field generated by the interlayer exchange coupling, $H_{int} = J_{f-af}/g\mu_B$. The anisotropy in the ferromagnet is $K_f = 0.009$ meV/spin.

2.10 Stability of spin-flop coupling

Koon demonstrated that bias for compensated systems is possible through an induced spin-flop coupling at the interface [297]. It was shown that frustration of the sublattice spins, resulting from a preferred antiparallel alignment between \vec{f}_0 , \vec{a}_0 and \vec{b}_0 , leads to a spin-canted state that generates a small net moment to which the ferromagnet can couple. Although the stability of this coupling was called into question from further theoretical studies by Schulthess and Butler [302, 306], the spin-flop interaction can give bias through partial wall formation provided the spins are constrained to rotate in the film plane. The details of planar rotation have been studied by Stamps and Wee [325], who showed that bias disappears when the planar anisotropy is below a certain critical value. The stability of the spin-flop coupling to variations in the strength of the interlayer coupling is studied in this section.

Bias is only non-zero for a finite range of $J_{\text{f-af}}$ values. In Figure 2.13, the results from hysteresis loops calculated for a series of $J_{\text{f-af}}$ values are shown. The applied field is oriented at $\theta_{\text{H}} = 80^\circ$, where the offset of 10° from the bias direction is chosen to minimize computation time. Two different antiferromagnet anisotropy constants are also considered: $K_{\text{af}} = 0.17$ and 0.34 meV/spin. For the first, the range of values for which $h_{\text{eb}} > 0$ is roughly $3J_{\text{af}} \leq J_{\text{f-af}} \leq 8J_{\text{af}}$. Outside of this range the hysteresis loops are symmetric about $h = 0$ and exhibit a coercive field that is comparable to the loop shift observed in the bias region. This behaviour is emphasized by plotting h_{eb} and h_{c} as a function of $J_{\text{f-af}}$ on the same graph, where the smooth variation in the non-zero values of h_{eb} and h_{c} can be seen. A similar trend is seen when K_{af} is halved, where the cut-offs for bias only differ in numerical value.

The stability of the spin-flop coupling is sensitive to the magnetic constants at the interface. The lower bound of $J_{\text{f-af}}$ required for bias indicates there is a threshold value for the net moment generated by spin canting to which the ferromagnet can couple.

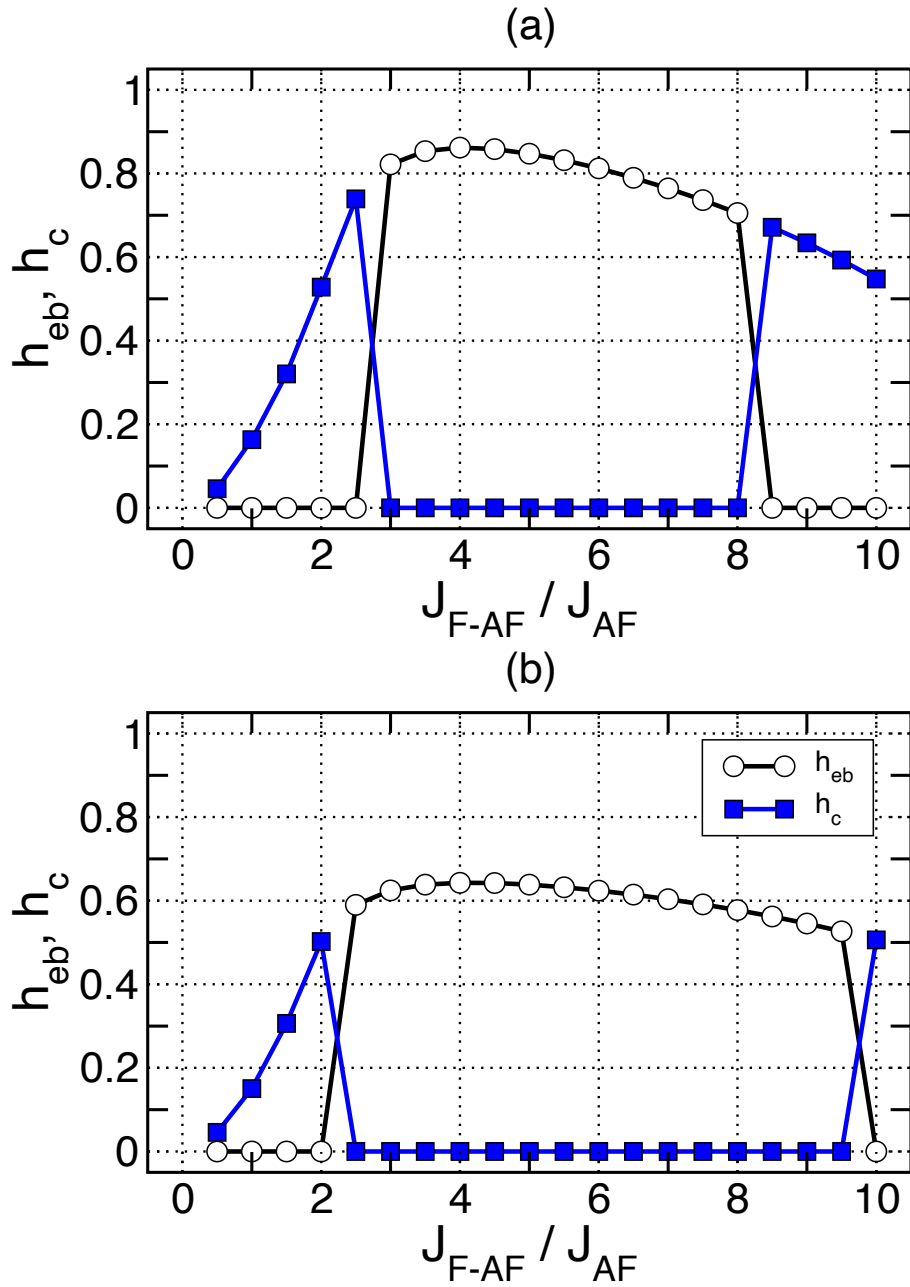


Figure 2.13: Stability of spin-flop coupling at compensated interfaces. The bias field h_{eb} and coercivity h_c are shown as a function of interlayer coupling strength J_{F-af} for two anisotropy constants: (a) $K_{af} = 0.34$ meV/spin and (b) 0.17 meV/spin. All fields are expressed in reduced units of $h = 2H_a M_t t_f / \sigma_{af}$

Below this limit the magnetization rotates irreversibly without dragging the interface spins along and no twist is formed. If this lower bound is greater than J_{af} , then an upper bound for J_{f-af} also exists. For sufficiently large interlayer coupling, the degree of spin canting can be so great that the interface spins become rigidly attached to the ferromagnet. For this scenario, the effective interface is displaced by one atomic layer and the interlayer coupling is identical to the antiferromagnet exchange. Bias then vanishes because $J_{f-af} = J_{af}$ is insufficient to stabilize spin-flop coupling in the first place.

Chapter 3

Interface roughness

The growth of thin films and layered materials is sensitive to many environmental factors, where, for example, the effects of imperfections on the substrate can propagate into the growth structure and appear as interfacial anomalies. This point is particularly important for exchange bias, because the effect relies on the exchange coupling between the ferromagnet and antiferromagnet layers. The presence of roughness has been demonstrated by many groups to impact significantly on the hysteresis properties [37, 43, 49, 51, 60, 74, 80, 102, 107, 117, 130, 131, 165, 195, 208, 233, 242], but it remains unclear whether bias is enhanced or degraded by the presence of interface impurities.

Frustration can arise as a result of modified interactions at a rough interface. Some examples of geometrical imperfections are given in Figure 3.1 for uncompensated and compensated interfaces. An irregular boundary separating the two magnetic layers causes an imbalance in the number of sublattices spins exposed to the ferromagnet. Suppose a monatomic bump extends from the ferromagnet layer into an uncompensated antiferromagnet (Fig. 3.1a). For the unit cell shown the protrusion introduces one unsatisfied bond (indicated by the cross) amongst five satisfied bonds, assuming an antiferromagnetic coupling across the interface. Although the direction of the net moment of the antiferromagnet interface has not changed, the introduction of the bump takes the system towards compensation. A more dramatic effect is obtained with monatomic steps

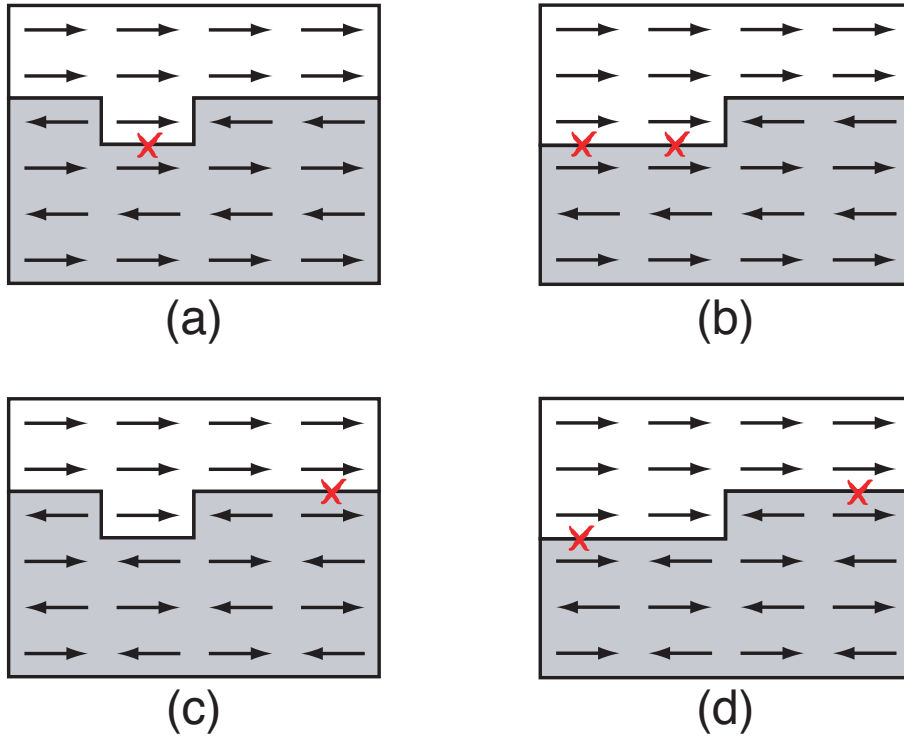


Figure 3.1: Frustrated spins at a rough interface in the form of geometrical imperfections. The number of unsatisfied bonds (indicated by the crosses) depend on the nature and period of the defects, and the type of interface between the two layers. Shown are (a) line and (b) step defects at uncompensated interfaces, and, (c) line and (d) step defects at compensated interfaces. Note that this is a schematic diagram and does not depict the equilibrium configuration of the bilayer.

(Fig. 3.1b), where perfect compensation is almost attained because the ferromagnet is exposed to both sublattices in almost equal proportions. Less dramatic effects are seen for compensated interfaces. For an atomic protrusion the number of favourable exchange bonds is actually increased by the defect, where there is one unsatisfied bond out of six in the unit cell shown (Fig. 3.1c). However, if the bump is displaced by one site the situation is altered dramatically, where five out of six bonds are unfavourable. On a macroscopic scale both scenarios are equally likely, so the net frustration is unchanged. The same behaviour occurs for stepped interfaces (Fig. 3.1d), where the degree of compensation remains the same.

In this chapter the effects of geometrical imperfections on the partial wall model of bias are studied. The focus is primarily on the effects of periodic imperfections, such as monatomic bumps and steps, where the emphasis is placed on the changes in the angular dependence that arises from the presence of such defects. Some consideration is given to

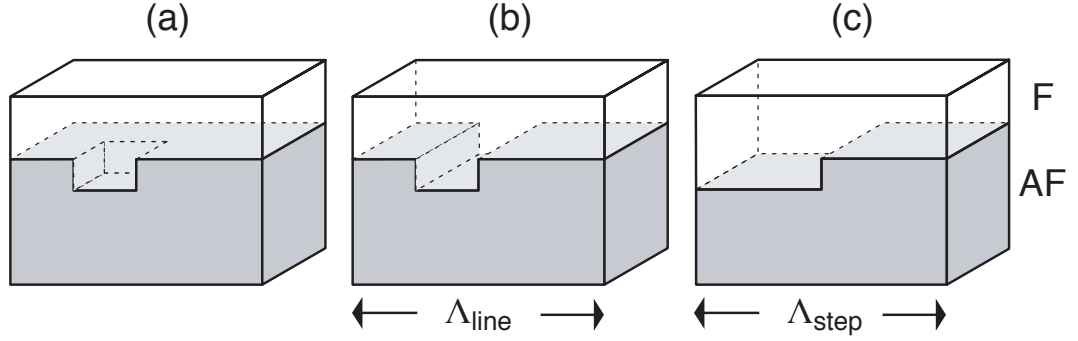


Figure 3.2: Geometry for interface roughness in the numerical model. The geometrical imperfections considered are (a) bump, (b) line and (c) step defects. Λ is the spatial period of the defects and is defined by the size of the unit cell used. All defects considered are one monolayer in height.

uncorrelated roughness at the end of the chapter.

3.1 Periodic defects

The effects of interface roughness on exchange bias are studied with the numerical model described in Section 2.7. The types of geometrical imperfections considered here are shown in Figure 3.2. For simplicity, all defects are assumed to be one atomic layer in height and extend from the ferromagnet into the antiferromagnetic layer. This is sufficient to obtain some general features of the problem, as the main function of the defects is to mix the relative populations of the sublattice spins at the interface. The periodicity of the interface structure is determined by the unit cell size parallel to the film plane.

Single atomic protrusions, referred to here as “bumps”, are equivalent to the substitution of an antiferromagnet spin at the interface with a ferromagnet spin. The difference is in the sign and magnitude of the exchange coupling associated with this protrusion. Because the bump forms part of the ferromagnetic material, the spin couples through J_f to its ferromagnetic neighbour above and J_{f-af} with its other five neighbours in the antiferromagnet. A continuous repetition of a bump defect along one direction gives a line defect, as shown in Figure 3.2(b). This type of imperfection is periodic in one dimension and is taken to be parallel to the easy axis of the antiferromagnet. The spacing between successive line defects is denoted by Λ_{line} . Exchange coupling within the line

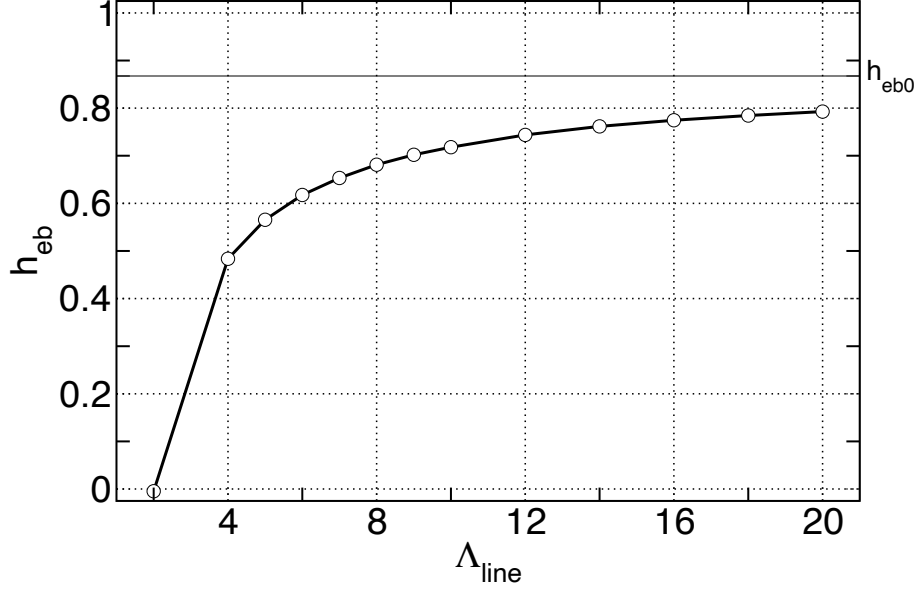


Figure 3.3: Bias field variation with line defect period Λ_{line} for uncompensated interfaces. The bias field h_{eb} is expressed in reduced units of $h = 2H_a M_f t_f / \sigma_{\text{af}}$. $h_{\text{eb}0}$ indicates the bias field value for perfect interfaces.

defect, along the direction in which it extends indefinitely, is assumed to be ferromagnetic and all other bonds to the antiferromagnet take the value $J_{\text{f-af}}$. Step defects are line defects with a width greater than one spin ([Fig. 3.2c), where exchange coupling within the step are ferromagnetic (J_f) and take the value $J_{\text{f-af}}$ with neighbouring antiferromagnetic spins. In the numerical simulation the steps cover half the unit cell so that the width is evenly distributed. The spacing between successive line defects is denoted by Λ_{step} .

Some salient features of rough interfaces are illustrated in Figure 3.3, where the effects of periodic line defects at an uncompensated interface are shown. A reduction in the bias field is observed as the spacing between the line defects decreases. For the closest spacing possible ($\Lambda_{\text{line}} = 2$), the interface attains full compensation and the bias is completely suppressed. This is not a surprising result because the preferred bas direction is perpendicular to the easy axis for compensated interfaces.

It is interesting to note that the bias field approaches perfect interface value $h_{\text{eb}0}$ slowly with increasing defect spacing (Fig. 3.3). This behaviour can be explained by the frustration close to the defect, which results in a non-uniform spin configuration within the film plane near the interface. Because the magnetization does not rotate coherently

within a layer the twist energy, and consequently the bias field, is modified. This point will be discussed in more detail later in this chapter.

3.2 Variations in the natural angle

Geometrical imperfections create an asymmetry between the relative number of sublattice a and b spins at the interface. From the analytical two-sublattice model presented in Chapter Two, this asymmetry can be described by taking the coupling between the ferromagnet and the two sublattices to be different, i.e. $J_a \neq J_b$, giving a combination of bilinear and biquadratic terms,

$$\mathcal{E}_{\text{int}} = -J_1 \cos \theta - J_2 \cos^2 \theta. \quad (3.1)$$

The angle θ here refers to the angle between the ferromagnet magnetization and the orientation of the net interfacial antiferromagnet moment, with J_1 and J_2 being phenomenological constants. As discussed previously the bilinear term is due to the coupling between the net antiferromagnet moment and the ferromagnet, and the biquadratic term arises from the spin-canting at the interface. The biquadratic coupling is consistent with the results derived by Slonczewski [362], who showed that oscillations in the interlayer exchange interaction in Fe/Cr/Fe trilayers due to variations in the Cr thickness can give rise to an effective perpendicular coupling between the two Fe layers.

A useful measure of interface mixing is the equilibrium orientation of the ferromagnet in the absence of an applied magnetic field. This orientation is characterized by a “natural angle”, θ_{nat} , measured from the easy axis of the antiferromagnet. For perfect uncompensation the equilibrium orientation is collinear with the easy axis, so the natural angle is either $\theta_{\text{nat}} = 0^\circ$ or $\theta_{\text{nat}} = 180^\circ$, depending on the sign of the interlayer coupling. For perfect compensation the spin-flop coupling ensures that the ferromagnet is aligned perpendicular to the easy axis, so $\theta_{\text{nat}} = 90^\circ$ or -90° . For a mixed interface, there is only a range of J_1/J_2 ratios for which the natural angle is not collinear with the easy axis.

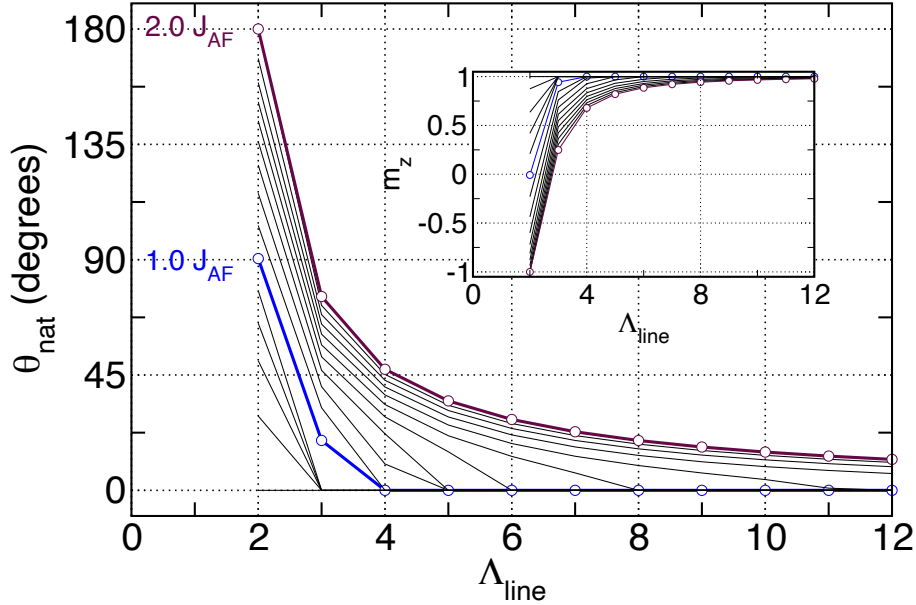


Figure 3.4: Natural angle θ_{nat} as a function of line defect period Λ_{line} for a series of interlayer coupling strengths. The interlayer exchange constants $J_{f\text{-af}}$ are expressed in terms of the antiferromagnet exchange J_{af} and are given in intervals of $0.1J_{\text{af}}$. The results shown are for uncompensated interfaces. In the inset, the component of magnetization along the easy axis direction (z -axis) is shown instead of the natural angle.

This range can be determined by minimizing the energy \mathcal{E}_{int} in Eq. 3.1 with respect to θ ,

$$\sin(\theta)(J_1 + 2J_2 \cos(\theta)) = 0. \quad (3.2)$$

The solutions for θ are:

$$\theta_{\text{nat}} = 0, \pi, \text{ or } \cos^{-1}\left(\frac{J_1}{2J_2}\right). \quad (3.3)$$

The first two solutions give the collinear alignment when the bilinear term dominates over the biquadratic term. For $J_1 < 2J_2$, the biquadratic term is dominant and the natural angle is given by the third solution in Eq. 3.3. This result demonstrates that a threshold exists for the biquadratic coupling to obtain a non-trivial value of θ_{nat} . This is equivalent to a threshold in the degree of partial (un)compensation at the interface.

An illustration of competing bilinear and biquadratic interactions is given in Figure 3.4, where variations in the natural angle with line defect spacing at an uncompensated interface are shown. These results are obtained by starting the initial spin configuration in an ordered state and then allowing the spins to relax to equilibrium in the absence of a magnetic field. The component of the magnetization parallel to the easy axis (m_z) and

the natural angle θ_{nat} are both shown for a series of interlayer exchange constants $J_{\text{f-af}}$.

A transition towards compensation is seen as the spacing between the defects is reduced. For wide spacings the natural angle takes the zero defect value of $\theta_{\text{nat}} = 0^\circ$, representing a parallel alignment with the easy axis. This value gradually shifts away from 0° as the defect separation decreases and the rate at which this shift occurs is governed by the interlayer coupling. The behaviour shown in Fig. 3.4 is almost counter-intuitive to that expected from Eq. 3.3. From the solution $\theta_{\text{nat}} = \cos^{-1}[J_1/(2J_2)]$, one may anticipate that small bilinear constants are preferred to obtain non-trivial values of the natural angle, because the argument of the $\cos^{-1}(x)$ term must be kept below unity. However, the numerical results show that the largest range for which the natural orientation is not collinear with the easy axis occurs for the largest value of $J_{\text{f-af}}$ considered. This is because the coupling constants J_1 and J_2 are not proportional to $J_{\text{f-af}}$ but depend on other quantities such as σ_{sf} , as shown in Section 2.6.

For periodic steps the relative number of J_{a} and J_{b} interactions are almost equal. The imbalance only arises from the coupling between the spins at the step edges parallel to the film plane. This interface is predominantly compensated, so one may expect spin-flop coupling to be dominant. Variations in the natural angle with step defect spacing are shown in Figure 3.5 for a series of interlayer exchange constants. When the interlayer coupling is identical to the antiferromagnetic exchange ($J_{\text{f-af}} = -3.4$ meV) there is little variation in the natural angle across all step widths, indicating that the interface behaves like a compensated system. Deviations from perpendicular coupling occur as the interlayer coupling is varied. For example, a transition from parallel to perpendicular alignment can be initiated by increasing $J_{\text{f-af}}$ to $2J_{\text{af}}$ for $\Lambda_{\text{step}} = 2$ steps.

The importance of induced anisotropies at crystallographic steps has been recognized by a number of experimental groups [365–368], in particular, to account for discrepancies between surface spin-wave data and existing models for epitaxial Fe/W (110) [369].

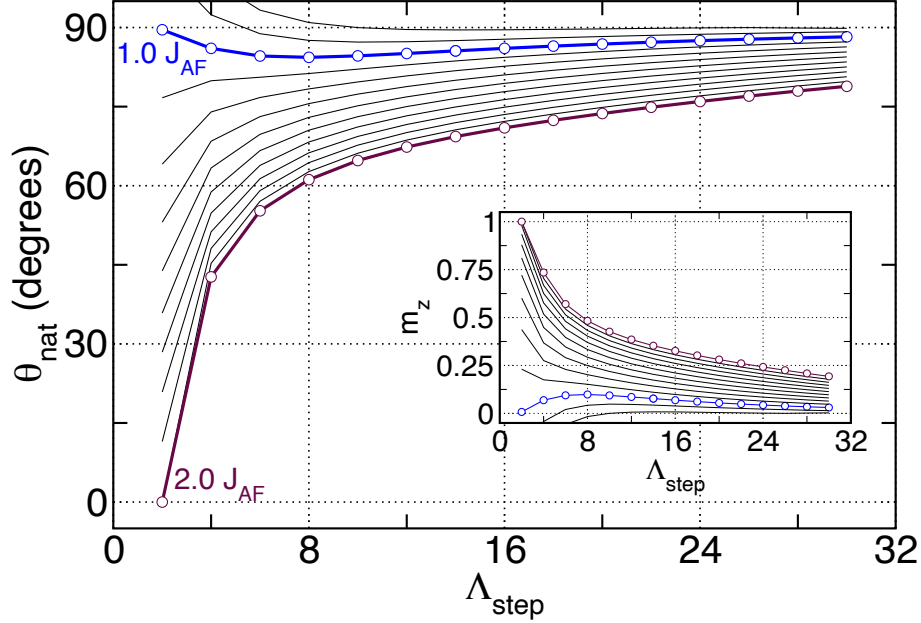


Figure 3.5: Natural angle θ_{nat} as a function of step defect period Λ_{step} for a series of interlayer coupling strengths. The interlayer exchange constants $J_{\text{f-af}}$ are expressed in terms of the antiferromagnet exchange J_{af} and are given in intervals of $0.1J_{\text{af}}$. The results shown are for uncompensated interfaces. In the inset, the component of magnetization along the easy axis direction (z -axis) is shown instead of the natural angle.

Step-induced behaviour has since been studied in terms of a variety of related phenomena, such as magnetization reversal [370–372] and reorientation transitions. A 90° switching of the magnetization of Fe films grown on stepped Cr, reminiscent of the surface-induced reorientation transitions, was recently observed attributed to step-induced anisotropy [67]. This observation is consistent with the results presented here, where the bias is modified by additional induced anisotropies that can be controlled by the defect spacing.

3.3 Angular dependence of exchange bias

Variations in the natural angle due to roughness suggest that the angular dependence of the exchange bias should also be affected. Because the natural angle represents the preferred bias direction (i.e. the direction along which the loop shift is greatest), the values of θ_{H} corresponding to the bias field maxima and minima are also expected to be shifted by periodic defects.

Some examples of roughness-induced effects for an uncompensated interface are

given in Figure 3.6, where the angular dependence of the bias field and coercivity is shown for a series of line defect periods. The interlayer coupling used here is $J_{\text{f-af}} = -6.8$ meV, which is chosen to be twice the antiferromagnet exchange to give a range of natural angles with varying defect spacings (see Fig. 3.4). A shift in the position of the bias field maximum is observed, which is particularly evident for $\Lambda_{\text{line}} = 2$ where the maximum is located at $\theta_{\text{H}} = 180^\circ$. A comparison with the data in Fig. 3.4 shows there is a good correspondence between the position of the bias field maxima and the natural angle for a particular defect separation.

A non-zero coercivity accompanies the bias for wider defect spacings, such as $\Lambda_{\text{line}} = 4$ and $\Lambda_{\text{line}} = 8$, and only appears for certain orientations of the applied field. The irreversible processes result from frustration at the interface. Consider the simplified picture in Figure 3.7, where three vectors are used to represent the spin configuration and effective interactions at the rough interface. The line defect allows coupling between the ferromagnet and the first two interfacial layers of the antiferromagnet simultaneously. However, there are always more exchange bonds to spins at the interface layer of the antiferromagnet than those in the second layer. In Fig. 3.7 this imbalance is represented by the different lengths of the sublattice vectors. Suppose the applied field angle is larger than the natural angle of the ferromagnet, where the configuration of the bilayer in forward field is shown in Fig. 3.7a. Reversal is executed in a clockwise direction (i.e. towards θ_{nat}) as the ferromagnet drags along the interface spins from the a' sublattice. However, the relatively weak coupling to the b' sublattice means that the b' spins do not rotate with the ferromagnet but instead make a transition in a counter-clockwise direction to the other side of the easy axis. The configuration at reverse field is shown in Fig. 3.7b. The combination of a reversible and an irreversible process gives rise to the simultaneous loop shift and coercivity enhancement.

A significant departure from a simple cosine form for the angular dependence is

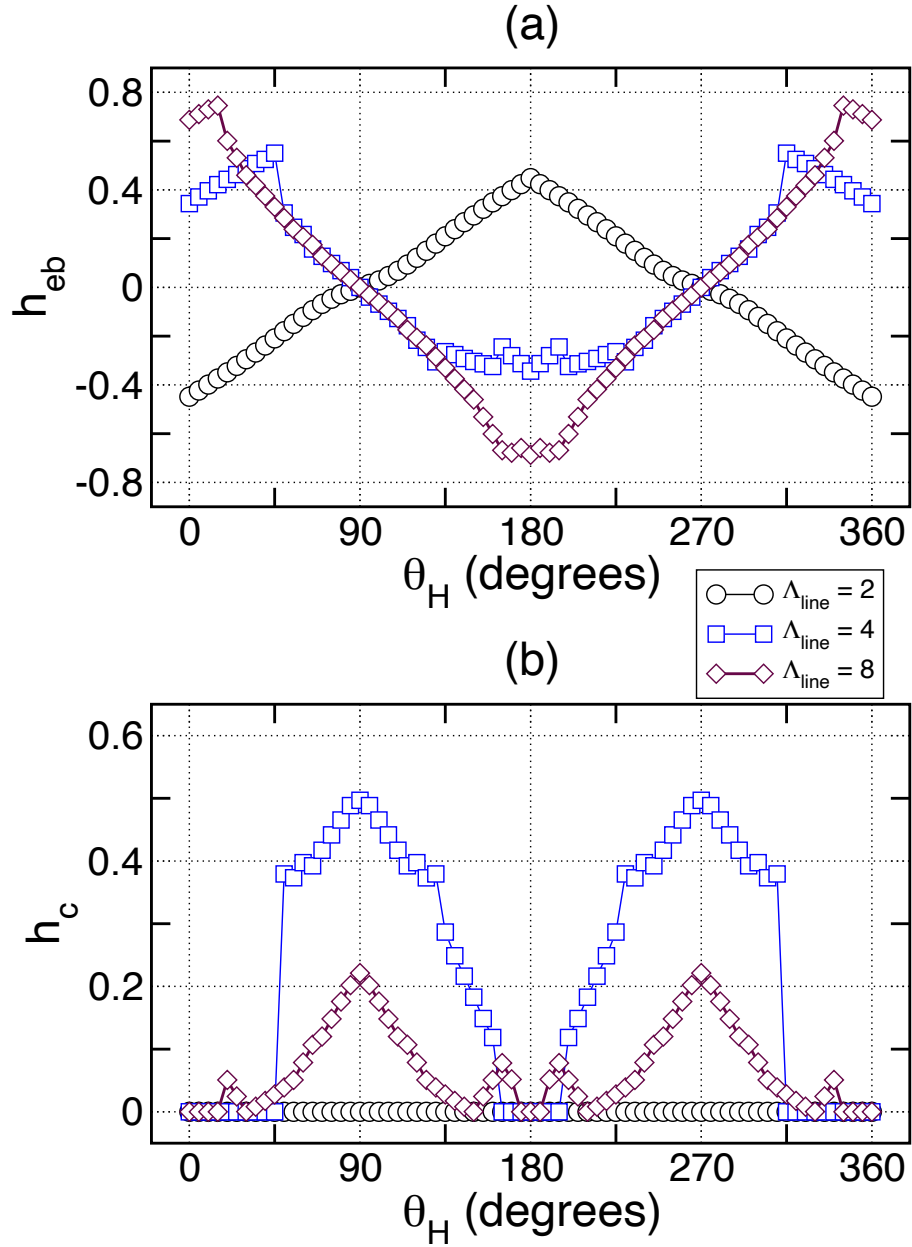


Figure 3.6: Angular dependence of exchange bias in the presence of line defects for uncompensated interfaces. (a) Bias field h_{eb} and (b) coercivity h_c as functions of the applied field angle θ_H are shown for a series of line defect periods $\Lambda_{line} = 2, 4$ and 8 . All fields are expressed in reduced units of $h = 2H_a M_t t / \sigma_{af}$.

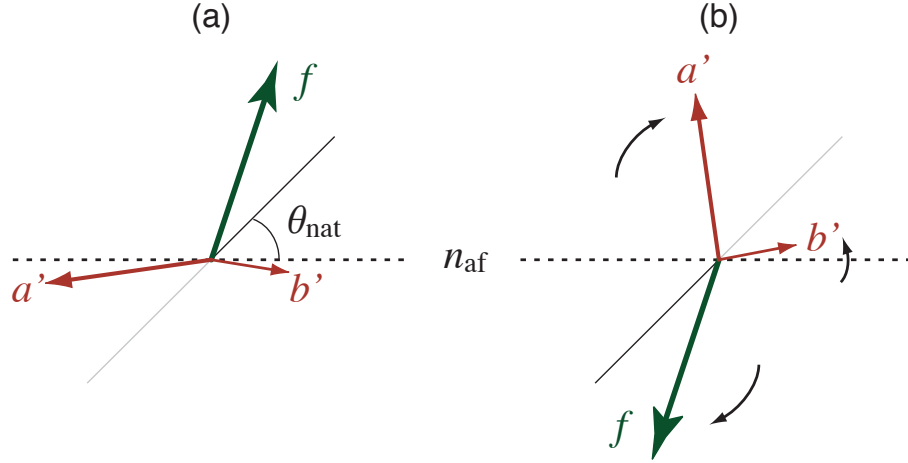


Figure 3.7: Irreversible behaviour at rough interfaces. The ferromagnet (f) is coupled to both antiferromagnet sublattices with different exchange constants, where the vectors a' and b' represent schematically the effective contributions from the two sublattices. (a) At forward field the ferromagnet is aligned parallel to the field direction with a spin-canted state in the antiferromagnet. (b) At reverse field the rotation of the ferromagnet causes a twist to form in one sublattice (a') but causes an irreversible transition in the other (b'). The direction of spin rotation is indicated by the arrows. θ_{nat} is the natural angle and n_{af} represents the easy axis of the antiferromagnet. After McGrath et al. [321].

also observed. For wide defect spacings ($\Lambda_{line} = 4, 8$) there is a discontinuity in the angular curve that accompanies the shift in the maxima and minima. The angular curves comprise two separate branches: an “ascending” branch for $0^\circ \leq \theta_H \leq \theta_{nat}$ and a “descending” branch for $\theta_{nat} \leq \theta_H \leq 180^\circ$, with the discontinuity taking place at $\theta_H = \theta_{nat}$. The mirror symmetry about the easy axis means that it is sufficient to only consider the range $0 \leq \theta_H \leq 180^\circ$. The sense of rotation of the ferromagnet is governed by the relative orientation of the applied field and the natural angle. Because the natural angle represents the equilibrium orientation at zero field, the rotation of the magnetization always occurs towards θ_{nat} during reversal (Fig. 3.8a and b). This behaviour is indicated in Figure 3.8. The ascending branch corresponds to $0^\circ \leq \theta_H \leq \theta_{nat}$, where reversal from forward field is executed in a counter-clockwise sense and the magnetization rotates towards the axis defined by θ_{nat} in negative field. During remagnetization the partial wall is unwound and rotation is in a clockwise sense. For $\theta_H > \theta_{nat}$, reversal occurs via clockwise rotation and remagnetization via counter-clockwise rotation, which accounts for the descending branch in Fig. 3.6.

Differences in H_{eb} between the two branches can be understood with a simple

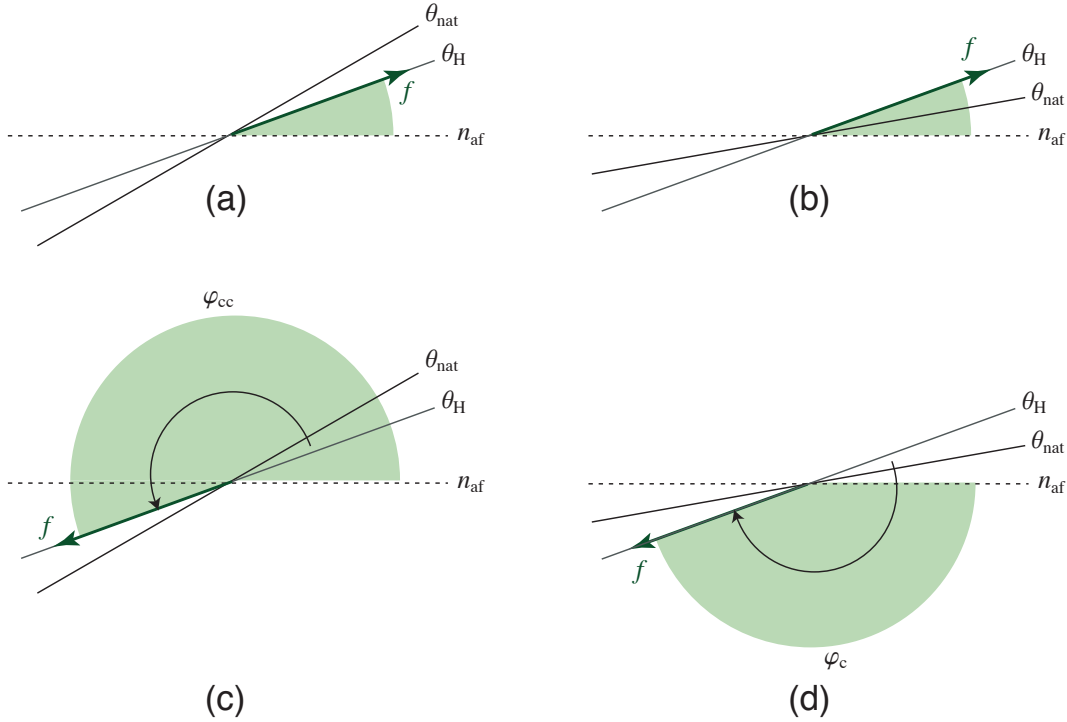


Figure 3.8: Sense of rotation of magnetization. The ferromagnet is shown at forward (a,b) and reverse (c,d) field for two different relative orientations of the applied field θ_H and the natural angle θ_{nat} . n_{af} represents the easy axis of the antiferromagnet. The rotation of the magnetization always occurs towards the direction of the natural angle. For $0^\circ \leq \theta_H \leq \theta_{nat}$ the counter-clockwise path results in a twist angle of φ_{cc} , which is generally larger than the twist angle φ_c for $\theta_H > \theta_{nat}$ that follows a clockwise reversal.

picture where the interface spins are rigidly coupled together. For $0^\circ \leq \theta_H \leq \theta_{nat}$, the counter-clockwise rotation during reversal forms an antiferromagnet twist with an angle of φ_{cc} , corresponding to an energy change of roughly $\sigma_{af}(1 - \cos(\varphi_{cc}))$.ⁱ For $\theta_H > \theta_{nat}$ the opposite rotation of the magnetization produces a wall with an interface angle of φ_c , representing an energy cost of $\sigma_{af}(1 - \cos(\varphi_c))$. The discontinuity at θ_{nat} arises because $\varphi_{cc} \neq \varphi_c$ for any natural angle that differs significantly from $\theta_{nat} = 0$.

The periodic defect leads to a bifurcation of the natural angle at 0° . Due to the two-fold symmetry of the antiferromagnet anisotropy, the bias field direction splits along two new axes defined by $\pm\theta_{nat}$. As shown in Fig. 3.6, the result is a more complicated angular dependence that is better described with higher order sinusoidal terms. This can be interpreted as the presence of additional anisotropies associated with the line

ⁱFor a true rigid coupling it is possible for the twist angle to exceed 180° . In this case, the total energy of the twist is a sum of a 180° wall term σ_{af} and a partial twist term $\sigma_{af}(1 - \cos(\varphi'_{cc}))$, where $\varphi'_{cc} = \varphi_{cc} - 180^\circ$. Note that the complete 180° wall formed is not localized to interface with the absence of any other pinning effects in the antiferromagnet.

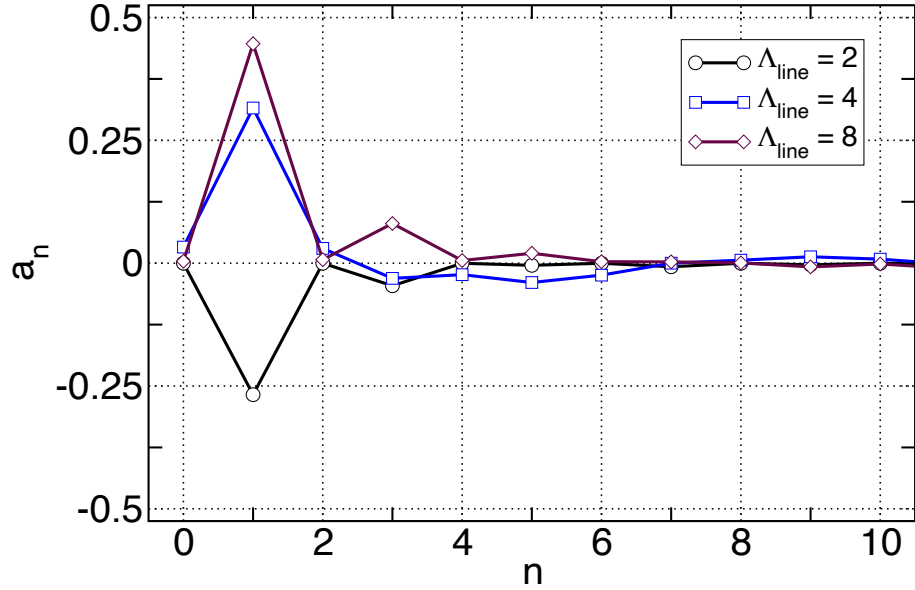


Figure 3.9: Fourier decomposition of the angular variations in the bias field for line defects. The coefficients of the first eleven terms in the cosine series used to represent the bias field as a function of θ_H are shown for the bias field curves given in Fig. 3.6.

defect, analogous to the step-induced anisotropies discussed earlier, and may provide an explanation for induced higher-order terms observed in certain experimental systems [143, 146].

The higher-order anisotropies can be quantified with a Fourier decomposition of the angular variations of H_{eb} . The curves in Fig. 3.6 are expanded in a cosine series (Eq. 2.40) and the series coefficients are shown in Figure 3.9. A comparison with Table 2.1 shows that higher-order contributions are more significant with defects, where the relative magnitudes of the $\cos(3\theta_H)$ term can be as large as 25% of the fundamental $\cos(\theta_H)$ component. This is not surprising given the complexity of the angular curves in Fig. 3.6.

Periodic interfacial steps also modify the angular dependence, as shown in Figure 3.10. Discontinuities in the curves are again a result of changes to the natural angle. The compensated appearance of the stepped interface shifts the bias maximum to around $\theta_H = 90^\circ$, a limit gradually approached as the terraces widen. Note that the magnetization curves are reversible for wide steps ($\Lambda_{\text{step}} = 8, 16$); a non-zero coercivity only appears when the interface is predominantly uncompensated ($\Lambda_{\text{step}} = 4$).

Aside from the positions of the bias field maxima and minima, there are distinct

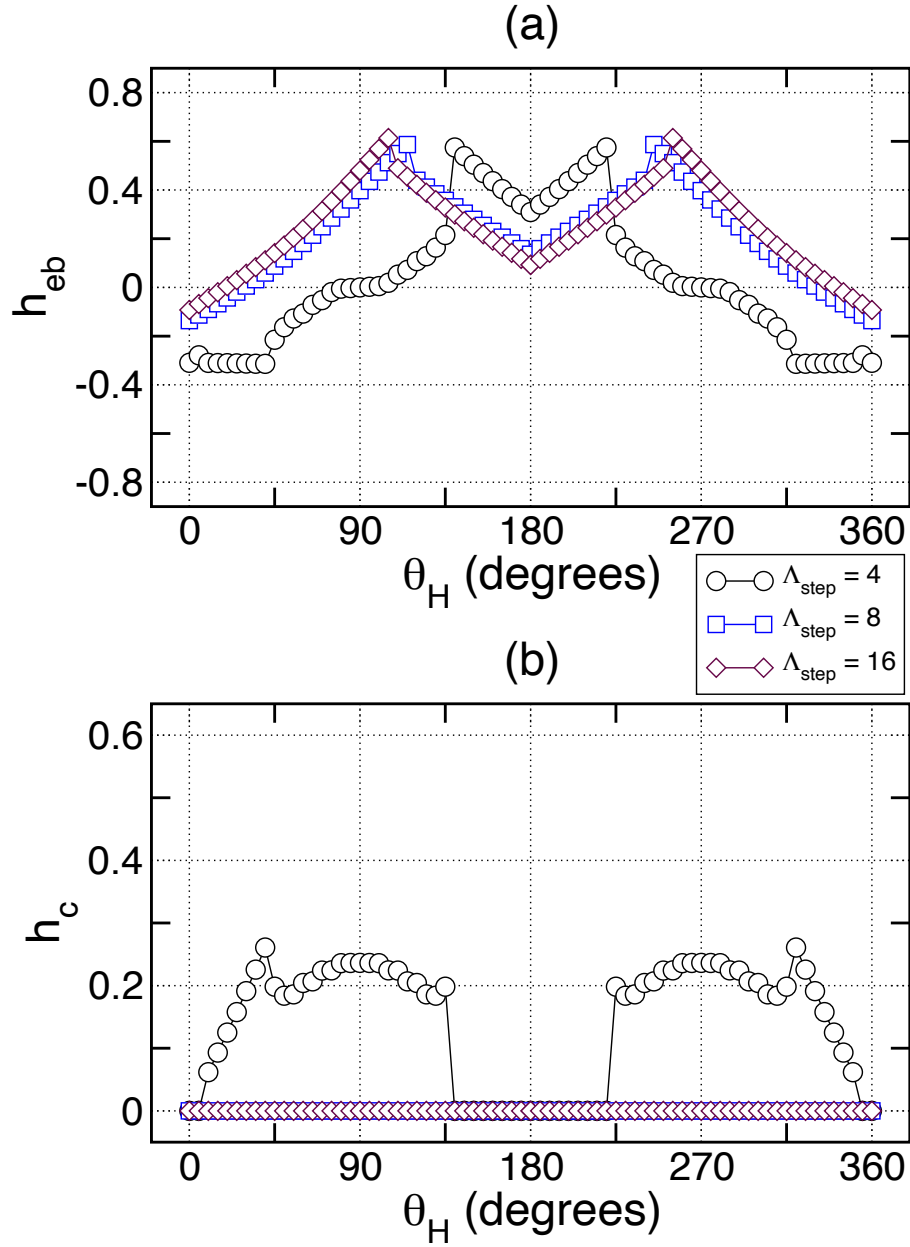


Figure 3.10: Angular dependence of exchange bias in the presence of step defects for uncompensated interfaces. (a) Bias field h_{eb} and (b) coercivity h_c as functions of applied field angle θ_H are shown for a series of step defect periods: $\Lambda_{\text{step}} = 4, 8$ and 16 . All fields are expressed in reduced units of $h = 2H_a M_f t_f / \sigma_{af}$.

differences between the qualitative behaviour of line and step defects. For the former, the point of frustration is always situated at the line defect (see Fig. 3.2) and the ratio of satisfied to unsatisfied exchange bonds perpendicular to the interface, ν , decreases as the spacing between defects increases. This is not true for step defects because ν is constant irrespective of the step width. The interface always appears compensated perpendicular to the film plane but uncompensated within the film plane due to the interlayer coupling at the step edges. A modest variation in the angular dependence results at wider steps, where the behaviour is mostly governed by the step edges. Despite the predominantly compensated appearance of the stepped interface, the angular curves retain a symmetry about the easy axis direction that distinguishes such a geometrical imperfection from a true compensated interface.

Modified angular dependences of exchange bias have been observed in a number of epitaxial [91, 143, 188] and polycrystalline materials in experiment [100, 146]. In these experiments the crystal structure at the interface is argued to give rise to spin frustration, which consequently leads to variations in the angular dependence. It has been demonstrated in this section that exchange coupling of the ferromagnet to both sublattices, with unequal exchange constants, can lead to similar frustration. Results of fourier decomposition of experimental angular curves presented by Maat et al. [100] exhibit similar features to the calculations presented here.

3.4 Random defects

A natural question is whether any changes to the natural angle are effected by uncorrelated roughness. To examine this point, the equilibrium orientation of the ferromagnet with the presence of randomly distributed bumps at an uncompensated interface is calculated. A 6×6 unit cell is used and the bump defect density ρ_{bump} is the fraction of the unit cell occupied by bumps. The results for a series of interlayer coupling strengths

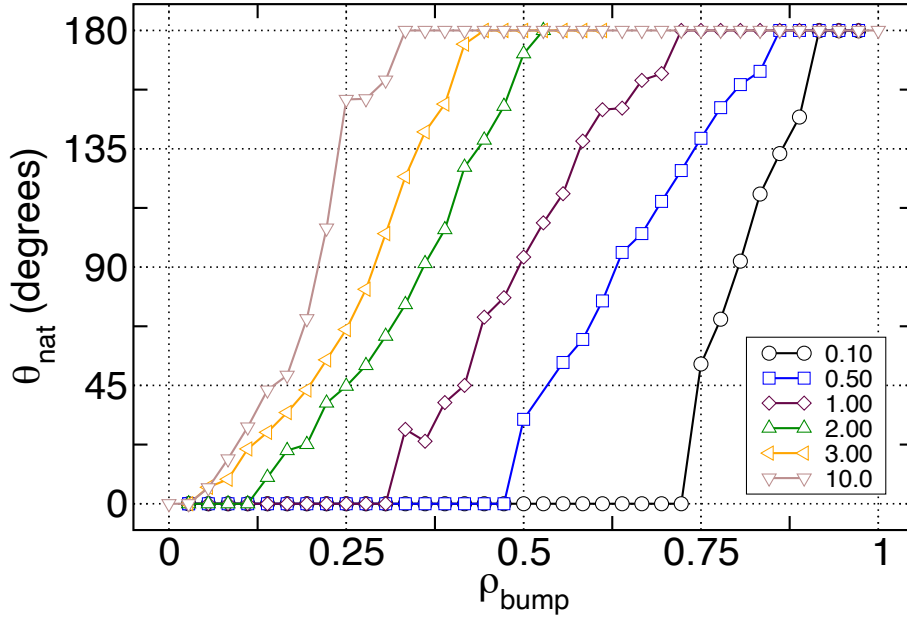


Figure 3.11: Variation in natural angle with bump defects. The natural angle θ_{nat} is shown as a function of bump defect density ρ_{bump} for a series of interlayer coupling strengths, which are given in the legend as fractions of the antiferromagnet exchange constant $J_{\text{af}} = -3.40$ meV.

are shown in Figure 3.11. A perfect interface is recovered at both extremes of zero density and 100% density, as evidenced by the transitions between $\theta_{\text{nat}} = 0^\circ$ and 180° common to all curves. For $\rho_{\text{bump}} = 1$ the ferromagnet couples entirely to the b sublattice, so the preferred alignment is opposite to that for zero density (where the interface consists of a sublattice spins). The interlayer coupling adjusts the transition point between parallel and antiparallel alignment. With small $J_{\text{f-af}}$ a relatively large defect density is required to reach the transition, where the midpoint $\theta_{\text{nat}} = 90^\circ$ occurs at approximately $\rho_{\text{bump}} = 0.8$ for $J_{\text{f-af}} = 0.1J_{\text{af}}$. The transition is shifted towards lower bump densities as the interlayer coupling is increased.

However, these variations in the natural angle do not result in the same angular behaviour as observed for periodic defects. The variations in the hysteresis properties are shown in Figure 3.12a. For all applied field orientations considered the bias field is observed to vary continuously from $h_{\text{eb}0}$ to $-h_{\text{eb}0}$ between $\rho_{\text{bump}} = 0$ and $\rho_{\text{bump}} = 1.0$, where $h_{\text{eb}0}$ refers to the value obtained at zero concentration. The initial decrease is due to the increasing degree of compensation effected by the bumps and culminates in

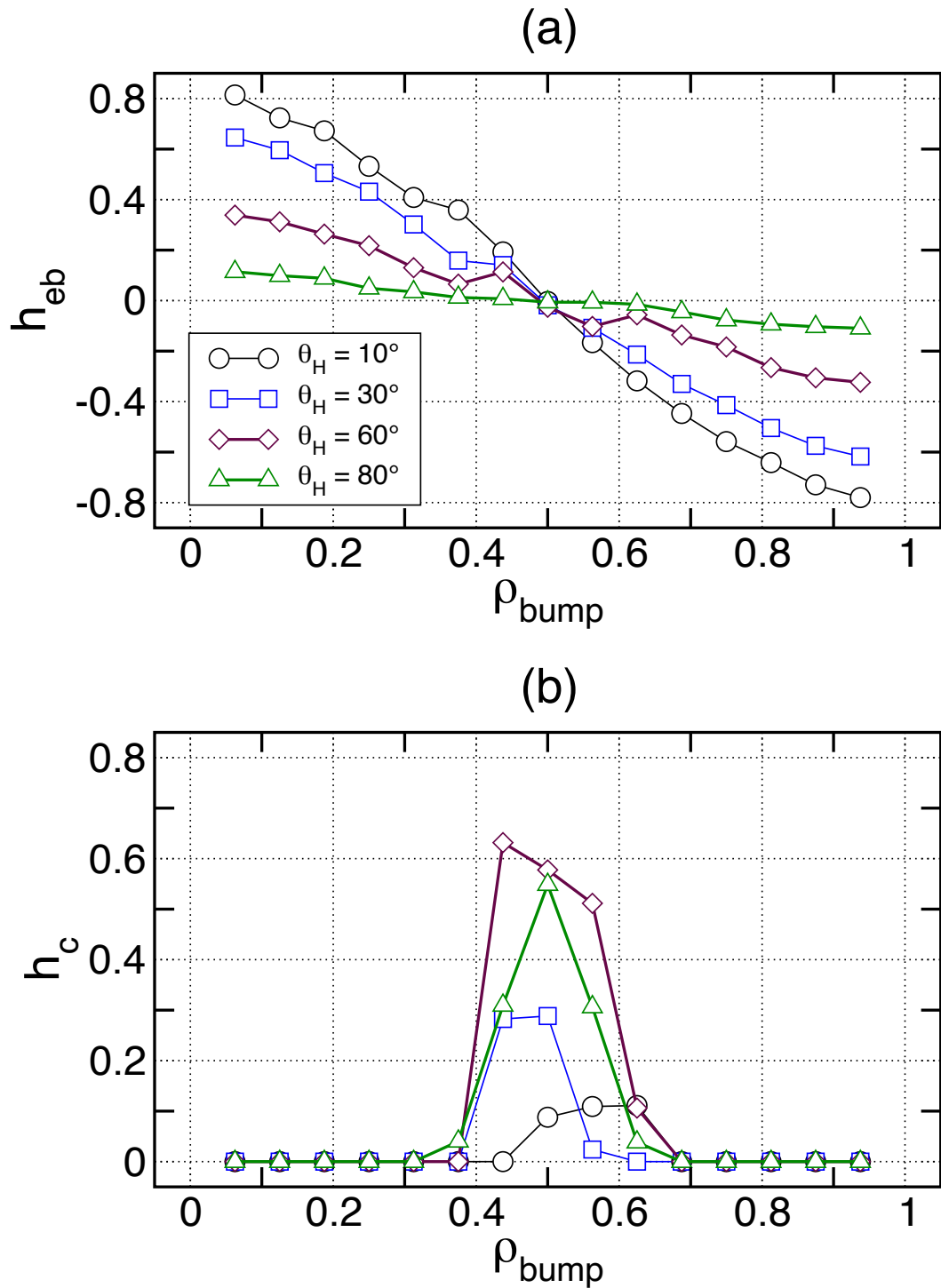


Figure 3.12: The (a) bias field H_{eb} and (b) coercivity H_c are shown as functions of bump defect density ρ_{bump} for a series of applied field angles θ_H . The results are for uncompensated interfaces. All fields are expressed in reduced units of $h = 2H_a M_{\text{f}} t_{\text{f}} / \sigma_{\text{af}}$.

the vanishing of the bias at $\rho_{\text{bump}} = 0.5$. For $\rho_{\text{bump}} > 0.5$, the introduction of more bumps leads to a smoother interface and one observes a corresponding increase in the loop shift, but with a change in direction. Note that vanishing of the bias field at 50% defect concentration does not correspond to a rotation of the natural angle in this case, because the same qualitative variation is seen for *all* applied field angles.

Around $\rho_{\text{bump}} = 0.5$, there are significant enhancements to the coercivity with little biasing (Fig. 3.11). At these concentrations the interface is predominantly compensated, but no spin-flop coupling exists to produce bias. This is most evident for $\theta_{\text{H}} = 80^\circ$, where a large bias field is usually seen for perfect compensated interfaces. The random distribution of the bumps means that the spin-canting at the interface is not uniform, which does not lead to a well-defined perpendicular coupling required for bias.

Chapter 4

Defect-induced domain wall pinning

The role of pinning centres restricting the propagation of domain walls has been studied extensively in ferromagnetic materials [373–383]. This is important for magnetization reversal as much of the hysteretic properties are determined by the wall pinning mechanisms in a material. In the context of domain-wall driven exchange bias, these results suggest the prospect of coercivity enhancement due to pinning processes in the antiferromagnet [59, 291–293].

In this chapter, mechanisms by which defects can modify bias shifts and associated coercivities are examined. These defects differ from geometrical roughness in that local variations in the exchange and anisotropy energies are effected throughout the antiferromagnet film. Particular attention is given to the pinning of the partial antiferromagnet twist and its effect on the hysteresis and angular dependence of bias.

4.1 Model for domain wall pinning

A simple model is developed in this section, following Braun’s work [360] on ferromagnetic domain walls, to study the effects of wall pinning in the antiferromagnet. The approach is based on the continuum theory for uncompensated interfaces, presented in Chapter Two, and involves the inclusion of a point-like impurity at an arbitrary position in the antiferromagnet. The aim is to examine how partial wall formation during reversal

is modified by the defect.

Suppose at some distance $x_d < 0$ from the interface exists a point-like defect, which consists of a single atom with a local anisotropy constant that differs from the bulk value. The total energy of the partial wall in the antiferromagnet (Eq. 2.11) is modified to be

$$\mathcal{E}_{\text{af}}[\varphi(x)] = \int_{-t_{\text{af}}}^0 dx \left[D_{\text{af}} \left(\frac{\partial \varphi}{\partial x} \right)^2 + K'_{\text{af}}(x) \sin^2(\varphi) \right]. \quad (4.1)$$

Recall that $\varphi(x)$ is the angle of the staggered magnetization with respect to the easy axis (z -axis) and D_{af} is the exchange stiffness. $K'_{\text{af}}(x)$ contains the information about the spatial fluctuation in the uniaxial anisotropy,

$$K'_{\text{af}}(x) = K_{\text{af}}(1 + n_d)\delta(x - x_d), \quad (4.2)$$

where n_d represents the fractional change in the local anisotropy at the impurity. In the weak pinning limit, $n_d K_{\text{af}} \ll \sigma_{\text{af}}$, deviations in the static Bloch wall profile due to the impurity can be neglected, so the pinning energy can be evaluated by substituting the solution for $\varphi(x)$ (Eq. 2.21) into the integral in Eq. 4.1, giving

$$\mathcal{E}_{n_d} = n_d K_{\text{af}} \operatorname{sech}^2 \left(\frac{x_c - x_d}{\delta_{\text{af}}} \right). \quad (4.3)$$

$\delta_{\text{af}} \equiv \sqrt{D_{\text{af}}/K_{\text{af}}}$ is the characteristic magnetic length in the antiferromagnet and x_c denotes the position of the wall centre (i.e. $\theta(x_c) = 0$). It is useful to express the energies in terms of the interface angle $\varphi_0 \equiv \varphi(x = 0)$. Using the relation

$$x_c = \delta_{\text{af}} \ln \tan \left(\frac{\varphi_0}{2} \right), \quad (4.4)$$

the total antiferromagnet energy becomes

$$\mathcal{E}(\varphi_0) = \frac{1}{2} \sigma_{\text{af}} (1 - \cos \varphi_0) + \frac{n_d K_{\text{af}} \sin^2 \varphi_0}{\left(\cosh \frac{x_d}{\delta_{\text{af}}} + \cos \varphi_0 \sinh \frac{x_d}{\delta_{\text{af}}} \right)^2}, \quad (4.5)$$

where σ_{af} is the energy for a 180° domain wall in the antiferromagnet. A plot of this function is shown in Fig. 4.1 for several defect strengths and distances from the interface.

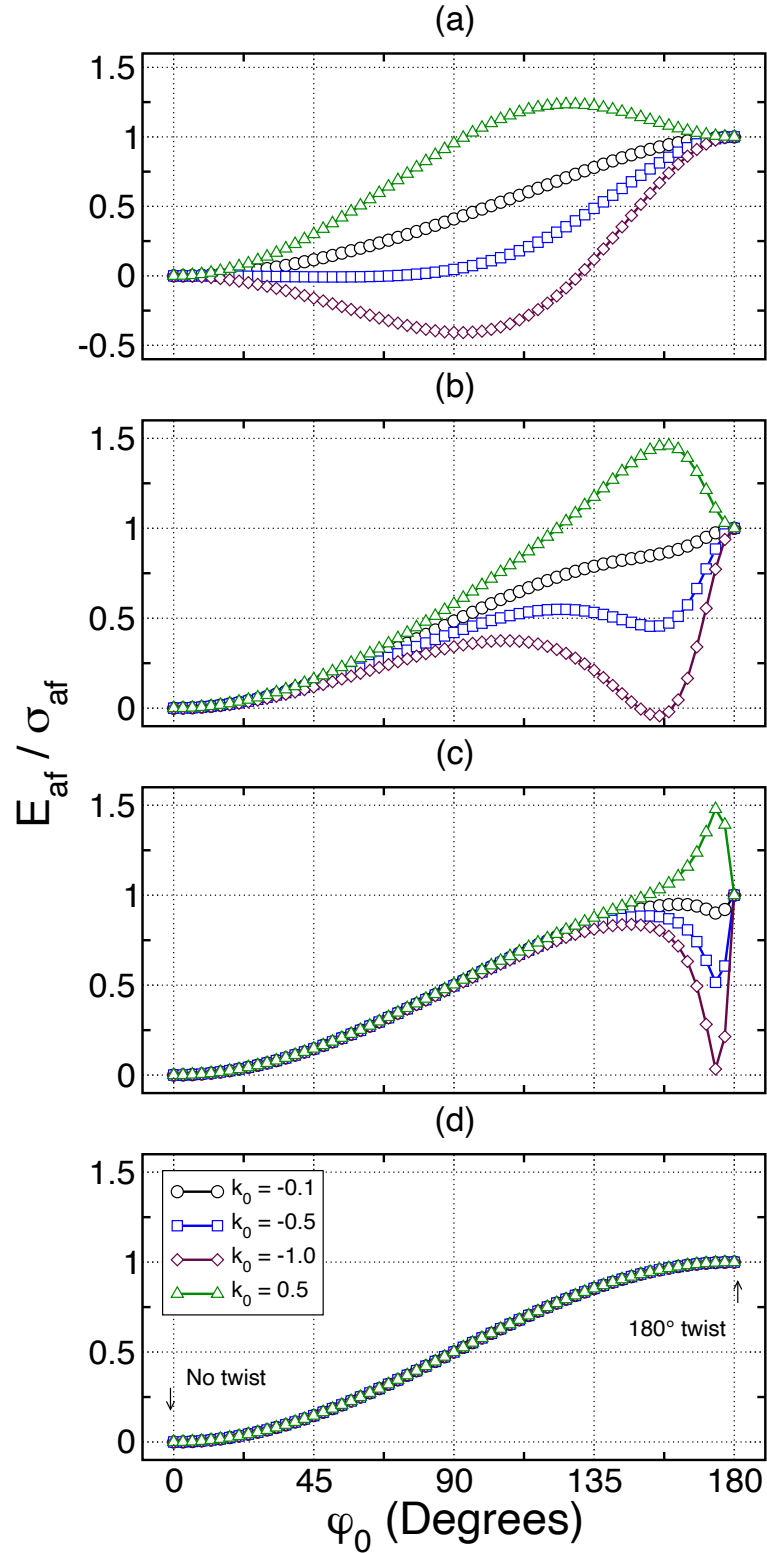


Figure 4.1: Partial wall energy with the presence of impurities. The normalized energy, $\mathcal{E}_{af}(\varphi_0)/\sigma_{af}$, is shown as a function of interface twist angle φ_0 for a series of impurity strengths and locations: (a) $x_d/\delta_{af} = 0.1\pi$, (b) $x_d/\delta_{af} = 0.5\pi$, (c) $x_d/\delta_{af} = \pi$, and (d) $x_d/\delta_{af} = 3\pi$. An interface angle of $\varphi_0 = 180^\circ$ corresponds to the formation of a 180° Bloch wall. $k_0 \equiv 2n_d K_{af}/\sigma_{af}$ represents a scaled pinning strength.

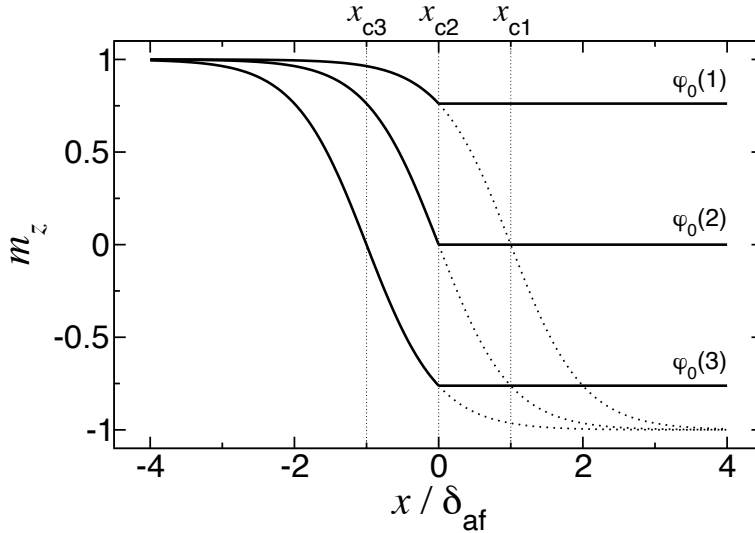


Figure 4.2: Partial wall formation viewed as soliton propagation. The magnetization profile of the bilayer (solid lines) is shown for a series of twist angles φ_0 . It is assumed that the ferromagnet is uniform and rigidly coupled to the antiferromagnet. The antiferromagnet occupies $x < 0$ and the ferromagnet $x \geq 0$. The formation of the twist can be treated as the propagation of a soliton from $x = \infty$; the complete soliton profile is indicated by the dotted lines.

$\varphi_0 = 0^\circ$ represents the untwisted state and $\varphi_0 = 180^\circ$ represents the configuration where a full 180° Bloch wall is generated in the antiferromagnet.

Reductions in the local anisotropy lead to a local minimum in the energy $\mathcal{E}_{\text{af}}(\varphi_0)$, which appears as an attractive potential for the domain wall. Suppose that the ferromagnet is rigidly coupled to the antiferromagnet. When the magnetization is rotated from $\varphi_0 = 0$, the interface antiferromagnet spin follows the rotation to form a partial twist. Because the shape of the Bloch wall is well-defined, the twist formation may be viewed as the propagation of an antiferromagnetic soliton from $x = \infty$ (Fig. 4.2). The wall becomes pinned when the centre is coincident with the impurity, $x_c = x_d$, which corresponds to the value of φ_0 for which the energy is a minimum. A reduction in wall energy occurs because the largest layer-to-layer variation in the magnetization (and hence the region with the highest energy density) becomes coincident with a region of reduced energy density. Defects located farther than half a domain wall width from the interface do not affect the twist formation, because the wall needs to de-pin completely from the interface to centre about the impurity (Fig. 4.1)

The depth of the energy well is governed by the magnitude of the local variation

in K_{af} . The position of the defect, relative to the interface, determines the width of the energy well measured in terms of φ_0 . Close to the interface the pinning potential causes a broad minimum in the energy, because an energy saving can be gained by situating any gradient in the wall profile about the defect. As the pinning site is located farther away the energy well becomes narrower, approaching a zero width as x_c gets close to half a wall width from the interface. No effects are seen for defects situated farther than half a domain wall width from the interface. For impurities that enhance the local anisotropy (e.g $k_0 = 0.5$ in Fig. 4.1), an energy barrier to domain wall formation occurs instead.

These results can be generalized to describe variations in the local exchange (connecting $\varphi(x)$ and $\varphi(x + \delta x)$, for example) under the same assumption that deviations from the static Bloch wall profile can be neglected. For a Bloch wall, the anisotropy energy $K_{\text{af}} \sin^2(\varphi(x))$ is equal to the exchange energy $D_{\text{af}}(\partial_x \varphi(x))^2$ at any part along the wall.ⁱ Therefore, the point defect term introduced into the anisotropy can equally represent a local variation in the exchange bond,

$$D'_{\text{af}} \left(\frac{\partial \varphi}{\partial x} \right)^2 = K'_{\text{af}} \sin^2(\varphi). \quad (4.6)$$

which generates a pinning term that is proportional to $\text{sech}^2(x)$ similar to that in Eq. 4.3.

It should be stressed that the continuum approach outlined here is only valid for weak pinning potentials. For stronger defects or defects with a finite spatial extent, the problem can be treated by considering the impurity as a separate region [376]. A boundary-value problem for a system of equations appropriate for a trilayer system is then obtained to describe the spin profile. The aim here is to understand the essential physics of wall pinning and to motivate the study in the rest of this chapter. The problem of strong pinning potentials will be considered in more detail in the following sections.

ⁱThis is a general property of solitons, where a dispersive component is always counterbalanced by another term that tends to diminish the spatial spread of the profile.

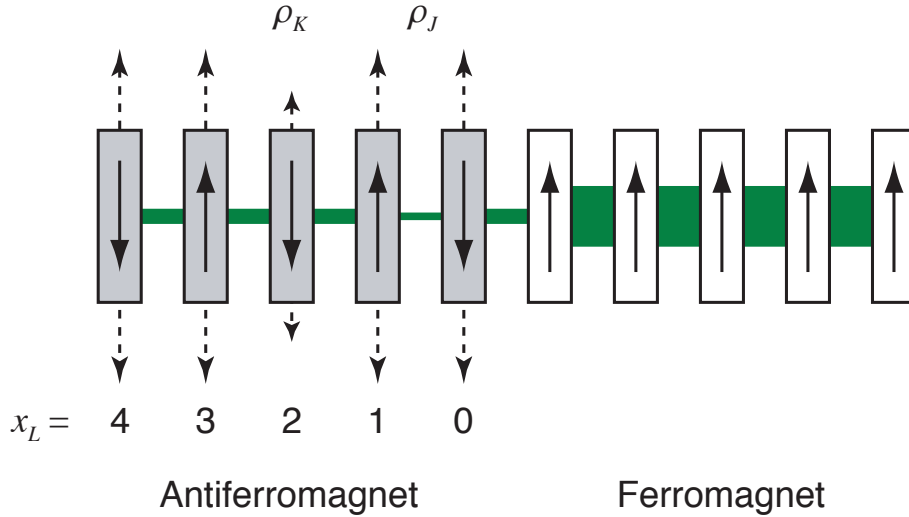


Figure 4.3: Geometry for reduced-exchange and modified-anisotropy defects in the antiferromagnet film. The lines connecting successive layers represent the exchange bonds and the thickness gives an indication of the relative strength. The magnitude of the local anisotropy constant in the antiferromagnet is represented by the length of the dotted arrow. Also shown is the scheme used to designate the defect location; in this example there is an exchange defect (ρ_J) at $x_L = 1$ and a reduced-anisotropy defect (ρ_K) at $x_L = 2$.

4.2 Bias field reduction and coercivity enhancement

The essential features of defect-modified exchange bias can be obtained by studying the effect of a point defect in a ferromagnet/antiferromagnet chain. Lateral fluctuations in the magnetization parallel to the film plane are ignored so that each spin represents the direction of uniform magnetization of a single layer. The presence of a single point defect in the antiferromagnet is considered. The defect is simulated as either a reduction in the exchange coupling between two spins (representing a reduction in the exchange between two successive atomic layers) or a local reduction in the uniaxial anisotropy. For the latter the direction of anisotropy remains unchanged, only its magnitude is reduced.

Pinning potentials of arbitrary strength are studied using the numerical approach presented in Section 2.7. This technique is not constrained by the weak-pinning approximation and therefore allows one to study non-trivial spin profiles that may result from strong pinning potentials. The sketch in Figure 4.3 shows the two kinds of defects realized in the one-dimensional model. The location of the point defect is denoted by x_L . For reduced-exchange defects the exchange constant between the layers x_L and $x_L - 1$ is re-

duced to J_d , while for reduced-anisotropy defects the anisotropy constant in the x_L is K_d . $x_L = 0$ is the interface layer and $x_L = t_{af} - 1$ is the surface layer of the antiferromagnet. The reduction factors $\rho_J \equiv 1 - J_d/J_{af}$ and $\rho_K \equiv 1 - K_d/K_{af}$ represent average defect densities for real materials.

The effects of reduced exchange are shown in Fig. 4.4a and b. Interfacial defects ($x_L = 0$) cause the bias field to decrease because the interlayer exchange coupling is reduced. As shown in Chapter Two and elsewhere [290,324], the bias field is proportional to the interlayer coupling J_{f-af} when $J_{f-af} \ll \sigma_{af}$, but is largely independent of J_{f-af} in the opposite limit $J_I \gg \sigma_{AF}$. This behaviour is reflected in the smooth decay of the bias field with defect concentration.

For bulk defects ($x_L > 0$) the reduction in the bias field arises from two sources. First, the reduction in the exchange coupling leads to an overall decrease in the partial wall energy as $\sigma_{af} \propto \sqrt{J_{af}}$. Second, the defect potential results in an energy barrier between the depinning and reattachment of the domain wall to the interface. The energies required for pinning the wall at the defect and its subsequent release differ, giving rise to a non-zero coercivity accompanying the loop shift. The results in Fig. 4.4a show the second process is more important for determining H_{eb} . For example, the bias field for a defect at $x_L = 6$ undergoes a rapid decay as the concentration is increased and reaches half its initial value at $\rho_J \simeq 0.3$, in contrast to the larger density required ($\rho_J \simeq 0.75$) to reduce H_{eb} by the same amount for a defect at $x_L = 2$.

Changes to the local anisotropy have a more modest effect on the hysteresis properties (Fig. 4.5a and b). The reduction in the bias field is comparatively small, particularly for defects close to the interface where a decrease of approximately 20% is observed. This is in stark contrast to reduction driven by exchange defects, where a complete suppression of the bias is seen at full concentration. Variations in the local anisotropy do not disconnect two regions of the antiferromagnet, they only induce an

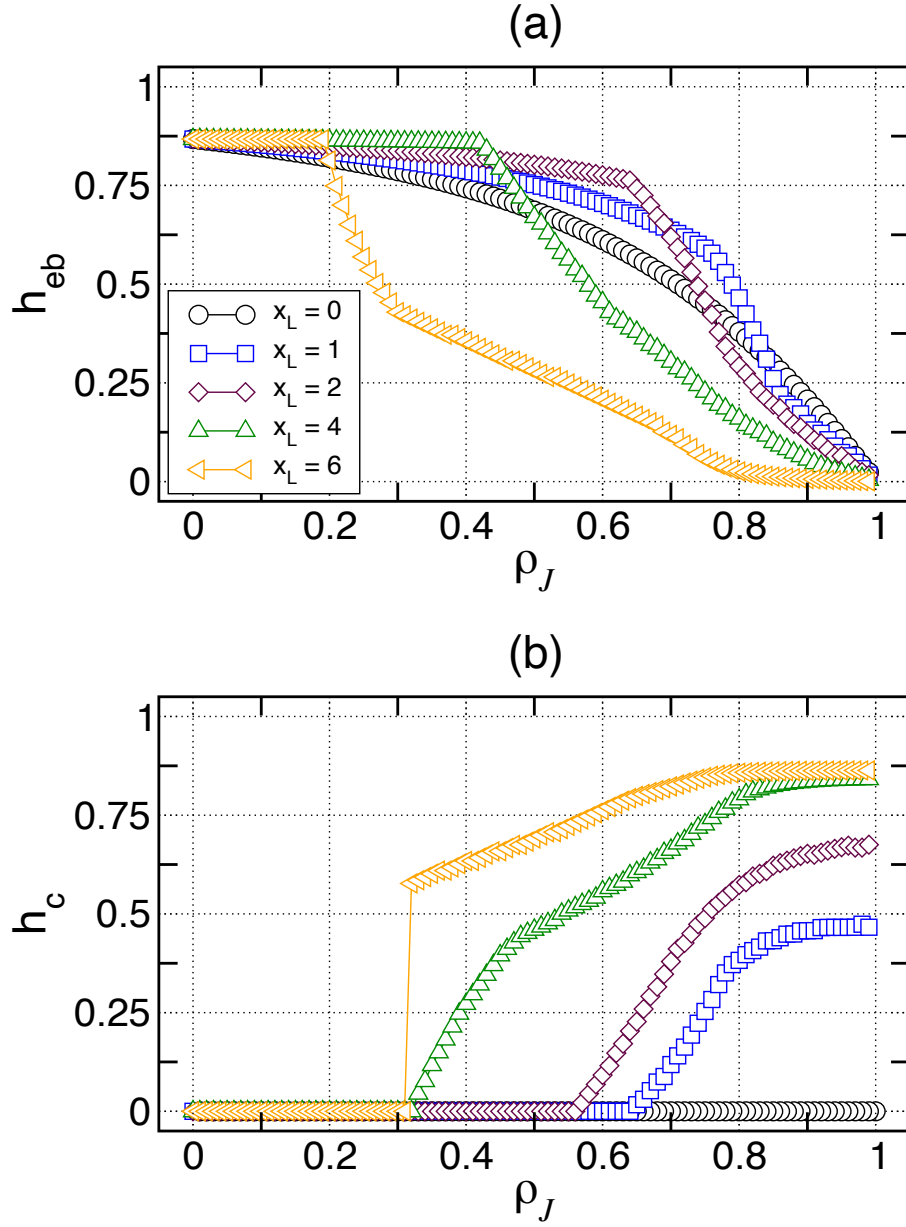


Figure 4.4: Bias field and coercivity variations for reduced-exchange defects. The (a) bias field h_{eb} and (b) coercivity h_c are shown as functions of defect strength $\rho_J \equiv 1 - J_d/J_{\text{af}}$ for a series of defect positions x_L in the antiferromagnet, where $x_L = 0$ corresponds to the interface layer and $x_L = t_{\text{af}} - 1$ the free surface. All fields are expressed in reduced units of $h = 2H_a M_{\text{ft}} t / \sigma_{\text{af}}$.

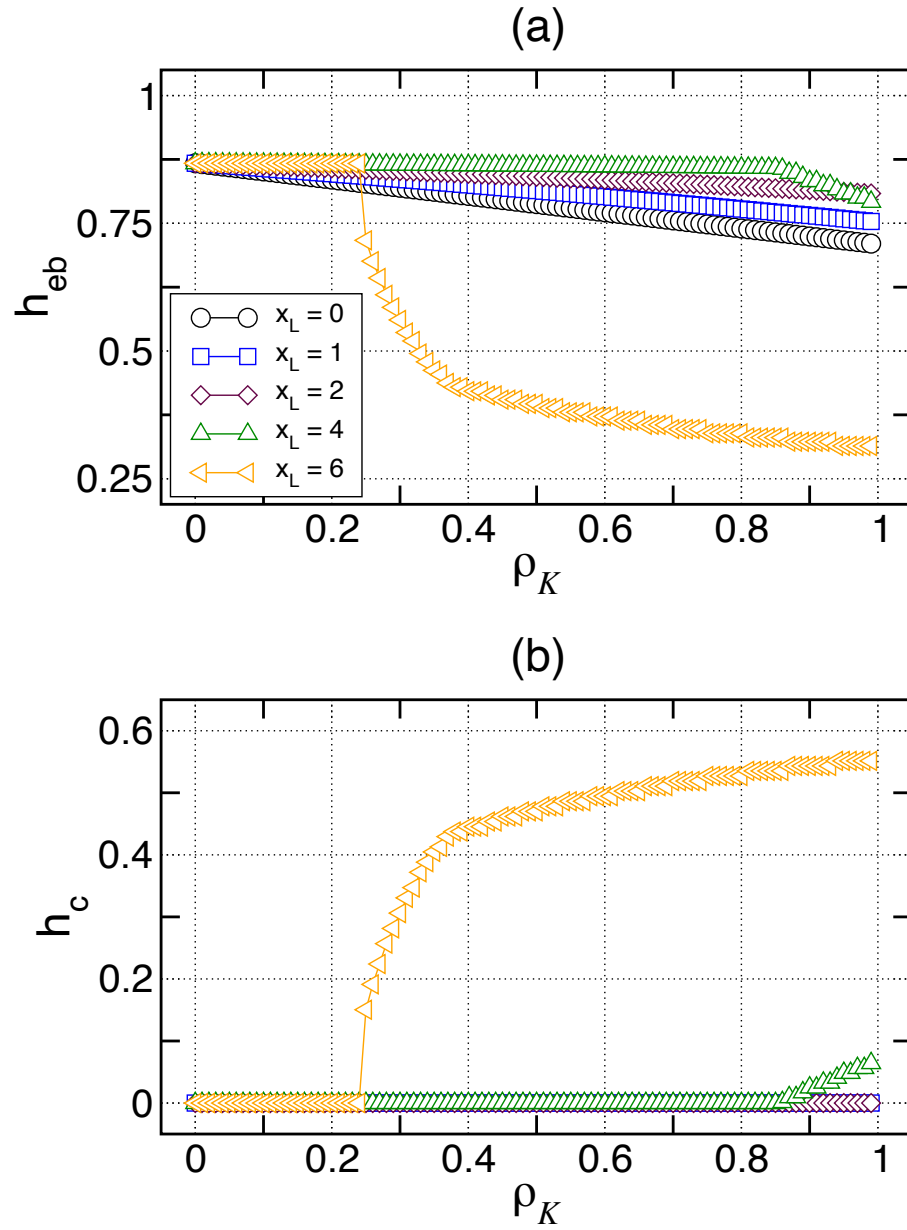


Figure 4.5: Bias field and coercivity variations for reduced-anisotropy defects. The (a) bias field h_{eb} and (b) coercivity h_c are shown as functions of defect strength $\rho_K \equiv 1 - K_d/K_{\text{af}}$ for a series of defect positions x_L in the antiferromagnet, where $x_L = 0$ corresponds to the interface layer and $x_L = t_{\text{af}} - 1$ the free surface. All fields are expressed in reduced units of $h = 2H_a M_f t_f / \sigma_{\text{af}}$.

attractive potential to pin the partial wall. Defects situated farther away from the interface have a greater effect, where for $x_L = 6$ a large coercivity enhancement is observed at high concentrations.

Defect-induced pinning of the partial wall can be seen in Figure 4.6, where the position of the wall centre is shown as a function of defect density. The values of x_c shown are taken at maximum reverse field in a hysteresis loop, which represents the point at which the extent of the partial wall formed is the greatest. The attraction of the wall to the pinning potential can be seen as the wall centre drifts from the zero density value $x_{c0} \simeq 2$ towards x_L with increasing defect concentration. Defects close to the interface move the wall centre closer to the ferromagnet.ⁱⁱ Farther into the bulk, the pinning potential can cause a complete detachment of the partial wall from the interface. These processes are indicated by the sharp transitions for $x_L = 6$ and $x_L = 8$ in Fig 4.6a, and $x_L = 8$ in Fig 4.6b. In these cases a complete loss of bias occurs and a large coercive loop is obtained.

The reduction in the bias field induced by the defects is consistent with early ion-irradiation experiments on exchange biased NiFe/FeMn systems [114], where it was observed that bias can be controlled by varying the dose of the incoming ions. However, more recent studies have indicated an enhancement in the bias field can be obtained using the same experimental technique [157, 227]. It is possible to account for the observed increase in the bias with the present model by increasing the local anisotropy, equivalent to a repulsive defect potential. Physically, structural changes leading to strain-related enhancements in the anisotropy have been shown to be possible [384–387]. This is explored in more detail later in the chapter.

ⁱⁱA similar effect can be achieved with a repulsive potential in the antiferromagnet (cf Fig. 4.1).

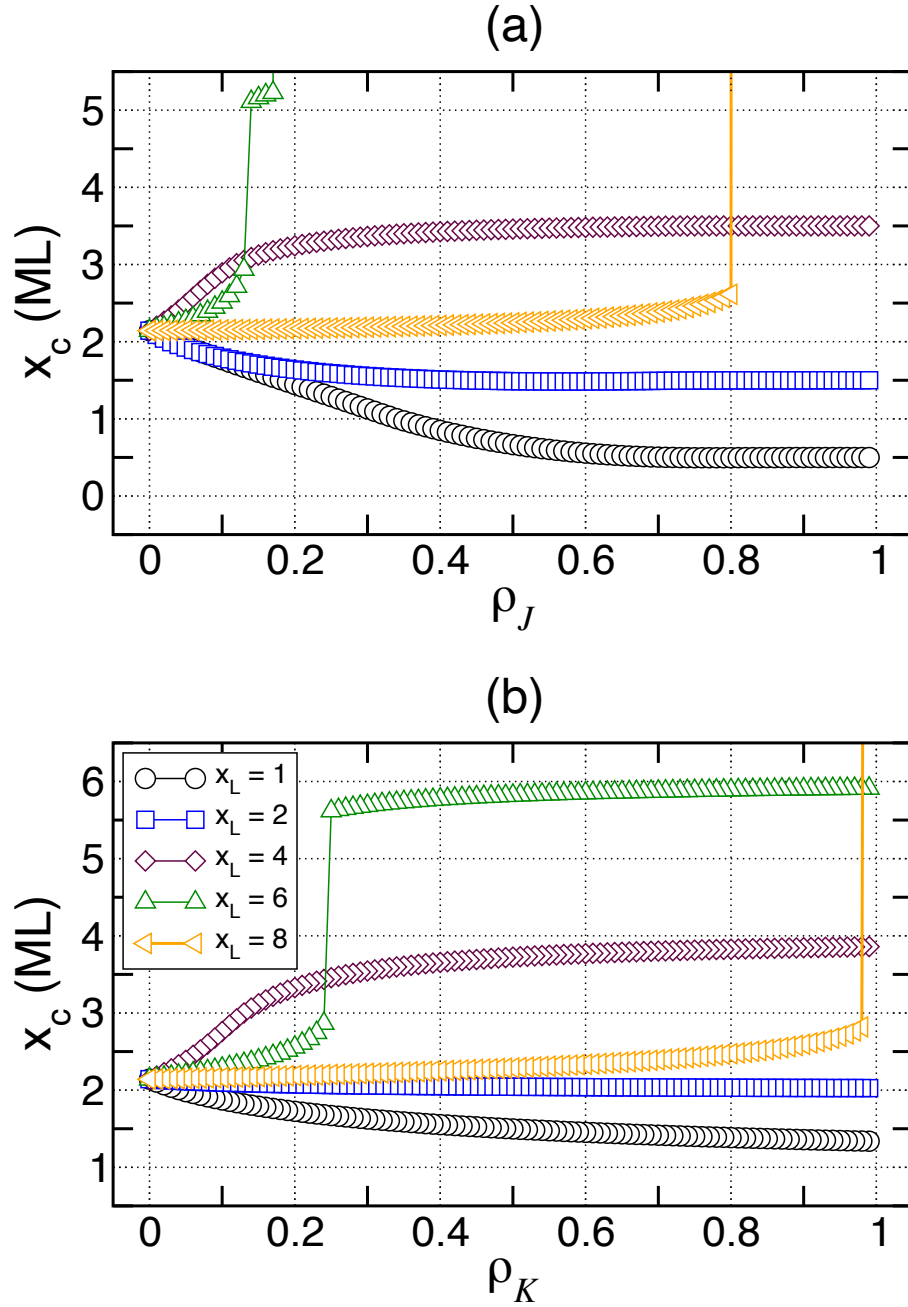


Figure 4.6: Variation in the position of partial wall centre with magnetic defects. The antiferromagnet wall centre, x_c , is shown as a function of defect density for (a) reduced-exchange and (b) reduced-anisotropy defects for a series of defect positions x_L , where $x_L = 0$ corresponds to the interface layer and $x_L = t_{\text{af}} - 1$ is the free surface. Note that ρ_J defects denoted by x_L modify the exchange between the layers at $x_L - 1$ and x_L .

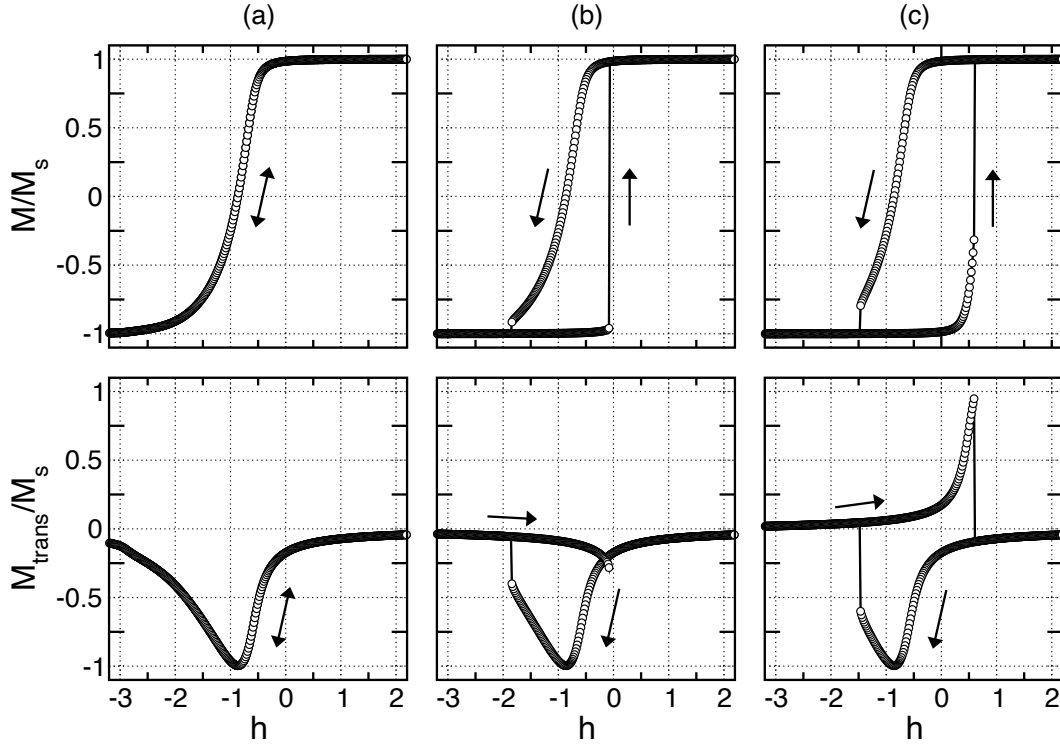


Figure 4.7: Defect-induced asymmetry in hysteresis loops. The hysteresis loops are shown for a reduced exchange defect at $x_L = 4$ for three concentrations: (a) $\rho_J = 0.15$, (b) $\rho_J = 0.45$ and (c) $\rho_J = 0.75$. The component of magnetization parallel to the field direction, M/M_s , and perpendicular to the field direction, M_{trans}/M_s , are shown. The arrows indicate the directions for reversal and remagnetization. All fields are expressed in reduced units of $h = 2H_a M_f t_f / \sigma_{\text{af}}$.

4.3 Asymmetric hysteresis

Irreversible rotations of the ferromagnet, due to a combination of wall pinning and depinning transitions, give rise to asymmetric hysteresis loops. Some examples are given in Figure 4.7. The loops are calculated with an exchange defect at $x_L = 4$ for three different values of ρ_J . At low concentrations, the pinning potential is insufficient to modify partial wall formation. The resulting magnetization curve is reversible and resembles the curve obtained with the absence of impurities (Fig. 4.7a). Depinning of the partial wall is triggered at moderate concentrations during reversal, which appears as a sharp rotation of the magnetization at negative fields (Fig. 4.7b). During remagnetization the wall is released from the pinning centre at a different field to H_{c1} , thus resulting in an asymmetry in the hysteresis loop. The release of the wall is indicated by a sharp transition in M_s . The energy barrier between wall pinning and release increases with defect concentration,

resulting in a larger coercivity and reduced bias (Fig. 4.7c).

The rotation sense of the ferromagnet is governed by the strength of the pinning potential and by the relative orientations of the ferromagnet, applied field and interface antiferromagnet spin. This can be seen by examining the component of magnetization perpendicular to the field direction, M_{trans}/M_s , during a hysteresis loop sweep. Reversal is executed with a counter-clockwise rotation for the three defect concentrations considered, as indicated by the negative values of M_{trans}/M_s along the path towards negative field. A clockwise rotation into forward field is executed at low concentrations, because the winding and unwinding of the partial wall is unhindered by the defect (Fig. 4.7a). However, the release of the partial wall after pinning can occur in two ways. For moderate concentrations (Fig. 4.7b) the partial wall, still under the influence of the interlayer coupling, reattaches itself to the ferromagnet after being released from the pinning site. Consequently, remagnetization occurs through clockwise rotation as for Fig. 4.7a. For strong pinning, the partial wall is not released and a second wall is wound instead during rotation into forward field. This process occurs from another clockwise rotation of the ferromagnet, indicated by the sign change in M_{trans}/M_s (Fig. 4.7c). In Figure 4.8 the angle of the interfacial antiferromagnet spin φ_0 is shown as a function of ρ_J for a series of x_L . φ_0 is measured at maximum reverse field and $\varphi_0(0)$ refers to the interface angle attained for no defects. For impurities close to the interface ($x_L = 1$) φ_0 decreases steadily as the concentration increases, indicating a shift in the wall centre towards the interface. This trend reverses close to $\rho_J = 0.5$, where φ_0 gradually increases past $\varphi_0(0)$ finally attains a value above θ_H . At higher concentrations the behaviour is a result of strong deformations in the domain wall profile centred about the impurity. Similar variations are observed for other defect positions.

If the twist angle φ_0 lags the ferromagnet, i.e. $\varphi_0 > \theta'_H$ (see Fig. 4.8), it is favourable for the wall to unwind and the remagnetization process occurs with a clockwise

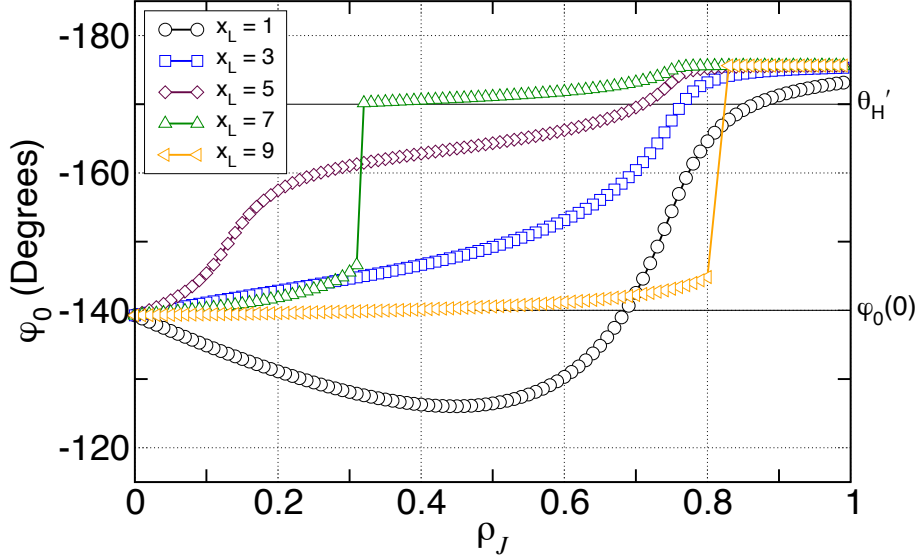


Figure 4.8: Variation in extent of partial twist with defects. The angle of the interfacial antiferromagnetic spin φ_0 as a function of reduced-exchange defect density ρ_J is shown for a series of defect positions x_L . Also indicated are the applied field angle $\theta'_H \equiv \theta_H - 180^\circ$ and the twist angle at zero defect concentration $\varphi_0(0)$.

rotation into forward field. Large distortions to the wall profile at higher concentrations mean that the interface spin angle φ_0 can lie between θ'_H and -180° . A sharper wall profile exploits the reduced exchange at the defect, resulting in a lower torque exerted by the twist. In this case, remagnetization proceeds by rotating through the easy axis a second time and initiates the formation of a second twist. In short, remagnetization in Fig. 4.7b represents the annihilation of two domain walls of opposite chirality, while in Fig. 4.7c, the ferromagnet rotation forms walls of the same chirality.ⁱⁱⁱ

Asymmetric hysteresis loops have been measured in a number of experimental systems [59, 113, 118, 137, 164, 166, 195, 216, 217, 220, 258, 266]. In certain cases, complementary polarized neutron reflectometry experiments have shown that these observations can be explained by a reversal via coherent rotation and a remagnetization process involving domain wall propagation [118]. Krivorotov et al. [216] explained asymmetric hysteresis

ⁱⁱⁱThe domain wall chirality in one dimension, C , can be defined by the integration over all space of the gradient in the angular variable θ parametrizing the domain wall profile,

$$C = \frac{1}{\pi} \int_{-\infty}^{\infty} \frac{\partial \theta}{\partial x} dx.$$

The chirality $C \pm 1$ characterizes the sense of rotation or handedness of the magnetization within the domain wall.

in their Fe/MnF₂ system by proposing the presence of a three-fold anisotropy term, but the results in this section instead offer an interpretation in terms of domain wall pinning processes in the antiferromagnet. This explanation is consistent with some recent work of Nikitenko et al. on the NiFe/FeMn system [113], who concluded the presence of an antiferromagnet wall at the interface is necessary to explain their hysteresis measurements.

4.4 Angular dependence of exchange bias

The pinning potentials are only effective within a certain angular range of the applied field. The angular dependence of the bias field and coercivity is shown for reduced-exchange defects in Figure 4.9. Reductions in the interlayer coupling, produced by interface defects ($x_L = 0$), cause a decrease in the bias field across the entire range of applied field angles (Fig. 4.9a). This behaviour is consistent with the continuum theory developed in Chapter Two, where the bias field dependence on $J_{\text{f-af}}$ enters in a straightforward way (Eq. 2.36). Because no frustration is introduced by interfacial defects, in contrast to rough interfaces, there is no change in the natural angle of the ferromagnet. For defects located farther into the bulk, the angular dependence can be modified significantly. Outside of an angular range $\Delta\theta_H$ measured about the hard axis of the antiferromagnet (shown for $\rho_J = 0.9$ in Fig. 4.9c), the bias field is observed to be largely suppressed and accompanied by an enhanced coercivity (Fig. 4.9b and c). Inside this angular range the hysteresis properties do not appear to be modified by the defect, where all the curves ‘collapse’ onto the zero-concentration curve.

The angular range $\Delta\theta_H$ defines a “passive region” in which bias is unaffected by the defect. The wall centre^{iv} does not propagate sufficiently close to the defect, away from the interface, to be affected by the pinning potential in the passive region. The resulting

^{iv}As shown in Chapter Two, the soliton nature of the partial Bloch wall means that its profile is completely determined by the exchange and anisotropy constants in the material. For a given wall chirality, there is a one-to-one correspondence between the interface angle and the wall centre. It is useful in this discussion to view the partial wall formation in terms of the distance travelled by the wall centre into the antiferromagnet layer.

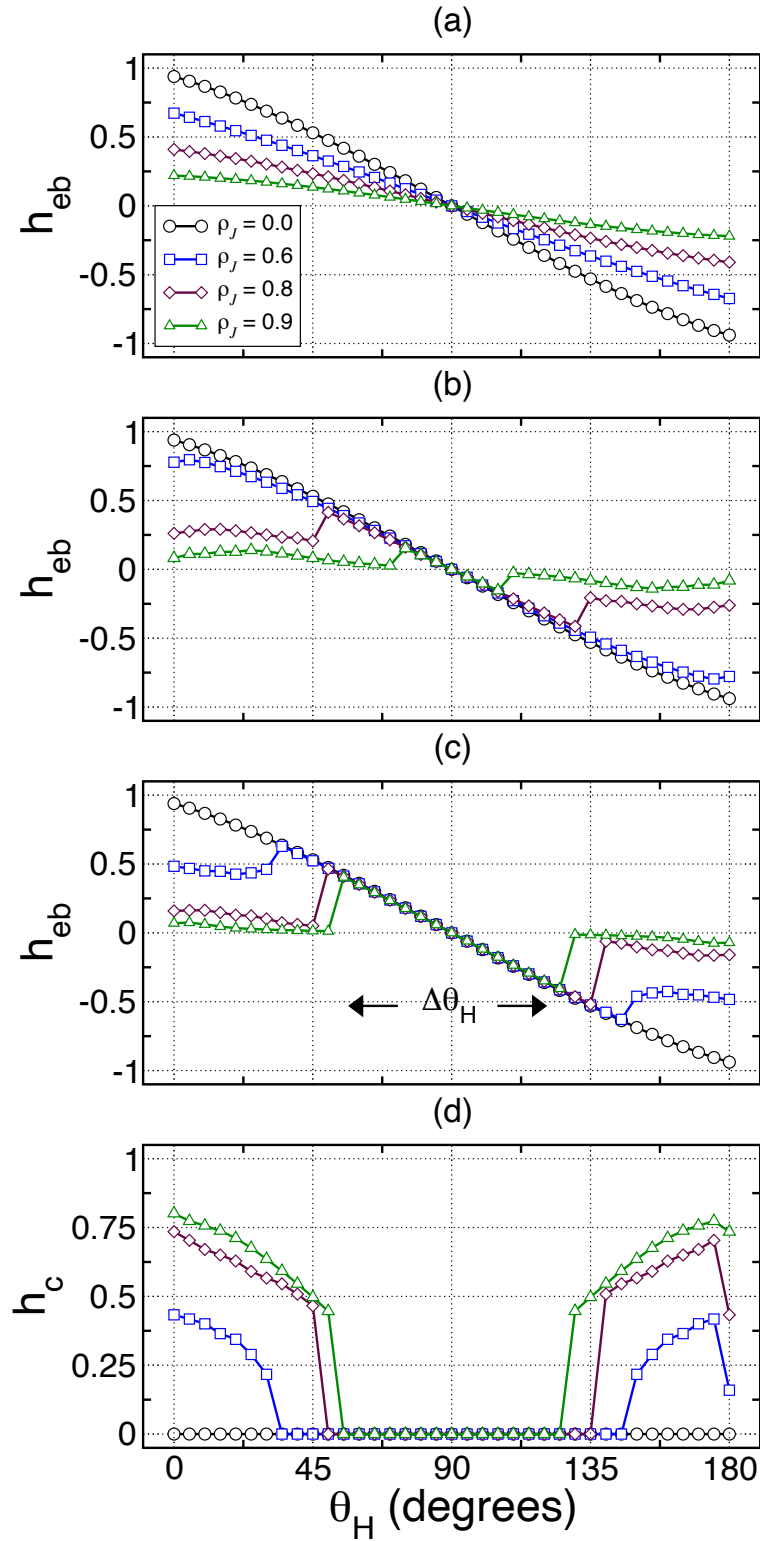


Figure 4.9: Defect-modified angular dependence of exchange bias. The bias field h_{eb} is shown as functions of the applied field orientation θ_H , for a series of reduced-exchange defect locations: (a) $x_L = 0$, (b) $x_L = 2$, (c) $x_L = 4$. The coercivity h_c is shown in (d) for the corresponding curves in (c). All fields are expressed in reduced units of $h = 2H_a M_{itf} / \sigma_{af}$.

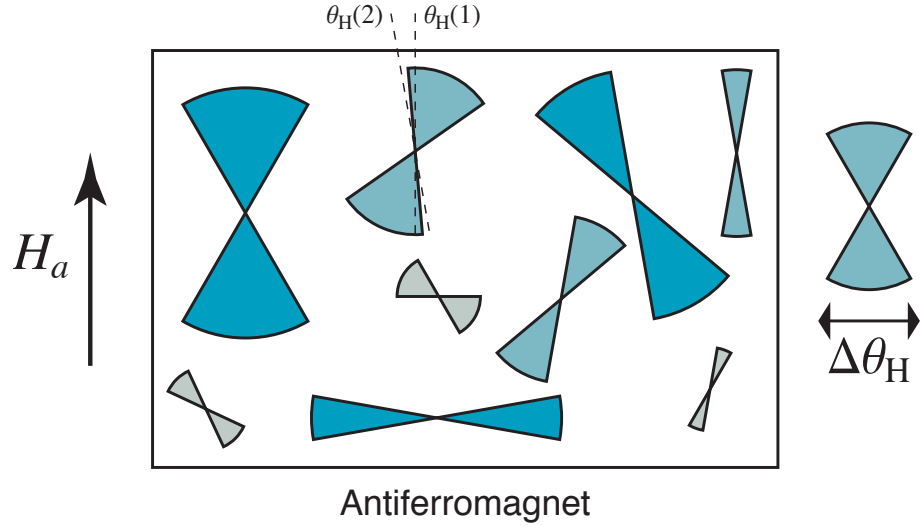


Figure 4.10: Model of rotational hysteresis. $\Delta\theta_H$ represents the passive region associated with a particular defect. Rotations that cross the boundary of a passive region lead to irreversible depinning transitions of the domain wall.

magnetization curves in this regime are similar to the zero-concentration case, where wall formation is unhindered. Defect-induced wall pinning is possible outside of the passive region, where the energy barrier imposed by the pinning potential largely determines the hysteresis properties. The size of the passive region depends on the position and magnitude of the pinning potential.

An interpretation of rotational hysteresis can be made in light of these results. In a realistic material, one may suppose that a large number of pinning sites in the antiferromagnet, of different magnitudes and distances from the interface, can give rise to an ensemble of passive regions as depicted in Figure 4.10. For a material with an ensemble of grains at the interface the easy axis direction may vary from grain to grain, so the orientation of these passive regions need not be collinear. Let $\theta_H(1)$ denote the nominated field orientation shown in Fig. 4.10. For a uniform ferromagnet an ensemble of partial twists is formed with magnitudes that are determined by the relative orientation of the local easy direction and $\theta_H(1)$. Suppose that the field is now rotated by a small amount to $\theta_H(2)$. If the new ferromagnet orientation remains within the passive region of a given grain, then the rotation causes the partial wall in the grain to wind or unwind

slightly and is a reversible process. However, if a transition is made across the boundary of a passive region the partial twist in the corresponding grain may be depinned from the interface due to the local defect. This is an irreversible process. Hence, the extent of the partial walls formed and the number of depinning transitions depend on the history of the rotation. For example, the rotation of the field from $\theta_H(2)$ to $\theta_H(1)$ would not necessarily produce the same results, because the configuration of partial twists at $\theta_H(2)$ may not lead to the same initial state at $\theta_H(1)$. This asymmetry between the two sense of rotation gives rise to rotational hysteresis.

In other theoretical studies, similar interpretations of rotational hysteresis are made in terms of grain sizes. For example, the model of Stiles and McMichael for polycrystalline systems [304, 330] assumes that reversible grains contribute to the unidirectional anisotropy and hysteretic grains contribute to irreversible effects. Whether a grain is reversible or irreversible depends on the extent of the partial wall that is allowed in that particular grain. The allowed wall size is governed by the size of the grain. Other approaches have yielded similar results [45, 120, 128, 343].

Domain wall pinning close to the interface suggests that bias may be possible for antiferromagnet films below the critical thickness. The calculation in Sec. 2.8 is repeated with the inclusion of a reduced-exchange defect, located at $x_L = 1$ with $\rho_J = 0.7$. For very thin films ($t_{af} = 2$ ML), the defect does not modify the antiferromagnet energy as a function of twist angle. However, departures from the defect-free case can be seen for films as thin as 4 ML, where evidence of twist formation can be seen in the high energy branch in Figure 4.11. The angular range for reversible twisting increases rapidly with t_{af} , where at $t_{af} = 6$ ML the film is sufficiently thick to support at 180° with the aid of the pinning potential. These results offer an explanation for the observation of bias in experiments with antiferromagnets under the critical thickness [39, 63, 72, 85, 139, 219, 250, 257, 270].

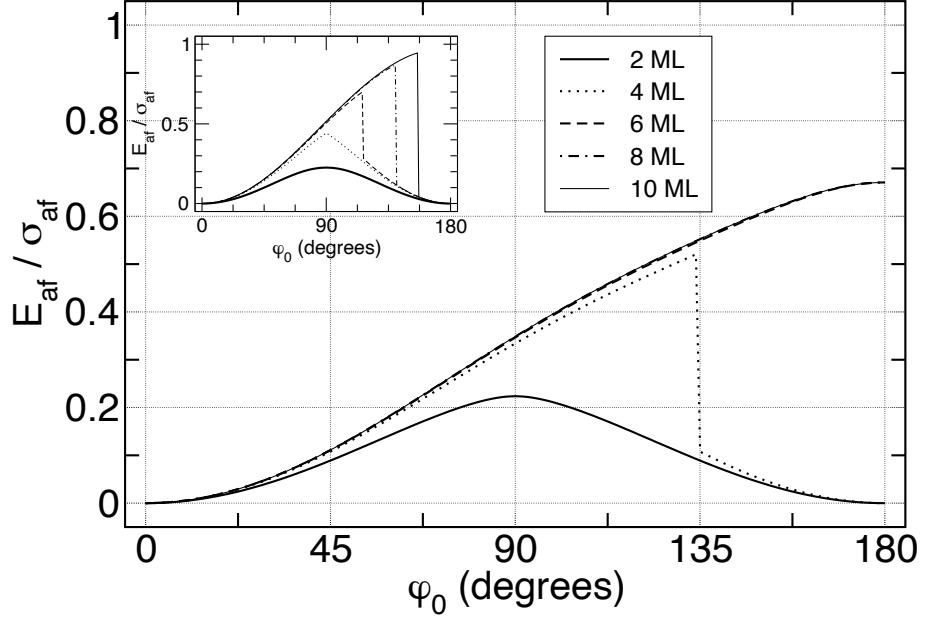


Figure 4.11: Defect-modified reversible and irreversible rotations. The normalized antiferromagnet energy, $\mathcal{E}_{\text{af}}/\sigma_{\text{af}}$, is shown as a function of twist angle φ_0 for a series of film thicknesses t_{af} . A reduced-exchange defect is located at $x_L = 1$ with concentration $\rho_J = 0.7$. Shown in the inset are energy curves for a defect-free system.

4.5 Spin dilution and site anisotropy variations

Variations in the magnetization within the film plane can be facilitated by extending the unit cell of each atomic layer. While the one-dimensional approach has been fruitful in obtaining some general features of defect-induced domain wall pinning, it is useful to compare these results with spin dilution and site anisotropy variations.

A 4×4 unit cell with periodic boundary conditions across the cell edges is used, with all other parameters remaining unchanged from Table 2.2. Spin dilution is simulated by removing spins from the lattice, where the dilution is restricted to a single atomic layer in which the defect sites are chosen at random. Variations in the local anisotropy are included for randomly selected defect sites, which also contained within one layer. x_L designates the position of the defect layer, which is referenced to the interfacial antiferromagnet layer $x_L = 0$ as shown in Fig. 4.3. ρ_J and ρ_K specify the density of defect sites within the designated plane and is equal to the fraction of the unit cell occupied by defect sites.

The results of spin-diluted exchange bias are shown in Figure 4.12. The features of these curves are similar to those obtained with the one-dimensional chain of spins. The bias field decay with defect concentration exhibits the same position dependence, where a change in the curvature of $H_{\text{eb}}(\rho_J)$ is observed as the defect layer is moved farther away from the interface. Again, changes to the bias field and coercivity are due to a reduction in the overall wall energy and wall pinning processes. One minor distinction between the one- and three-dimensional results is the smoothness of the $h_{\text{eb}}(\rho_J)$ curves for the latter. Sharp changes in the gradient of $H_{\text{eb}}(\rho_J)$, present for the one-dimensional chain, are absent for spin dilution.

For a compensated interface, exchange coupling between the ferromagnet and antiferromagnet layers rely on the spin-canted state at the interface to facilitate the spin-flop coupling. This energy has already been shown to be extremely sensitive to the magnitude of the interlayer exchange as well as the magnitude of the in-plane anisotropy [325].

The spin-flop coupling at compensated interfaces is sensitive to dilution effects. In Figure 4.13, the results show that bias can be suppressed for low concentrations of dilution at the interface. For defects farther from the interface the stability of the spin-flop improves and bias is obtained. Pinning of the domain wall is again evident, where a non-zero coercivity accompanying the loop shift is seen for a range of defect locations $x_L > 0$. The magnitude of the coercivity enhancement is largely governed by the proximity of the defects to the interface (Fig. 4.13b). The range of concentrations over which $H_c > 0$ increases as the defects are situated farther into the bulk.

One noticeable feature distinguishing the compensated interface from the uncompensated system is the coercivity for interfacial defects. From Fig. 4.13b, a decrease in the coercivity is seen to follow an increase in defect concentration. This is the only case where this trend occurs and is due to the instability of the spin-flop coupling. For all other $x_L > 0$ a steady increase in H_c is observed with concentration.

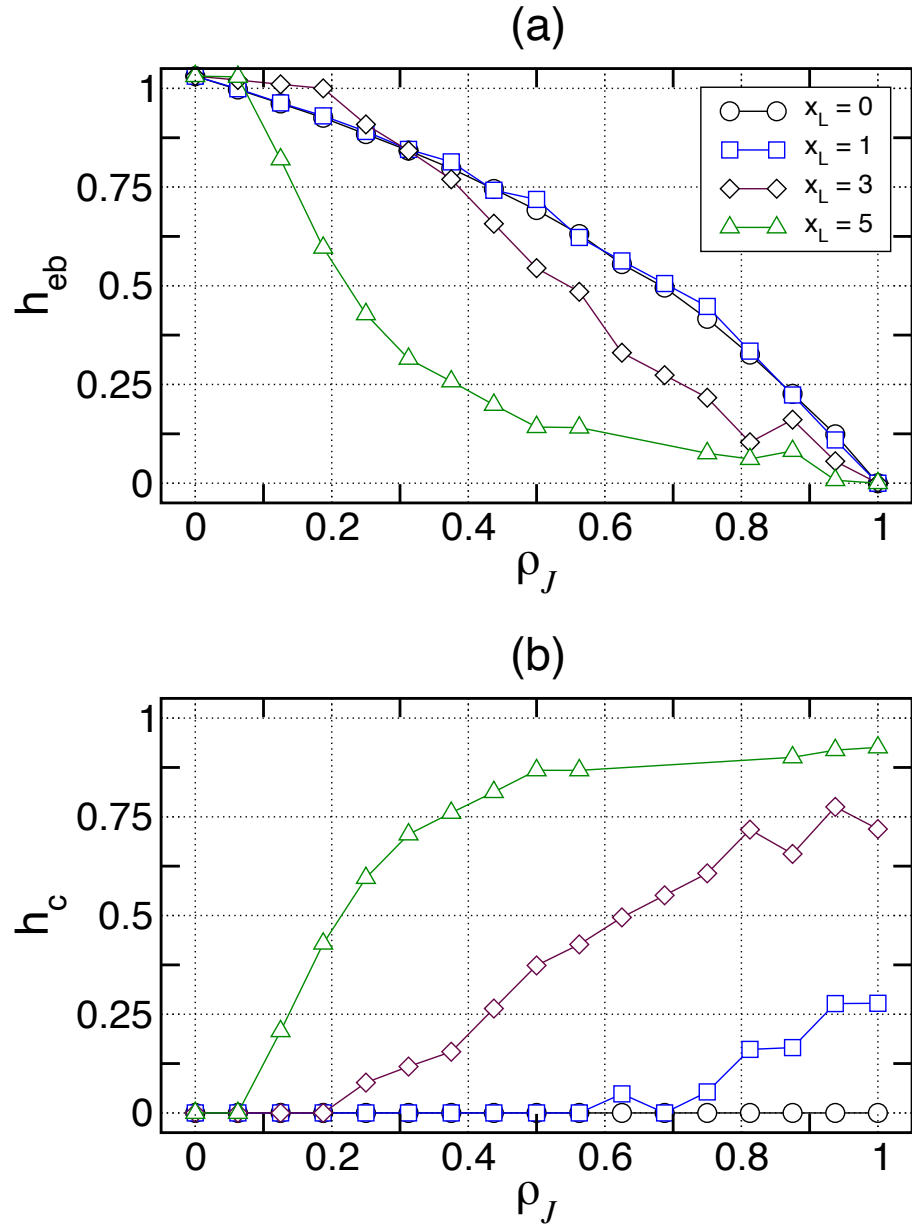


Figure 4.12: Modified exchange bias through spin dilution for uncompensated interfaces. The (a) bias field h_{eb} and (b) coercivity h_c as functions of the density of diluted spins ρ_J are shown for a series of defect layers x_L . All fields are expressed in reduced units of $h = 2H_a M_f t_f / \sigma_{\text{af}}$.

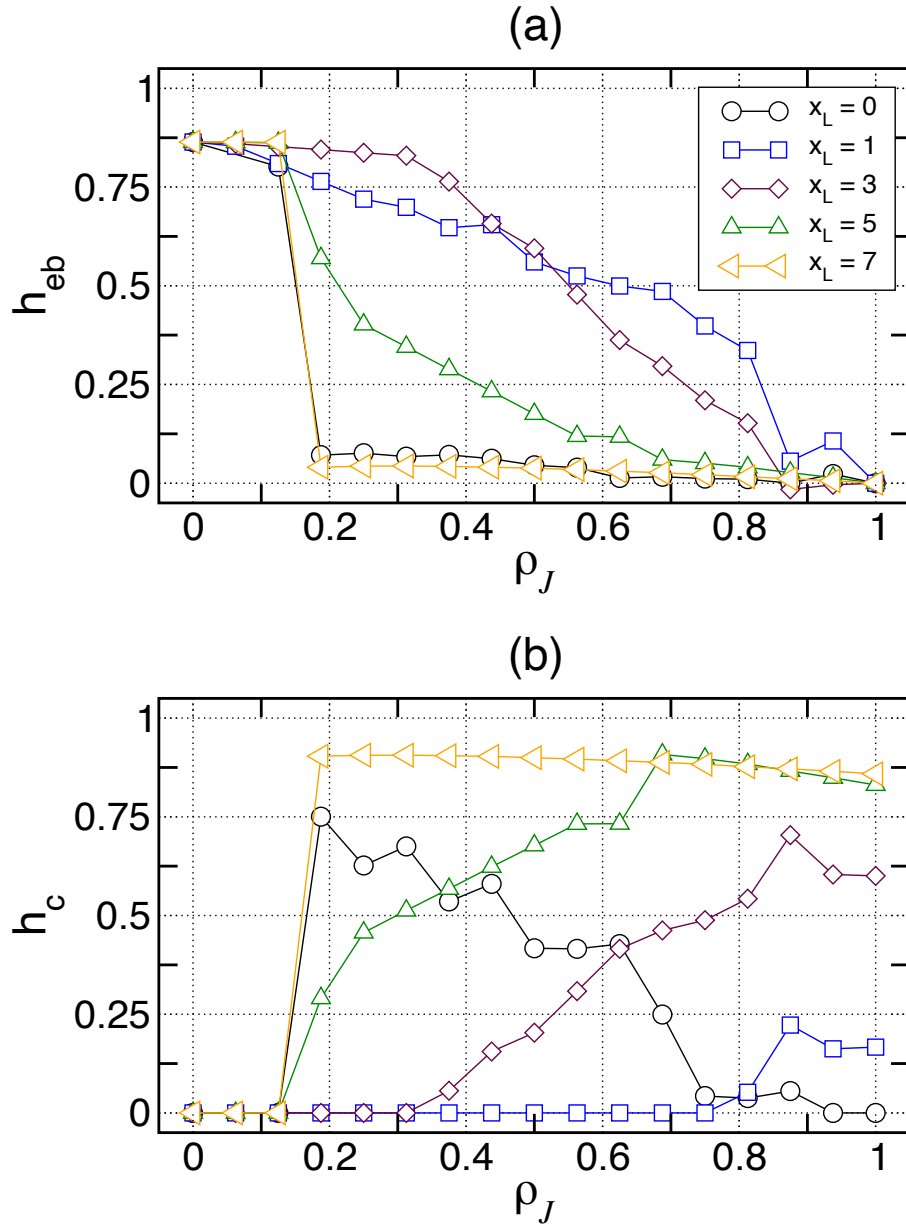


Figure 4.13: Modified exchange bias through spin dilution for compensated interfaces. The (a) bias field h_{eb} and (b) coercivity h_c as functions of the density of diluted spins ρ_J are shown for a series of defect layers x_L . All fields are expressed in reduced units of $h = 2H_a M_f t_f / \sigma_{af}$.

The effects of local anisotropy variations are shown in Figure 4.14. At each defect site, uniaxial anisotropy constant is increased by a factor of five but the direction of anisotropy is retained. This is carried out under the assumption that defects may lower the symmetry of the crystal fields at a nearby site through elastic deformations accompanying the imperfection. The magnitude of these anisotropy variations may vary considerably, but it has been suggested that strain related interface anisotropies can be up to an order of magnitude larger than bulk values for moderate strains of 1–2% [384–387].

For uncompensated interfaces these defects cause a modest enhancement in the bias field with no changes to the coercivity. The largest enhancement occurs for interfacial defects, with the magnitude of the enhancement decreasing rapidly as the defect layer is located farther from the interface. This behaviour can be understood in terms of a positive (and therefore repulsive) pinning potential. The influence of the defect is greatest at the interface because it is guaranteed that the wall centre passes through this point, and in doing so, surmounts the energy barrier induced. The bias field enhancement becomes less dramatic as the defects are located farther into the bulk, because the wall centre experiences less of the repulsive potential. The spin-flop coupling is also sensitive to local variations in the anisotropy, where the bias shift is observed to be completely suppressed at low concentrations. The bias and coercive fields are shown simultaneously in Figure 4.14b to emphasize that there is no simultaneous bias and coercivity for this type of defect in compensated systems.

Recent experiments with non-magnetic impurities in Co/CoO bilayers have demonstrated the importance of spin dilution in the antiferromagnet layer [132, 250, 257]. In these studies, the CoO antiferromagnet is diluted with non-magnetic Mg atoms during film growth, resulting in a $\text{Co}_x\text{Mg}_{1-x}\text{O}$ alloy exchange coupled to the ferromagnetic Co layer. An enhancement in the bias field is observed within a certain range of Mg concentration, where it is argued that the volume part of the antiferromagnet is responsible for

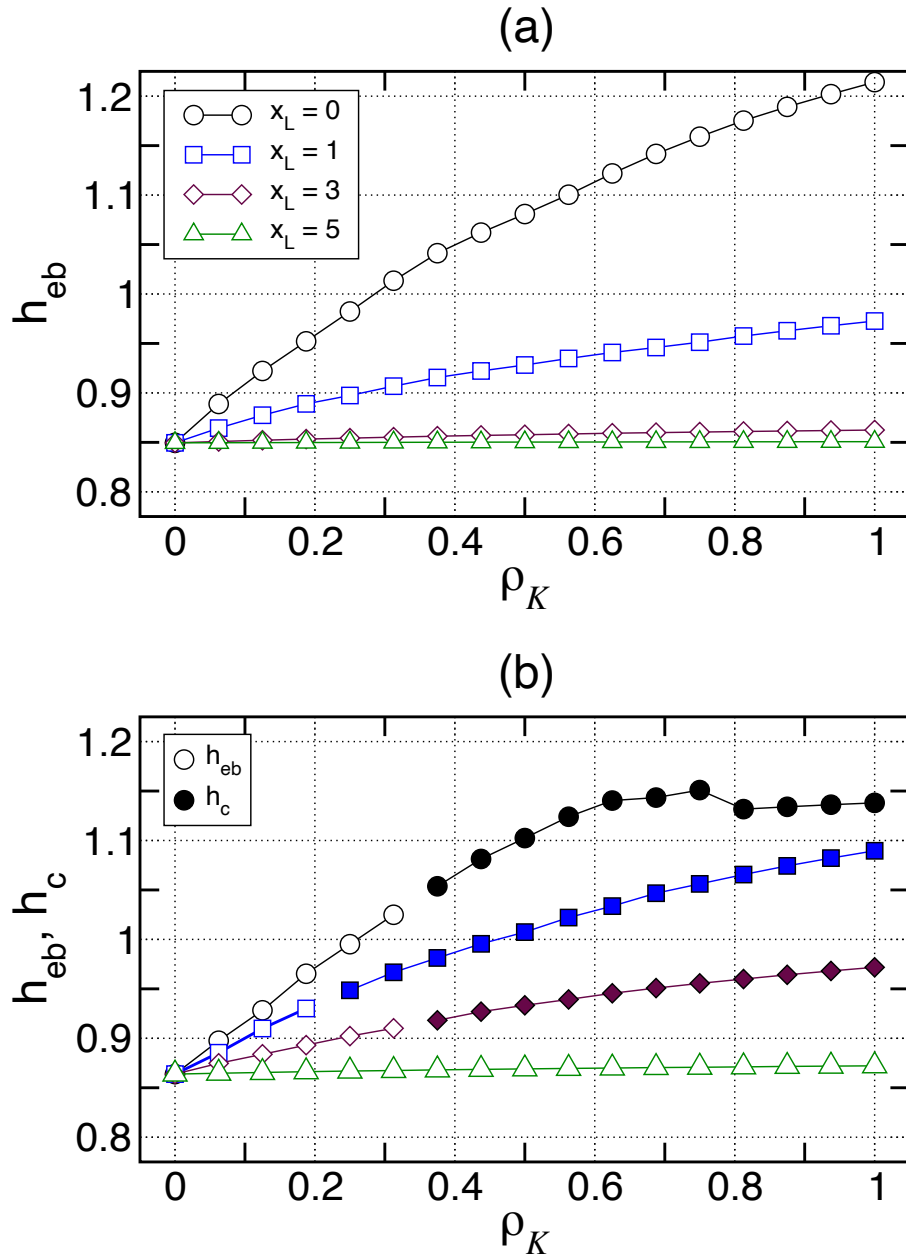


Figure 4.14: Modified exchange bias through local site anisotropy enhancements. The bias field h_{eb} and coercivity h_c are shown as functions of the density of sites with increases in the anisotropy constant ρ_K , where $K_d = 10K_{af}$. (a) For uncompensated interfaces no changes to the coercivity are observed. (b) For compensated interfaces there is no simultaneous shift and loop widening.

the strong bias shifts [333,352,353]. The experimental observations can be explained with the wall pinning model presented here if local enhancements in the anisotropy accompany the spin dilution. The results in this section show an enhancement in the bias field can occur if a repulsive pinning potential for the domain wall is generated. For spin dilution in real materials, lattice strains resulting from the embedded non-magnetic impurities may give rise to such a variation in the local anisotropy.

Chapter 5

Finite temperature effects

The effects of temperature on the partial wall model of exchange bias are examined in this chapter. Temperature enters into the coupled equations of motion for the spins through a local mean-field approach. Particular attention is given to how the hysteresis properties of the bilayer are modified at finite temperatures. Thermally-induced domain wall pinning is shown to be important in governing the hysteresis close to the Néel temperature. This pinning leads to modifications in the angular dependence of the bias, analogous to the behaviour observed for defect-induced pinning. Finally, suggestions for an alternative means of characterizing antiferromagnetic order are made in light of studies of the magnetic heat capacity.

5.1 Local mean-field approach

Mean-field theory is an approximation for the thermodynamic properties of a system by treating the order parameter of the system as spatially constant. This is a useful description when spatial fluctuations are not important and can be neglected. In the local mean-field treatment the thermal averaged spin magnitude at a given site i , $\langle S_i \rangle$, as seen by nearest-neighbours is given by [388]

$$\langle S_i \rangle = S_0 B_S \left(\frac{\langle \vec{H}_i^{\text{eff}} \rangle \cdot \vec{S}_i}{k_B T} \right), \quad (5.1)$$

where S_0 is the spin magnitude at zero temperature. The effective field contains thermal averages of nearest-neighbour spins,

$$\langle \vec{H}_i^{\text{eff}} \rangle = \vec{H}_a + \frac{1}{g\mu_B} \left(\sum_j J_{ij} \langle \vec{S}_j \rangle + 2K_i (\langle \vec{S}_i \rangle \cdot \vec{z}) \vec{z} \right). \quad (5.2)$$

The Brillouin function $B_S(x)$ is

$$B_S(x) = \left(1 + \frac{1}{2S} \right) \coth \left[\left(1 + \frac{1}{2S} \right) x \right] - \frac{1}{2S} \coth \left(\frac{x}{2S} \right) \quad (5.3)$$

and represents a statistical average over the possible values of S_0 along the local field direction. In the limit that the spin vector takes on a continuum of values the Brillouin function reduces to the Langevin function,

$$B_\infty(x) \equiv L(x) = \coth(x) - \frac{1}{x}. \quad (5.4)$$

The temperature dependence can be incorporated into the numerical model presented in Section 2.7 by including an extra step to calculate the thermal average $\langle S \rangle$ self-consistently using Eqs. 5.1 and 5.4.

The mean-field thermal dependence is based on an average over the effective fields generated by the nearest-neighbours of each spin, so it disregards any correlations between the magnetic moments in the system. This is valid for temperatures sufficiently far from the critical point, where it is well known that the correlation length diverges and critical fluctuations dominate the thermodynamics of the system. Mean-field theory also fails to describe the magnetization at low temperatures, for which spin-wave theory [389] is better suited to explain the $T^{3/2}$ dependence observed in experiment. The aim here is to develop an intuition for how finite temperatures affect the partial wall formation, rather than determining accurate forms of the thermal dependences or critical exponents at the ordering temperature. Such issues are beyond the scope of this dissertation and are left open for future exploration.

5.2 Thermal domain wall profiles

Before discussing the effects of finite temperatures on the exchange bias system, it is useful to examine first the thermal properties of an isolated antiferromagnet domain wall. A profile for the antiferromagnet Bloch wall can be found numerically by following the approach of Papanicolaou [361]. Consider a chain consisting of $2N$ spins, where N is an even number. The formation of a Bloch wall profile can be motivated by commencing the chain in a two domain state. In the first half of the chain, the spins are in a Néel state where the first spin points up ($+z$) and the last spin points down ($-z$). The second half of the chain is also in a Néel state, except that the first spin points down and the last spin points up. A non-trivial domain wall separating the two regions can be obtained by allowing this configuration to relax. It is useful to characterize the domain wall by a stiffness parameter η ,

$$\eta \equiv \sqrt{\frac{2K_{\text{af}}}{J_{\text{af}}}}. \quad (5.5)$$

This calculation is repeated for a series of temperatures and with different anisotropy constants to give a range of η .

The thermal averaged moment $\langle S \rangle$ is shown as a function of spin position along the domain wall in Figure 5.1. The curves are arranged such that $x = 0$ corresponds to the centre of the domain wall. The interesting feature common to all η considered is the sharp reduction in $\langle S(x) \rangle$ at the centre of the domain wall. Because the gradient in the spin orientation is largest at the wall centre, the effective field acting on the centre spin is reduced by the mean-field averaging. This is a compounding effect as a reduction in the effective field leads to a further reduction in $\langle S \rangle$. The spin gradient at the wall centre is greater for narrower walls, which leads to the large reduction in $\langle S \rangle$ seen in Fig. 5.1c and d.

The spatial profile of the domain wall does not vary significantly with temperature. In Figure 5.2, the staggered magnetization is shown for the different values of η

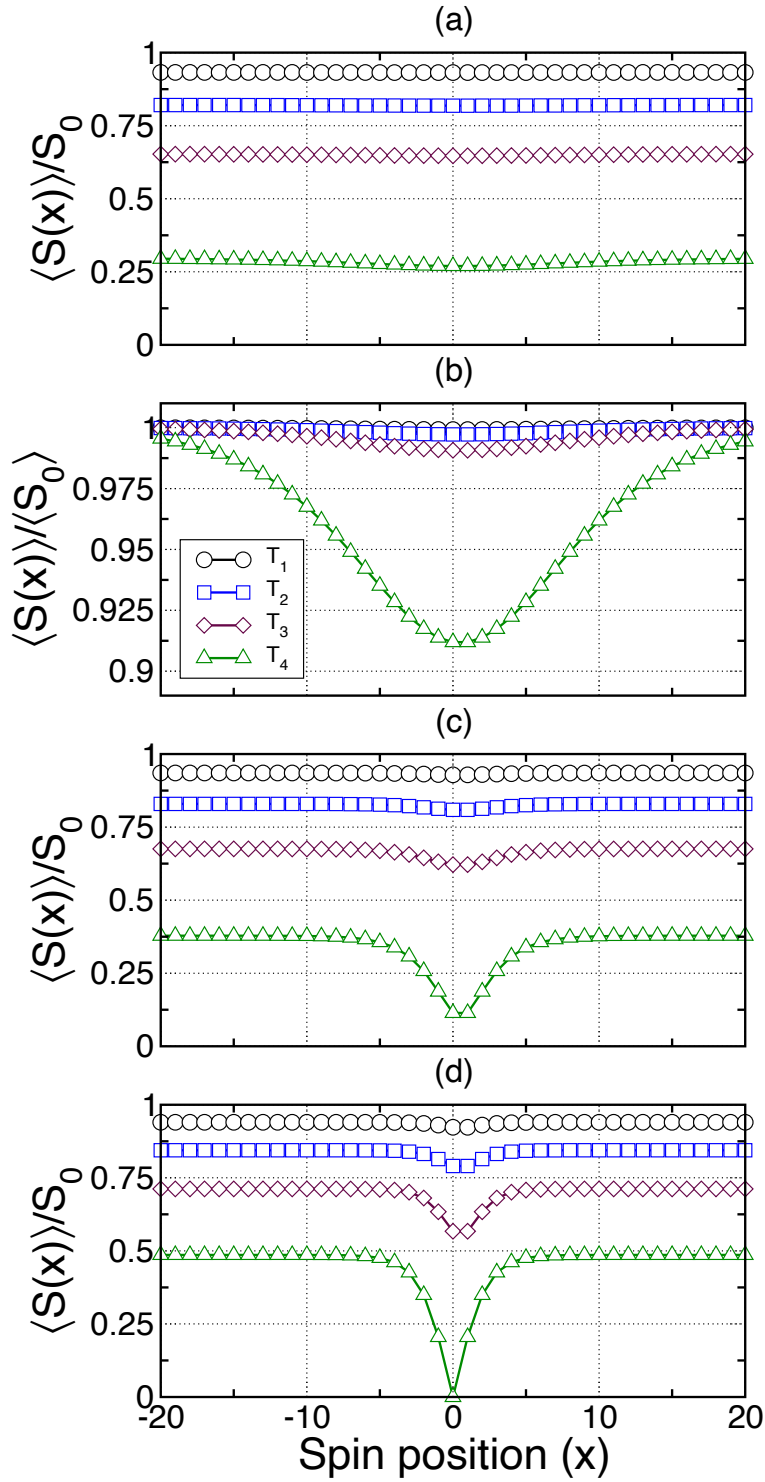


Figure 5.1: Thermally averaged spin profile for antiferromagnetic domain wall. $\langle S \rangle$, as a function of position along the antiferromagnet with a 180° Bloch wall, is shown for a series of temperatures: $T_1 = 0.125 T_N$, $T_2 = 0.375 T_N$, $T_3 = 0.625 T_N$ and $T_4 = 0.875 T_N$. The variations are shown for three different uniaxial anisotropy constants: (a,b) $K_{af} = 0.17$ meV/spin, (c) $K_{af} = 0.34$ meV/spin and (d) $K_{af} = 0.68$ meV/spin. A relative spatial variation in $\langle S \rangle$ is given in (b).

considered at several temperatures. For the wider walls (Fig. 5.2a and b), the profiles remain almost identical over the entire temperature range considered. Some evidence of thermally-induced narrowing at higher temperatures is seen for thinner walls (Fig. 5.2c and d). However, these walls only span a few atomic sites so the changes are mainly in the spin gradients at the centre.

5.3 Hysteresis

Exchange bias occurs only below the Néel temperature because it relies on magnetic order in the antiferromagnet to exist [6, 7, 10, 15, 19–21, 23, 31–33, 35–39, 42, 45, 48, 52, 56, 63, 65, 68, 70, 72, 80–82, 85, 89, 95, 96, 107–110, 117, 125, 136, 137, 139, 141, 144, 148, 152, 153, 155, 156, 158, 160, 163, 165, 166, 169, 177, 181, 185, 192, 194, 195, 200, 202, 209–211, 213, 215, 232, 235, 237, 240, 242, 245–247, 250, 252, 255, 256, 261, 264, 271, 272, 274, 279]. The bias shift is largest at $T = 0$ K and gradually diminishes as the temperature is increased. In the mean-field picture, this thermal dependence can be understood as a reduction in the local effective fields. The variation of $\langle \vec{H}_i^{\text{eff}} \rangle$ with temperature is determined by the Brillouin function through its dependence on $\langle S_i \rangle$. In Figure 5.3, the temperature dependence of the bias field and coercivity is presented for three different antiferromagnet anisotropy constants. The bias field is observed to decrease monotonically to zero as a function of temperature, where h_{eb} vanishes below the Néel temperature close to $T \simeq 0.9T_N$ for all three cases considered. As discussed shortly, this Blocking temperature is a result of domain wall pinning processes in the antiferromagnet that occur at elevated temperatures.

A non-zero coercivity accompanies the bias field at higher temperatures (Fig. 5.3b). This phenomenon is observed for the three wall stiffness values considered and is only seen in the approximate range $0.8T_N \leq T \leq T_N$ close to the ordering temperature. The magnitude of the coercivity enhancement is also observed to be proportional the stiffness of the domain wall, where the largest increase in h_c is seen for $\eta = 0.632$ and the smallest

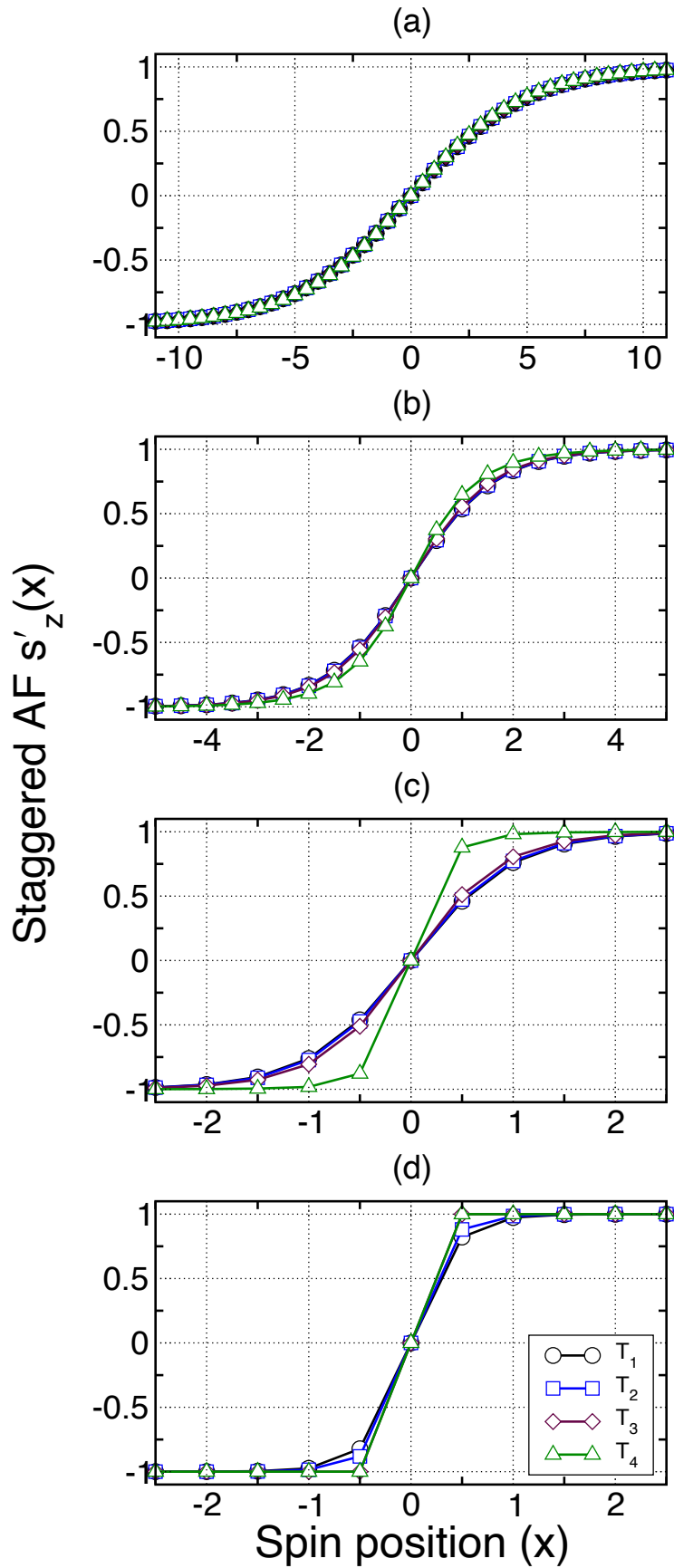


Figure 5.2: Variation in antiferromagnetic domain wall width with temperature. The spatial variation in the staggered magnetization $s'_z(x)$ is shown for a series of temperatures: $T_1 = 0.125 T_N$, $T_2 = 0.375 T_N$, $T_3 = 0.625 T_N$ and $T_4 = 0.875 T_N$. Four different wall stiffness values $\eta \equiv \sqrt{2K_{af}/J_{af}}$ are compared: (a) $\eta = 0.1$, (b) $\eta = 0.3$, (c) $\eta = 0.5$ and (d) $\eta = 1.0$.

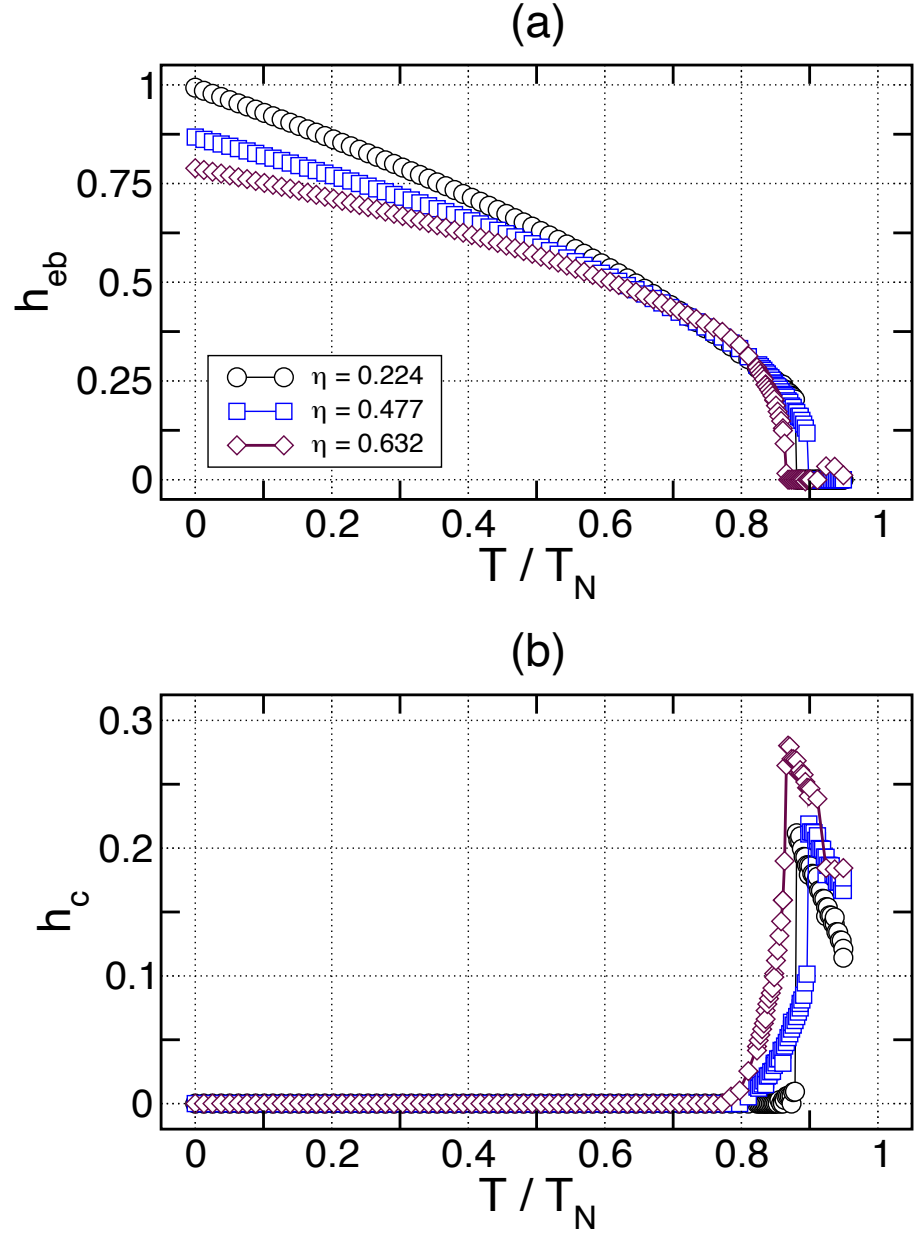


Figure 5.3: Thermal dependence of exchange bias. The (a) bias field h_{eb} and (b) coercivity h_c are shown as functions of reduced temperature T/T_N for three wall-stiffness values $\eta \equiv \sqrt{2K_{af}/J_{af}}$: (a) $\eta = 0.224$, (b) $\eta = 0.447$ and (c) $\eta = 0.632$. All fields are expressed in reduced units of $h = 2H_a M_f t_f / \sigma_{af}$.

increase for $\eta = 0.224$. This suggests that the irreversible behaviour is driven by a domain wall process, where the energy barriers that facilitate the irreversible transitions are governed by the wall energy in some way. The coercivity peaks at the Blocking temperature where the bias vanishes and then continues to decrease as the system is heated. This peak has been reported for a few experimental systems [20, 21, 153] and has been attributed to the rearrangement of magnetic domains at the critical temperature. As shown in the next section, this behaviour can be explained by a thermally-induced domain wall pinning.

5.4 Temperature induced domain wall pinning

The reduction in the spatial profile of $\langle S \rangle$ for an antiferromagnet wall represents a region of low energy density. This is analogous to the situation created by a ρ_J defect, where the reduction in the exchange energy at the impurity is favoured by the wall centre. Thus, the reduction in $\langle S \rangle$ can be viewed as a pinning potential that is generated by the thermal averaging.

To see how this relates to the exchange bias system, the spatial variation in $\langle S \rangle$ for the partial antiferromagnet wall during a hysteresis loop measurement is examined in Figure 5.4. At forward field (Fig. 5.4a), where there is no twist, the thermal magnitude of the antiferromagnet spins decreases sharply from the interface and attains a constant average value throughout the remainder of the film. The environment at the interface is strongly influenced by the ferromagnetic layer. This is seen in the thermal magnitude of the interface antiferromagnet spin, which is generally larger than the average bulk antiferromagnet value due to the order-of-magnitude difference in the ordering temperature of the two materials. The decay from the interface to the bulk $\langle S \rangle$ is characterized by a penetration length λ_p , which is dependent on temperature and is a measure of how strongly the ferromagnet spins influence the antiferromagnet moments located away from the interface. λ_p is shown for $T_4 = 0.875 T_N$ in Fig. 5.4a.

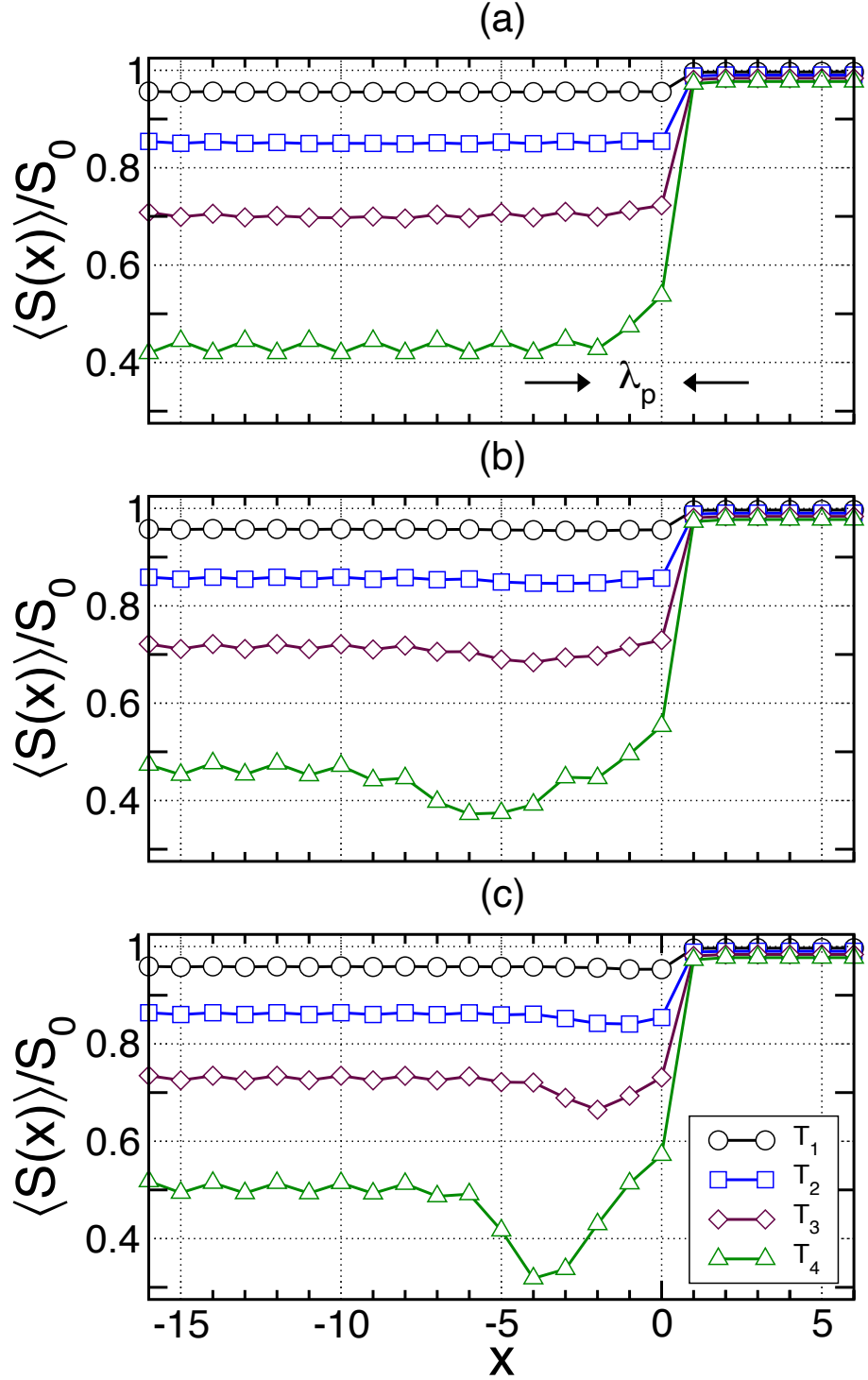


Figure 5.4: Thermal spin profile of an exchange coupled ferromagnet/antiferromagnet bilayer. The spatial variation of $\langle S \rangle$ is shown at (a) forward field for $\eta = 0.224$, (b) maximum reverse field for $\eta = 0.224$, and (c) maximum reverse field for $\eta = 0.447$. The curves are shown for four different temperatures: $T_1 = 0.125 T_N$, $T_2 = 0.375 T_N$, $T_3 = 0.625 T_N$ and $T_4 = 0.875 T_N$. $\eta \equiv \sqrt{2K_{af}/J_{af}}$ is a wall stiffness parameter, where $\eta = 0.224$ corresponds to $K_{af} = 0.085$ meV/spin and $\eta = 0.447$ corresponds to $K_{af} = 0.34$ meV/spin. The interface layer of the antiferromagnet is situated at $x = 0$ and the antiferromagnet occupies the region $-t_{af} - 1 \leq x \leq 0$. In (a) the penetration length of the ferromagnet λ_p is shown for T_4 .

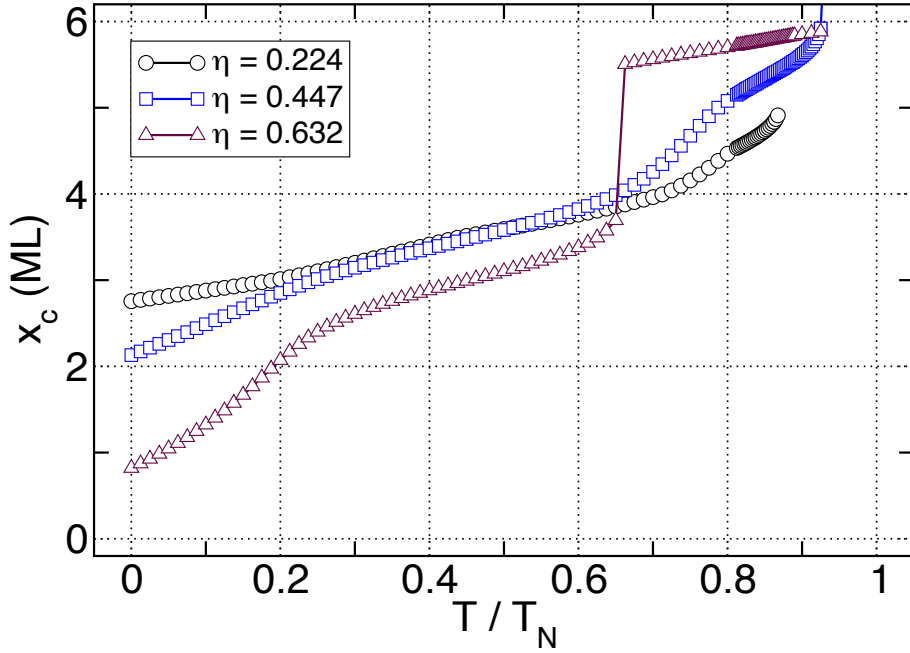


Figure 5.5: Variation of partial antiferromagnet wall centre with temperature. The wall centre x_c at maximum reverse field in a hysteresis loop is shown as a function of reduced temperature T/T_N for a series of wall stiffness values $\eta \equiv \sqrt{2K_{\text{af}}/J_{\text{af}}}$, where $\eta = 0.224$ corresponds to $K_{\text{af}} = 0.085$ meV/spin, $\eta = 0.447$ corresponds to $K_{\text{af}} = 0.34$ meV/spin and $\eta = 0.632$ corresponds to $K_{\text{af}} = 0.68$ meV/spin.

At reverse field the partial wall profile appears in the spatial variation of $\langle S \rangle$ (Fig. 5.4b and c). A sharp reduction is again observed at the wall centre and becomes more pronounced at high temperatures. For both antiferromagnets the wall centre appears to migrate away from the interface as the system is heated. This is particularly evident for the stiffer antiferromagnet $\eta = 0.447$ (Fig 5.4c). With the minimum in $\langle S \rangle$ as a guide for the wall centre, one sees that x_c moves from $x \approx 2$ at T_3 to $x \approx 4$ at T_4 . Since the wall width is of the order of ten atomic sites, this represents a significant change in the position of the wall profile with temperature.

This observation is quantified by examining the wall centre as a function of temperature. In Figure 5.5, the value of x_c obtained at maximum reverse field is shown for three wall stiffness parameters. The wall is observed to shift away from the interface as the temperature is increased for all three cases. For a large range of temperatures below T_B the wall centre remains within a penetration length of the interface, which means that the partial wall can wind and unwind reversibly to give a shifted magnetization curve

with zero coercivity. The discontinuity in $x_c(T)$ at higher temperatures indicate that the partial wall is no longer pinned to the interface. This irreversible process is analogous to the pinning/depinning transition effected by impurities, resulting in a hysteresis loop with non-zero width.

Thermally-induced (de)pinning is a result of the wall being repelled from the interface at elevated temperatures. Within a penetration length of the interface the proximity of the ferromagnet spins results in an enhanced $\langle S \rangle$ in the first few layers of the antiferromagnet (Fig. 5.4). An overall reduction in the wall energy can therefore be gained by positioning the region of reduced $\langle S \rangle$ (coinciding with x_c) in a region where $\langle S \rangle$ is small. This is in contrast with pinning potentials generated by defects, which rely on suitable placement or strength to cause a wall to de-pin from the interface.

5.5 Angular dependence of exchange bias

By analogy with the results of defect-induced bias, the repulsion of the partial wall from the interface at high temperatures should lead to similar variations in the angular dependence. The bias field and coercivity as a function of applied field angle are shown for a series of temperatures in Figure 5.6. In the first three panels (Fig. 5.6a-c) the angular variation in the loop shift is shown for antiferromagnets with three different anisotropies. The angular dependence does not appear to depart significantly from simple sinusoidal behaviour for weak anisotropy $\eta = 0.224$ (Fig. 5.6a), where a mostly uniform decrease in the bias field is observed at all angles with temperature. For larger anisotropies (Fig. 5.6b and c) the maximum in the bias field appears to shift away from the easy axis direction, for example, from $\theta_H = 0$ to $\theta_H \approx 10^\circ$ at $T = T_3$ and to $\theta_H \approx 30^\circ$ at $T = T_4$ in Fig. 5.6b with corresponding shifts in the minimum. A suppression in the bias field is observed, for a range of angles about the easy axis, close to the Blocking temperature for $\eta = 0.632$ (Fig. 5.6c).

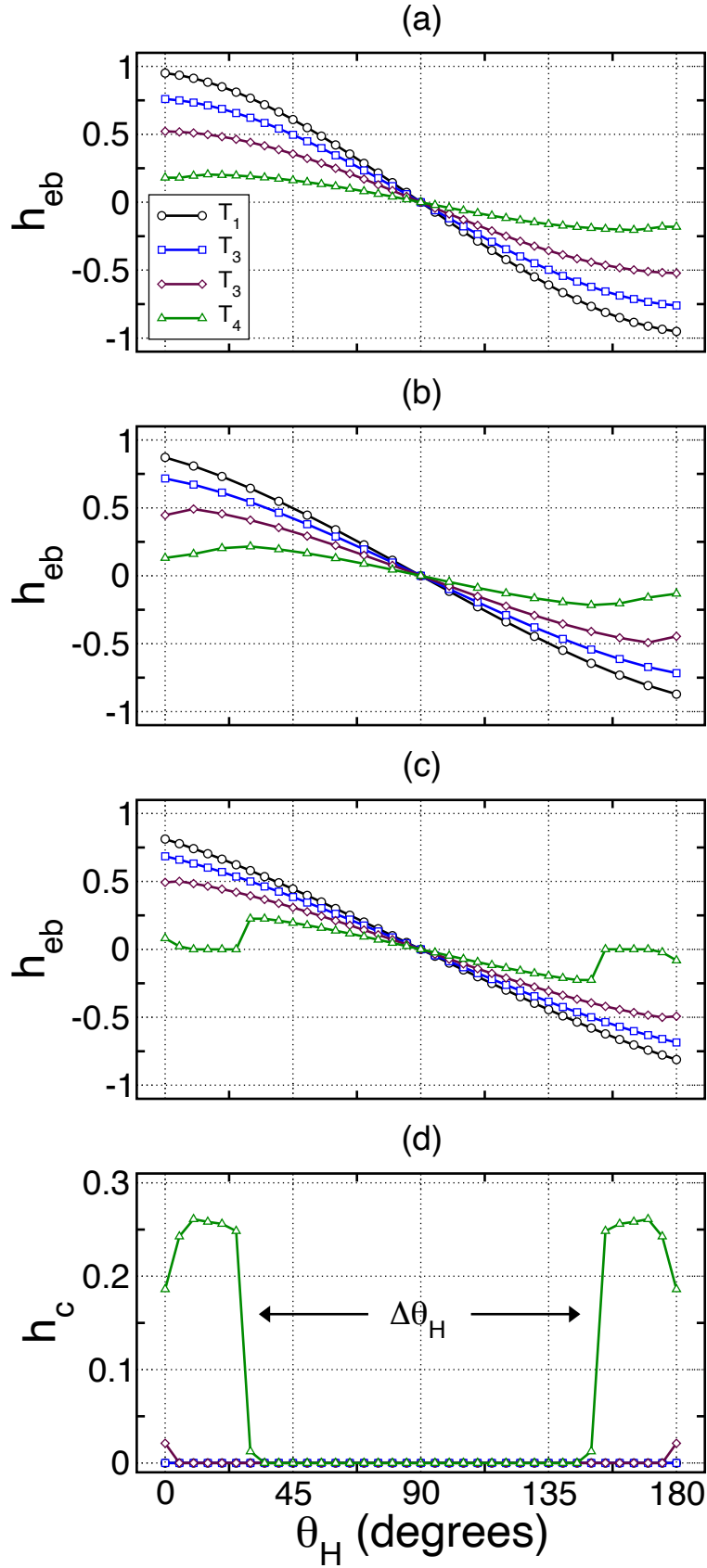


Figure 5.6: Angular dependence of exchange bias at finite temperatures. The bias field h_{eb} as a function of applied field angle θ_H is shown for a series of wall stiffness values: (a) $\eta = 0.224$, (b) $\eta = 0.447$ and (c) $\eta = 0.632$. The angular variation in the coercivity h_c for $\eta = 0.224$ is given in (d). The curves are shown for four different temperatures: $T_1 = 0.125T_N$, $T_2 = 0.375T_N$, $T_3 = 0.625T_N$ and $T_4 = 0.875T_N$. All fields are expressed in reduced units of $h = 2H_a M_f t_f / \sigma_{af}$.

These features are reminiscent of the defect-modified angular dependence examined earlier in Chapter Four. For thermal-induced pinning there is an analogous passive region $\Delta\theta_H$, shown for $\eta = 0.632$ at $T = 0.825 T_N$ in Fig. 5.6d, in which the hysteresis is not modified. Outside the passive region a large enhancement in the coercivity with a vanishing loop shift is observed.

This behaviour can be explained along the same lines as defect-induced pinning. Applied fields oriented close to the easy axis result in a partial wall with a large spatial extent. As discussed previously, it is more preferable for this wall to centre away from the ferromagnet penetration region because a reduction in wall energy can be gained. Such domain wall processes are less likely to occur if the applied field is orientated away from the easy axis, because the partial wall size is not as great. In such cases it energetically favourable for the wall to remain pinned at the interface, resulting in a reversible magnetization curve.

5.6 Thermal-enhanced impurity pinning

The repulsion of the antiferromagnetic domain wall from the interface can be viewed, alternatively, as the result of a fictitious attractive potential located somewhere in the antiferromagnet film. This pinning potential can be realized with the presence of magnetic impurities that cause spin-dilution or reductions in the exchange bond. To probe the possibility of a correlation between the thermal- and impurity-induced wall pinning, point defects in the one-dimensional ferromagnet/antiferromagnet chain are examined at finite temperatures. The variation of the bias field with the presence of a reduced-exchange defect, $\rho_J = 0.5$, is shown in Figure 5.7. The results show distinct regions of behaviour that are driven by defect placement. Within a penetration depth λ_p of the interface the defects do not appear to affect the hysteresis properties ($x_L \geq 1$), where a uniform decrease in the bias field accompanied by a small coercivity close to T_B is observed.

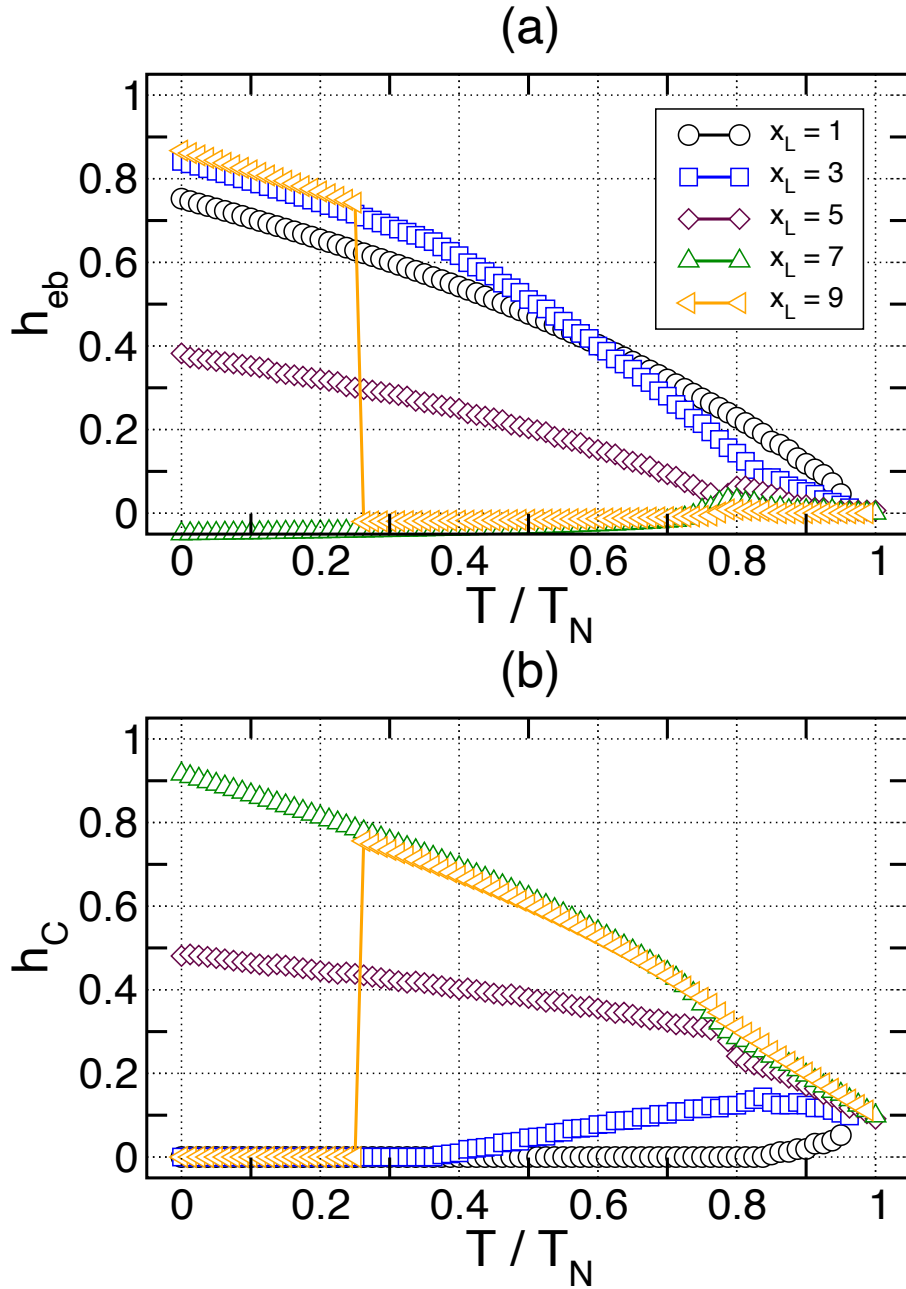


Figure 5.7: Defect enhanced thermal pinning of domain wall. (a) Bias field h_{eb} and (b) coercivity h_c as functions of reduced temperature T/T_N are shown for a series of exchange-defect position x_L , for $\rho_J = 0.5$. All fields are expressed in reduced units of $h = 2H_a M_f t_f / \sigma_{af}$.

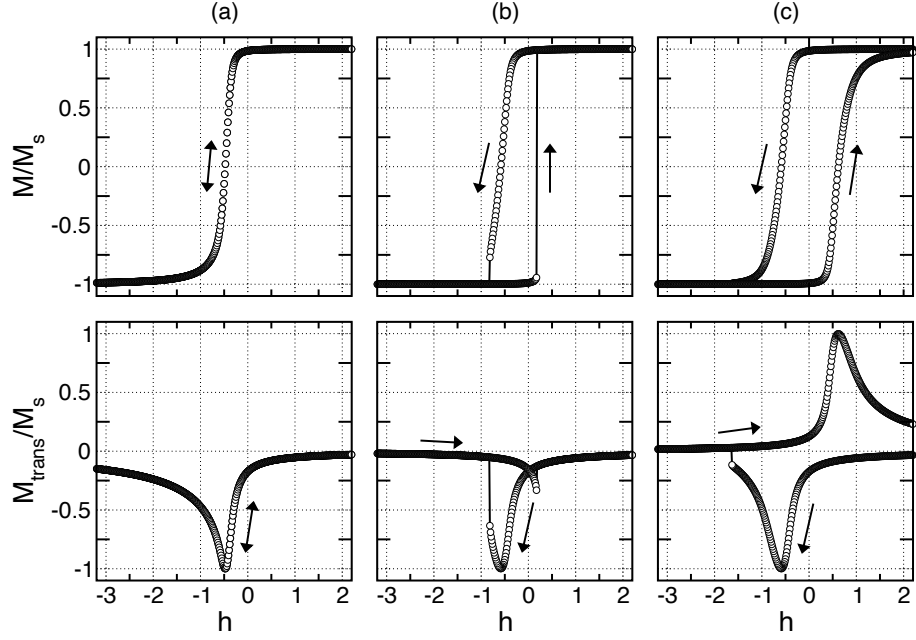


Figure 5.8: Asymmetric hysteresis due to thermally enhanced impurity domain wall pinning. The components of the magnetization parallel (M/M_s) and perpendicular (M_{trans}/M_s) to the applied field are shown for three different pinning potentials at $T = 0.5T_N$: (a) $x_L = 1$, (b) $x_L = 5$ and (c) $x_L = 9$. For all three locations a reduced-exchange defect with $\rho_J = 0.5$ is used. The arrows indicate the directions for reversal and remagnetization. All fields are expressed in reduced units of $h = 2H_a M_{\text{eff}} / \sigma_{\text{af}}$.

The proximity of the defect to the interface does not allow it to function effectively as a pinning centre, particularly at higher temperatures, because the thermal magnitude $\langle S \rangle$ is relatively large within the penetration region and the reduction in the exchange is insufficient to counter the influence of the ferromagnet. Evidence of a correlation between the thermal and impurity pinning can be seen for moderate to large defect distances from the interface ($x_L \geq 3$), where the temperature range over which non-zero coercive fields appear become broader. The coercivity is due to wall pinning at the defect site, where the pinning potential is enhanced at finite temperatures due to a further reduction in $\langle S \rangle$ at the wall centre.

Some examples of asymmetric hysteresis loops due to wall pinning are given in Figure 5.8. Reversible rotation of the magnetization is observed for defects close to the interface ($x_L = 1$), where the partial wall can wind and unwind without any hindrance. The impurity does not affect the rotation because thermal effects do not contribute to the pinning potential. Bias with a non-zero coercivity is seen for defects situated at moderate

distances ($x_L = 5$) from the interface (Fig. 5.8b). The variation of the perpendicular component of magnetization shows a twist formation during reversal followed by a depinning of the wall at the first coercive field H_{c1} . The wall is released during remagnetization at the second coercive field H_{c2} and leads to a sharp rotation of the ferromagnet in the opposite sense. The formation of two walls, the first during reversal and a second during remagnetization, occurs for defects situated far from the interface ($x_L = 9$). The sense of rotation of the ferromagnet is the same in both directions in this case. The first wall is pinned at the defect and is stable to subsequent rotations of the ferromagnet because of thermal enhancements to the pinning potential. The position of the defect is also sufficiently far into the bulk such that room exists for a second twist. In such cases the hysteresis curves are almost symmetric about the origin because the coercive fields are both due to wall formation.

5.7 Heat capacity as probe of antiferromagnetic order

A tantalizing prospect for probing antiferromagnetic order was recently demonstrated by the direct measurement of heat capacities in antiferromagnetic superlattices [390]. The procedure is sufficiently sensitive to observe distinct peaks in the magnetic heat capacity as the ordering temperature of the superlattice is reached. The technique provides a direct means of measuring changes in the antiferromagnetic order, particularly at phase transitions, that is not possible with conventional magnetometry techniques. A recent theoretical study of thin antiferromagnet films by Camley demonstrated that variations in the heat capacity may be used to identify the spin-flop transition [391]. It was shown that this transition should appear as a sharp feature in the magnetic heat capacity as a function of applied field, where the magnitude of the feature was calculated to be approximately 6 – 10% of the heat capacity itself. In this section, the possibility of studying the partial wall structure in an exchange biased bilayer with heat capacity measurements is

explored.

The heat capacity of interest for the exchange bias system is taken at constant field,

$$c_H = \left(\frac{\partial U}{\partial T} \right)_{H_a}, \quad (5.6)$$

representing the rate of change of the energy U , computed using the Hamiltonian given in Eq. 2.1, with temperature T at constant applied field H_a . The heat capacity is determined at each increment of the applied field once the equilibrium configuration has been found. The average energy is evaluated at a given temperature and the derivative in Eq. 5.6 is found numerically by taking the difference of the energies at nearby temperatures. This is accomplished with a four-point derivative method,

$$\left(\frac{\partial U}{\partial T} \right) \simeq \frac{1}{12\Delta T} (U_{-2} - 8U_{-1} + 8U_1 - U_2), \quad (5.7)$$

where U_n is a shorthand notation that represents

$$U_n \equiv U(T + n\Delta T, H). \quad (5.8)$$

A temperature interval of $\Delta T = 0.0001\text{K}$ is used in the calculations.

The aim is to study possible correlations between partial wall formation and features in the heat capacity that may appear. Some examples of heat capacities calculated during a hysteresis loop sweep are shown in Figure 5.9 for an uncompensated system. The magnetic parameters used are given in Table 2.2. For all temperatures considered, there is an increase in the heat capacity at maximum reverse field when the antiferromagnet partial wall has been wound to its fullest extent. At low temperatures, this change in the heat capacity takes the form of a broad increase that is largest when the wall is being wound. This broad peak becomes gradually sharper and increases in relative magnitude, as evidenced by the curves for $T = 60\text{ K}$ and 70 K [Fig. 5.9(d)]. For $T = 70\text{ K}$ there are two peaks in the heat capacity, corresponding to the initial depinning of the domain wall from the interface and its subsequent annihilation upon remagnetization.

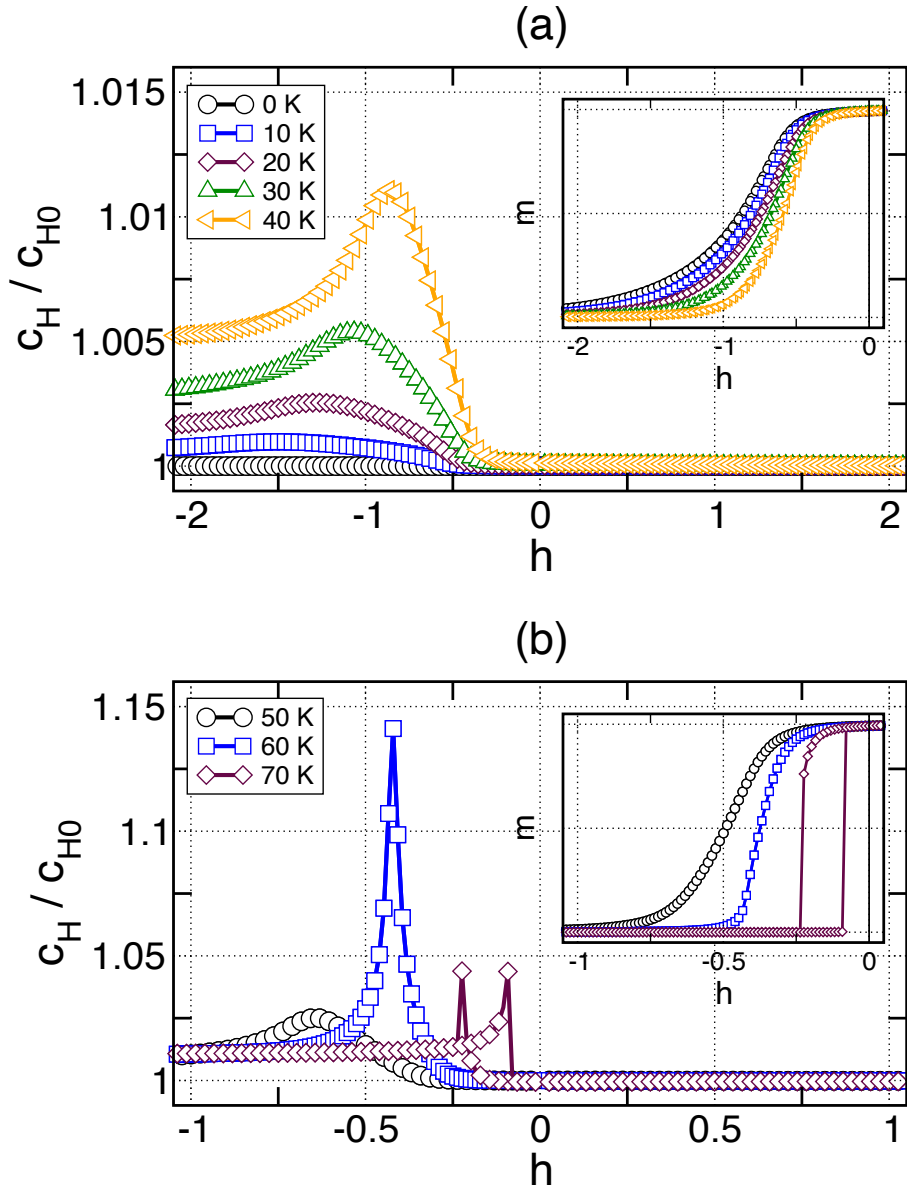


Figure 5.9: Magnetic heat capacity for uncompensated interfaces with large J_{F-af} . The normalized heat capacity c_H/c_{H0} as a function of applied field during a hysteresis loop sweep is shown for a series of temperatures, with $J_{F-af} = J_{af}$. The constant c_{H0} is the value of c_H at maximum forward field. The corresponding magnetization curves are shown in the inset. All fields are expressed in reduced units of $h = 2H_a M_{ft} / \sigma_{af}$.

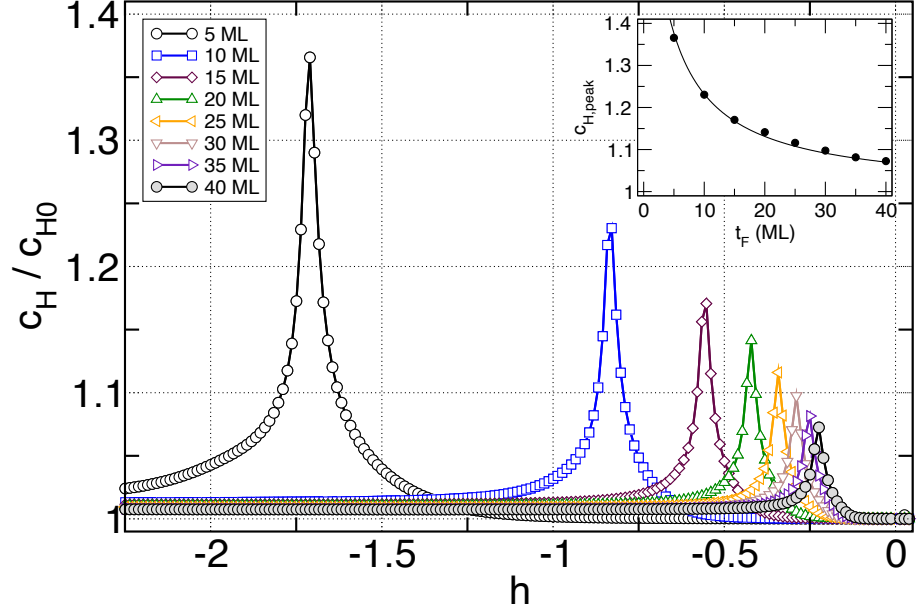


Figure 5.10: Magnetic heat capacity for varying ferromagnet film thickness. The normalized magnetic heat capacity c_H/c_{H0} as a function of applied field during a hysteresis loop sweep is shown for a series of ferromagnet film thickness t_f at $T = 60$ K. The constant c_{H0} is the value of c_H at maximum forward field. In the inset, the magnitude of the heat capacity peak is shown as a function of ferromagnet film thickness, with the line of best fit given by $c_{H,\text{peak}} = 1 + 3.02/(t_f + 3.02)$. All fields are expressed in reduced units of $h = H_a M_f t_{f0} / (2\sigma_{af})$, where $t_{f0} = 20$ ML.

The results in Figure 5.10 demonstrate that these features do indeed emanate from the antiferromagnet. The heat capacity is shown for a series of ferromagnet film thicknesses at $T = 60$ K. The peak in the heat capacity during reversal is largest for the thinnest ferromagnet film considered ($t_f = 5$ ML), where a 37% relative increase is observed. As the ratio ferromagnet to antiferromagnet spins is increased the magnitude of the peaks is observed to decrease, which indicates that the origin of the heat capacity feature is in the antiferromagnet layer. This trend is shown in the inset of Fig. 5.10, where the magnitude of the peak is plotted as a function of ferromagnet film thickness.

It is instructive to examine how c_H changes with the twist angle of the antiferromagnet. An antiferromagnet chain of 30 spins is considered, where one end is rotated between 0° and 180° in increments of 2.5° . The heat capacity is computed at each increment of the twist angle and the results are shown in Figure 5.11. At zero temperature, a maximum is observed when the twist angle reaches 90° and c_H decreases for further windings of the twist. This local maximum evolves into a saddle point as the temperature is

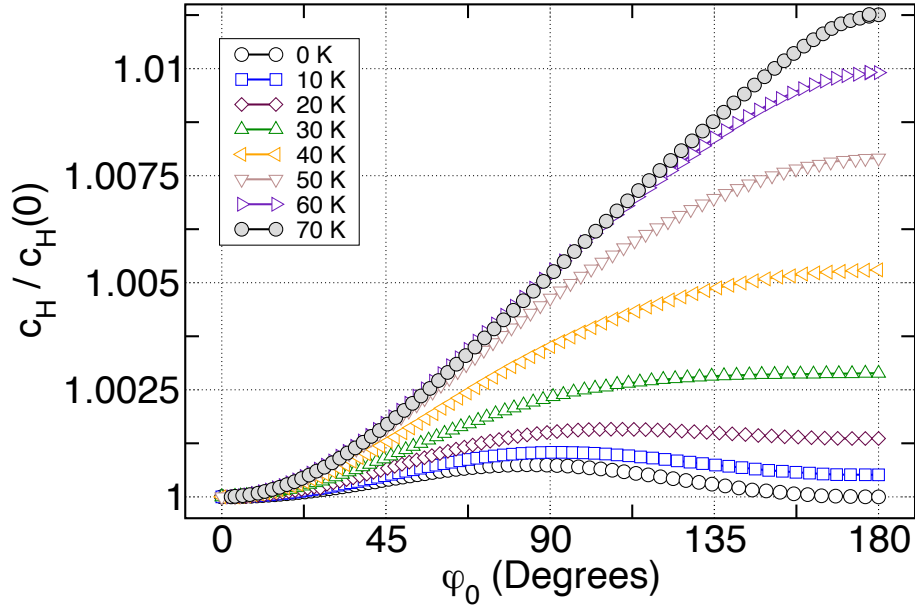


Figure 5.11: Heat capacity of an antiferromagnetic twist. The normalized heat capacity $c_H/c_H(0)$ as a function of twist angle φ_0 is shown for a series of temperatures. The constant $c_H(0)$ is the value of c_H at zero twist.

increased and a new maximum at 180° results. For the range of temperatures considered the largest relative change in the heat capacity occurs at high temperatures, but this only amounts to $\sim 1\%$. Therefore, the winding of the twist alone cannot account for the large c_H enhancements observed during the hysteresis loop sweeps.

At low temperatures (Fig. 5.9a) the peaks do not coincide with the bias field. For example, at $T = 40$ K the zero crossing of the magnetization occurs at $h = -0.592$ but the peak is located at $h = -0.855$. This is in contrast to the behaviour at high temperatures (Fig. 5.9b), where better agreement between the peak position and the shift field is seen. At $T = 60$ K, the zero crossing of M occurs at $h = -0.374$ compared to the position of the peak at $h = -0.421$. This behaviour is due to the stability of the partial wall structure at reverse field. At low temperatures the process of partial wall formation extends over a large field range. Small fluctuations in the temperature do not affect the equilibrium spin profile in this regime, so a small change in the heat capacity is observed. At high temperatures the wall forms over a narrower field range resulting in a sharp transition in the magnetization during reversal. Because $\langle S \rangle$ is more sensitive to

changes in T close to T_N , the reversal field is also strongly temperature dependent and fluctuations in T can lead to large changes to the equilibrium spin structure.

The importance of the wall structure for the heat capacity peaks can be seen by examining bias with a weaker interlayer exchange $J_{f-af} = 0.1J_{af}$. The coupling is small compared to the antiferromagnet wall energy, $J_{f-af} \ll \sigma_{af}$, so bias can be described by the coherent-rotation model of Meiklejohn and Bean [9, 10] with no twist. The resulting heat capacity curves are shown in Figure 5.12. The heat capacity varies like a step function at low temperatures (Fig. 5.12a), indicating the two numerical values of c_H for the parallel and antiparallel configurations of the ferromagnet relative to the antiferromagnet interface. At higher temperatures (Fig. 5.12b) a peak develops during reversal. This arises due to small deformations in the antiferromagnet spins at the interface and is most prominent at $T = 70$ K. The feature represents a relative change of a few percent, which is an order of magnitude smaller than the corresponding peaks for the partial wall case. Thus, the measurement of the heat capacity can provide a means of distinguishing between the partial wall and rigid-antiferromagnet mechanisms for exchange bias.

Finally, the heat capacity is examined for compensated interfaces. The results are given in Figure 5.13. Recent studies have shown the spin-flop coupling to be sensitive to finite temperature effects [331]. The instability is observed here, where bias is observed to vanish above $T = 20$ K (Fig. 5.13). Changes in the heat capacity due to wall formation are a fraction of a percent at low temperatures. As the spin-flop coupling becomes unstable, unbiased hysteresis loops are obtained and have corresponding peaks in c_H of between $\sim 5\%$ and $\sim 15\%$ in size. The peaks are indicative of the irreversible rotations of the interface antiferromagnet spins. As the coercive field is approached the reversible rotation of the twist reaches a maximum, where further rotations of the ferromagnet cause a complete loss in the partial wall (*cf.* Fig. 2.8). Small fluctuations in the temperature at this point, particularly at higher temperatures, can destabilize the wall, leading to an

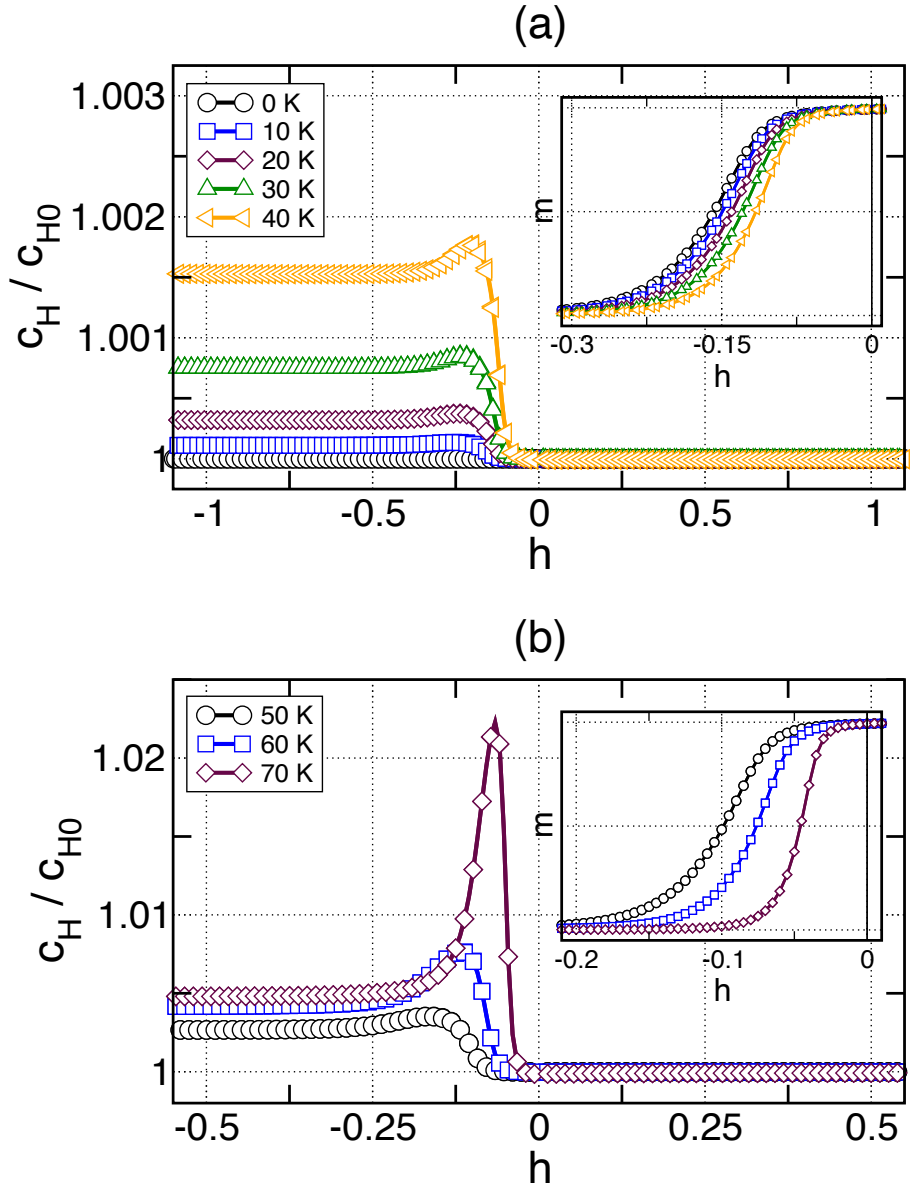


Figure 5.12: Magnetic heat capacity for uncompensated interfaces with small J_{f-af} . The normalized heat capacity c_H/c_{H0} as a function of applied field during a hysteresis loop sweep is shown for a series of temperatures, with $J_{f-af} = 0.1J_{af}$. The constant c_{H0} is the value of c_H at maximum forward field. The corresponding magnetization curves are shown in the inset. All fields are expressed in reduced units of $h = 2H_a M_{ft} / \sigma_{af}$.

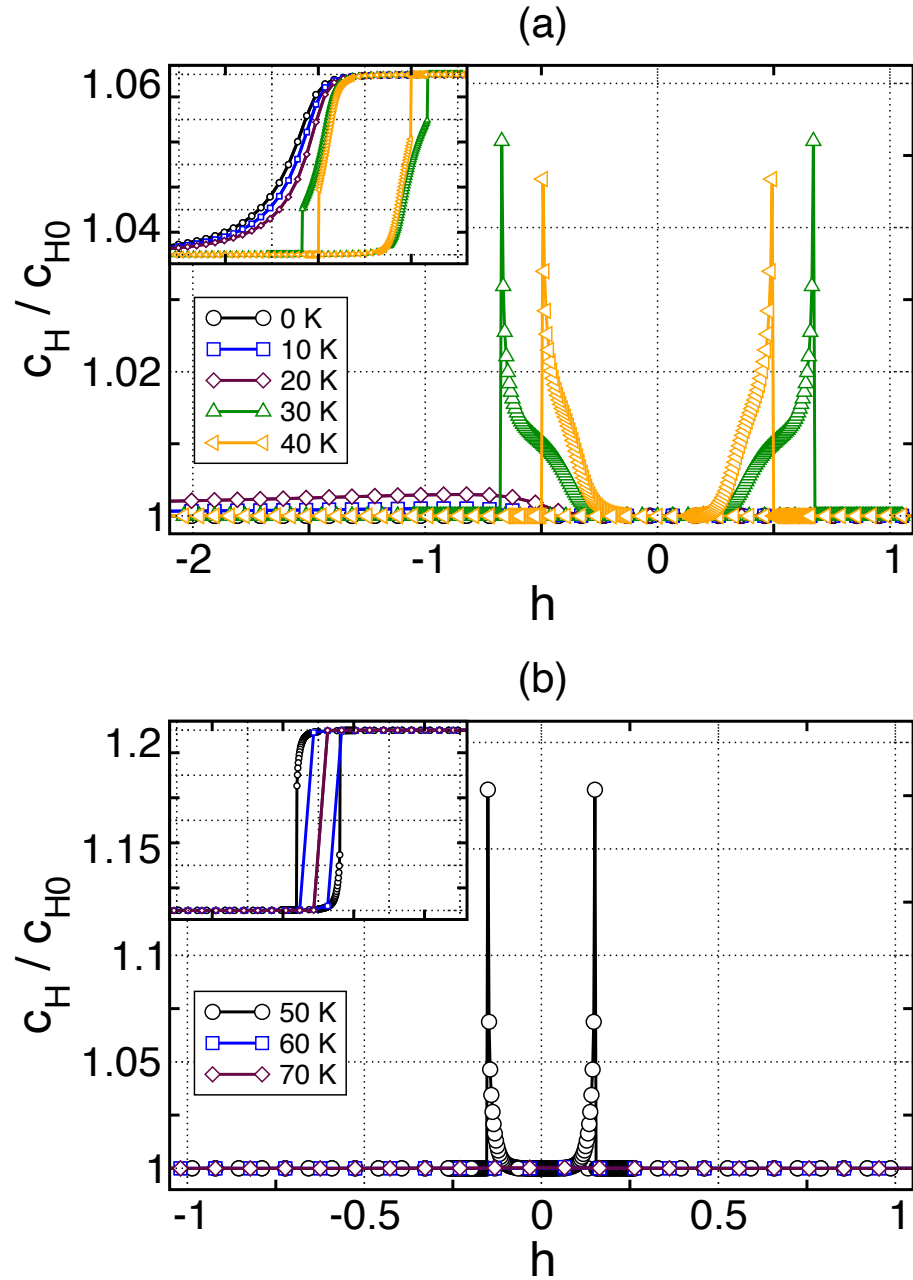


Figure 5.13: Magnetic heat capacity for compensated interfaces. The normalized heat capacity c_H / c_{H0} as a function of applied field during a hysteresis loop sweep is shown for a series of temperatures, with $J_{F\text{-af}} = J_{\text{af}}$. The constant c_{H0} is the value of c_H at maximum forward field. The corresponding magnetization curves are shown in the inset. All fields are expressed in reduced units of $h = 2H_a M_t t_f / \sigma_{\text{af}}$.

irreversible transition and a peak in c_H .

Chapter 6

Long-wavelength spin dynamics

Precise estimates of the interlayer exchange coupling can be difficult to obtain in experiment because measurements of loop shifts and coercivities do not translate directly into a measure of J_{f-af} . A useful method of investigating buried interfaces is to probe the spin waves of the magnetic system. There have been several theoretical [288, 295, 300, 312, 315, 327, 336, 337, 339, 392] and experimental [24, 27, 29, 58, 77, 95, 109, 119, 125, 144, 155, 167, 177, 213, 237, 261, 263, 283] investigations into how ferromagnet spin wave frequencies are modified by the presence of the antiferromagnetic layer. Ferromagnetic resonance experiments [24, 27, 29, 95, 109, 119, 125, 155, 167, 177, 211, 213, 237, 255, 261, 263, 283] have demonstrated shifts in the resonance frequency consistent with the presence of an additional unidirectional field, accompanied by changes to linewidth broadening [29, 177, 213]. Similar effects have also been observed in light scattering experiments [58, 77, 144, 146, 167]. In this chapter, the long-wavelength spin waves are studied in the context of domain wall mediated bias. Particular attention is given to establishing a potential link between observed frequencies and the microscopic details of the antiferromagnet.

6.1 Linear spin wave theory

The equations of motion of a magnetic moment are constructed by using commutation relations for spin operators with the Heisenberg hamiltonian given in Eq. 2.1.

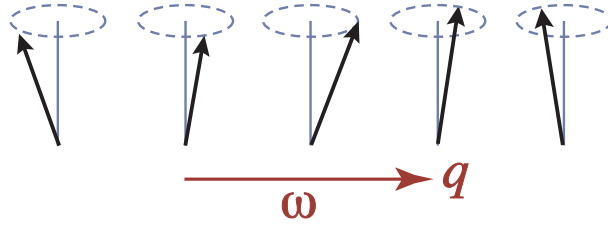


Figure 6.1: Schematic diagram of a spin wave. These excitations represent the precessional motions of the moments about a local field axis. Spin waves are characterized by a frequency ω and wavevector q .

With the usual definition for circular variables $S_i^\pm = S_i^x \pm iS_i^y$, the commutation relations can be expressed as

$$[S_i^z, S_j^+] = S_i^+ \delta_{ij}, \quad (6.1)$$

$$[S_i^z, S_j^-] = -S_i^- \delta_{ij}, \quad (6.2)$$

where $\vec{S}^2 = S(S+1)$. In the large S limit the resulting equations become classical torque equations,ⁱ

$$\frac{1}{\gamma} \frac{\partial \vec{S}_i}{\partial t} = \vec{S}_i \times \vec{H}_i^{\text{eff}}, \quad (6.3)$$

which represent the precessional motion of the magnetic moments about their local field axis. γ is a gyromagnetic constant and is equal to $g\mu_B/\hbar$. The local field comprises contributions from an external magnetic field, exchange coupling to nearest neighbour spins and fields arising from any magnetocrystalline anisotropies. The equations of motion in Eq. 6.3 represent a set of coupled non-linear differential equations, which means that the time evolution of the spin motion can be quite complicated.

Ferromagnetic resonance and Brillouin light scattering experiments typically probe the linear regime of the dynamics. In this regime the spin wave frequencies are calculated by neglecting quadratic terms in the fluctuations transverse to the direction of the local field in Eq. 6.3, which is equivalent to restricting the spin motion to lie within a small cone centred about the local field direction. The equations of motion are linearized by separating the spin variables into a static component \vec{S}_0 and a dynamic component

ⁱA derivation is given by Herring and Kittel [363].

$\vec{s}(t)$,

$$\vec{S}(t) = \vec{S}_0 + \vec{s}(t), \quad (6.4)$$

and neglecting terms second order in $\vec{s}(t)$. The torque equation becomes

$$\frac{1}{\gamma} \frac{\partial \vec{s}_i(t)}{\partial t} = \vec{s}_i(t) \times \vec{H}_i^{\text{eff}} + \vec{S}_i \times \vec{h}_i^{\text{eff}}(t), \quad (6.5)$$

where \vec{H}_i^{eff} and $\vec{h}_i^{\text{eff}}(t)$ represent the static and dynamic components of the effective field, respectively.

6.2 Spin waves in non-uniform ground states

The properties of the allowed spin waves also depend on the magnetic structure. Modifications of the spin wave frequencies due to non-uniform ground states have been examined in several theoretical treatments [288, 289, 312, 332, 393–399]. In this section, a method is described to study spin waves in the partial wall model.

The spin wave calculation here closely follows the method of Nörtemann et al. in Ref. [394]. It involves finding the equilibrium state with the time-integration scheme in Section 2.7 and then examining the perturbations about this configuration. The geometry used is identical to that presented in Chapter Two, where the ferromagnet occupies the space $0 \leq x < t_f$ and the antiferromagnet $-t_{\text{af}} \leq x < 0$. An additional dipole-dipole interaction \mathcal{H}^d between the spins is included into the Hamiltonian given in Eq. 2.1,

$$\mathcal{H}^d(\vec{r}) = (g\mu_B)^2 \sum_{\vec{r}'} \left(\frac{\vec{S}(\vec{r}) \cdot \vec{S}(\vec{r}')}{|\vec{r} - \vec{r}'|^3} - 3 \frac{[\vec{r} \cdot \vec{S}(\vec{r})][\vec{r}' \cdot \vec{S}(\vec{r}')] }{|\vec{r} - \vec{r}'|^5} \right). \quad (6.6)$$

This is required because demagnetizing effects are important for out-of-plane fluctuations, particularly for uncompensated interfaces where the net antiferromagnetic moment does not vanish, but are less significant in determining the equilibrium state where the moments lie in the film plane. The dipolar interaction is long ranged and couples all spins in the bilayer.

Translational invariance in the plane of the film within each layer is assumed. Thus, the orientation of the magnetization is allowed to vary from layer to layer but remains constant in the yz -plane. The spin vector for each layer can simply be indexed by the layer number,

$$\vec{S}(\vec{r}) = \vec{S}_n.$$

Plane wave solutions for the excitations are assumed,

$$\vec{s}(\vec{r}, t) = \vec{s}_n e^{i(\vec{q}\vec{r} - \omega t)},$$

so the resulting linearized equations of motion (Eq. 6.5) become

$$\begin{aligned} -\frac{i\omega}{\gamma} \vec{s}_n &= \vec{s}_n \times [g\mu_B(\vec{H}_a + \vec{H}^d) + 4J_{n,n}\vec{S}_n + J_{n,n-1}\vec{S}_{n-1} + J_{n,n+1}\vec{S}_{n+1} + K_n S_{nz} \vec{z}] \\ &+ \vec{S}_n \times [g\mu_B \vec{h}^d(\vec{q}) + 2J_{n,n}\vec{s}_n [\cos(q_y a) + \cos(q_z a)] + J_{n,n-1}\vec{s}_{n-1} + J_{n,n+1}\vec{s}_{n+1} + K_n s_{nz} \vec{z}]. \end{aligned} \quad (6.7)$$

$J_{i,j}$ represents the exchange coupling between layers i and j , and K_n is the anisotropy constant for layer n . All information about the dipolar interaction is contained within the dipolar fields \vec{H}_d and $\vec{h}_d(\vec{q})$, where only the fluctuating component depends on the wavevector of the excitations. The dipolar fields can be represented in terms of the components of a tensor $\mathbf{d}(\vec{q}; n - n')$,

$$H_{d,n}^\alpha = g\mu_B \sum_{n'} d_{\alpha\beta}(0; n - n') S_{n'}^\beta, \quad (6.8)$$

$$h_{d,n}^\alpha = g\mu_B \sum_{n'} d_{\alpha\beta}(\vec{q}; n - n') s_{n'}^\beta, \quad (6.9)$$

where $\alpha, \beta = x, y$ or z and the summation convention is used. The tensor \mathbf{d} contains information about the dipolar coupling between the spins in layer n and layer n' . The forms for \mathbf{d} used involve rapidly convergent sums and are given in Appendix B.

The linear dynamics constitute a large eigenvalue problem and can be expressed compactly as

$$\left[\mathbf{M} - \frac{i\omega}{\gamma} \mathbf{I} \right] \begin{bmatrix} \vec{s}_1 \\ \vec{s}_2 \\ \vdots \\ \vec{s}_N \end{bmatrix} = \overset{\leftrightarrow}{0}, \quad (6.10)$$

where \mathbf{I} is the identity matrix and \mathbf{M} is the dynamical matrix containing all the cross product terms defined in Eq. 6.7.ⁱⁱ The normal mode frequencies correspond to the eigenvalues of \mathbf{M} and the mode amplitudes are described by the eigenvectors. The elements of \mathbf{M} contain static spin components \vec{S}_n and can be evaluated after the ground state is found using the time-integration method. The eigenvalues and eigenvectors are calculated using some numerical routinesⁱⁱⁱ after \mathbf{M} is constructed.

The presence of dipolar coupling and non-collinear ground states complicates the eigenvalue problem by making the matrix \mathbf{M} non-Hermitian^{iv} [400]. Hence, there are *two* eigenvectors corresponding to each eigenvalue Ω_i . The eigenvector that satisfies Eq. 6.10 corresponding to the eigenvalue Ω is designated the *right* eigenvector $\vec{\xi}_r(\Omega)$. The *left* eigenvector $\vec{\xi}_l(\Omega)$ satisfies the orthonormality condition^v

$$\vec{\xi}_l(\Omega) \cdot \vec{\xi}_r(\Omega') = \delta_{\Omega, \Omega'}, \quad (6.11)$$

and is a solution to the matrix equation involving the complex-conjugate transpose of \mathbf{M} ,

$$\mathbf{M}^\dagger \vec{\xi}_l(\Omega) = \Omega \vec{\xi}_l(\Omega). \quad (6.12)$$

The left and right eigenvectors diagonalize the matrix \mathbf{M} to give the corresponding eigenvalues,

$$\vec{\xi}_l(\Omega) \mathbf{M} \vec{\xi}_r(\Omega) = \Omega. \quad (6.13)$$

In terms of the precessional motion, the two eigenvectors represent opposite directions in which the spins precess.

6.3 Antiferromagnetic spin-flop

The strength of the interactions in the bilayer can be obtained by studying the spin wave frequencies in an applied magnetic field. An example is given here for a four

ⁱⁱExplicit forms for the matrix \mathbf{M} can be found in Appendix C.

ⁱⁱⁱFor this portion of the computation, the software package *Mathematica* was used.

^{iv}Note that \mathbf{M} is a dynamical matrix; the original hamiltonian is Hermitian.

^vA detailed discussion of right and left eigenvectors is given by Friedman [401].

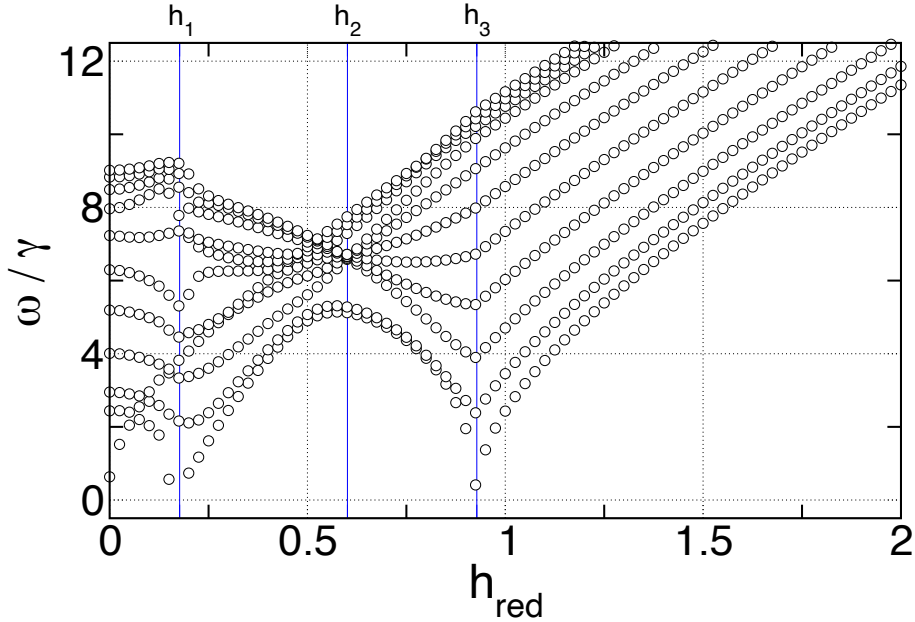


Figure 6.2: Spin waves in a canted antiferromagnet. The frequencies of the normal modes ω/γ , normalized to the gyromagnetic constant, are shown for a 10 ML antiferromagnet film as functions of the reduced magnetic field strength $h_{\text{red}} \equiv g\mu_B H_a / (4J_{\text{af}})$. Changes in the ground state result in characteristic features in the spin wave spectrum, as indicated by h_1 , h_2 and h_3 .

layer ferromagnet in contact with a ten layer antiferromagnet film. It is instructive to consider the features of an uncoupled bilayer first, where the interlayer exchange coupling $J_{\text{f-af}}$ is turned off and dipolar interactions between the two layers are neglected.^{vi} It is convenient to define a reduced field unit in terms of the antiferromagnetic exchange,

$$h_{\text{red}} = \frac{g\mu_B H_a}{4|J_{\text{af}}|}.$$

The external field is applied parallel to the easy axis direction ($\theta_H = 0^\circ$), but all other magnetic constants are given in Table 2.2.

Variations in the spin wave frequencies with the applied field are shown in Figure 6.2. For the ferromagnet film, the magnetization remains uniform for all field values so there are no changes to the ground state. The antiferromagnet undergoes a series of changes to the ground state as the applied field is increased. A schematic diagram of the spin configurations in the antiferromagnet is given in Figure 6.3. Initially at zero field, the antiferromagnet spins are oriented antiparallel to each other along the easy axis (Fig. 6.3a).

^{vi}The phase diagram of thin antiferromagnet films in large magnetic fields has been studied by Carriço et al. [402]. Detailed calculations of the spin wave spectra in antiferromagnetic multilayers can be found in Refs. [394, 399].

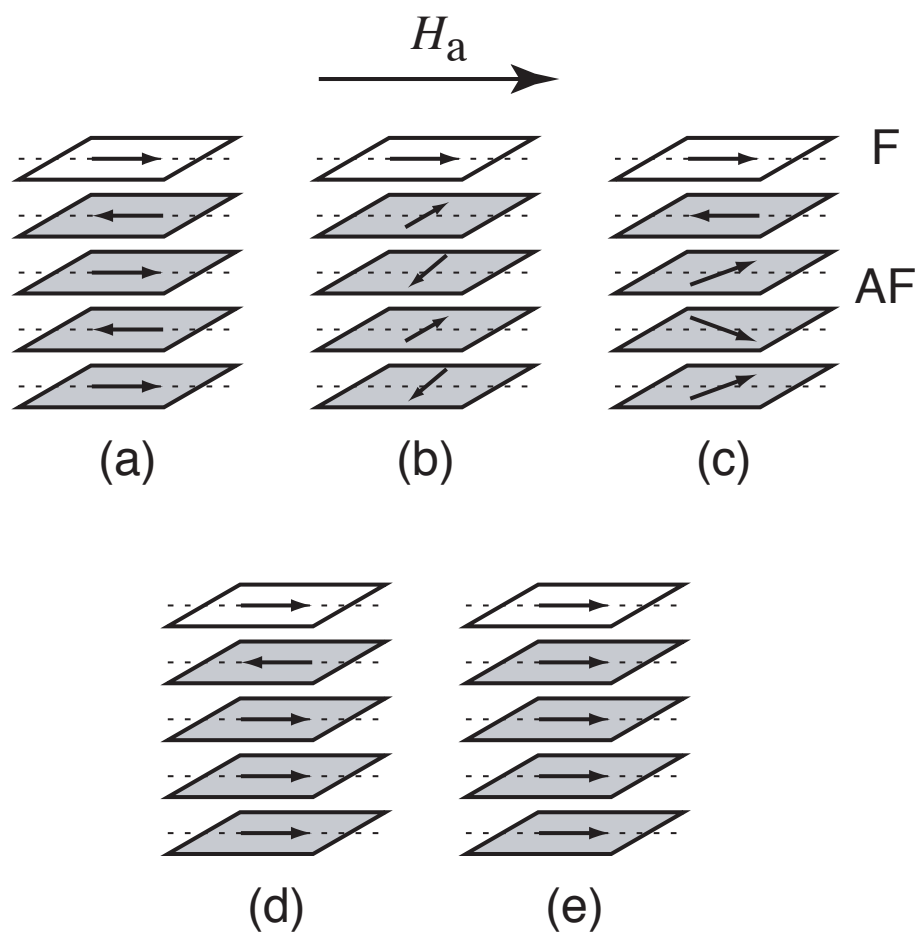


Figure 6.3: Spin structure of canted antiferromagnet coupled to a ferromagnet film. Schematic diagrams of the spin configuration are shown for a series of applied field values H_a . (a) At low fields the spins in the antiferromagnet are ordered antiparallel to each neighbouring spin in the Néel state. (b) As the applied field is increased beyond h'_1 (see Fig. 6.4) a transition is made to a spin-flop state. (c) At h'_2 the canting angle between the spins is roughly 90° , resulting in a degeneracy in the spin wave frequencies. (d) At h'_{3a} saturation is attained in the antiferromagnet except for the interface layer due to the exchange coupling to the ferromagnet. (e) At h'_{3b} complete saturation in the antiferromagnet is attained.

As the field is increased, this configuration becomes less stable to fluctuations due to the growing contribution of the Zeeman energy. The energy barrier imposed by the uniaxial anisotropy is surmounted at some critical field, where the spins on opposing sublattices cant towards the applied field and acquire a net moment in this direction (Fig. 6.3b). This transition appears as a cusp in the spin wave frequencies at h_1 in Fig. 6.2. Spin canting continues as the applied field is increased, resulting in a reduction in the angle between neighbouring spins.

At h_2 the neighbouring spins are perpendicular to each other, giving rise to the intersection of several branches. The degeneracy in the frequencies can be understood with the analogous mass-spring system, where the exchange in the spin system plays the role of a spring constant. The separation between the normal mode frequencies ω_n in the mass-spring system is governed by the spring constant K ,

$$\omega_n^2 \sim K q_n^2. \quad (6.14)$$

In the limit where K vanishes the excitation frequencies become degenerate. The exchange energy is varied by the relative orientation between neighbouring moments in the spin system, so for a relative perpendicular orientation a degeneracy in the mode frequencies is observed. The frequencies in Fig. 6.2 are not all degenerate because spins at the surfaces of the film experience conditions that differ to those in the bulk. Consequently, spin canting need not remain constant throughout the entire film so this degeneracy is only an approximate one, as the moments are only *nearly* perpendicular to each other at h_2 .

For a sufficiently large field h_3 , the Zeeman energy completely dominates the antiferromagnet exchange and the antiferromagnet is saturated (Fig. 6.3e). This is signalled by a cusp in the mode with the lowest frequency, where the longest wavelength acoustic mode in the sample evolves into the uniform mode of the saturated state.

The position of these features at h_1 , h_2 and h_3 allows one to estimate the magni-

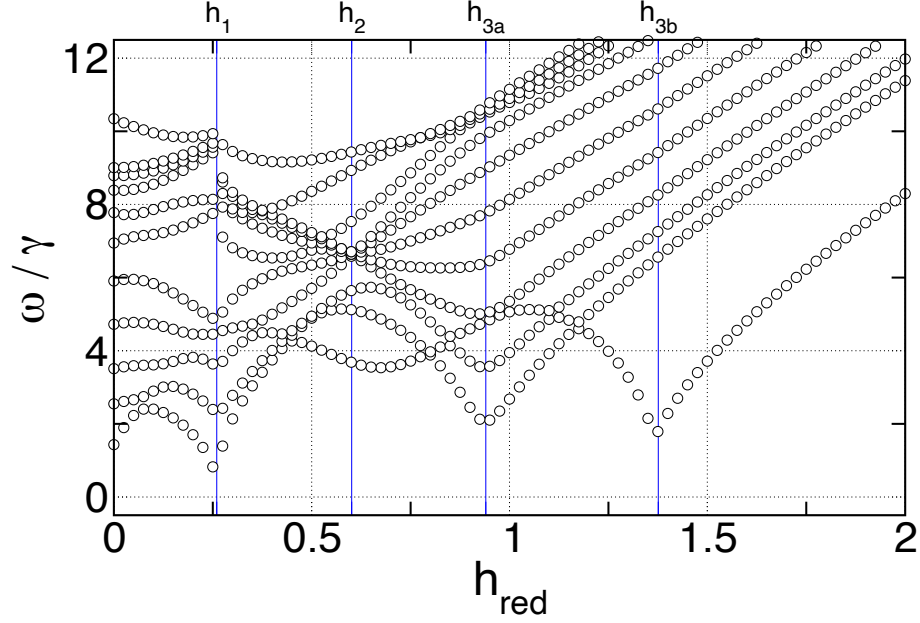


Figure 6.4: Spin waves in a canted antiferromagnet coupled to a ferromagnet film. The frequencies of the normal modes ω/γ , normalized to the gyromagnetic constant, are shown for a 10 ML antiferromagnet film coupled to a 5 ML ferromagnet film, with $J_{\text{f-af}} = J_{\text{af}}$, as functions of the reduced magnetic field strength $h_{\text{red}} \equiv \frac{g\mu_B H_a}{4J_{\text{af}}}$. Changes in the ground state result in characteristic features in the spin wave spectrum, as indicated by h_1 , h_2 , h_{3a} and h_{3b} .

tudes of the magnetic constants. For the first critical field the spin-flop transition results from the competition between the Zeeman and anisotropy energies, where h_1 is related to a geometric mean of the exchange and anisotropy fields [402],

$$h_1 = \frac{1}{2|J_{\text{af}}|} \sqrt{2|J_{\text{af}}| K_{\text{af}} - K_{\text{af}}^2}. \quad (6.15)$$

An estimate of the anisotropy constant can be obtained from h_1 if the exchange is known. Similarly, expressions for the fields h_2 and h_3 can be derived from an infinite chain to give information about the exchange coupling.^{vii}

The effects of interlayer coupling on the spin wave frequencies, for $J_{\text{f-af}} = J_{\text{af}}$, are shown in Figure 6.4. Coupling between the two magnetic layers causes a mixing of the ferromagnetic and antiferromagnet modes, where the resulting hybrid excitations represent standing waves across the entire bilayer. The interlayer coupling also pins the interface antiferromagnet spin for all fields below saturation. After the spin-flop transition at h_1 , the interface spin remains aligned antiparallel to the ferromagnet while the rest of

^{vii}Derivations for the critical fields h_1 , h_2 and h_3 are given in the Appendix D.

the antiferromagnet is canted towards the field (Fig. 6.3c). The spin-flop transition occurs at a larger field value due to the stabilizing effect of the ferromagnet layer. No changes are observed for the second critical field h_2 , indicating that the degeneracy is due to the bulk antiferromagnet spins. A second cusp in the frequencies is seen at higher fields, leading to two critical fields h_{3a} and h_{3b} at saturation. h_{3a} refers to the field required to saturate all spins except the interface spin (Fig. 6.4d), while full saturation is attained at h_{3b} (Fig. 6.4e). The fields h_{3a} and h_{3b} give information about the strengths of the interlayer exchange and the antiferromagnetic coupling. Coupling to the ferromagnet results in a bifurcation of the critical field h_3 in Fig. 6.2; h_{3a} merges with h_{3b} in the limit that J_{f-af} vanishes.

Some comment should be made at this point about the fields required to perform this experiment. The anisotropy fields for crystalline antiferromagnets, such as FeF_2 , are typically on the order of 10^2 kG in magnitude [402], which means it may be difficult to perform the kinds of measurements discussed above in experiment. In comparison, the spin-flop transitions in Fe/Cr superlattices can be studied in the laboratory due to the relatively low crystalline anisotropy of the Fe layer (~ 0.5 kG) [403]. Such artificial antiferromagnets may be more suitable to study the kinds of transitions discussed in this section.

6.4 Ferromagnetic hysteresis

The influence of partial wall formation on the spin wave frequencies is studied in this section. Three limiting cases of partial wall formation are considered, where the corresponding hysteresis loops are presented in Figure 6.5. For the first case with $\theta_H = 10^\circ$ and $J_{f-af} = J_{af}$, the interlayer coupling ensures that the interface spins rotate coherently to form a partial wall in the antiferromagnet. For the second, $\theta_H = 90^\circ$ and $J_{f-af} = J_{af}$, the external field is applied along the hard axis of the antiferromagnet resulting in zero

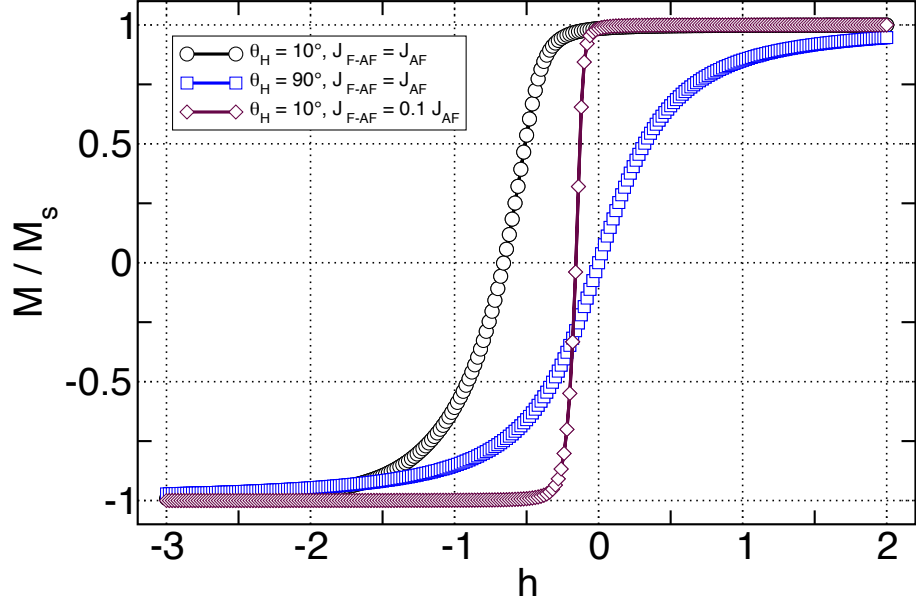


Figure 6.5: Hysteresis curves for limiting cases of partial wall formation. The magnetization curves are shown for strong and weak exchange coupling, and for an external field applied perpendicular to the easy axis. The magnetic parameters are given in the legend.

bias. The third case corresponds to the coherent rotation limit, $\theta_H = 10^\circ$, $J_{f-af} = 0.1J_{af}$, where partial wall formation is not favourable. The chosen parameters give three distinct magnetic configurations in reverse field. The wavevector for the excitations parallel to the film plane is $q\delta = 0.001$ along the easy axis, where δ is the lattice constant.

The frequencies of the five lowest-order modes in the bilayer structure are shown in Figures 6.6–6.8. In the first example the effect of the partial wall is present in the spin wave frequencies, where large changes in the gradient of $\omega(h)$ are observed in reverse field as the twist forms (Fig. 6.6). The lowest frequency branch corresponds to a resonance mode of the bilayer, where the uniform ferromagnet precession drives its neighbours in the antiferromagnet.^{viii} For $h > -h_{eb}$ a fit is made to the bilayer resonance frequency based on the resonance frequency of a thin ferromagnet film

$$\frac{\omega}{\gamma} = \sqrt{(H_a + H_{eb})(H_a + H_{eb} + 4\pi M_f)}, \quad (6.16)$$

where the effective field acting on the ferromagnet comprises the applied field and the unidirectional (bias) field. However, the frequency branch is not symmetric about $h =$

^{viii}Detailed discussion of the mode profiles can be found in the following section.

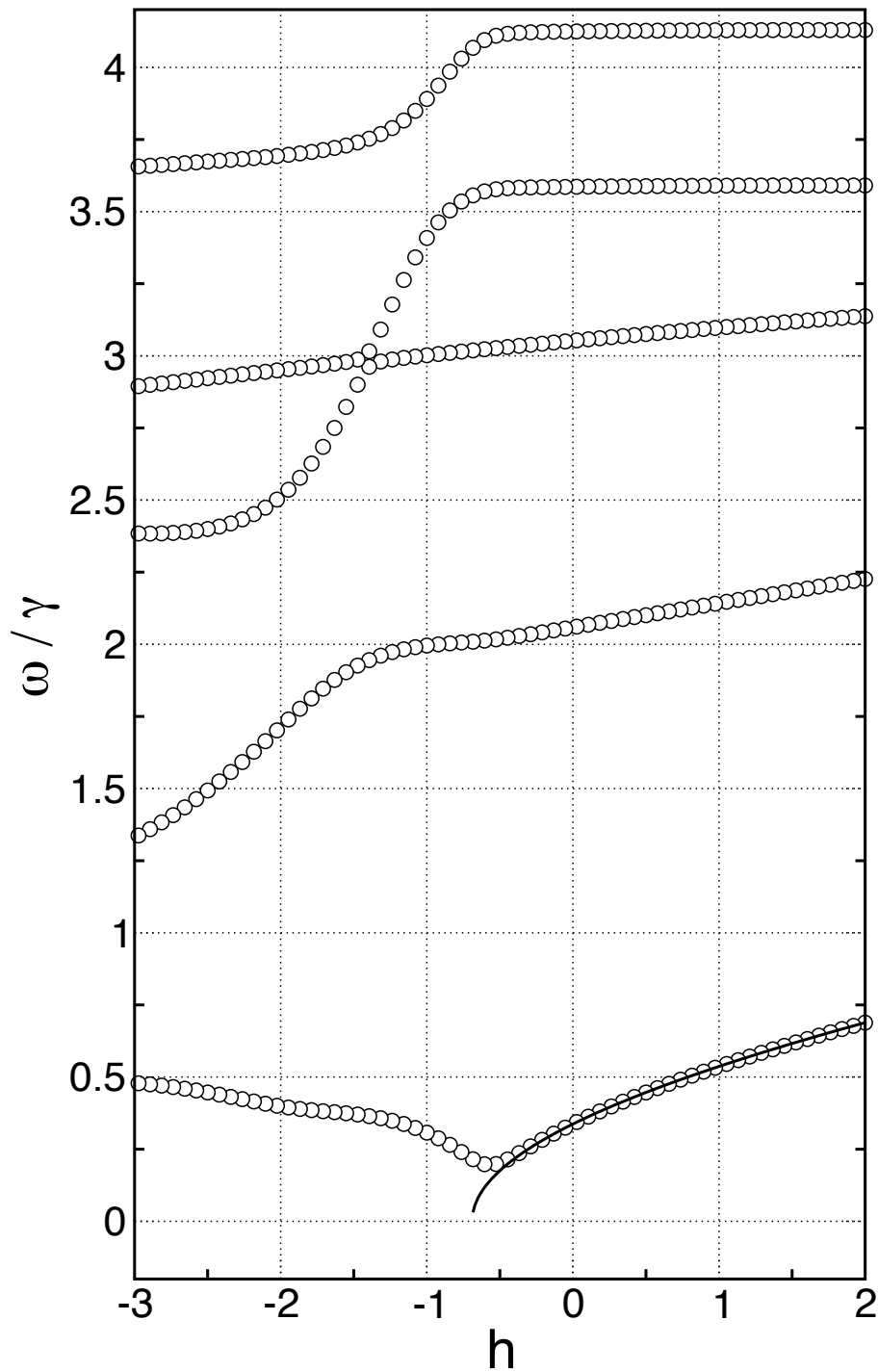


Figure 6.6: Spin waves in a ferromagnet/antiferromagnet bilayer. The normalized frequencies ω/γ are shown for the five lowest-order modes in the 20 ML/20 ML ferromagnet/antiferromagnet bilayer as a function of applied field during a hysteresis loop sweep, with $\theta_H = 10^\circ$ and $J_{f-af} = J_{af}$. The solid line represents a fit based on Eq. 6.16. All fields are expressed in reduced units of $h = 2H_a M_{f\bar{t}}/\sigma_{af}$.

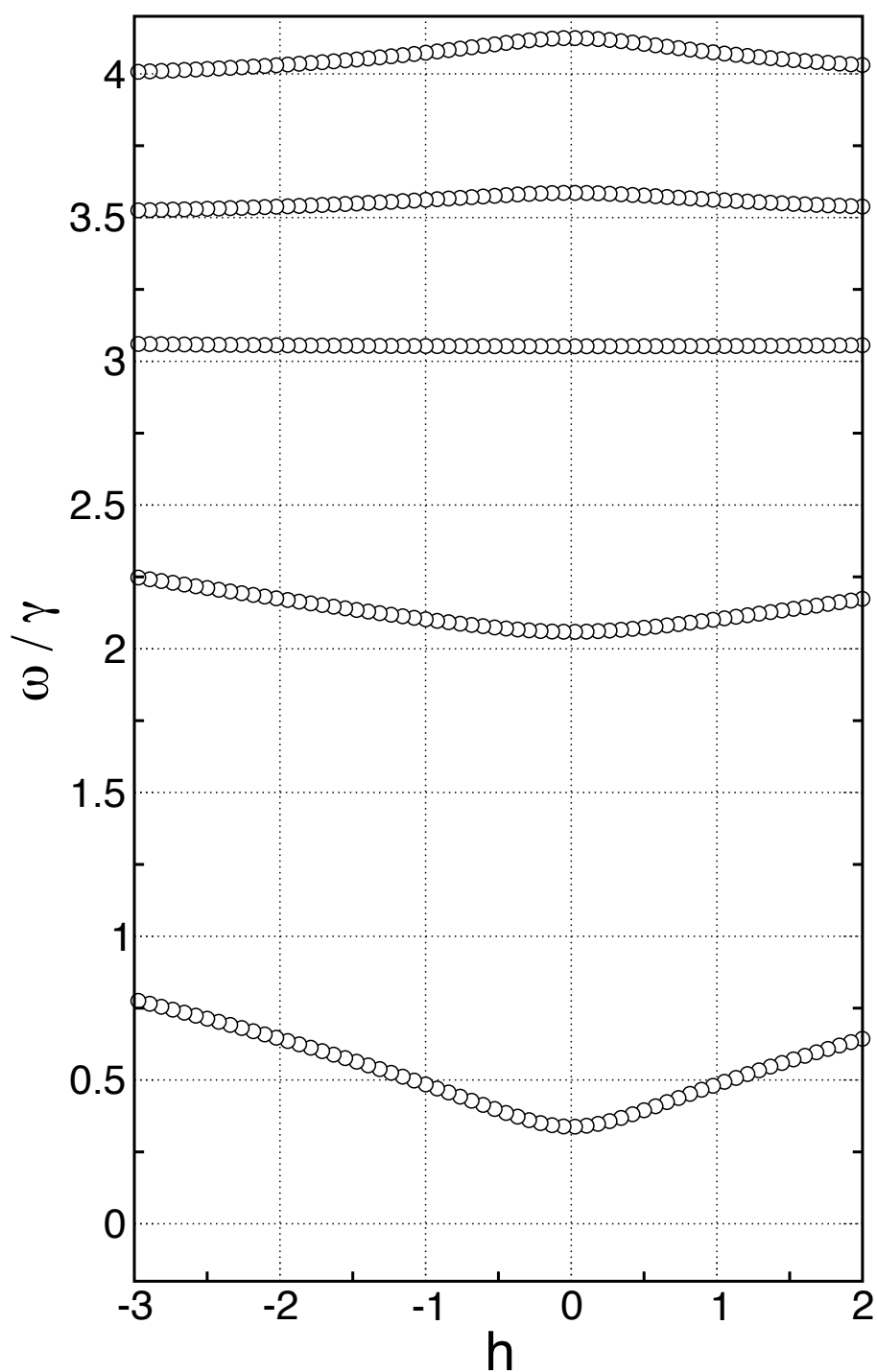


Figure 6.7: Spin waves in a ferromagnet/antiferromagnet bilayer. The normalized frequencies ω/γ are shown for the five lowest-order modes in the 20 ML/20 ML ferromagnet/antiferromagnet bilayer as a function of applied field during a hysteresis loop sweep, with $\theta_H = 90^\circ$ and $J_{f-af} = J_{af}$. All fields are expressed in reduced units of $h = 2H_a M_f t_f / \sigma_{af}$.

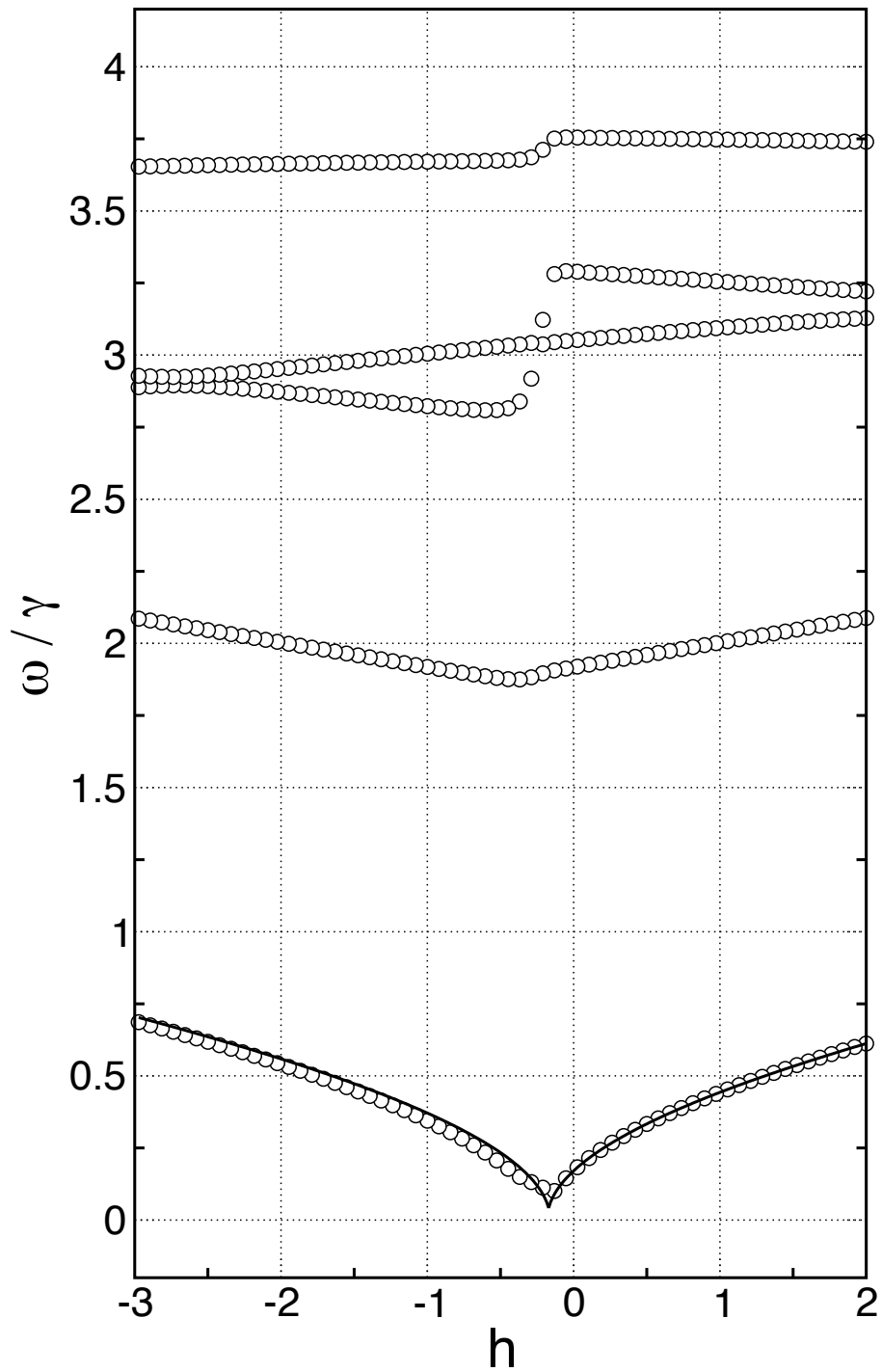


Figure 6.8: Spin waves in a ferromagnet/antiferromagnet bilayer. The normalized frequencies ω/γ are shown for the five lowest-order modes in the 20 ML/20 ML ferromagnet/antiferromagnet bilayer as a function of applied field during a hysteresis loop sweep, with $\theta_H = 10^\circ$ and $J_{f-af} = 0.1J_{af}$. The solid line represents a fit based on Eq. 6.16. All fields are expressed in reduced units of $h = 2H_a M_{f\bar{t}}/\sigma_{af}$.

$-H_{\text{eb}}$ due to wall formation, and so a similar fit cannot be made for the opposite branch in reverse field. Large variations in the gradient $\partial_h \omega$, due to the reversal of the ferromagnet and the formation of the partial twist, are observed for the other branches. A comparison with the frequency branches from the second example emphasizes the influence of the wall structure. No bias occurs when the external field is applied perpendicular to the easy axis because no partial wall is formed. The frequency branches are symmetric about $h = 0$ and exhibit only gradual variations with increasing field magnitude.

For coherent rotation, variations in the spin wave frequencies are modest in comparison with the partial wall case (Fig. 6.8). The resonance frequency is shifted from $h = 0$ by an amount equal to the bias field, where a fit based on Eq. 6.16 shows good agreement for the ferromagnet in forward orientation. In contrast to the partial wall case a good fit can also be obtained for the reverse orientation, indicating that the deviations due to the antiferromagnet are not very significant. The positions of the gradient changes in $\omega(h)$ coincide better with the bias field, which shows that these changes are effected by the relative orientation of the interface spins.

6.5 Excitation profiles

Some examples of the profiles associated with the low-order excitations considered in the previous section are shown in Figures 6.9–6.11. The component of the spin motion perpendicular to the film plane, s_x , obtained from the solution of the right eigenvectors, is shown at positive and negative fields. The spin wave profiles corresponding to the modes presented in Fig. 6.6 are shown in Fig. 6.9. At forward field, the bilayer resonance (mode 1) can be identified where the amplitude of precession is almost constant across the ferromagnet layer. Associated with this mode is an interface excitation in the antiferromagnet, where the amplitude of the precessional motion decays rapidly away from the interface. Localization is also seen in the next two modes (modes 2 and

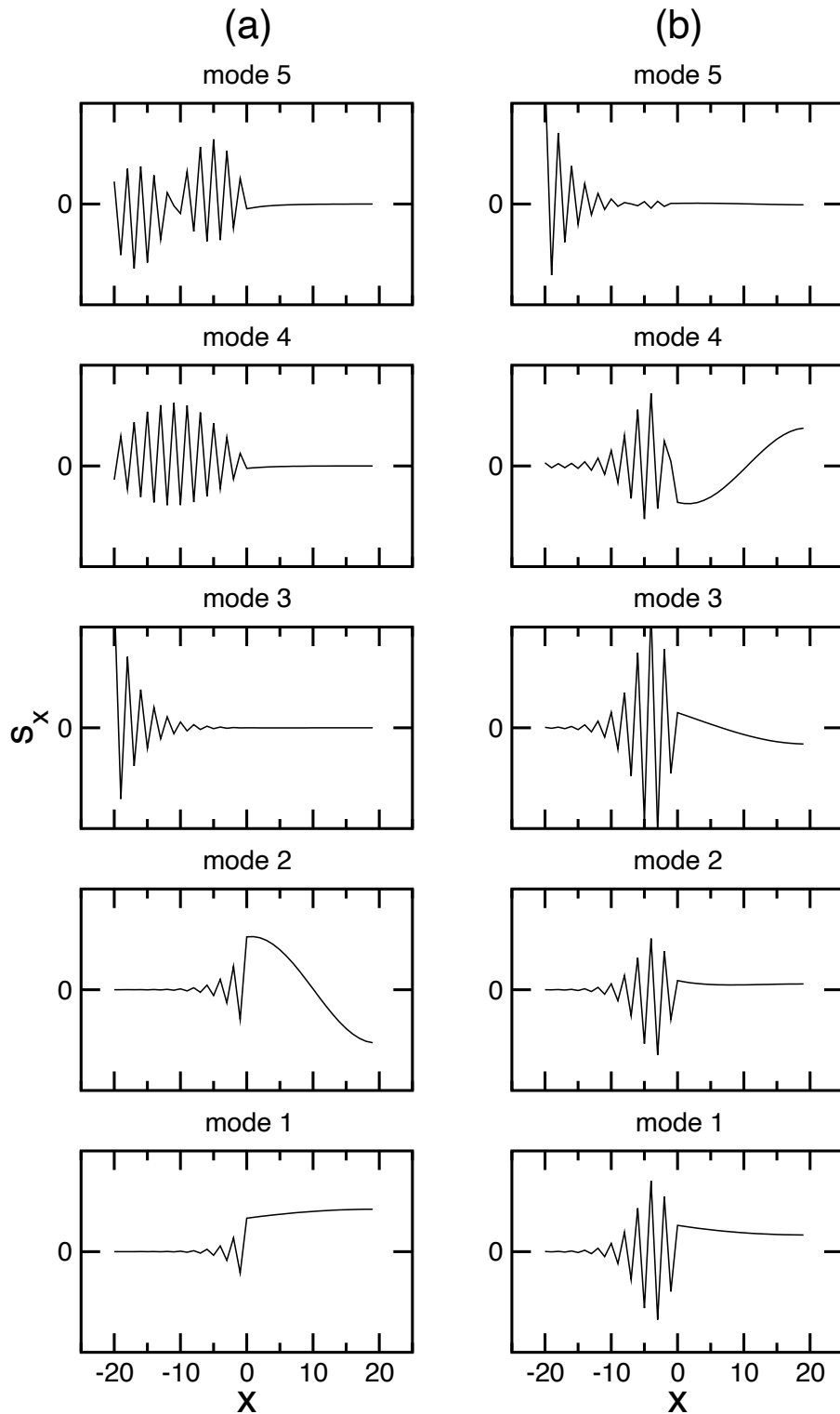


Figure 6.9: Mode profiles in a ferromagnet/antiferromagnet bilayer. The spatial profile of the five lowest-order modes (with corresponding frequencies shown in Fig. 6.6) are shown for maximum (a) forward field and (b) reverse field during a hysteresis loop sweep. The component of the fluctuations out of the film plane is shown. The antiferromagnet occupies the region $x < 0$.

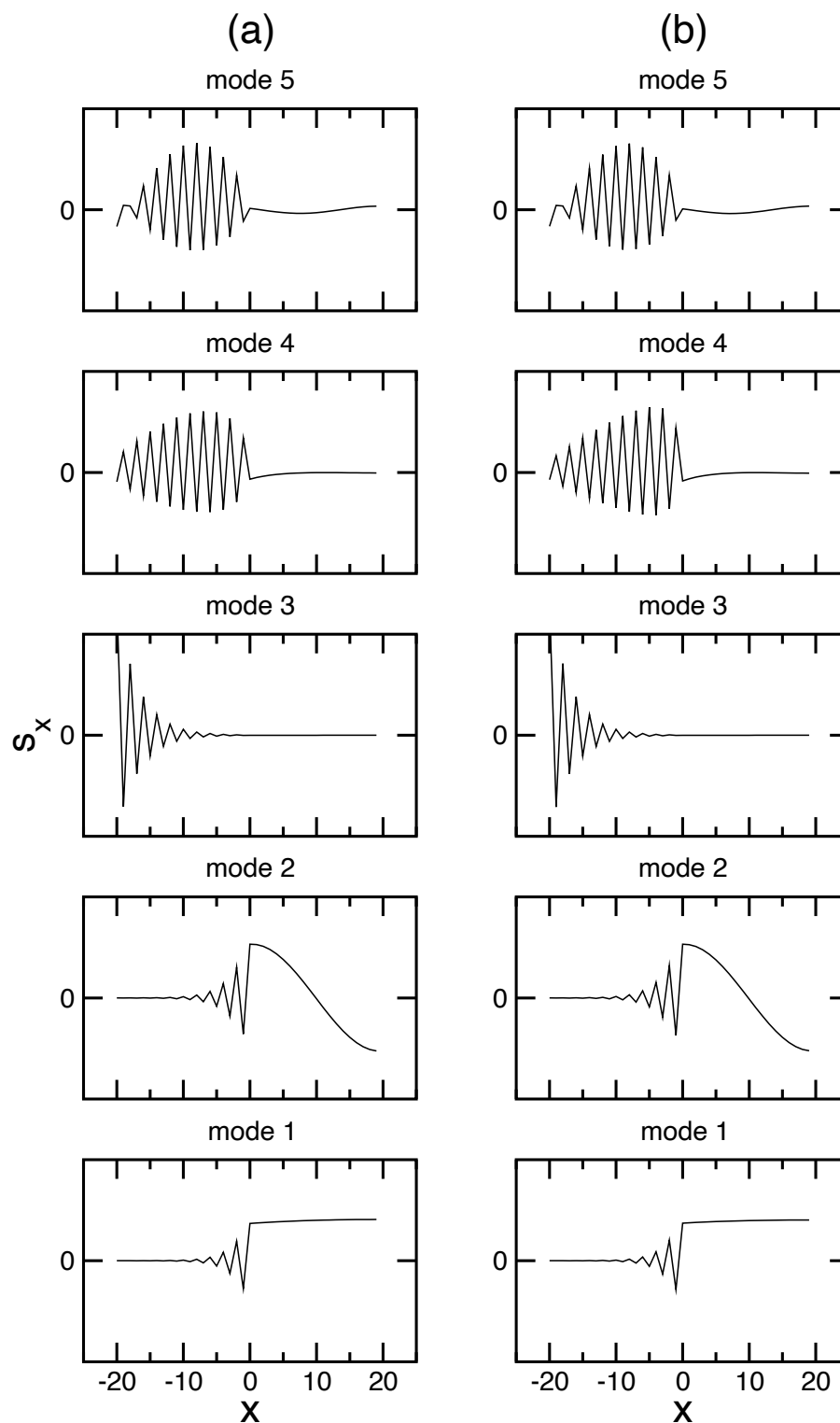


Figure 6.10: Mode profiles in a ferromagnet/antiferromagnet bilayer. The spatial profile of the five lowest-order modes (with corresponding frequencies shown in Fig. 6.7) are shown for maximum (a) forward field and (b) reverse field during a hysteresis loop sweep. The component of the fluctuations out of the film plane is shown. The antiferromagnet occupies the region $x < 0$.

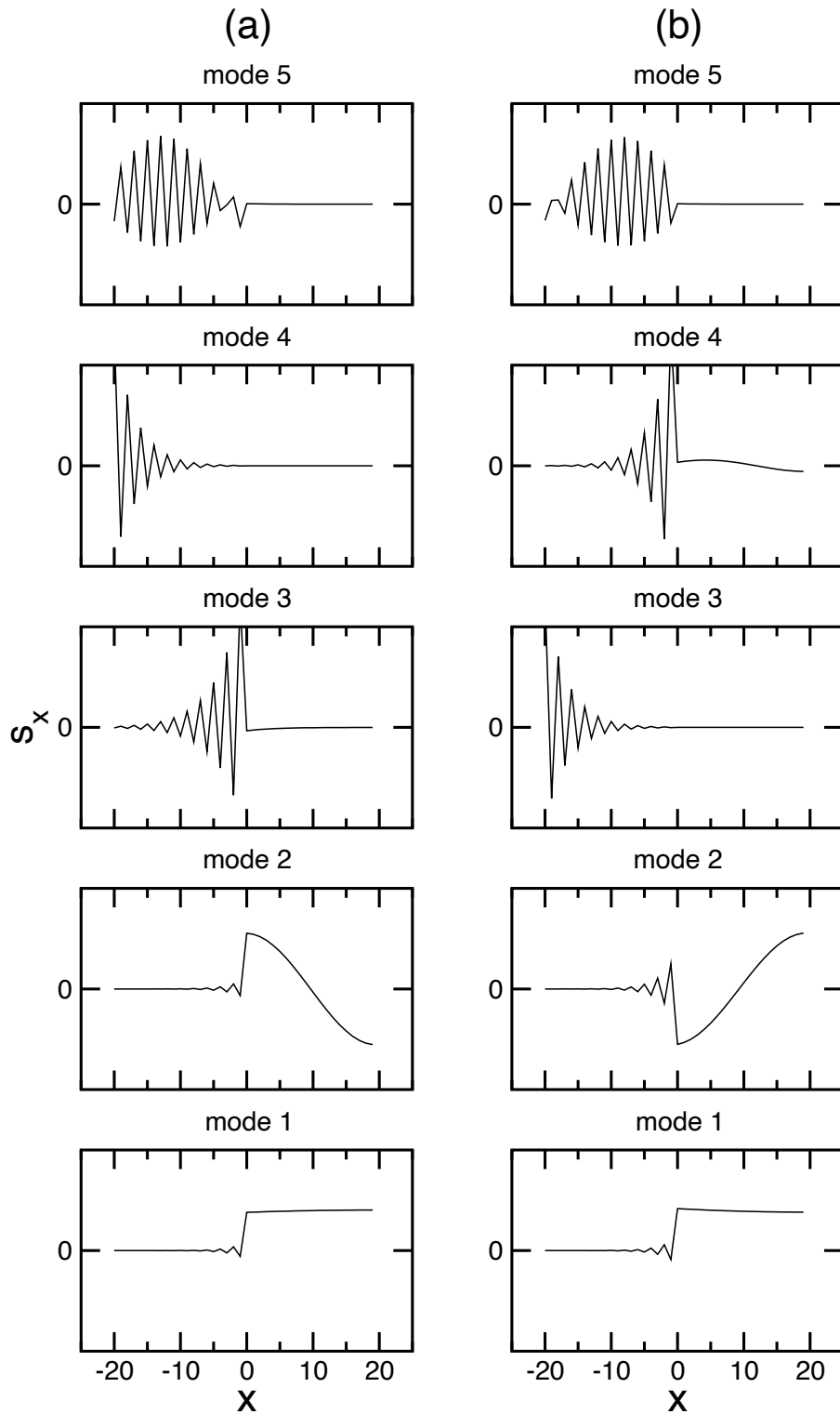


Figure 6.11: Mode profiles in a ferromagnet/antiferromagnet bilayer. The spatial profile of the five lowest-order modes (with corresponding frequencies shown in Fig. 6.8) are shown for maximum (a) forward field and (b) reverse field during a hysteresis loop sweep. The component of the fluctuations out of the film plane is shown. The antiferromagnet occupies the region $x < 0$.

3), which correspond to another interface mode and a surface mode at the free surface of the film.

Spin excitations localized to a Bloch domain wall have been investigated by several authors [404–409]. These excitations can be categorized into spin wave modes, which represent travelling waves, and bound states, which represent localized excitations that can lead to translations of the wall structure itself. Examples of spin excitations localized to the partial wall structure can be seen at maximum reverse field in Fig. 6.9b. Associated with the four lowest-order modes considered are spin wave excitations localized to the partial wall, where the largest amplitude of the oscillations occur in the wall centre. Variations in the gradient of $\omega(h)$ observed earlier at reverse fields (Fig. 6.6) can be attributed to the appearance of these wall modes.

Perpendicular alignment of the ferromagnet relative to the easy axis does not produce significant features in spin wave spectrum. The symmetry of the frequency branches with respect to zero field is reflected in the mode profiles, as shown in Figure 6.10. The profiles are identical at forward and negative fields $h = \pm 2$. Despite the perpendicular orientation the presence of the antiferromagnet is still felt, where interface excitations are observed to accompany the ferromagnet oscillations.

Changes to the mode profiles for coherent rotation are also modest in comparison with the first example, as shown in Figure 6.11. At reverse field there is a slight enhancement in the magnitude of the interface mode in the antiferromagnet due to the magnetic configuration, an example of which is mode 2 in Fig. 6.11b. This enhancement is due to the increase in exchange energy tied-up at the interface, where the parallel alignment of the two layers represents the absolute maximum exchange energy possible for the interlayer coupling.

6.6 Angular dependence of resonance frequency

The angular dependence of the spin wave frequencies can yield much information about the magnetic anisotropies present. The resonance condition for a ferromagnet in general terms is given by [410],

$$\left(\frac{\omega}{\gamma}\right)^2 = \frac{1}{M_s^2 \sin \theta} \left(\frac{\partial^2 \mathcal{E}_{\text{tot}}}{\partial \theta^2} \frac{\partial^2 \mathcal{E}_{\text{tot}}}{\partial \phi^2} - \frac{\partial^2 \mathcal{E}_{\text{tot}}}{\partial \theta \partial \phi} \right), \quad (6.17)$$

where θ and ϕ are the polar and azimuthal angles, respectively, that define the orientation of the magnetization. All magnetic interactions experienced by the ferromagnet appear in the total energy term \mathcal{E}_{tot} , so the contributions from the various anisotropies present can be extracted by examining the angular dependence of the resonance field. Recent theoretical studies of ferromagnetic resonance in exchange bias systems have used Eq. 6.17 as a starting point [284, 337], where the energy terms that enter into \mathcal{E}_{tot} include the partial wall energy, the interlayer coupling energy and any other crystalline anisotropy terms appropriate for the particular material. In this study, the bilayer resonance is examined for non-trivial ground states explicitly using the numerical model.

Two methods for calculating the bilayer resonance fields are considered. In the first, the bias direction is set along the positive z -axis and rotations of the field orientation are made from this reference direction. A hysteresis measurement made with an applied field in the range $-90^\circ \leq \theta_{\text{H}} \leq 90^\circ$ always yields $H_{\text{eb}} \geq 0$, and conversely a negative bias field $H_{\text{eb}} < 0$ is observed for $90^\circ < \theta_{\text{H}} < 270^\circ$.^{ix} This convention has been used in all work presented so far. For this type of measurement, the angular variation of the resonance frequency does not possess any inversion symmetry at $\theta_{\text{H}} = 90^\circ$, such as that exhibited by a cosine curve, due to the large deformation of the antiferromagnet spins in the form of a partial wall for $90^\circ < \theta_{\text{H}} \leq 180^\circ$. In the second, the orientation of the field defines a “field-cooling” direction such that $H_{\text{eb}} \geq 0$ for all applied field angles. The resulting

^{ix}Note that $H_{\text{eb}} < 0$ here does not imply *positive* bias; the sign of the loop shift is simply a convention used to indicate the exchange bias direction.

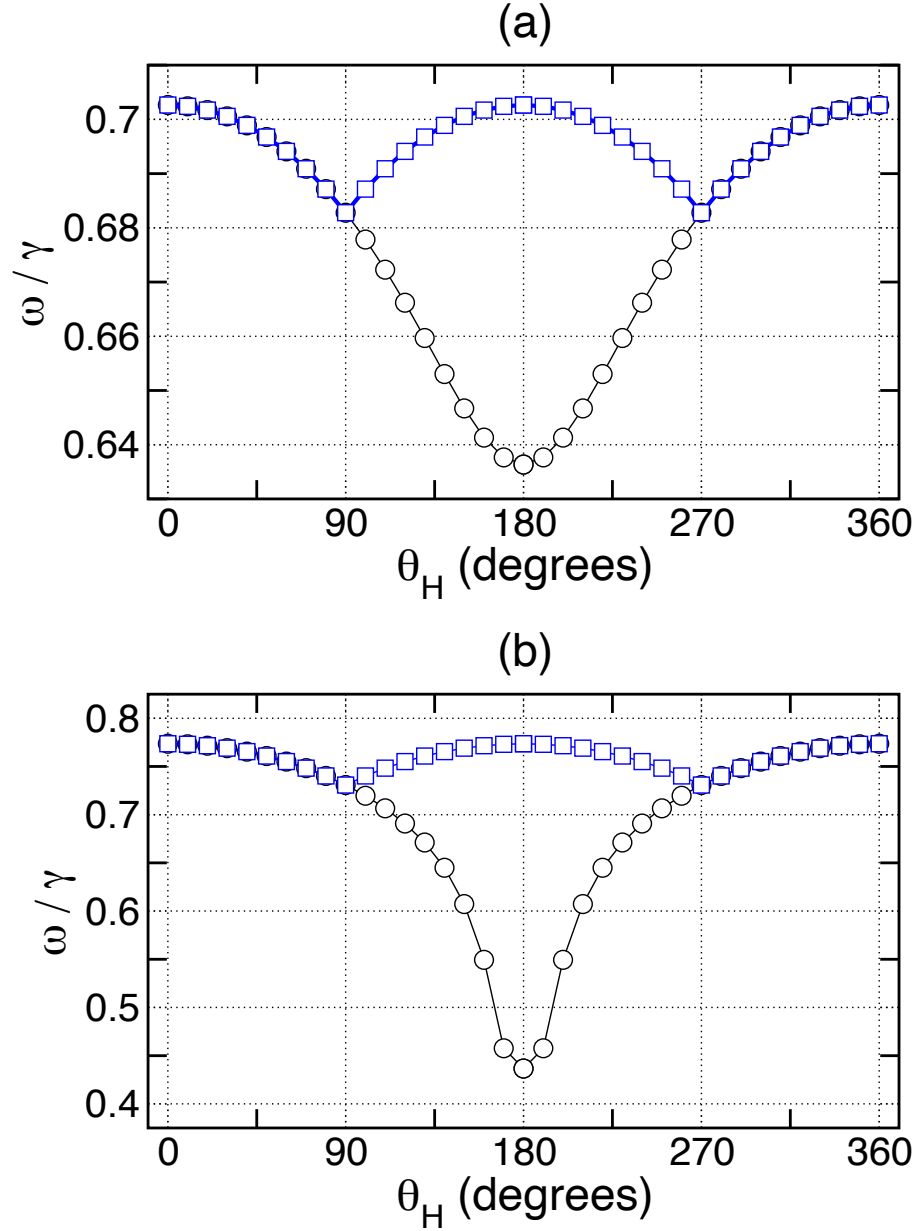


Figure 6.12: Angular dependence of the bilayer resonance mode. The normalized frequency ω/γ of the lowest-order bilayer mode is shown as a function of applied field angle θ_H at maximum forward field. Two interlayer coupling constants are considered: (a) $J_{F-af} = 0.1J_{af}$ and (b) $J_{F-af} = J_{af}$. The circles indicate results taken for a set field-cooled direction (i.e. along the positive z direction) and the squares are for multiple field cooling.

curves in this case exhibit reflection symmetry about $\theta_H = 90^\circ$ and $\theta_H = 180^\circ$.

The angular variation of the bilayer resonance frequency is considered for two interlayer coupling constants. For weak interlayer coupling $J_{f-af} = 0.1J_{af}$, where the coherent-rotation picture is appropriate, the resonance frequency exhibits a sinusoidal variation (Fig. 6.12a). This behaviour can be attributed to the simple cosine form of the interlayer coupling energy when there are no deformations in the antiferromagnet structure. The formation of a partial wall, with $J_{f-af} = J_{af}$, results in a clear departure from the cosine dependence due to the energy difference between the twisted and untwisted states (Fig. 6.12b). Similar features have been obtained by Geshev et al. [337], who calculated the angular dependence of the FMR resonance frequency using Eq. 6.17 with the inclusion of a partial wall energy term.

The main difference between the two measurement schemes is in the probing of the partial wall structure. With the second method the interface antiferromagnet spin can only wind to 90° at most, which means that the shift in the spin wave frequencies is mostly due to the interlayer coupling. This is corroborated by the results in Fig. 6.12b, where the variations due to J_{f-af} are about a sixth of those arising from partial wall formation.

6.7 Linewidth enhancement

Linewidth broadening results from the finite lifetime of spin waves. Physical structures, such as interface roughness, can give rise to localized magnon states that can interact with the normal modes of the material. Imperfect contact between films or grain structures at the interface can give rise to different resonance conditions across the film, where each condition may be characterized by a local J_{f-af} or θ_H .

The influence of the interlayer coupling on the bilayer resonance frequency can be seen in Figure 6.13, where the mode frequency is shown during a hysteresis loop sweep. For weak coupling, where bias is described by coherent rotation, a sharp dip in

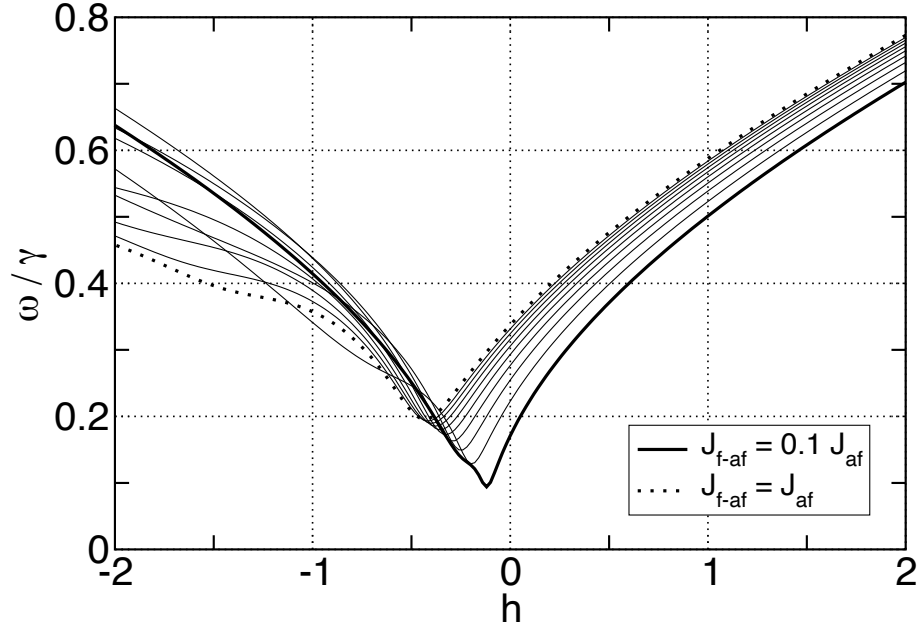


Figure 6.13: Bilayer resonance mode frequency for varying interlayer coupling. The normalized frequency ω/γ of the lowest-order bilayer mode is shown as a function of applied field h during a hysteresis loop sweep for a series of interlayer coupling strengths J_{f-af} , with $\theta_H = 10^\circ$. Ten values of J_{f-af} are considered, from $J_{f-af} = 0.1J_{af}$ to $J_{f-af} = J_{af}$ in increments of $0.1J_{af}$. All fields are expressed in reduced units of $h = 2H_a M_{ftf}/\sigma_{af}$.

the resonance frequency at the bias field is observed. For progressively larger values of the interlayer coupling, the extent of the partial wall formed during reversal also increases. The resonance frequency for the largest value of J_{f-af} considered ($J_{f-af} = J_{af}$) exhibits a broader decrease at the bias field corresponding to the formation of the twist. The position of the frequency minimum correlates well with the bias field.

The extent of the partial wall formed can also be controlled by the orientation of the external field. For $J_{f-af} = J_{af}$, the interlayer coupling is sufficiently strong such that the orientation of the ferromagnet in reverse field gives a good indication of the size of the partial wall formed. The spin wave frequencies for a series of applied field angles θ_H are shown in Figure 6.14. The angular dependence of the bias field is reflected in the spin wave frequencies: $\omega(h)$ is symmetric for $\theta_H = 90^\circ$ where no twist forms and is very asymmetric for $\theta_H = 10^\circ$ where a large twist forms. The winding and unwinding of the antiferromagnet twist results in a reduction in frequency, where the magnitude of this reduction is determined by the size of the partial twist. Again, the position of the

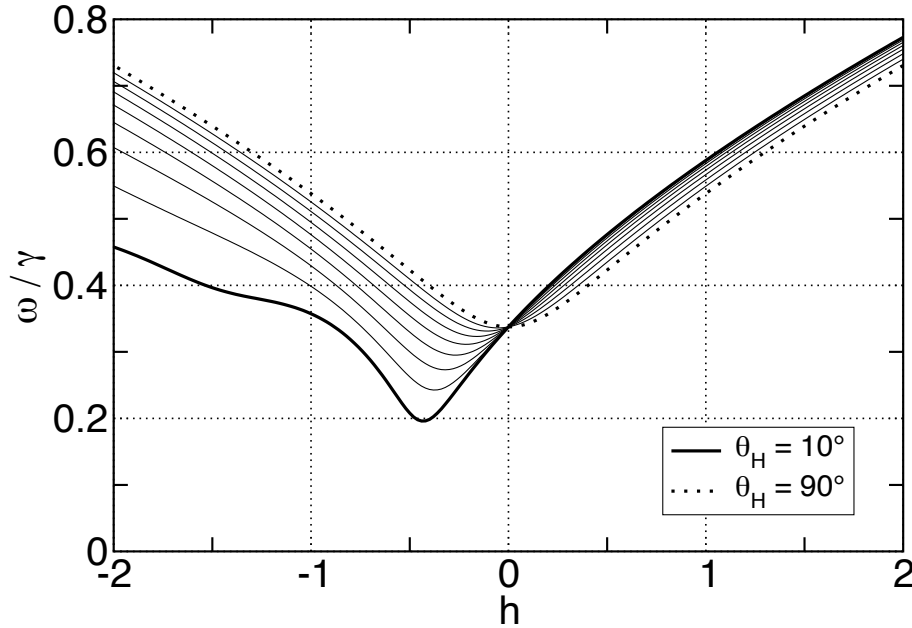


Figure 6.14: Bilayer resonance mode frequency for varying applied field orientation. The normalized frequency ω/γ of the lowest-order bilayer mode is shown as a function of applied field h during a hysteresis loop sweep for a series of applied field angles θ_H , with $J_{f-af} = J_{af}$. Nine values of θ_H are considered, from $\theta_H = 10^\circ$ to $\theta_H = 90^\circ$ in increments of 10° . All fields are expressed in reduced units of $h = 2H_a M_{f\bar{t}}/\sigma_{af}$.

resonance frequency minimum appears to correlate well with the bias field.

An example of variations due to domain wall depinning is given in Figure 6.15. The depinning transition considered is driven by a reduced exchange defect positioned at $x_L = 4$ with $\rho_J = 0.5$ (refer to Fig. 4.3 for geometry). Recall the transition is a result of an attractive potential that pins the wall at the defect site. The frequencies show two distinct features at reverse fields that reflect the wall dynamics in the antiferromagnet. At small negative fields after reversal, there is a sharp drop in the frequency due to the rotation of the ferromagnet and results in a minimum at the shift field (Fig. 6.15a). At larger negative fields, a second drop followed by a transition to a higher frequency is observed. This feature corresponds to the depinning of the partial wall from the interface, where the drop corresponds to the winding of the wall and the sharp transition to the depinning itself. During remagnetization, the reattachment of the wall to the interface results in a small drop in frequency and appears to be larger independent of the field orientation (Fig. 6.15b).

Extensions of the partial wall model to treat real interfaces as an ensemble of

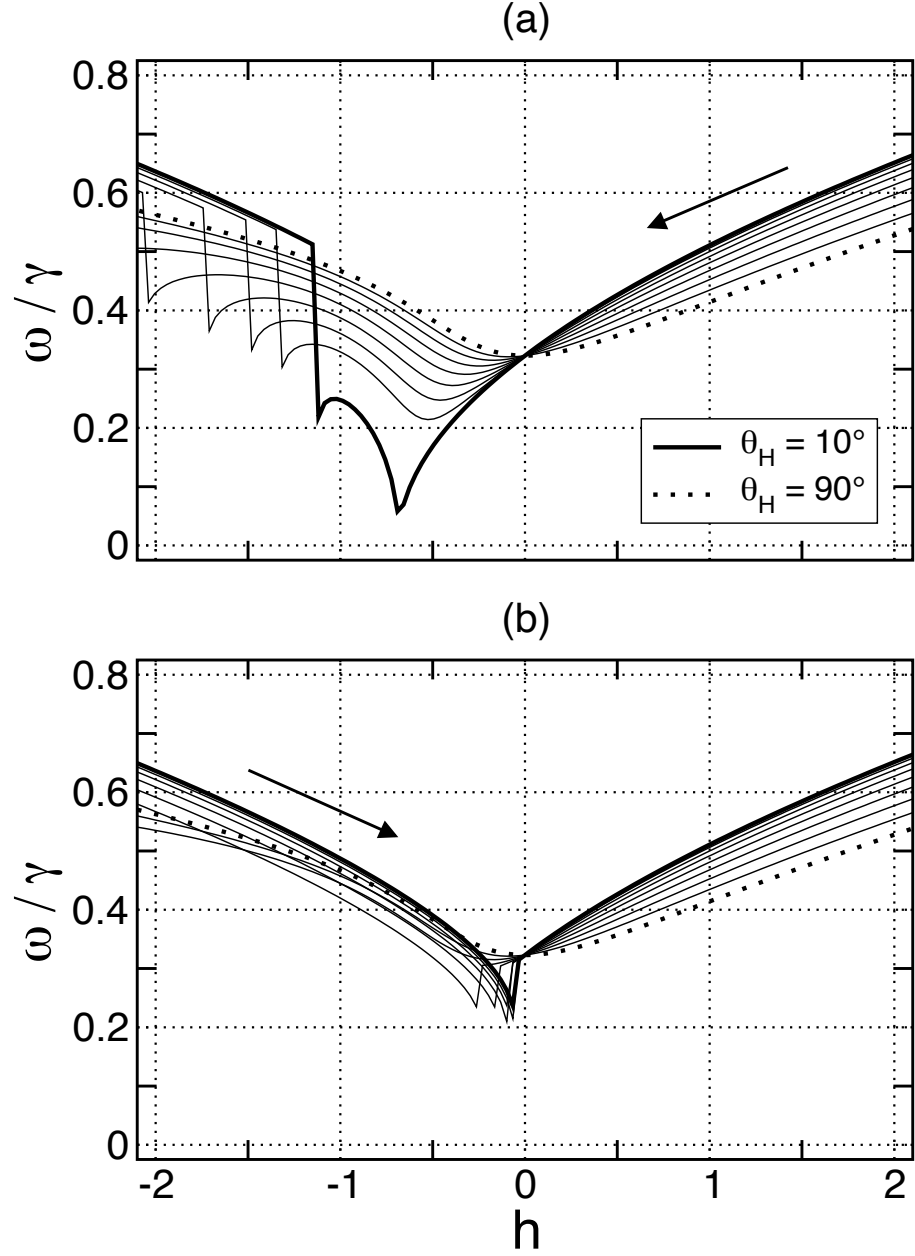


Figure 6.15: Bilayer resonance mode frequency with reduced exchange defects. The normalized frequency ω/γ of the bilayer resonance mode is shown as a function of applied field h during a hysteresis loop sweep for a series of applied field angles θ_H , with $J_{f-af} = J_{af}$. A reduced-exchange defect is located at $x_L = 4$ with $\rho_J = 0.5$. The frequencies are shown for (a) reversal and (b) remagnetization, where the arrows indicate the direction of the field variation. Nine values of θ_H are considered, from $\theta_H = 10^\circ$ to $\theta_H = 90^\circ$ in increments of 10° . All fields are expressed in reduced units of $h = 2H_a M_f t_f / \sigma_{af}$.

antiferromagnet grains or domains have been made by several groups [120, 304, 309, 320, 330]. In such treatments a distribution of anisotropy axis orientations at the interface is assumed, and so the macroscopic bias field observed represents an average over the ensemble of partial walls with varying twist sizes. Supposing that the antiferromagnet can be viewed as a distribution of single-domain grains, the results from Figure 6.14 suggest a possible origin of the linewidth enhancement observed recently in experiment [58, 77]. The broadening here does not occur because of damping, but results from a complicated superposition of different resonance conditions across the film [411–413].

As a first approximation, the linewidth broadening can be estimated by the spread in frequencies due to the different field orientations in Fig. 6.14. As the field is decreased from the positive direction, the linewidth remains almost constant until it vanishes rapidly at zero field. As the ferromagnet rotates into reverse field, the extent of the partial wall formed determines the amount by which the resonance frequency drops. The difference between the system with zero bias and one with the largest loop shift is approximately 0.3 in units of ω/γ , compared to ≈ 0.1 in forward field. Thus, one would expect a three-fold increase in the linewidth broadening due to a distribution of partial walls based on this crude estimate. Variation in the linewidth can also occur from a distribution of interlayer coupling constants J_{f-af} across the contact area between the two films, based on the results in Fig. 6.13 within the same approximation. If wall pinning is significant, the results from Fig. 6.15 suggest that linewidth variations may differ between reversal and remagnetization.

The frequency shift at zero field depends on the strength of the interlayer coupling. For an ensemble of anisotropy axis orientations with constant J_{f-af} , the frequency shift at zero field is common to all curves. However, the frequency curves intersect at negative fields (close to $h = -0.5$ in Fig. 6.13) for a distribution of J_{f-af} . This suggests a measurement of linewidth narrowing should distinguish between the two ensembles.

Frequency variations similar to those depicted in Figs. 6.13–6.15 have been reported in light scattering experiments on the exchange spring Fe/SmCo [414]. In this material, a twist in the magnetization forms in the soft ferromagnetic Fe layer during reversal, where the Fe plays the analogous role of the antiferromagnet in the bias system. The experimental results show that the formation of a twist in the soft ferromagnetic Fe layer can result in the reduction of the mode frequency as shown above, with good agreement from numerical calculations performed by Camley et al. [312].

Chapter 7

Concluding remarks and outlook

An overview of the work presented in this dissertation is given in this chapter. A summary of the main results is first given, followed by a critique of the partial wall model. Some comments are made about the validity and limitations of the theory, and suggestions for new experiments to test the predictions from this model are proposed. Finally, an outline of possible extensions and improvements to the partial wall theory are presented.

7.1 Overview of results

The main topic of this dissertation was the partial domain wall theory of exchange bias, which supposes that the magnetic domain structure at the antiferromagnet interface governs the observed bias properties. The aim of this work was to extend this description to include the effects of interface roughness, bulk magnetic impurities and finite temperatures, and to study the long-wavelength spin dynamics in the bilayer.

Perfect interfaces

Exchange bias in a ferromagnet/antiferromagnet bilayer film was studied using a Heisenberg model with classical spins. The hamiltonian of the bilayer was taken to

consist of Zeeman, nearest-neighbour exchange and uniaxial anisotropy terms,

$$\mathcal{H}_i = -g\mu_B \vec{H}_a \cdot \vec{S}_i - \sum_j J_{ij} \vec{S}_i \cdot \vec{S}_j - K_i (\vec{S}_i \cdot \vec{n}_i)^2. \quad (2.1)$$

Solution to the ground state configuration of the bilayer was sought using analytical and numerical techniques.

Following the work of Mauri et al. [290], a partial wall model based on a continuum approximation to Eq. 2.1 was developed to treat uncompensated interfaces. Expressions for the magnetization curve and bias field were derived in the limit of strong interlayer coupling. The angular dependence of the bias field was also derived,

$$H_{\text{eb}} = -\frac{J_{\text{f-af}}}{M_{\text{f-af}}} \frac{\cos(\theta_{\text{H}})}{\sqrt{\mathcal{J}_1^2 + 2\mathcal{J}_1 \sin(\theta_{\text{H}}) + 1}}, \quad (2.36)$$

demonstrating a departure from a simple cosine dependence on θ_{H} for intermediate values of the interlayer exchange $J_{\text{f-af}}$. Contributions from higher order sinusoidal terms predicted by this equation were shown to be in good agreement with experimental observations from amorphous $\text{Co}_{65}\text{Mo}_2\text{B}_{33}$ ferromagnets [61]. The continuum theory was extended to treat compensated and mixed interfaces by including the two-sublattice structure of the antiferromagnet explicitly. The resulting partial wall structure was found to comprise two interwoven soliton profiles, one describing a partial 180° Bloch wall in the longitudinal component of the antiferromagnet magnetization and the other describing a partial 90° wall in the spin-canting at the interface. Explicit forms for the magnetization profiles were obtained in the limit of weak antiferromagnet anisotropy, which allows for the separation of two profiles to give closed-form expressions for the antiferromagnet energy. Bilinear and biquadratic forms were derived explicitly for the interlayer coupling at mixed interfaces,

$$\mathcal{E}_{\text{f-af}} = -\frac{\kappa_c \sigma_{\text{sf}}}{\gamma} \cos(\phi_0 - \lambda_0) - \frac{J_+(1 - \kappa_c^2)}{\gamma} \sin^2(\phi_0 - \lambda_0). \quad (2.76)$$

making a connection between the phenomenological coupling constants and the microscopic structure.

To allow for non-trivial ground states that follow, for example, from imperfections, interface roughness or finite temperatures, a numerical model was developed to calculate the equilibrium spin configuration for arbitrary magnetic parameters. The bilayer was taken to consist of an ensemble of localized moments with the Heisenberg hamiltonian given by Eq. 2.1. The equilibrium configuration was found by integrating the equation of motion for each spin,

$$\frac{\partial \vec{S}_i}{\partial t} = \gamma \vec{S}_i \times \vec{H}_i^{\text{eff}} - \alpha \vec{S}_i \times \dot{\vec{S}}_i \times \vec{H}_i^{\text{eff}}, \quad (2.84)$$

where the Landau-Lifshitz damping form was chosen for the relaxational dynamics to ensure conservation of spin magnitude. This represents a large set of coupled non-linear differential equations, the solution to which was obtained by a combination of standard time-integration techniques.

An application of the numerical approach was made to study the film thickness dependence of exchange bias. For variations in the ferromagnet film thickness, it was found that partial wall formation in the ferromagnet should lead to a deviation from a $1/t_f$ to a $1/t_f^2$ dependence for thick films. For partial wall formation in the antiferromagnet a critical value for the antiferromagnet film thickness for bias was found to correlate well with the domain wall width, consistent with experimental observations [32, 34, 38, 85, 119, 120, 145, 203, 279].

The stability of the spin-flop coupling at compensated interfaces was also investigated. The existence of bias was shown to be sensitive to the magnitude of the interlayer coupling relative to the antiferromagnet exchange and anisotropy constants. It was found that bias only exists for a certain range of $J_{\text{f-af}}$ values. Outside this range the bias disappears and the interlayer coupling gives rise to a centred hysteresis loop with large coercivity.

Interface roughness

The role of interface roughness in the form of geometrical imperfections was investigated with the numerical approach. Three different types of deformations were considered: bumps, lines and steps. The presence of a geometric imperfection was shown to result in frustration amongst the interfacial spins, where mixing at the interface occurs through the coupling to both antiferromagnet sublattices.

For periodic imperfections, such as lines and steps, the degree of mixing can be controlled by the spacing between successive defects. The primary effect of such imperfections is to cause a bifurcation in the exchange bias direction, introducing a set of new axes along which the equilibrium ferromagnet magnetization lies in the absence of an applied field (natural angle θ_{nat}). The result is a strongly modified angular dependence that can be described with additional anisotropies induced by the imperfections. Irreversible rotations were also observed at rough interfaces, which can be explained using a simple two-sublattice model with unequal exchange coupling $J_a \neq J_b$. The results are consistent with modified angular dependences observed in experiment [91, 100, 143, 146, 188].

Uncorrelated roughness, such as randomly distributed bumps, was shown to cause a reduction in the bias field but no changes to the natural angle.

Bulk magnetic defects

Bulk magnetic defects, in the form of local variations in the exchange or anisotropy constants, lead to domain wall pinning processes in the antiferromagnet. The weakening of an exchange bond between two successive layers in the antiferromagnet, for example, creates an attractive potential for the domain wall, and it was shown that such defects can alter the reversal mechanisms dramatically. Depending on the defect magnitude and its position relative to the interface, a complete depinning of the partial wall from the interface was shown to be possible, and in such instances, enhancements in the coercive

field were observed to accompany a reduced bias shift. Large departures from a simple sinusoidal angular dependence were also observed, where pinning was shown to be only effective within a certain angular range about the easy axis. The chirality of the domain walls formed during the pinning and depinning transitions was shown to be important for the hysteresis properties. Asymmetric hysteresis loops are another result of defect-induced pinning. Some features of the defect-modified bias, such as the bias field reduction and coercivity enhancement, have been observed in ion-irradiation [114,157,227] and spin dilution [132,202,250,257] experiments. An explanation of rotational hysteresis was proposed based on an ensemble of passive regions, facilitated by pinning centres in the antiferromagnet

Finite temperatures

The inclusion of finite temperatures was made using a local mean-field theory, where the effective fields of neighbouring spins are weighted using a Brillouin function. The bias field was observed to vanish at a blocking temperature below T_N , at which a peak in the coercivity was seen, consistent with some experimental observations [20,21,153]. The numerical simulations also showed that the partial wall can de-pin from the interface at sufficiently high temperatures much in the same way as impurity-driven transitions. This behaviour is attributed to a reduction in wall energy resulting from a non-uniform spatial profile of the mean-field thermal spin magnitudes, where the effective fields at the centre of the domain wall are reduced significantly at elevated temperatures. Such domain wall processes were shown to modify the angular dependence of bias at finite temperatures. Studies of the magnetic heat capacity demonstrated that the formation of the partial wall should appear as distinct peaks as large as 15% of the heat capacity itself. This suggests an alternative means of characterizing antiferromagnetic order in an exchange bias system.

Long-wavelength spin excitations

Finally, the linear long-wavelength dynamics of the bilayer was studied. Changes to the spin configuration, arising from a spin-flop transition in the antiferromagnet, for example, were shown to result in measurable features in the spin waves frequencies. Low frequency modes in the ferromagnet layer, most accessible to ferromagnetic resonance and light scattering experiments, were shown to exhibit frequency shifts that are sensitive to the strength of the interlayer coupling and the details of the magnetic structure in the antiferromagnet. Some estimates were made of possible linewidth broadening due to different resonance conditions across the film, arising from interface roughness or an ensemble of grains, for example. Based on these estimates, a method of characterizing the interfacial structure using linewidth variations was proposed. Examination of the excitation profiles showed the presence of modes localized to the interface and the partial wall structure, some of which couple to the uniform mode of the ferromagnet.

7.2 Criticisms and limitations of the partial wall model

7.2.1 Critique of model Hamiltonian and geometry

The model for exchange bias studied in this dissertation is based on a localized classical spin picture with a Heisenberg hamiltonian. This description is most suitable for magnetic insulators and to a large extent rare earth metals, where the localization of electron states give rise to well-defined local atomic moments. Antiferromagnetic materials commonly used in exchange bias systems, such as CoO, NiO and FeF₂, are insulators and are therefore well represented by localized spins. For rare earths, the hybridization between $4f$ states and metallic bands ($5s$ and $5p$) is sufficiently small to ensure that the moments retain a localized character. However, it is not possible to account for ferromagnetism in terms of localized electron states for transition metals such as Fe,

Ni and Co. Itinerant models, such as the Hubbard model, offer a different approach and provide a temperature dependence for the magnetization that better matches experimental observations for many metallic ferromagnets. In addition to metallic ferromagnets, it is questionable whether the validity of the local moment approach extends to manganese-based alloys such as antiferromagnetic FeMn, where RKKY interactions between the Fe and Mn atoms are long-ranged and the constituents may be randomly distributed forming a disordered alloy with no magnetic unit cell.

However, localized moment models appear to work well in describing the low-energy and low-temperature behaviour of many magnetic metals. For example, the long wavelength behaviour of spin waves in metallic ferromagnets can be explained with a Heisenberg picture in useful terms. Other magnetic properties such as domain sizes and domain wall widths can be predicted with some success using localized spins [415]. The advantage of a local moment hamiltonian is its simplicity. With a local moment model it is possible to study the effects of energies that are high-order perturbative corrections in ab-initio calculations, such as magnetic anisotropies and applied fields. Such an approach can offer predictions for experiments that are otherwise too difficult to obtain from first-principle calculations.ⁱ

Finite temperatures are included using mean field theory. The limitations of mean field theory are well known in condensed matter physics, where there are two regimes in which significant deviations from observed physical properties occur. The first is at low temperatures, where the magnitude of the spontaneous magnetization is overestimated. The behaviour is better described using a spin wave theory first presented by Bloch [389], which correctly predicts a $T^{3/2}$ dependence at low temperatures. The second significant deviation occurs near the critical temperature of a magnet, usually overestimated by mean field theory, where again fluctuations dominate the physics. Ignoring fluctuations

ⁱA detailed discussion comparing localized moment and itinerant electron models is given by Moriya [416].

means viscous effects are not described and in order to study processes that result from thermal activation, for example, it is necessary to include a stochastic field with the correct statistical properties.ⁱⁱ

Despite these limitations, mean field theory predicts qualitative features of the phase diagram of three dimensional systems correctly and can describes most types of magnetic order occurring in three-dimensional magnets. For the study of exchange bias here, the thermal dependence of the bias field and coercivity predicted using a mean field approach is in agreement with some experimental observations, and highlights essential features governing the hysteresis properties.

Another issue worth mentioning here is the relevance of crystal structure to exchange bias. The bilayer considered here possesses a simple cubic structure. However, common exchange bias antiferromagnets, such as NiO (fcc), FeMn (fcc), FeF₂ (bc tetr) and CoO (fcc), and ferromagnets, such as Fe (bcc), Ni (fcc), Co (hcp) and permalloy (fcc), possess more complicated crystal structures. In this study details of realistic crystal structures have been neglected. Instead, only the most important symmetries, such as the uniaxial anisotropy in the antiferromagnet, are considered as a compromise needed for analytic calculations and numerical constraints. For example, bias at compensated interfaces obtained by Koon [297] with a body-centred tetragonal crystal structureⁱⁱⁱ exhibits the same qualitative features as the results obtained from the simple cubic model here. First-principle calculations of magnetic structures at compensated interfaces have also demonstrated a perpendicular coupling arising from biquadratic exchange and canting of the interfacial moments [340], which is in agreement with the results from the simplified geometry considered.

Finally, some comment should be made about the validity of the atomistic view of the partial wall mechanism. The model relies on perfect contact and lattice match-

ⁱⁱThis is referred to as Langevin dynamics in the literature. For examples of recent studies on thermal activation using this computational technique, the reader is referred to Refs. [417–420].

ⁱⁱⁱThis calculation assumes in-plane rotation of the spins.

ing between the ferromagnet and antiferromagnet layers, and where there are deviations from a smooth interface, the roughness takes the form of geometrical structures that are commensurate with the lattice. Furthermore, the magnetic constants are assumed to be well-defined throughout the structure. This supposes the chemical composition is coherent in both materials near the interface, and that the chemical bonding across the interface is uniform to give a constant exchange constant. These assumptions are unrealistic for experimental systems.

7.2.2 Limitations of present theory

Partial wall bias requires the antiferromagnet film to be sufficiently thick to support the spatial extent of the twist. For films under the critical thickness the entire antiferromagnet is rotated coherently, resulting in a large coercivity but no loop shift. In some experimental systems, bias has been observed to occur for a range of thicknesses below the theoretical domain wall width in the material [39,63,72,85,139,219,250,257,270]. For CoO systems a $1/t_{\text{af}}$ dependence for the bias field has been reported [63], while for FeMn a more complicated $t_{\text{af}}^{-0.3}$ variation has been observed [85]. Some of these variations can be explained by the presence of imperfections, which allow the partial wall to be pinned for thin films below the critical thickness as shown in Chapter Four. However, the partial wall model does not predict any dependence on the antiferromagnet film thickness apart from the critical thickness required for wall formation. This is an important point that requires further exploration.

In many systems, a linear dependence of the bias field on temperature has been observed [10,20,23,31–33,38,45,63,65,70,80,82,85,95,109,110,136,148,152,158,181,200,209,210,232,235,250,264], while in others the shift is almost independent of T for a range of temperatures well below the Blocking temperature [52,56,63,89,141,153,165]. Some groups have reported an exponential-like decrease in the bias field with temperature [81,

185,192,247,271,272], differences in the temperature dependence between the two coercive fields H_{c1} and H_{c2} [163], and effects due to particular crystallographic orientations of the films grown [38,165]. The temperature dependence of the bias field predicted by the partial wall model has been observed in some experiments [38, 45, 63, 72, 80, 85, 96, 117, 125, 137, 141, 144, 156, 169, 202, 240, 256, 279], but most observations are inconsistent with the mean field theory. More care is required to include proper thermal dependencies of anisotropy constants, for example, in order to give quantitative predictions for experiment.

One particularly interesting observation made by Zhou et al. is the departure from a $1/M_f$ dependence predicted for the bias field [159]. The experiments on Co-Ni/FeMn bilayers show that the exchange coupling energy $\mathcal{E} = H_{\text{eb}} M_f t_f$ is not constant but varies as $c M_f^{1/2}$, where c is a constant. This behaviour is attributed to the role of the ferromagnet magnetization during the field-cooling process, in which the effective fields generated by the ferromagnet spins are important for determining the antiferromagnet order when M_f is large. The role of M_f is neglected in this treatment.

Bias field enhancements that follow ion-irradiation and non-magnetic impurity implantation are not explained suitably with the partial wall theory. In ion-irradiation experiments, two-fold enhancements in H_{eb} were obtained for suitable doses of helium ions on FeNi/FeMn [157, 227], while similar increases were observed after substitution of magnetic Co for non-magnetic Mg atoms in Co/CoO systems [132, 250, 257]. One of the main difficulties in making direct contact with experimental data is the uncertainty in the microscopic changes effected by the imperfections. Ion-irradiation, whose importance in creating patterned media is growing rapidly [421–423], can lead to significant changes to the interlayer coupling [424] and anisotropies [425] in magnetic multilayers. In some instances a magnetization reorientation from out-of-plane to in-plane has been observed due to the suppression of large perpendicular anisotropies brought about by the ion bombardment [426]. Modest bias field increases can be obtained with enhancements

in the site anisotropy using the numerical model, but these changes do not account for the magnitudes seen in experiment.

Translational invariance within the film plane, at least outside a small primitive cell, has been assumed for much of this work, so little effort has been made to examine the effects of polycrystallinity or randomness parallel to the interface. The inability to study training effects and other phenomena arising from the statistics of an ensemble of crystalline grains at the interface is a major drawback of this approach. Lateral domain walls and domain structures, arising from random fields [291–293], for example, also deserve more consideration in further numerical studies of exchange bias. However, the statics and dynamics of a coupled single-domain material have been examined in great detail, with the view that this system is a building block for a more sophisticated theory to describe more complicated cooperative phenomena.

7.3 Suggestions for new experiments

Despite the limitations of the partial wall theory at present, the model offers several new tests for exchange bias in the laboratory. The new experiments proposed can help to determine whether the formation of a planar antiferromagnet wall is adequate or appropriate to describe exchange bias for a particular system.

To explain bias at compensated interfaces, M. Kiwi et al. suggested a partial ferromagnetic twist to account for observations in materials such as Fe/FeF₂. The anisotropy fields for the antiferromagnetic FeF₂ are quite large, so it is argued that deformations in the antiferromagnet cannot account for the observed bias shifts. In their model, spins near the interface freeze during field cooling and retain this configuration below the Néel temperature, which remains unperturbed by the rotation of the ferromagnet. The deformation occurs in the ferromagnet spin structure instead, and it is shown with numerical simulations that bias fields comparable to experimental measurements can be obtained. It

was shown in Chapter Two that twists in the ferromagnet should lead to deviations from the $1/t_f$ dependence of the bias field, where a $1/t_f^2$ form is predicted for thicker films. This result is supported in a recent numerical study by Lopez et al. [356], who showed a $1/t_f^{1.9}$ behaviour for thick ferromagnets. Experiments to date, however, have not presented any clear evidence to support this model. Thus, a litmus test for the partial ferromagnetic twist is the $1/t_f^2$ dependence of the bias field for thick ferromagnet films.

The angular dependence of exchange bias is extremely useful for extracting information about the interface quality and the presence of domain-wall pinning processes in the antiferromagnet. It was shown that geometrical imperfections with a well defined spatial period can alter the natural angle of the ferromagnet and modify the angular dependence dramatically. The natural angle gives an indication of the interface mixing and can be obtained from the remanence of the magnetization. The results show that uncorrelated roughness, such as random bumps, do not produce shifts in the natural angle. This provides a means of distinguishing between the two types of geometrical roughness.

Defects in the antiferromagnet film, involving local variations in the exchange or anisotropy constants, act as pinning centres for the partial wall. The strength of these variations and their position relative to the interface were found to be crucial parameters for governing partial wall pinning. With sufficiently strong pinning centres the partial wall can completely de-pin from the interface during the rotation of the magnetization. Sharp transitions in the bias field angular dependence separate regions with and without wall depinning. The observation of such behaviour in experiment would allow one to identify the presence of strong pinning centres in the antiferromagnet. Conversely, hysteresis can be tailored by the placement of such defect. This can be controlled by the introduction of impurities during film growth, for example, or by modifying individual layers or spacer thicknesses in artificial antiferromagnets.

Domain wall pinning arising from thermal effects can also be probed with angular

dependence measurements. As discussed in Chapter Five, the thermal pinning exhibits similar features to defect-induced pinning at zero temperature. The angular curves do not exhibit sharp transitions as the defect case, but there are tell-tale signs at elevated temperatures such as the gradual shift in the bias field extrema and the appearance of a passive region in θ_H .

Further evidence of the partial antiferromagnet wall can be obtained from heat-capacity measurements. The magnetic heat capacity at constant field taken throughout a hysteresis loop exhibits sharp features that are attributed to partial wall formation. These peaks are similar to the features seen at phase transitions, such as the spin-flop transition driven by an external field [391] or the magnetic ordering at the Néel temperature [390]. The heat capacity features for partial wall formation represent an increase of approximately 15% of the forward field value, compared to 1% for coherent rotation, which gives a tool to probe antiferromagnet order during reversal.

Insight into buried interfaces can be gained by studying the precessional dynamics of the ferromagnet layer. Calculations of the long-wavelength spin waves show shifts in the excitation frequencies resulting from the exchange coupling between the two magnetic layers. The variation in the bilayer resonance frequency as a function of applied field during a hysteresis loop measurement is shown to be sensitive to the applied field orientation and the magnitude of the interlayer coupling. For the former the frequency branches for varying θ_H converge at $h = 0$ as the field is decreased and diverge again at negative fields due to the formation of the partial wall. It is argued that this gives a rough indication of the corresponding linewidth variations due to different resonance conditions across the film. For variations in the interlayer coupling, the frequency branches converge at negative fields close to the bias field. This distinction between the two behaviours offers a means of distinguishing between roughness due to spatial variations in the interlayer coupling, arising from non-uniform contact points between the two films, for example,

and a polycrystalline structure where there exists a distribution of easy axis directions.

7.4 Future work

The foundations for studying the static and dynamic behaviour of a ferromagnet/antiferromagnet bilayer with the partial wall model has been established. The limitations and deficiencies of the partial wall approach has been discussed in some detail throughout this chapter. These shortcomings serve as a starting point for what may be explored in future work. In this final section, a brief overview is given of some possible avenues of research to develop this theory further.

All hysteresis loops calculated have all been obtained after allowing the system to reach equilibrium at each field increment. The study of non-equilibrium processes may be facilitated by removing this constraint. This is straightforward because the calculations are based on the time-integration of the equations of motion and not a stochastic method such as a Monte-Carlo approach. It would be interesting to study how partial wall formation responds to varying sweep rates of the external field.

The study of linear dynamics can also be extended to calculate the response of the system to a driving field. Radio frequency techniques, such as Brillouin light scattering and ferromagnetic resonance, probe the linear response of the system. It is convenient to use Green's functions as a mathematical description to study the linear response of the bilayer, from which one can extract important features of the excitations such as the spectral density. Green's functions can be constructed from the right and left eigenvectors of the dynamical matrix \mathbf{M} computed in Chapter Six,

$$G_{\alpha\beta}(n, n'; \omega) = \sum_{\Omega} \frac{\xi_{r\alpha, n}(\Omega) \xi_{l\beta, n}(\Omega)}{\omega/\gamma - \Omega}, \quad (7.1)$$

from which the spectral density of the spin waves can be calculated,

$$\mathcal{S}_{\alpha}(\omega) = -\frac{1}{\pi} \sum_n \text{Im}[G_{\alpha\alpha}(n, n; \omega)]. \quad (7.2)$$

Here, $\alpha, \beta = x, y$ or z , and n denotes the layer number. The Green's function can provide power absorption spectra, light scattering [427] and neutron scattering cross-sections, for example, which will allow for direct comparisons with experimental data. Furthermore, they can form the basis for constructing theories that go beyond the linear approximation, such as spin wave interactions and non-linear dynamic response.

An important aspect that has been neglected is the question of fluctuations and the stability of the partial wall formed in the antiferromagnet. The latter is especially important for compensated interfaces, where no demagnetizing fields are present to encourage planar rotation of the spins during reversal. The presence of a planar anisotropy is crucial to the existence of the bias, where it has been demonstrated in numerical simulations that spin fluctuations out of the film plane can destabilize the twist resulting in zero bias [302]. Some preliminary work has already been conducted on this subject by Stamps et al. [325], who have examined the role of the planar anisotropy on wall stability.

Fluctuations are also important in initiating transitions between metastable states and are particularly relevant in frustrated spin systems, where there are a multitude of configurations almost degenerate in energy. Magnetization reversal can be viewed as the traversal along a non-trivial path on this energy landscape. Hysteresis arises because the forward and reverse trajectories differ, and training effects can be explained by the different path adopted with each loop measurement. One way of reproducing a complex energy landscape that may exist in real exchange bias systems is to consider an ensemble of antiferromagnetic grains in contact with the ferromagnet layer^{iv} [128, 206, 304, 309, 330]. Issues likely to affect the hysteresis on a macroscopic scale include the distribution of grain sizes, the importance of interactions between grains, and the uniformity of the interlayer coupling across all grains. Other constraints can also be relaxed, for example, by allowing: (1) domains to form in the ferromagnet within the film plane; (2) the direction of the antiferromagnet axis to vary from grain to grain; (3) the sizes of the grains to vary.

^{iv}Much work has been conducted on granular ferromagnets, see Refs. [428–431], for example.

Some attempts to treat the spatial inhomogeneities of real materials have begun with micromagnetic simulations [432], and the results have so far been quite encouraging.

Thermal fluctuations at finite temperatures can be studied using a Monte-Carlo approach instead of mean field theory. The Monte Carlo scheme is a stochastic approach that does not attempt to follow an equation of motion, where transitions in the spin orientations are governed by a probability determined by the Boltzmann factor.^v Some applications of the Monte Carlo technique have already been made in the study of magnetic viscosity and dynamic hysteresis in exchange bias, with some success in describing training effects and thermal variations of the bias field [320]. Langevin dynamics has also been used with success to study thermal activation processes with numerical simulations [417–420].

^vAn excellent discussion of the Monte Carlo method for problems in statistical physics is given by Landau and Binder [433].

Appendix A

Numerical time-integration model

In this chapter, a brief discussion is given on the numerical time-integration techniques used in this dissertation. The algorithms used to integrate the spin equations of motion are presented in the first section, while tests for the performance of the numerical techniques are given in the remainder of the chapter.

A.1 Algorithm

The time evolution of each moment \vec{S}_i in the ferromagnet/antiferromagnet bilayer is governed by the Landau-Lifshitz equation,

$$\frac{\partial \vec{S}_i}{\partial t} = \gamma \vec{S}_i \times \vec{H}_i^{\text{eff}} - \alpha \vec{S}_i \times \dot{\vec{S}}_i \times \vec{H}_i^{\text{eff}}. \quad (2.84)$$

The equilibrium spin configuration is found by integrating the coupled set of non-linear differential equations, defined above, with a suitable numerical scheme. A combination of single-step and multistep time-integration methods is used.

A fourth-order Runge-Kutta scheme is used primarily for difficult regions of phase space where large changes to the spin configuration take place, such as the formation of the partial twist during reversal, for example. Suppose one wishes to determine the solution to the generic first order initial-value problem,

$$y' = f(t, y), \quad (\text{A.1})$$

where the state at the initial time t_i is known, $y(t_i) = y_i$. Then the value of y at the next time step $t_{i+1} = t_i + \delta t$ is given by

$$y_{i+1} \equiv y(t_i + \delta t) = y(t_i) + \frac{\delta t}{6} (k_1 + k_2 + k_3 + k_4), \quad (\text{A.2})$$

where

$$k_1 = f(t_i, y_i), \quad (\text{A.2a})$$

$$k_2 = f\left(t_i + \frac{\delta t}{2}, y_i + \frac{\delta t k_1}{2}\right), \quad (\text{A.2b})$$

$$k_3 = f\left(t_i + \frac{\delta t}{2}, y_i + \frac{\delta t k_2}{2}\right), \quad (\text{A.2c})$$

$$k_4 = f(t_i, y_i + \delta t k_3), \quad (\text{A.2d})$$

This technique has a local truncation error of $O(\delta t^4)$ and is referred to as a one-step method because the solution for each successive time step only requires knowledge of the previous time step.

When changes to the orientations of the moments are small, such as in forward field during a hysteresis loop sweep, it is possible to obtain solutions much faster by using multistep methods. One excellent approach is to use a predictor-corrector method, such as the four-step method as described in Ref. [434]. This technique is a combination of explicit and implicit methods; the explicit method predicts an approximation and the implicit method corrects this prediction. Initially, four time steps must be generated and stored using a one-step method such as the Runge-Kutta scheme. A prediction of the solution at the next step $t_i + \delta t$ can then be made using a four-step Adams-Bashforth predictor,

$$y_{i+1} = y_i + \frac{1}{24} \delta t (55f(t_i, y_i) - 59f(t_{i-1}, y_{i-1}) + 37f(t_{i-2}, y_{i-2}) - 9f(t_{i-3}, y_{i-3})), \quad (\text{A.3})$$

which is followed by a three-step Adams-Moulton corrector,

$$y_{i+1} = y_i + \frac{1}{24} \delta t (9f(t_{i+1}, y_{i+1}) + 19f(t_i, y_i) - 5f(t_{i-1}, y_{i-1}) + f(t_{i-2}, y_{i-2})), \quad (\text{A.4})$$

For this method it is always necessary to keep the spin configuration for four time steps in memory. A more detailed discussion of these techniques can be found in Ref. [435].

The overall performance of these schemes depends largely on the nature of the magnetic system and the kinds of transitions that take place during a hysteresis loop. In general, the calculations presented here involve a combination of predictor-corrector and backward differentiation methods supplied by the CVODE package [436,437] in conjunction with a fourth-order Runge-Kutta scheme that is activated when large changes to the spin configuration take place. Details of convergence properties are found in the next section.

A.2 Convergence tests

Some example ground state calculations are presented to illustrate the differences between the Runge-Kutta scheme and the multistep methods provided by the CVODE package.

An important performance test for an algorithm is the rate at which the ground state can be determined. In the first example, an isotropic ferromagnet with dimensions $4 \times 4 \times 40$ spins is considered. The gyromagnetic constant is $\gamma = 1.0$ and the time step for each iteration is taken to be $\delta t = 0.0001$. The system is begun in a randomized state and allowed to relax to equilibrium via Eq. 2.84 in the presence of an applied field. The mean spin deviation between successive iterations,

$$\langle \Delta S \rangle \equiv \frac{1}{n} \sum_i |\vec{S}_i(t + \delta t) - \vec{S}_i(t)|, \quad (\text{A.5})$$

is shown as a function of the number of iterations in Figure A.1. n is the total number of spins. The convergence to equilibrium with the Runge-Kutta method begins with large changes in the spin orientation followed by an exponential decay with the number of iterations. Convergence is attained with fewer steps for larger damping constants, as expected, but the size of α must be sufficiently small for the spin magnitudes to be

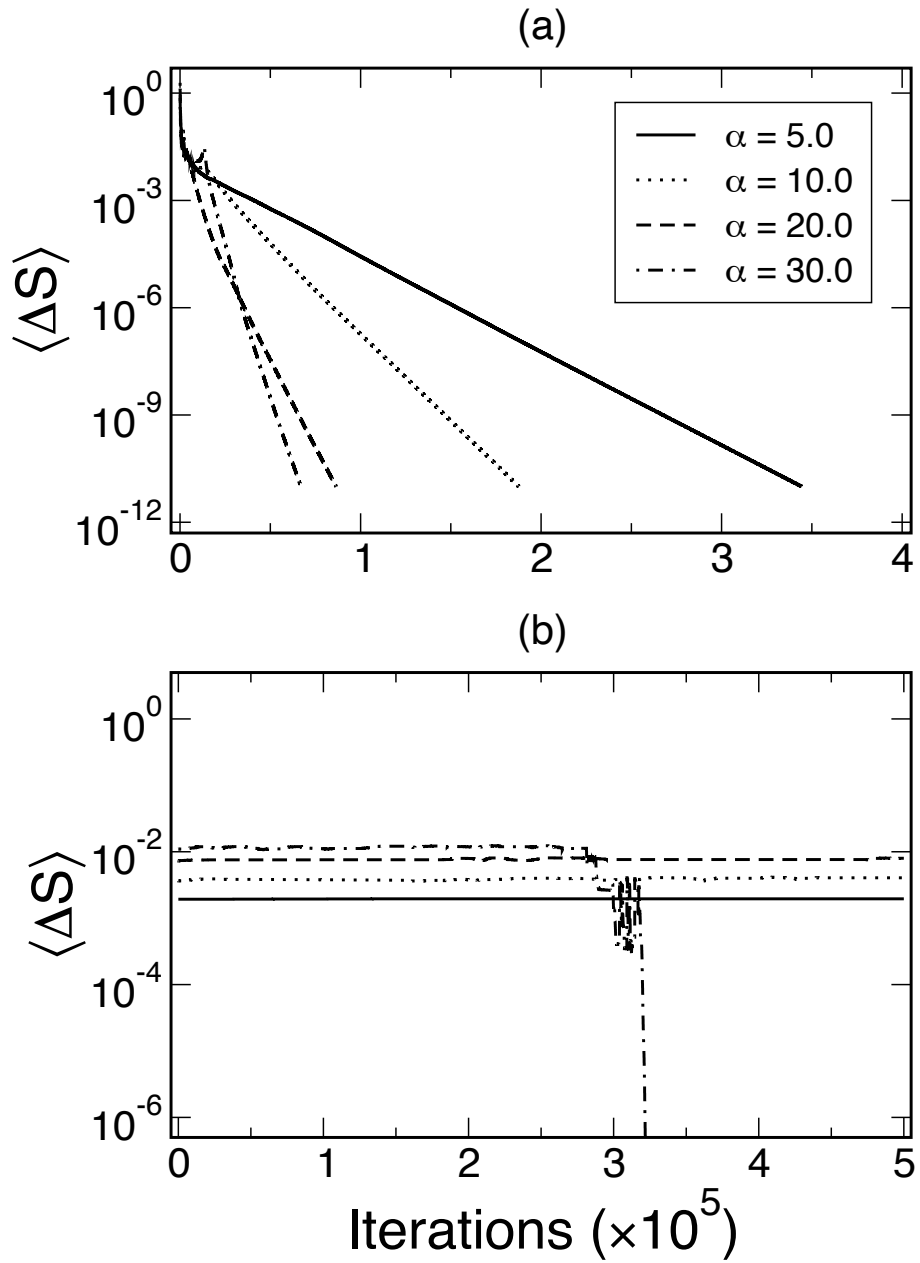


Figure A.1: Convergence of numerical model from random initial state. The change in spin orientation, $\langle \Delta S \rangle$, of a $4 \times 4 \times 40$ ferromagnet is shown as a function of iterations, for the (a) fourth-order Runge Kutta and (b) CVODE predictor-corrector schemes, for a series of damping constants α . The spin orientations are initially randomized and are then allowed to relax in the presence of an applied field.

conserved. For the parameters used, a value of $\alpha = 30.0$ is close to the upper limit for the damping constant. In contrast, the predictor-corrector scheme does not converge at all for three of the damping constants ($\alpha = 5.0, 10.0, 20.0$) within the first 50 000 iterations. Equilibrium is attained for $\alpha = 30$ but only after 30 000 iterations, five times larger than the Runge-Kutta calculation. The multistep method performs poorly in this case because forward extrapolation from the random initial state is not useful.

In the second example, a ferromagnet with the same dimensions and parameters is begun in a saturated state. The magnet then relaxes towards an applied field directed 10° from its initial orientation. The multistep method performs much better than the Runge-Kutta scheme for this calculation, where equilibrium is attained around 500 iterations for the former compared with 10 000 iterations for the latter, as shown in Figure A.2. For the Runge-Kutta method the convergence to equilibrium does not appear to be affected by the initial state. The curves in Fig A.2b also show that the damping constant does not play a large role for the multistep method, as equilibrium is attained with approximately the same number of iterations for all values of α considered.

The primary concern is the calculation of hysteresis loops for the ferromagnet/antiferromagnet bilayer in this dissertation. In forward field, where little changes in the magnetization orientation take place, the Predictor-Corrector scheme is used because equilibrium can be attained within a few thousand iterations. During reversal, where large changes in the antiferromagnet order occur, the Runge-Kutta scheme is activated. An illustration of these two integration schemes in action is given in Figure A.3. The formation of the partial antiferromagnet wall represents a significant change in the magnetic order. At low temperatures, the wall formation process occurs over a large range of field values in negative fields (Fig. A.3a). The results show that the Predictor-Corrector method is capable of handling these changes, where equilibrium at each field increment is attained within a few thousand iterations. At higher temperatures the reversal of the

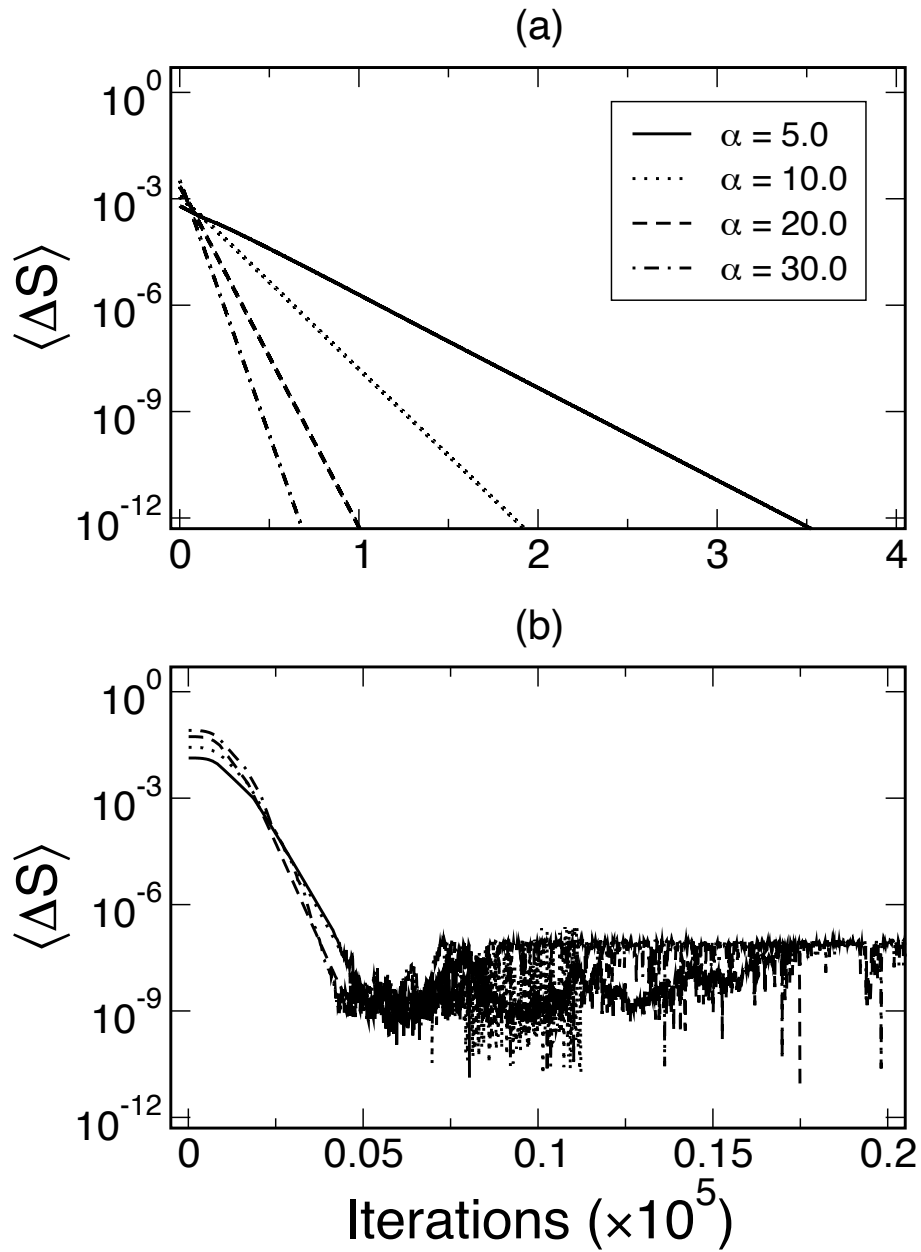


Figure A.2: Convergence of numerical model from saturated initial state. The change in spin orientation, $\langle \Delta S \rangle$, of a $4 \times 4 \times 40$ ferromagnet is shown as a function of iterations, for the (a) fourth-order Runge Kutta and (b) CVODE predictor-corrector schemes, for a series of damping constants α . The ferromagnet is begun in a saturated state and is then allowed to rotate into the an applied field at 10° from its initial orientation.

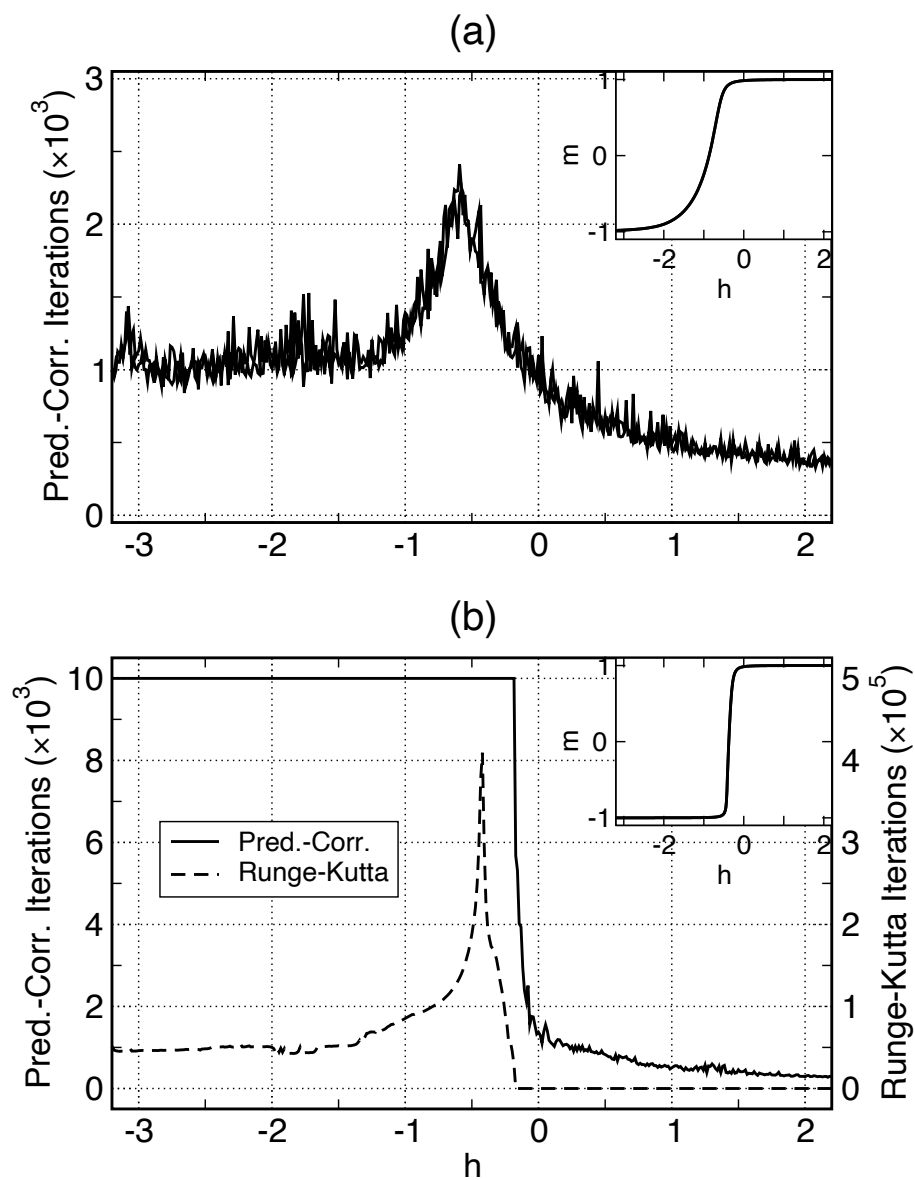


Figure A.3: Algorithm performance for hysteresis loop calculation. The number of iterations used to obtain equilibrium at each field increment of a hysteresis loop is shown. (a) At low temperatures ($T = 0$ K) the partial wall formation extends over a range of a few field units, indicating a gradual change in the magnetic structure. This calculation is handled entirely by the Predictor-Corrector scheme. (b) At higher temperatures ($T = 0$ K) the reversal of the ferromagnet occurs over a smaller field range. The sharp transition is better handled by the Runge-Kutta method. The magnetization curve for each case is shown in the inset. All fields are expressed in reduced units of $h = 2H_a M_f t_f / \sigma_{af}$

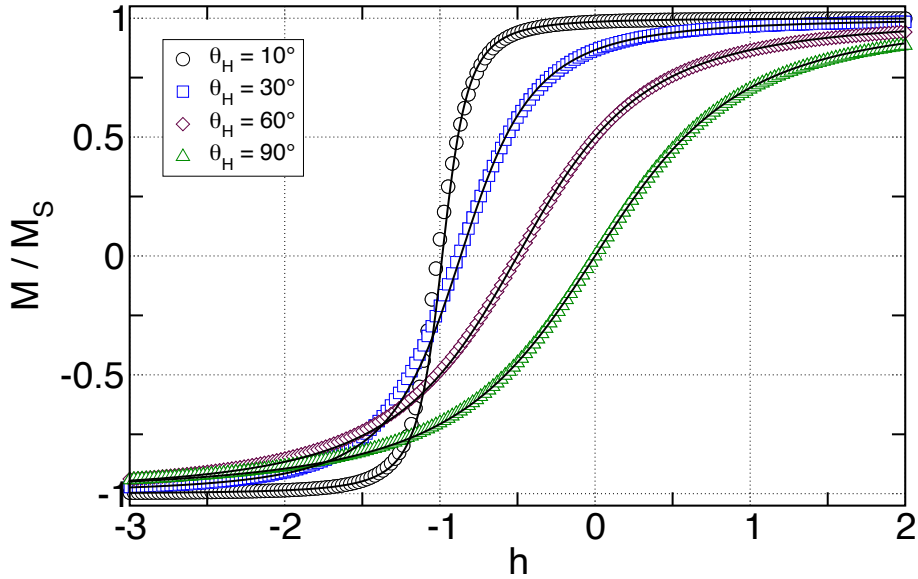


Figure A.4: Comparison of analytical and numerical magnetization curves. Results from the numerical simulation for $J_{f-af} = -J_f$ are shown for a series of applied field angles θ_H . The solid lines are fits based on Eq. 2.30.

ferromagnet occurs over a smaller range of fields (Fig. A.3b). Consequently, large changes in the antiferromagnet order occur at each field increment near the bias field and this leads to a divergence in the number of predictor-corrector steps used for equilibrium.

Performance degradation due to this divergence can be avoided by introducing a cut-off for the number of predictor-corrector steps. Above this cut-off the Runge-Kutta method is used, as shown in Fig. A.3b, where the cut-off is chosen to be 10 000 iterations. Although the number of Runge-Kutta steps required for convergence is much greater than the cut-off, the actual computation time is reduced significantly in practice.

A.3 Hysteresis curves

A series of hysteresis curves calculated with the numerical simulation is shown in Figure A.4. A large interlayer exchange $J_{f-af} = -J_f$ is chosen to simulate rigid coupling between the interface spins. The results show good agreement with the analytical expression for the magnetization curve derived earlier (Eq. 2.30). Some finite-size effects are seen for applied field orientations close to the easy axis directions, where the partial wall formed is the largest. Agreement between the analytical and numerical results improve

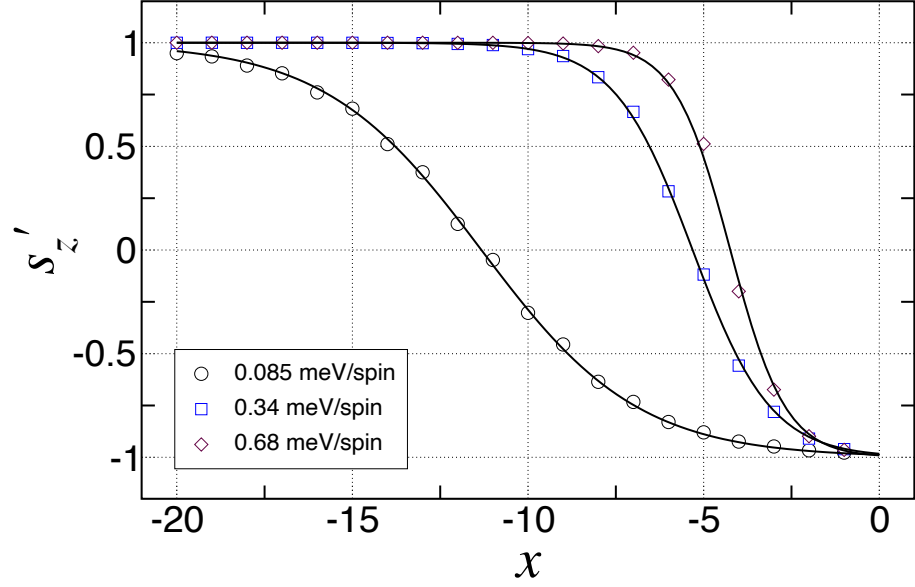


Figure A.5: Comparison of analytical and numerical wall profiles. The component of the antiferromagnet staggered magnetization along the easy axis, s'_z , is shown as a function of position at maximum reverse field in a hysteresis loop sweep. The antiferromagnet occupies the space $-t_{\text{af}} \leq x < 0$. Three different anisotropy constants K_{af} are considered. The solid lines represent fits based on Eq. A.6.

as the field is rotated away from the easy axis.

A.4 Partial wall profile

Magnetization profiles in the antiferromagnet, computed with the numerical model, are shown in Figure A.5. The profiles correspond to the configuration at maximum reverse field in a hysteresis loop sweep, where the extent of the partial wall formed is greatest. Three different anisotropy constants are considered to give a range of domain wall widths. For $K_{\text{af}} = 0.085$ meV/spin, a thicker antiferromagnet film (30 ML) is used to accommodate the partial wall. Based on the profile derived in Chapter Two,

$$\varphi(x) = 2 \tan^{-1} \left[\exp \left(\frac{x - x_{\text{AF}}}{\lambda_{\text{AF}}} \right) \right], \quad (2.21)$$

the component of the staggered magnetization along the easy axis is

$$s'_z(x) = \cos[\varphi(x)] = \tanh \left[\frac{-x + x_{\text{AF}}}{\delta_{\text{af}}} \right], \quad (\text{A.6})$$

where the shift constant x_{AF} is determined by the angle of the interfacial spin and $\delta_{\text{af}} \equiv \sqrt{D_{\text{af}}/K_{\text{af}}}$ is the characteristic length of the antiferromagnet domain wall. The results in

Fig. A.5 show good agreement between the form predicted by Eq. A.6 and the numerical results for all three cases, where the only adjustable parameter used in the fits is x_{AF} .

Appendix B

Rapidly converging dipole sums

In this section, the forms of the dipole sums used in the spin wave calculations in Chapter Six are derived. This calculation follows the work of Benson and Mills [438].

Consider a simple cubic lattice with a classical spin \vec{S}_i at each lattice site i . The energy resulting from dipolar interactions between \vec{S}_i and all other spins in the lattice is

$$\mathcal{E}_d(i) = \frac{\mu_0(g\mu_B)^2}{4\pi} \sum_j \frac{1}{r_{ij}^3} [\vec{S}_i \cdot \vec{S}_j - 3(\vec{S}_i \cdot \hat{r}_{ij})(\vec{S}_j \cdot \hat{r}_{ij})], \quad (\text{B.1})$$

where \vec{r}_{ij} represents the vector connecting sites i and j , and \hat{r}_{ij} is a unit vector. The effective field experienced by \vec{S}_i is

$$\vec{H}_{\text{eff,d}}(i) = -\frac{\mu_0(g\mu_B)^2}{4\pi} \sum_j \frac{1}{r_{ij}^3} [\vec{S}_j - 3(\vec{S}_j \cdot \hat{r}_{ij})\hat{r}_{ij}]. \quad (\text{B.2})$$

Let the lattice constant be denoted by a , such that $\vec{r}_{ij} = a(r_x, r_y, r_z)$. Using greek letters to represent the cartesian components (x, y, z) , the summation can be expressed as

$$H_{\text{eff,d}}^\alpha(i) = -\frac{\mu_0(g\mu_B)^2}{4\pi} \sum_\beta \sum_j \frac{1}{r_{ij}^3} \left[\delta_{\alpha\beta} - \frac{3r_\alpha r_\beta}{r_x^2 + r_y^2 + r_z^2} \right] S_j^\beta, \quad (\text{B.3})$$

where the summation over j represents a sum over all r_x, r_y and r_z , and $\delta_{\alpha\beta}$ is the Kronecker delta function. Next, translational invariance is assumed in the film plane (yz -plane),

$$\vec{S}(\vec{r}) = \vec{S}(x)e^{i(q_y r_y + q_z r_z)}. \quad (\text{B.4})$$

The dipole sums of interest involve contributions from other layers in the film, which take the form

$$d_{\alpha\beta}(q_y, q_z; r_x) = \sum'_{r_y, r_z} e^{iq_y r_y} e^{iq_z r_z} \left[\frac{\delta_{\alpha\beta}}{(r_x^2 + r_y^2 + r_z^2)^{3/2}} - \frac{3r_\alpha r_\beta}{(r_x^2 + r_y^2 + r_z^2)^{5/2}} \right]. \quad (\text{B.5})$$

The prime indicates that when $r_x = 0$, the term $r_y, r_z = 0$ is to be excluded. Thus, the dipolar field can be represented as

$$H_{\text{eff,d}}^\alpha(i) = -\frac{\mu_0(g\mu_B)^2}{4\pi} \sum_{r_x} d_{\alpha\beta} S^\beta(r_y), \quad (\text{B.6})$$

where the Einstein summation convention over repeated indices is used. It is convenient to express the dipolar sums in terms of the quantity

$$\mathfrak{D}(q_y, q_z; r_x) = \sum'_{r_y, r_z} \frac{e^{iq_y r_y} e^{iq_z r_z}}{(r_x^2 + r_y^2 + r_z^2)^{5/2}}. \quad (\text{B.7})$$

Thus,

$$d_{xx}(q_y, q_z; r_x) = \left(-\frac{\partial^2}{\partial q_y^2} - \frac{\partial^2}{\partial q_z^2} - 2r_x^2 \right) \mathfrak{D}(q_y, q_z; r_x), \quad (\text{B.8})$$

$$d_{yy}(q_y, q_z; r_x) = \left(-\frac{\partial^2}{\partial q_z^2} + 2\frac{\partial^2}{\partial q_y^2} + r_x^2 \right) \mathfrak{D}(q_y, q_z; r_x), \quad (\text{B.9})$$

$$d_{zz}(q_y, q_z; r_x) = \left(-\frac{\partial^2}{\partial q_y^2} + 2\frac{\partial^2}{\partial q_z^2} + r_x^2 \right) \mathfrak{D}(q_y, q_z; r_x), \quad (\text{B.10})$$

$$d_{xy}(q_y, q_z; r_x) = 3\imath r_x \frac{\partial}{\partial q_y} \mathfrak{D}(q_y, q_z; r_x), \quad (\text{B.11})$$

$$d_{xz}(q_y, q_z; r_x) = 3\imath r_x \frac{\partial}{\partial q_z} \mathfrak{D}(q_y, q_z; r_x), \quad (\text{B.12})$$

$$d_{yz}(q_y, q_z; r_x) = 3r_x \frac{\partial^2}{\partial q_y \partial q_z} \mathfrak{D}(q_y, q_z; r_x). \quad (\text{B.13})$$

Case $r_x \neq 0$

First, let's consider the case where $r_x \neq 0$. Using the identity

$$\frac{1}{\alpha^{5/2}} = \frac{4}{3\sqrt{\pi}} \int_0^\infty dt t^{3/2} e^{-\alpha t}, \quad (\text{B.14})$$

the quantity \mathfrak{D} may be written as

$$\mathfrak{D}(q_y, q_z; r_x) = \frac{4}{3\sqrt{\pi}} \int_0^\infty dt t^{3/2} e^{-r_x^2 t} \left[\sum_{r_y=-\infty}^\infty e^{-r_y^2 t} e^{iq_y r_y} \right] \left[\sum_{r_z=-\infty}^\infty e^{-r_z^2 t} e^{iq_z r_z} \right]. \quad (\text{B.15})$$

Next, a second identity

$$\sum_{r=-\infty}^{\infty} e^{-r^2 t} e^{iqr} = \sqrt{\frac{\pi}{t}} \sum_{n=-\infty}^{\infty} \exp \left[-\frac{1}{t} \left(\pi n + \frac{1}{2} q \right)^2 \right] \quad (\text{B.16})$$

is used to simplify \mathfrak{D} further,

$$\begin{aligned} \mathfrak{D}(q_y, q_z; r_x) = \frac{4\sqrt{\pi}}{3} \sum_{mn} \int_0^{\infty} dt t^{1/2} \exp[-r^2 t] \\ \times \exp \left\{ -\frac{1}{t} \left[\left(\pi m + \frac{1}{2} q_y \right)^2 + \left(\pi n + \frac{1}{2} q_z \right)^2 \right] \right\}. \end{aligned} \quad (\text{B.17})$$

The integral

$$\int_0^{\infty} dx x^{1/2} e^{-ax} e^{-b/x} = \frac{1 + 2\sqrt{ab}}{2a} \sqrt{\frac{\pi}{a}} e^{-2\sqrt{ab}} \quad (\text{B.18})$$

can be evaluated in closed form. With the definition

$$\gamma_{mn}(q_y, q_z) = \left[\left(\pi m + \frac{1}{2} q_y \right)^2 + \left(\pi n + \frac{1}{2} q_z \right)^2 \right]^{\frac{1}{2}}, \quad (\text{B.19})$$

the following simplification can be made,

$$\mathfrak{D}(q_y, q_z; r_x) = \frac{4\pi}{3} \sum_{mn} \frac{1}{2|r_x|^3} (1 + 2|r_x|\gamma_{mn}(q_y, q_z)) e^{-2|r_x|\gamma_{mn}(q_y, q_z)}. \quad (\text{B.20})$$

Following the notation of Nörtemann et al. [394], define

$$\psi_m = \frac{1}{2} q \sin \phi + m\pi, \quad (\text{B.21})$$

$$\psi_n = \frac{1}{2} q \cos \phi + n\pi, \quad (\text{B.22})$$

where ϕ is the angle of the wavevector q relative to the z axis. Hence

$$\gamma_{mn} = (\psi_m^2 + \psi_n^2)^{\frac{1}{2}}. \quad (\text{B.23})$$

With these results the dipolar sums can be evaluated explicitly,

$$d_{xx}(q, \phi; r_x) = -4\pi \sum_{mn} \sqrt{\psi_m^2 + \psi_n^2} \exp(-2|r_x| \sqrt{\psi_m^2 + \psi_n^2}), \quad (\text{B.24})$$

$$d_{yy}(q, \phi; r_x) = 4\pi \sum_{mn} \frac{\psi_m^2}{\sqrt{\psi_m^2 + \psi_n^2}} \exp(-2|r_x| \sqrt{\psi_m^2 + \psi_n^2}), \quad (\text{B.25})$$

$$d_{zz}(q, \phi; r_x) = 4\pi \sum_{mn} \frac{\psi_n^2}{\sqrt{\psi_m^2 + \psi_n^2}} \exp(-2|r_x| \sqrt{\psi_m^2 + \psi_n^2}), \quad (\text{B.26})$$

$$d_{xy}(q, \phi; r_x) = -4\pi \iota \operatorname{sgn}(r_x) \sum_{mn} \psi_m \exp(-2|r_x| \sqrt{\psi_m^2 + \psi_n^2}), \quad (\text{B.27})$$

$$d_{xz}(q, \phi; r_x) = -4\pi \iota \operatorname{sgn}(r_x) \sum_{mn} \psi_n \exp(-2|r_x| \sqrt{\psi_m^2 + \psi_n^2}), \quad (\text{B.28})$$

$$d_{yz}(q, \phi; r_x) = 4\pi \sum_{mn} \frac{\psi_m \psi_n}{\sqrt{\psi_m^2 + \psi_n^2}} \exp(-2|r_x| \sqrt{\psi_m^2 + \psi_n^2}). \quad (\text{B.29})$$

In essence, the summation over all lattice points in space is reduced to a sum in reciprocal space. The forms given in Eqs. B.24– B.29 converge much more rapidly, where the evaluation of the first few terms is usually sufficient.

Case $r_x = 0$

In a similar fashion, the dipole sums for $r_x = 0$ can be evaluated to give rapidly convergent forms. To begin, one can immediately recognize that for $\alpha \neq \beta$ the sums $d_{\alpha\beta}(q_y, q_z; 0)$ are odd functions in r_y and r_z , so they vanish identically. Using the definition

$$\mathfrak{D}_{y,z}(q_y, q_z) = \sum'_{r_y, r_z} \frac{r_{y,z}^2}{(r_y^2 + r_z^2)^{\frac{5}{2}}} e^{\iota q_y r_y} e^{\iota q_z r_z}. \quad (\text{B.30})$$

the dipole sums can be rewritten as

$$d_{xx}(q_y, q_z; 0) = \mathfrak{D}_y(q_y, q_z) + \mathfrak{D}_z(q_y, q_z), \quad (\text{B.31})$$

$$d_{yy}(q_y, q_z; 0) = -2\mathfrak{D}_y(q_y, q_z) + \mathfrak{D}_z(q_y, q_z), \quad (\text{B.32})$$

$$d_{zz}(q_y, q_z; 0) = -2\mathfrak{D}_z(q_y, q_z) + \mathfrak{D}_y(q_y, q_z). \quad (\text{B.33})$$

Proceeding as before, the summation over the position variables can be replaced by an integral involving the wavevector components,

$$\mathfrak{D}_z(q_y, q_z) = \frac{4}{3\sqrt{\pi}} \sum'_{r_y} \sum'_{r_z} r_z^2 e^{i q_y r_y} e^{i q_z r_z} \int_0^\infty dt t^{3/2} e^{-(r_y^2 + r_z^2)t}, \quad (\text{B.34})$$

$$= \frac{4}{3} \sum'_{r_z} \sum'_n r_z^2 e^{i q_z r_z} \int_0^\infty dt t \exp[-r_z^2 t] \exp\left[-\frac{1}{t} \left(n\pi + \frac{1}{2} q_y\right)^2\right], \quad (\text{B.35})$$

with a similar expression for $\mathfrak{D}_y(q_y, q_z)$. Now,

$$\sum'_{r_z} e^{i q_z r_z} = \frac{1}{2} \sum'_{r_z} (\cos q_z r_z + i \sin q_z r_z). \quad (\text{B.36})$$

Since $\sin x$ is an odd function in x , the sum over r_z of $\sin q_z r_z$ vanishes, which gives

$$\mathfrak{D}_z(q_y, q_z) = -\frac{4}{3} \sum'_{r_z} \sum'_n \cos(q_z r_z) r_z \frac{\partial}{\partial r_z} \int_0^\infty dt t \exp[-r_z^2 t] \exp\left[-\frac{1}{t} \left(n\pi + \frac{1}{2} q_y\right)^2\right]. \quad (\text{B.37})$$

The following identity is useful,

$$\int_0^\infty dt e^{-bt} e^{-a/t} = 2\sqrt{\frac{a}{b}} K_1(2\sqrt{ab}), \quad (\text{B.38})$$

to reduce $\mathfrak{D}_z(q_y, q_z)$ to the form

$$\mathfrak{D}_z(q_y, q_z) = \frac{16}{3} \sum_{m=1}^\infty \sum_{n=-\infty}^\infty \cos(mq_z) \left(n\pi + \frac{1}{2} q_y\right)^2 K_2(2m|n\pi + \frac{1}{2} q_y|), \quad (\text{B.39})$$

where K_n represents the modified Bessel's function of order n . Similarly,

$$\mathfrak{D}_y(q_y, q_z) = \frac{16}{3} \sum_{m=1}^\infty \sum_{n=-\infty}^\infty \cos(mq_y) \left(n\pi + \frac{1}{2} q_z\right)^2 K_2(2m|n\pi + \frac{1}{2} q_z|). \quad (\text{B.40})$$

Using ϕ to represent the orientation of the wavevector q as before, the dipole sums can be expressed as

$$d_{xx}(q, \phi; 0) = \frac{16}{3} \sum_{m=1}^{\infty} \sum_{n=-\infty}^{\infty} \left\{ \cos(mq \cos \phi) \left[n\pi + \frac{1}{2}q \sin \phi \right]^2 K_2(2m|n\pi + \frac{1}{2}q \sin \phi|) \right. \\ \left. + \cos(mq \sin \phi) \left[n\pi + \frac{1}{2}q \cos \phi \right]^2 K_2(2m|n\pi + \frac{1}{2}q \cos \phi|) \right\}, \quad (\text{B.41})$$

$$d_{yy}(q, \phi; 0) = \frac{16}{3} \sum_{m=1}^{\infty} \sum_{n=-\infty}^{\infty} \left\{ \cos(mq \cos \phi) \left[n\pi + \frac{1}{2}q \sin \phi \right]^2 K_2(2m|n\pi + \frac{1}{2}q \sin \phi|) \right. \\ \left. - 2 \cos(mq \sin \phi) \left[n\pi + \frac{1}{2}q \cos \phi \right]^2 K_2(2m|n\pi + \frac{1}{2}q \cos \phi|) \right\}, \quad (\text{B.42})$$

$$d_{zz}(q, \phi; 0) = \frac{16}{3} \sum_{m=1}^{\infty} \sum_{n=-\infty}^{\infty} \left\{ \cos(mq \sin \phi) \left[n\pi + \frac{1}{2}q \cos \phi \right]^2 K_2(2m|n\pi + \frac{1}{2}q \cos \phi|) \right. \\ \left. - 2 \cos(mq \cos \phi) \left[n\pi + \frac{1}{2}q \sin \phi \right]^2 K_2(2m|n\pi + \frac{1}{2}q \sin \phi|) \right\}. \quad (\text{B.43})$$

Appendix C

Construction of dynamical matrix

As discussed in Chapter Six, the linear excitations in the bilayer can be found by separating the spin variables into a static $[\vec{S}(\vec{r})]$ and a dynamic part $[\vec{s}(\vec{r}, t)]$. The dynamics for each spin, neglecting dissipation, is governed by

$$\frac{1}{\gamma} \frac{\partial \vec{s}_i(t)}{\partial t} = \vec{s}_i(t) \times \vec{H}_i^{\text{eff}} + \vec{S}_i \times \vec{h}_i^{\text{eff}}(t), \quad (\text{C.1})$$

where the effective fields consists of contributions from the Zeeman, exchange, anisotropy and dipolar interactions,

$$\vec{H}_i^{\text{eff}} = \vec{H}_a + \sum_j J_{ij} \vec{S}_j + K_i (\vec{S}_i \cdot \hat{z}) \hat{z} + \vec{H}_d \quad (\text{C.2})$$

$$\vec{h}_i^{\text{eff}}(t) = \sum_j J_{ij} \vec{s}_j(t) + K_i (\vec{s}_i(t) \cdot \hat{z}) \hat{z} + \vec{h}_d(\vec{q}, t) \quad (\text{C.3})$$

Terms second order in $\vec{s}(\vec{r}, t)$ are neglected and translational invariance in the plane of the film within each layer is assumed. The spin vector for each layer is indexed by the layer number n ,

$$\vec{S}(\vec{r}) = \vec{S}_n. \quad (\text{C.4})$$

and plane wave solutions for the excitations are assumed,

$$\vec{s}(\vec{r}, t) = \vec{s}_n e^{i(\vec{q} \cdot \vec{r} - \omega t)}. \quad (\text{C.5})$$

The resulting linearized equations of motion can be written as

$$\begin{aligned}
-\frac{i\omega}{\gamma}\vec{s}_n &= \vec{s}_n \times [g\mu_B(\vec{H}_a + \vec{H}^d) + 4J_{n,n}\vec{S}_n + J_{n,n-1}\vec{S}_{n-1} + J_{n,n+1}\vec{S}_{n+1} + K_n S_{nz}\vec{z}] \\
+ \vec{S}_n \times [g\mu_B \vec{h}^d(\vec{q}) + 2J_{n,n}\vec{s}_n[\cos(q_y a) + \cos(q_z a)] + J_{n,n-1}\vec{s}_{n-1} + J_{n,n+1}\vec{s}_{n+1} + K_n s_{nz}\vec{z}],
\end{aligned} \tag{C.6}$$

where $J_{n,n'}$ denotes the exchange coupling between layers n and n' , and K_n is the anisotropy constant for layer n . At equilibrium the moments in all layers are oriented in the film plane (yz -plane), so all static S_n^x components vanish,

$$\vec{S}_n = (0, S_n^y, S_n^z), \tag{C.7}$$

$$\vec{s}_n(t) = (s_n^x, s_n^y, s_n^z), \tag{C.8}$$

$$\vec{H}_a = (0, H_a^y, H_a^z). \tag{C.9}$$

Next, the equations of motion are evaluated to give

$$\begin{aligned}
-\frac{i\omega}{\gamma}s_n^x &= (g\mu_B h_d^z + J_{n,n-1}s_{n-1}^z + J_{n,n+1}s_{n+1}^z)S_n^y \\
&+ (g\mu_B h_d^y + J_{n,n-1}s_{n-1}^y + J_{n,n+1}s_{n+1}^y)S_n^z - m_{13}s_n^z + m_{12}s_n^y,
\end{aligned} \tag{C.10}$$

$$-\frac{i\omega}{\gamma}s_n^y = (g\mu_B h_d^x + J_{n,n-1}s_{n-1}^x + J_{n,n+1}s_{n+1}^x)S_n^z + m_{21}s_n^x, \tag{C.11}$$

$$-\frac{i\omega}{\gamma}s_n^z = (g\mu_B h_d^x + J_{n,n-1}s_{n-1}^x + J_{n,n+1}s_{n+1}^x)S_n^y - m_{31}s_n^x, \tag{C.12}$$

where, for convenience, the following quantities are defined,

$$\begin{aligned}
m_{12} &= g\mu_B(H_a^z + H_{d,n}^z) + J_{n,n-1}S_{n-1}^z + J_{n,n+1}S_{n+1}^z \\
&+ [4J_n - 2J_n(\cos q_y a + \cos q_z a) + K_n]S_n^z,
\end{aligned} \tag{C.13}$$

$$\begin{aligned}
m_{13} &= g\mu_B(H_a^y + H_{d,n}^y) + J_{n,n-1}S_{n-1}^y + J_{n,n+1}S_{n+1}^y \\
&+ [4J_n - 2J_n(\cos q_y a + \cos q_z a) - K_n]S_n^y,
\end{aligned} \tag{C.14}$$

$$m_{21} = -m_{12}, \tag{C.15}$$

$$\begin{aligned}
m_{13} &= g\mu_B(H_a^y + H_{d,n}^y) + J_{n,n-1}S_{n-1}^y + J_{n,n+1}S_{n+1}^y \\
&+ [4J_n - 2J_n(\cos q_y a + \cos q_z a)]S_n^y.
\end{aligned} \tag{C.16}$$

The dipolar fields involve sums over all spins. The static component can be evaluated once the equilibrium configuration is known,

$$H_{d,n}^\alpha = g\mu_B \sum_{n'} d_{\alpha\beta}(0; n - n') S_{n'}^\beta. \quad (\text{C.17})$$

The components of the dipolar matrix $d_{\alpha\beta}$ are derived in the previous section. The dynamic component of the dipolar field depends on all the other fluctuating spin components in the system,

$$h_{d,n}^\alpha = g\mu_B \sum_{n'} d_{\alpha\beta}(\vec{q}; n - n') s_{n'}^\beta. \quad (\text{C.18})$$

The dynamical matrix representing the equations of motion for N spins can be expressed in the following compact form,

$$\left[\mathbf{M} - \frac{i\omega}{\gamma} \mathbf{I} \right] \begin{bmatrix} \vec{s}_1 \\ \vec{s}_2 \\ \vdots \\ \vec{s}_N \end{bmatrix} = \mathbf{0}, \quad (\text{C.19})$$

where \mathbf{I} is the identity matrix and the dynamical matrix \mathbf{M} ,

$$\mathbf{M} = \begin{pmatrix} \mathbf{m}_1 + \mathbf{g}_{1,1} & \mathbf{l}_{1,2} + \mathbf{g}_{1,2} & \mathbf{g}_{1,3} & \cdots & \cdots & \mathbf{g}_{1,N} \\ \mathbf{l}_{2,1} + \mathbf{g}_{2,1} & \mathbf{m}_2 + \mathbf{g}_{2,2} & \mathbf{l}_{2,3} + \mathbf{g}_{2,3} & \mathbf{g}_{2,4} & & \vdots \\ \mathbf{g}_{3,1} & \mathbf{l}_{3,2} + \mathbf{g}_{3,2} & \mathbf{m}_3 + \mathbf{g}_{3,3} & \mathbf{l}_{3,4} + \mathbf{g}_{3,4} & \mathbf{g}_{3,5} & \vdots \\ \vdots & & \ddots & & & \vdots \\ \vdots & & & \ddots & & \vdots \\ \mathbf{g}_{N,1} & \cdots & \cdots & \mathbf{g}_{N,N-2} & \mathbf{l}_{N,N-1} + \mathbf{g}_{N,N-1} & \mathbf{m}_N + \mathbf{g}_{N,N} \end{pmatrix}, \quad (\text{C.20})$$

is constructed from a set of 3×3 matrices, \mathbf{m}_n , $\mathbf{l}_{n,n'}$ and $\mathbf{g}_{n,n'}$, which represent the interactions between successive layers,

$$\mathbf{m}_n = \begin{pmatrix} 0 & m_{12} & m_{13} \\ m_{21} & 0 & 0 \\ m_{13} & 0 & 0 \end{pmatrix}, \quad (\text{C.21})$$

$$\mathbf{l}_{n,n'} = \begin{pmatrix} 0 & -J_{n,n'} S_n^z & J_{n,n'} S_n^y \\ J_{n,n'} S_n^z & 0 & 0 \\ -J_{n,n'} S_n^y & 0 & 0 \end{pmatrix}, \quad (\text{C.22})$$

$$\mathbf{g}_{n,n'} = \begin{pmatrix} d_{yx}S_n^z + d_{zx}S_n^y & d_{yy}S_n^z + d_{zy}S_n^y & d_{yz}S_n^z + d_{zz}S_n^y \\ d_{yx}S_n^z & d_{yy}S_n^z & d_{yz}S_n^z \\ -d_{zx}S_n^y & -d_{zy}S_n^y & -d_{zz}S_n^y \end{pmatrix}, \quad (\text{C.23})$$

where it is understood in the last equation that $d_{\alpha\beta} = d_{\alpha\beta}(\vec{q}; n - n')$.

Appendix D

Derivation of antiferromagnet critical fields

Derivation of spin-flop field H_{sf} (h_1)

Consider the two configurations of the antiferromagnet shown in Figure D.1. For fields less than the spin-flop field, the antiferromagnet spins are aligned along the easy axis and antiparallel to each other. The energy of this configuration is

$$\mathcal{E}_1 = -|J_{\text{af}}|. \quad (\text{D.1})$$

Above the spin-flop field the antiferromagnet is in a canted state (Fig. D.1b), with an energy

$$\mathcal{E}_2 = |J_{\text{af}}| \cos(2\theta) + K_{\text{af}} \sin^2(\theta) - g\mu_B H_a \cos(\theta). \quad (\text{D.2})$$

The equilibrium angle between the two sublattice spins is found by minimizing this energy with respect to θ ,

$$[g\mu_B H_a - 2(2|J_{\text{af}}| - K_{\text{af}}) \cos(\theta)] \sin(\theta) = 0, \quad (\text{D.3})$$

which yields the solutions

$$\theta = 0, \pi, \cos^{-1} \left[\frac{g\mu_B H_a}{2(2|J_{\text{af}}| - K_{\text{af}})} \right]. \quad (\text{D.4})$$

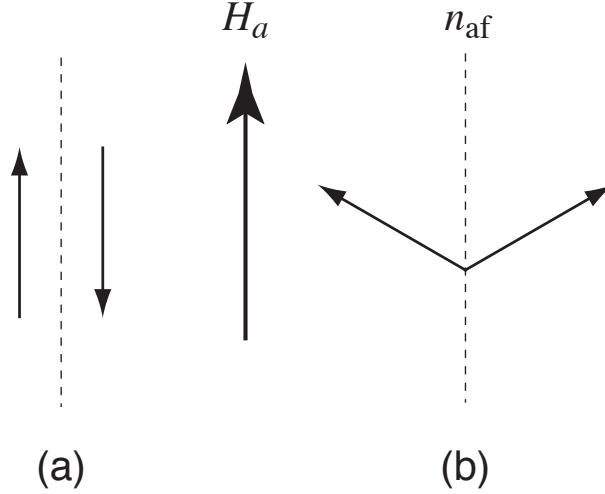


Figure D.1: Antiferromagnetic spin-flop transition. (a) For $H_a < H_{sf}$ the antiferromagnet spins are aligned antiparallel along the anisotropy axis. (b) For $H_a > H_{sf}$ a spin-flop transition occurs, where the spins cant towards the applied field H_a . n_{af} represents the easy axis.

For $H_a > 0$ the solution $\theta = \pi$ represents the global maximum, since

$$\left. \frac{\partial^2 \mathcal{E}_2}{\partial \theta^2} \right|_{\theta=0} = -g\mu_B H_a - 4|J_{af}| - 2K_{af}. \quad (\text{D.5})$$

The solution $\theta = 0$ represents the saturated state and is a local maximum for $g\mu_B H_a - 4|J_{af}| + 2K_{af} < 0$. The canted state is represented by the third solution, which upon substitution into the expression for \mathcal{E}_2 gives

$$\mathcal{E}_2 = -\frac{(g\mu_B H_a)^2}{4(2|J_{af}| - K_{af})} - |J_{af}| + K_{af}. \quad (\text{D.6})$$

At the spin-flop transition the energies of the two configurations are equal, so the spin-flop field can be found by equating \mathcal{E}_1 and \mathcal{E}_2 ,

$$H_{sf} = \frac{2}{g\mu_B} \sqrt{2|J_{af}| K_{af} - K_{af}^2}. \quad (\text{D.7})$$

The critical field h_1 discussed in Chapter Six differs from H_{sf} by a multiplicative factor,

$$h_1 = \frac{g\mu_B H_{sf}}{4|J_{af}|}. \quad (\text{D.8})$$

Derivation of critical fields h_2 and h_3

The second critical field h_2 represents the point at which the sublattice spins are oriented perpendicular to each other ($\theta = \pi/4$). This can be evaluated from the third

solution of Eq. D.4,

$$h_2 = \frac{1}{\sqrt{2}} \left(1 - \frac{K_{\text{af}}}{2|J_{\text{af}}|} \right). \quad (\text{D.9})$$

The third critical field is the saturation field of the antiferromagnet. Again, this can be evaluated from the third solution of Eq. D.4 with $\theta = 0$,

$$h_3 = 1 - \frac{K_{\text{af}}}{2|J_{\text{af}}|}. \quad (\text{D.10})$$

References

- [1] G. A. Prinz, “Spin polarized transport”, *Phys. Today* **48**, 58 (1995).
- [2] P. Grünberg, “Layered magnetic structures: facts, figures, future”, *J. Phys.: Condens. Matter* **13**, 7691 (2001).
- [3] B. Dieny, V. S. Speriosu, S. S. P. Parkin, B. A. Gurney, D. R. Wilhoit, and D. Mauri, “Giant magnetoresistance in soft ferromagnetic multilayers”, *Phys. Rev. B* **43**, 1297 (1991).
- [4] B. Dieny, “Giant magnetoresistance in spin-valve multilayers”, *J. Magn. Magn. Mater.* **136**, 335 (1994).
- [5] R. D. McMichael, W. F. Egelhoff, Jr., and L. H. Bennett, “Thermal Degradation of Exchange Biased Films in Spin-Valves”, *IEEE Trans. Magn.* **31**, 3930 (1995).
- [6] C. Cowache, B. Dieny, S. Auffret, M. Cartier, R. H. Taylor, R. O’Barr, and S. Y. Yamamoto, “Spin-valve structures with NiO pinning layers”, *IEEE Trans. Magn.* **34**, 843 (1998).
- [7] R. H. Taylor, R. O’Barr, S. Y. Yamamoto, and B. Dieny, “Thermal relaxation of the pinned layer magnetization in NiO spin valves”, *J. Appl. Phys.* **85**, 5036 (1999).
- [8] C. H. Marrows, F. E. Stanley, and B. J. Hickey, “Canted exchange bias in antiparallel biased spin valves”, *J. Appl. Phys.* **87**, 5058 (2000).
- [9] W. H. Meiklejohn and C. P. Bean, “New Magnetic Anisotropy (Letter)”, *Phys. Rev.* **102**, 1413 (1956).
- [10] W. H. Meiklejohn and C. P. Bean, “New Magnetic Anisotropy”, *Phys. Rev.* **105**, 904 (1957).
- [11] J. Nogués and I. K. Schuller, “Exchange bias”, *J. Magn. Magn. Mater.* **192**, 203 (1999).
- [12] A. E. Berkowitz and K. Takano, “Exchange anisotropy - a review”, *J. Magn. Magn. Mater.* **200**, 552 (1999).
- [13] R. L. Stamps, “Mechanisms for exchange bias”, *J. Phys. D: Appl. Phys.* **33**, R247 (2000).
- [14] M. Kiwi, “Exchange bias theory”, *J. Magn. Magn. Mater.* **234**, 584 (2001).
- [15] I. S. Jacobs and J. S. Kouvel, “Exchange Anisotropy in Mixed Manganites with the Hausmannite Structure”, *Phys. Rev.* **122**, 412 (1961).
- [16] W. H. Meiklejohn, “Exchange Anisotropy – A Review”, *J. Appl. Phys.* **33**, 1328 (1962).

- [17] A. E. Berkowitz and J. H. Greiner, "Exchange Anisotropy and Strain Interactions in the Ni-NiO System", *J. Appl. Phys.* **36**, 3330 (1965).
- [18] D. Paccard, C. Schlenker, O. Massenet, R. Montmory, and A. Yelon, "A New Property of Ferromagnetic-Antiferromagnetic Coupling", *Phys. Status Solidi* **16**, 301 (1966).
- [19] C. Schlenker and D. Paccard, "Couplages ferromagnétiques-antiferromagnétiques : Étude des contractions de cycles d'hystérésis à l'aide d'un traceur de cycle très basses fréquences", *J. Phys. (Paris)* **28**, 611 (1967).
- [20] C. Schlenker, "Couplage ferro-antiferromagnétique et traînage magnétique dans des couches minces multiples Co-CoO et Ni-NiO", *Phys. Status Solidi* **28**, 507 (1968).
- [21] E. Fulcomer and S. H. Charap, "Temperature and frequency dependence of exchange anisotropy effects in oxidized NiFe films", *J. Appl. Phys.* **43**, 4184 (1972).
- [22] C. Tsang, N. Heiman, and K. Lee, "Exchange induced unidirectional anisotropy at FeMn-Ni₈₀Fe₂₀ interfaces", *J. Appl. Phys.* **52**, 2471 (1981).
- [23] C. Tsang and K. Lee, "Temperature dependence of unidirectional anisotropy effects in the Permalloy-FeMn systems", *J. Appl. Phys.* **53**, 2605 (1982).
- [24] J. C. Scott, "Ferromagnetic resonance studies in the bilayer system Ni_{0.80}Fe_{0.20}/Mn_{0.50}Fe_{0.50}: Exchange anisotropy", *J. Appl. Phys.* **57**, 3681 (1985).
- [25] C. Schlenker, S. S. P. Parkin, J. C. Scott, and K. Howard, "Magnetic disorder in the exchange bias bilayered FeNi-FeMn system", *J. Magn. Magn. Mater.* **54-57**, 801 (1986).
- [26] D. Mauri, E. Kay, D. Scholl, and J. K. Howard, "Novel method for determining the anisotropy constant of MnFe in a NiFe/MnFe sandwich", *J. Appl. Phys.* **62**, 2929 (1987).
- [27] V. S. Speriosu, S. S. P. Parkin, and C. H. Wilts, "Standing spinwaves in FeMn/NiFe/FeMn exchange-bias structures", *IEEE Trans. Magn.* **23**, 2999 (1987).
- [28] G. L. Bona, F. Meier, H. C. Siegmann, and R. J. Gambino, "Unidirectional anisotropy in surface magnetism of amorphous GdCo", *Appl. Phys. Lett.* **52**, 166 (1988).
- [29] W. Stoecklein, S. S. P. Parkin, and J. C. Scott, "Ferromagnetic resonance studies of exchange-biased Permalloy thin films", *Phys. Rev. B* **38**, 6847 (1988).
- [30] L. Smardz, U. Köbler, and W. Zinn, "Oxidation kinetics of thin and ultrathin cobalt films", *J. Appl. Phys.* **71**, 5199 (1992).
- [31] M. J. Carey and A. E. Berkowitz, "Exchange anisotropy in coupled films of Ni₈₁Fe₁₉ with NiO and Co_xNi_{1-x}O", *Appl. Phys. Lett.* **60**, 3060 (1992).
- [32] O. Allegranza and M.-M. Chen, "Effect of substrate and antiferromagnetic film's thickness on exchange-bias field", *J. Appl. Phys.* **73**, 6218 (1993).
- [33] M. J. Carey and A. E. Berkowitz, "CoO-NiO superlattices: Interlayer interactions and exchange anisotropy with Ni₁₈Fe₁₉ (invited)", *J. Appl. Phys.* **73**, 6892 (1993).

- [34] R. Jungblut, R. Coehoorn, M. T. Johnson, J. aan de Stegge, and A. Reinders, “Orientational dependence of the exchange biasing in molecular-beam-epitaxy-grown $\text{Ni}_{80}\text{Fe}_{20}/\text{Fe}_{50}\text{Mn}_{50}$ bilayers (invited)”, *J. Appl. Phys.* **75**, 6659 (1994).
- [35] X. Lin, G. C. Hadjipanayis, and S. I. Shah, “Magnetic and structural properties of Co/CoO bilayers”, *J. Appl. Phys.* **75**, 6676 (1994).
- [36] T. Ambrose and C. L. Chien, “Magnetic properties of exchange coupled NiFe/CoO/NiFe trilayers”, *Appl. Phys. Lett.* **65**, 1967 (1994).
- [37] T. J. Moran, J. M. Gallego, and I. K. Schuller, “Increased exchange anisotropy due to disorder at permalloy/CoO interfaces”, *J. Appl. Phys.* **78**, 1887 (1995).
- [38] R. Jungblut, R. Coehoorn, M. T. Johnson, C. Sauer, P. J. van der Zaag, A. R. Ball, T. G. S. M. Rijks, J. aan de Stegge, and A. Reinders, “Exchange biasing in MBE-grown $\text{Ni}_{80}\text{Fe}_{20}/\text{Fe}_{50}\text{Mn}_{50}$ bilayers”, *J. Magn. Magn. Mater.* **148**, 300 (1995).
- [39] P. J. van der Zaag, R. M. Wolf, A. R. Ball, C. Bordel, L. F. Feiner, and R. Jungblut, “A study of the magnitude of exchange biasing in [111] $\text{Fe}_3\text{O}_4/\text{CoO}$ bilayers”, *J. Magn. Magn. Mater.* **148**, 346 (1995).
- [40] A. J. Devasahayam and M. H. Kryder, “The Effect of Sputtering Conditions on the Exchange Fields of $\text{Co}_x\text{Ni}_{1-x}\text{O}$ and NiFe”, *IEEE Trans. Magn.* **31**, 3820 (1995).
- [41] T. Ambrose and C. L. Chien, “Finite-Size Effects and Uncompensated Magnetization in Thin Antiferromagnetic CoO Layers”, *Phys. Rev. Lett.* **76**, 1743 (1996).
- [42] H. Fujiwara, K. Nishioka, C. Hou, M. R. Parker, S. Gangopadhyay, and R. Metzger, “Temperature dependence of the pinning field and coercivity of NiFe layers coupled with an antiferromagnetic FeMn layer”, *J. Appl. Phys.* **79**, 6286 (1996).
- [43] J. Nogués, D. Lederman, T. J. Moran, I. K. Schuller, and K. V. Rao, “Large exchange bias and its connection to interface structure in FeF_2 -Fe bilayers”, *Appl. Phys. Lett.* **68**, 3186 (1996).
- [44] J. Nogués, D. Lederman, T. J. Moran, and I. K. Schuller, “Positive Exchange Bias in FeF_2 -Fe Bilayers”, *Phys. Rev. Lett.* **76**, 4624 (1996).
- [45] K. Nishioka, C. Hou, H. Fujiwara, and R. D. Metzger, “Grain size effect on ferromagnetic coupling of NiFe/FeMn systems”, *J. Appl. Phys.* **80**, 4528 (1996).
- [46] R. F. C. Farrow, R. F. Marks, S. Gider, A. C. Marley, and S. S. P. Parkin, “ $\text{Mn}_x\text{Pt}_{1-x}$: A new exchange anisotropy bias material for Permalloy”, *J. Appl. Phys.* **81**, 4986 (1997).
- [47] D.-H. Han, J.-G. Zhu, and J. H. Judy, “NiFe/NiO bilayers with high exchange coupling and low coercive fields”, *J. Appl. Phys.* **81**, 4996 (1997).
- [48] V. Ström, B. J. Jönsson, K. V. Rao, and D. Dahlberg, “Determination of exchange anisotropy by means of ac susceptibility in Co/CoO bilayers”, *J. Appl. Phys.* **81**, 5003 (1997).
- [49] H. W. Zhao, M. Lu, Y. X. Sui, H. R. Zhai, D. Feng, Y. Chen, G. S. Dong, and X. F. Jin, “A mechanism of the exchange anisotropy in $\text{Co}_{1-x}\text{Mn}_x/\text{Mn}$ bilayers: Interfacial influences”, *Appl. Phys. Lett.* **70**, 2906 (1997).
- [50] T. Ambrose, R. L. Sommer, and C. L. Chien, “Angular dependence of exchange coupling in ferromagnet/antiferromagnet bilayers”, *Phys. Rev. B* **56**, 83 (1997).

- [51] D. Lederman, J. Nogués, and I. K. Schuller, “Exchange anisotropy and the antiferromagnetic surface order parameter”, *Phys. Rev. B* **56**, 2332 (1997).
- [52] K. Takano, R. H. Kodama, A. E. Berkowitz, W. Cao, and G. Thomas, “Interfacial Uncompensated Antiferromagnetic Spins: Role in Unidirectional Anisotropy in Polycrystalline Ni₈₁Fe₁₉/CoO Bilayers”, *Phys. Rev. Lett.* **79**, 1130 (1997).
- [53] H. Uyama, Y. Otani, K. Fukamichi, O. Kitakami, Y. Shimada, and J. ichi Echigoya, “Effect of antiferromagnet grain size on exchange-coupling field of Cr₇₀Al₃₀/Fe₁₉Ni₈₁”, *Appl. Phys. Lett.* **71**, 1258 (1997).
- [54] N. J. Gökemeijer, T. Ambrose, and C. L. Chien, “Long-Range Exchange Bias across a Spacer Layer”, *Phys. Rev. Lett.* **79**, 4270 (1997).
- [55] Y. Ijiri, J. A. Borchers, R. W. Erwin, S.-H. Lee, P. J. van der Zaag, and R. M. Wolf, “Perpendicular Coupling in Exchange Biased Fe₃O₄/CoO Superlattices”, *Phys. Rev. Lett.* **80**, 608 (1998).
- [56] P. A. A. van der Heijden, T. F. M. M. Maas, W. J. M. de Jonge, J. C. S. Kools, F. Roozeboom, and P. J. van der Zaag, “Thermally assisted reversal of exchange biasing in NiO and FeMn based systems”, *Appl. Phys. Lett.* **72**, 492 (1998).
- [57] T. J. Moran, J. Nogués, D. Lederman, and I. K. Schuller, “Perpendicular coupling at Fe-FeF₂ interfaces”, *Appl. Phys. Lett.* **72**, 617 (1998).
- [58] C. Mathieu, M. Bauer, B. Hillebrands, J. Fassbender, G. Güntherodt, R. Jungblut, J. Kohlhepp, and A. Reinders, “Brillouin light scattering investigations of exchange biased (110)-oriented NiFe/FeMn bilayers”, *J. Appl. Phys.* **83**, 2863 (1998).
- [59] V. I. Nikitenko, V. S. Gornakov, L. M. Dedukh, Y. P. Kabanov, A. F. Khapikov, A. J. Shapiro, R. D. Shull, A. Chaiken, and R. P. Michel, “Asymmetry of domain nucleation and enhanced coercivity in exchange-biased epitaxial NiO/NiFe bilayers”, *Phys. Rev. B* **57**, R8111 (1998).
- [60] D. G. Hwang, S. S. Lee, and C. M. Park, “Effect of roughness slope on exchange biasing in NiO spin valves”, *Appl. Phys. Lett.* **72**, 2162 (1998).
- [61] X. W. Wu, T. Ambrose, and C. L. Chien, “Exchange bias and spin-valve structures using amorphous ferromagnetic Co₆₅Mo₂B₃₃ layers”, *Appl. Phys. Lett.* **72**, 2176 (1998).
- [62] K. M. Krishnan, C. Nelson, C. J. Echer, R. F. C. Farrow, R. F. Marks, and A. J. Kellock, “Exchange biasing of permalloy films by Mn_xPt_{1-x}: role of composition and microstructure”, *J. Appl. Phys.* **83**, 6810 (1998).
- [63] T. Ambrose and C. L. Chien, “Dependence of exchange coupling on antiferromagnetic layer thickness in NiFe/CoO”, *J. Appl. Phys.* **83**, 6822 (1998).
- [64] P. A. A. van der Heijden, T. F. M. M. Maas, J. C. S. Kools, F. Roozeboom, P. J. van der Zaag, and W. J. M. de Jonge, “Influences on relaxation of exchange biasing in NiO/Ni₆₆Co₁₈Fe₁₆ bilayers”, *J. Appl. Phys.* **83**, 7207 (1998).
- [65] A. J. Devasahayam, P. J. Sides, and M. H. Kryder, “Magnetic, temperature, and corrosion properties of the NiFe/IrMn exchange couple”, *J. Appl. Phys.* **83**, 7216 (1998).
- [66] T. Ambrose and C. L. Chien, “Dependence of exchange field and coercivity on cooling field in NiFe/CoO bilayers”, *J. Appl. Phys.* **83**, 7222 (1998).

- [67] E. J. Escorcia-Aparicio, H. J. Choi, W. L. Ling, R. K. Kawakami, and Z. Q. Qiu, “90° Magnetization Switching in Thin Fe Films Grown on Stepped Cr(001)”, *Phys. Rev. Lett.* **81**, 2144 (1998).
- [68] X. W. Wu and C. L. Chien, “Exchange Coupling in Ferromagnet/Antiferromagnet Bilayers with Comparable T_C and T_N ”, *Phys. Rev. Lett.* **81**, 2795 (1998).
- [69] R. P. Michel, A. Chaiken, C. T. Wang, and L. E. Johnson, “Exchange anisotropy in epitaxial and polycrystalline NiO/NiFe bilayers”, *Phys. Rev. B* **58**, 8566 (1998).
- [70] C. A. Kleint, M. K. Krause, R. Höhne, T. Walter, H. C. Semmelhack, M. Lorenz, and P. Esquinazi, “Exchange anisotropy in epitaxial $\text{Fe}_3\text{O}_4/\text{CoO}$ and $\text{Fe}_3\text{O}_4/\text{Co}_x\text{Fe}_{3-x}\text{O}_4$ ”, *J. Appl. Phys.* **84**, 5097 (1998).
- [71] G. Ju, A. V. Nurmikko, R. F. C. Farrow, R. F. Marks, M. J. Carey, and B. A. Gurney, “Ultrafast optical modulation of an exchange biased ferromagnetic/antiferromagnetic bilayer”, *Phys. Rev. B* **58**, R11857 (1998).
- [72] D. V. Dimitrov, S. Zhang, J. Q. Xiao, G. C. Hadjipanayis, and C. Prados, “Effect of exchange interactions at antiferromagnetic/ferromagnetic interfaces”, *Phys. Rev. B* **58**, 12090 (1998).
- [73] S. M. Zhou, K. Liu, and C. L. Chien, “Exchange coupling and macroscopic domain structure in a wedged permalloy/FeMn bilayer”, *Phys. Rev. B* **58**, R14717 (1998).
- [74] D. G. Hwang, C. M. Park, and S. S. Lee, “Exchange biasing in NiO spin valves”, *J. Magn. Magn. Mater.* **186**, 265 (1998).
- [75] G. van der Laan and H. A. Dürr, “Magnetic anisotropy and exchange biasing in heterojunctions studied by transverse magnetic circular X-ray dichroism”, *Physica B* **248**, 121 (1998).
- [76] C. Mocuta, A. Barbier, G. Renaud, and B. Dieny, “Growth and magnetism of Co/NiO(111) thin films”, *Thin Solid Films* **336**, 160 (1998).
- [77] P. Miltényi, M. Gruyters, G. Güntherodt, J. Nogués, and I. K. Schuller, “Spin waves in exchange-biased Fe/FeF₂”, *Phys. Rev. B* **59**, 3333 (1999).
- [78] J. J. Freijo, A. Hernando, M. Vázquez, A. Méndez, and V. R. Ramanan, “Exchange biasing in ferromagnetic amorphous wires: A controllable micromagnetic configuration”, *Appl. Phys. Lett.* **74**, 1305 (1999).
- [79] D. Martien, K. Takano, A. E. Berkowitz, and D. J. Smith, “Increasing the exchange-bias field of Ni_{0.5}Co_{0.5}O films by microstructural control”, *Appl. Phys. Lett.* **74**, 1314 (1999).
- [80] J. Nogués, T. J. Moran, D. Lederman, I. K. Schuller, and K. V. Rao, “Role of interfacial structure on exchange-biased FeF₂-Fe”, *Phys. Rev. B* **59**, 6984 (1999).
- [81] I. Panagiotopoulos, C. Christides, N. Moutis, M. Pissas, and D. Niarchos, “Exchange biasing in La_{2/3}Ca_{1/3}MnO₃/La_{1/3}Ca_{2/3}MnO₃ multilayers”, *J. Appl. Phys.* **85**, 4913 (1999).
- [82] T. Pokhil, S. Mao, and A. Mack, “Study of exchange anisotropy in NiFe/NiMn and NiFe/IrMn exchange coupled films”, *J. Appl. Phys.* **85**, 4916 (1999).
- [83] M. Tsunoda, K. Uneyama, T. Suzuki, K. Yagami, and M. Takahashi, “Enhanced exchange anisotropy of Ni-Fe/Mn-Ni bilayers fabricated under the extremely clean sputtering process”, *J. Appl. Phys.* **85**, 4919 (1999).

- [84] M. Konoto, M. Tsunoda, and M. Takahashi, "Orientational dependence of the exchange biasing in Ni-Fe/Mn_{1-x}Ni_x ($x = 0.11, 0.18, 0.23$) bilayers", *J. Appl. Phys.* **85**, 4925 (1999).
- [85] H. Sang, Y. W. Du, and C. L. Chien, "Exchange coupling in Fe₅₀Mn₅₀/Ni₈₁Fe₁₉ bilayer: Dependence on antiferromagnetic layer thickness", *J. Appl. Phys.* **85**, 4931 (1999).
- [86] H. S. Cho, C. Hou, M. Sun, and H. Fujiwara, "Characteristics of 360-domain walls observed by magnetic force microscope in exchange-biased NiFe films", *J. Appl. Phys.* **85**, 5160 (1999).
- [87] Z. Qian, M. T. Kief, P. K. George, J. M. Sivertsen, and J. H. Judy, "Kerr effect observations of magnetization reversal process in antiferromagnetically pinned peralloy thin films", *J. Appl. Phys.* **85**, 5525 (1999).
- [88] J. A. Borchers, Y. Ijiri, D. M. Lind, P. G. Ivanov, R. W. Erwin, S. H. Lee, and C. F. Majkrzak, "Polarized neutron diffraction studies of exchange-coupled Fe₃O₄/NiO superlattices", *J. Appl. Phys.* **85**, 5883 (1999).
- [89] Z. Qian, J. M. Sivertsen, J. H. Judy, B. A. Everitt, S. Mao, and E. S. Murdock, "Exchange coupling of radio frequency sputtered NiMn/NiFe and NiFe/NiMn bilayers", *J. Appl. Phys.* **85**, 6106 (1999).
- [90] S. Mao, J. Giusti, N. Amin, J. Van ek, and E. Murdock, "Giant magnetoresistance properties of patterned IrMn exchange biased spin valves", *J. Appl. Phys.* **85**, 6112 (1999).
- [91] S. Riedling, M. Bauer, C. Mathieu, B. Hillebrands, R. Jungblut, J. Kohlhepp, and A. Reinders, "In-plane anomalies of the exchange bias field in Ni₈₀Fe₂₀/Fe₅₀Mn₅₀ bilayers on Cu(110)", *J. Appl. Phys.* **85**, 6648 (1999).
- [92] H. Xi, M. H. Kryder, and R. M. White, "Study of the angular-dependent exchange coupling between a ferromagnetic and an antiferromagnet layer", *Appl. Phys. Lett.* **74**, 2687 (1999).
- [93] G. Ju, A. V. Nurmikko, R. F. C. Farrow, R. F. Marks, M. J. Carey, and B. A. Gurney, "Ultrafast Time Resolved Photoinduced Magnetization Rotation in a Ferromagnetic/Antiferromagnetic Exchange Coupled System", *Phys. Rev. Lett.* **82**, 3705 (1999).
- [94] S. Mangin, G. Marchal, and B. Barbara, "Evidence of Exchange-Bias-Like Phenomenon in GdFe/TbFe/GdFe Domain Wall Junctions", *Phys. Rev. Lett.* **82**, 4336 (1999).
- [95] A. S. Edelstein, R. H. Kodoma, M. Miller, V. Browning, P. Lubitz, S. F. Cheng, and H. Sieber, "Interlayer coupling and enhanced coercivity in ferromagnetic/antiferromagnetic structures", *Appl. Phys. Lett.* **74**, 3872 (1999).
- [96] N. J. Gökemeijer, J. W. Cai, and C. L. Chien, "Memory effects of exchange coupling in ferromagnet/antiferromagnet bilayers", *Phys. Rev. B* **60**, 3033 (1999).
- [97] Y. J. Tang, B. Roos, T. Mewes, S. O. Demokritov, B. Hillebrands, and Y. J. Wang, "Enhanced coercivity of exchange-bias Fe/MnPd bilayers", *Appl. Phys. Lett.* **75**, 707 (1999).
- [98] W. J. A. Jr, F. Perjeru, and G. R. Harp, "Spin Structure at the Interface of Exchange Biasd FeMn/Co Bilayers", *Phys. Rev. Lett.* **83**, 1439 (1999).

- [99] P. Miltényi, M. Gierlings, M. Bamming, U. May, G. Güntherodt, J. Nogués, M. Gruyters, C. Leighton, and I. K. Schuller, “Tuning exchange bias”, *Appl. Phys. Lett.* **75**, 2304 (1999).
- [100] S. Maat, L. Shen, and G. J. Mankey, “Fourier Analysis of exchange biased $\text{Ni}_{80}\text{Fe}_{20}/\text{Fe}_{50}\text{Mn}_{50}/\text{Ni}_{80}\text{Fe}_{20}$ trilayers”, *Phys. Rev. B* **60**, 10252 (1999).
- [101] H. Xi and R. M. White, “Angular dependence of exchange anisotropy in $\text{Ni}_{81}\text{Fe}_{19}/\text{CrMnPt}_x$ bilayers”, *J. Appl. Phys.* **86**, 5169 (1999).
- [102] C. Leighton, J. Nogués, H. Suhl, and I. K. Schuller, “Competing interfacial exchange and Zeeman energies in exchange biased bilayers”, *Phys. Rev. B* **60**, 12837 (1999).
- [103] J. Sort, J. Nogués, X. Amils, S. Suriñach, J. S. Muñoz, and M. D. Baró, “Room-temperature coercivity enhancement in mechanically alloyed antiferromagnetic-ferromagnetic powders”, *Appl. Phys. Lett.* **75**, 3177 (1999).
- [104] K. Nishioka, “Thermal decay of ferro/antiferromagnetic exchange coupling in Co/CrMnPt systems”, *J. Appl. Phys.* **86**, 6305 (1999).
- [105] H. Xi, R. M. White, and S. M. Rezende, “Irreversible and reversible measurements of exchange anisotropy”, *Phys. Rev. B* **60**, 14837 (1999).
- [106] S. G. E. te Velthuis, G. P. Felcher, J. S. Jiang, A. Inomata, C. S. Nelson, A. Berger, and S. D. Bader, “Magnetic configurations in exchange-biased superlattices”, *Appl. Phys. Lett.* **75**, 4174 (1999).
- [107] S. Zhang, D. V. Dimitrov, G. C. Hadjipanayis, J. W. Cai, and C. L. Chien, “Coercivity induced by random field at ferromagnetic and antiferromagnetic interfaces”, *J. Magn. Magn. Mater.* **198-199**, 468 (1999).
- [108] Z. Celinski, D. Lucic, N. Cramer, R. E. Camley, R. B. Goldfarb, and D. Skrzypek, “Exchange biasing in ferromagnet/antiferromagnet Fe/KMnF_3 ”, *J. Magn. Magn. Mater.* **202**, 480 (1999).
- [109] M. Rubinstein, P. Lubitz, and S.-F. Cheng, “Ferromagnetic-resonance field shift in an exchange-biased $\text{CoO}/\text{Ni}_{80}\text{Fe}_{20}$ bilayer”, *J. Magn. Magn. Mater.* **195**, 299 (1999).
- [110] J. F. Bobo, S. Dubourg, E. Snoeck, B. Warot, P. Baulès, and J. C. Ousset, “Exchange anisotropy in epitaxial $\text{NiO}(0\ 0\ 1)$ -FCC Co bilayers”, *J. Magn. Magn. Mater.* **206**, 118 (1999).
- [111] F. T. Parker, K. Takano, and A. E. Berkowitz, “Exchange coupling mechanisms at ferromagnetic/CoO interfaces”, *Phys. Rev. B* **61**, R866 (2000).
- [112] J. Nogués, C. Leighton, and I. K. Schuller, “Correlation between antiferromagnetic interface coupling and positive exchange bias”, *Phys. Rev. B* **61**, 1315 (2000).
- [113] V. I. Nikitenko, V. S. Gornakov, A. J. Shapiro, R. D. Shull, K. Liu, S. M. Zhou, and C. L. Chien, “Asymmetry in Elementary Events of Magnetization Reversal in a Ferromagnetic / Antiferromagnetic Bilayer”, *Phys. Rev. Lett.* **84**, 765 (2000).
- [114] T. Mewes, R. Lopusnik, J. Fassbender, B. Hillebrands, M. Jung, D. Engel, A. Ehresmann, and H. Schmoranzler, “Suppression of exchange bias by ion irradiation”, *Appl. Phys. Lett.* **76**, 1057 (2000).
- [115] J. Nogués, L. Morellon, C. Leighton, M. R. Ibarra, and I. K. Schuller, “Antiferromagnetic spin flop and exchange bias”, *Phys. Rev. B* **61**, R6455 (2000).

- [116] J. S. Jiang, G. P. Felcher, A. Inomata, R. Goyette, C. Nelson, and S. D. Bader, “Exchange-bias effect in Fe/Cr(211) double superlattice structures”, *Phys. Rev. B* **61**, 9653 (2000).
- [117] C. Leighton, J. Nogués, B. Jönsson-Åkerman, and I. K. Schuller, “Coercivity Enhancement in Exchange Biased Systems Driven by Interfacial Magnetic Frustration”, *Phys. Rev. Lett.* **84**, 3466 (2000).
- [118] M. R. Fitzsimmons, P. Yashar, C. Leighton, I. K. Schuller, J. Nogués, C. F. Majkrzak, and J. A. Dura, “Asymmetric Magnetization Reversal in Exchange-Biased Hysteresis Loops”, *Phys. Rev. Lett.* **84**, 3986 (2000).
- [119] H. Xi, K. R. Mountfield, and R. M. White, “Ferromagnetic resonance studies of exchange biasing in Ni₈₁Fe₁₉/Pt₁₀Mn₉₀ bilayers”, *J. Appl. Phys.* **87**, 4367 (2000).
- [120] M. Tsunoda, Y. Tsuchiya, T. Hashimoto, and M. Takahashi, “Magnetic anisotropy and rotational hysteresis loss in exchange coupled Ni-Fe/Mn-Ir films”, *J. Appl. Phys.* **87**, 4375 (2000).
- [121] S. Dubourg, N. Negre, B. Warot, E. Snoeck, M. Goiran, J. C. Ousset, and J. F. Bobo, “Exchange anisotropy in epitaxial NiO(001)-fcc Co bilayers”, *J. Appl. Phys.* **87**, 4936 (2000).
- [122] H. Xi, R. M. White, and S. M. Rezende, “Measurement dependence of exchange bias”, *J. Appl. Phys.* **87**, 4960 (2000).
- [123] H. C. Tong, C. Qian, L. Miloslavsky, S. Funada, X. Shi, F. Liu, and S. Dey, “The spin flop of synthetic antiferromagnetic films”, *J. Appl. Phys.* **87**, 5055 (2000).
- [124] T. Mewes, B. F. P. Roos, S. O. Demokritov, and B. Hillebrands, “Oscillatory exchange bias effect in FeNi/Cu/FeMn and FeNi/Cr/FeMn trilayer systems”, *J. Appl. Phys.* **87**, 5064 (2000).
- [125] R. D. McMichael, C. G. Lee, M. D. Stiles, F. G. Serpa, P. J. Chen, and W. F. Egelhoff, Jr., “Exchange bias relaxation in CoO-biased films”, *J. Appl. Phys.* **87**, 6406 (2000).
- [126] A. M. Goodman, H. Laider, K. O’Grady, N. W. Owen, and A. K. Petford-Long, “Magnetic viscosity effects on the pinned layer of spin-valve materials”, *J. Appl. Phys.* **87**, 6409 (2000).
- [127] X. Portier, A. K. Petford-Long, A. de Morais, N. W. Owen, H. Laider, and K. O’Grady, “Magnetization reversal processes in exchange-biased systems”, *J. Appl. Phys.* **87**, 6412 (2000).
- [128] M. Tsunoda and M. Takahashi, “Field independent rotational hysteresis loss on exchange coupled polycrystalline Ni-Fe/Mn-Ir bilayers”, *J. Appl. Phys.* **87**, 6415 (2000).
- [129] T. Gredig, I. N. Krivorotov, C. Merton, A. M. Goldman, and E. D. Dahlberg, “Rotation of exchange anisotropy in biased Co/CoO bilayers”, *J. Appl. Phys.* **87**, 6418 (2000).
- [130] C. Liu, C. Yu, H. Jiang, L. Shen, C. Alexander, and G. J. Mankey, “Effect of interface roughness on the exchange bias NiFe/FeMn”, *J. Appl. Phys.* **87**, 6644 (2000).

- [131] N. Cheng, K. M. Krishnan, E. Girt, R. F. C. Farrow, R. F. Marks, A. Kellock, A. Young, and C. H. A. Huan, “Exchange biasing and interface structure in MnNi/Fe(Mo) bilayers”, *J. Appl. Phys.* **87**, 6647 (2000).
- [132] P. Miltényi, M. Gierlings, J. Keller, B. Beschoten, G. Güntherodt, U. Nowak, and K. D. Usadel, “Diluted Antiferromagnets in Exchange Bias: Proof of the Domain State Model”, *Phys. Rev. Lett.* **84**, 4224 (2000).
- [133] H. D. Chopra, D. X. Yang, P. J. Chen, H. J. Brown, L. J. Swartzendruber, and W. F. Egelhoff, Jr., “Nature of magnetization reversal in exchange-coupled polycrystalline NiO-Co bilayers”, *Phys. Rev. B* **61**, 15312 (2000).
- [134] F. Nolting, A. Scholl, J. Stöhr, J. W. Seo, J. Fompeyrine, H. Siegwart, J.-P. Locquet, S. Anders, J. Lüning, E. E. Fullerton, M. F. Toney, M. R. Scheinfein, and H. A. Padmore, “Direct observation of the alignment of ferromagnetic spins by antiferromagnetic spins”, *Nature* **405**, 767 (2000).
- [135] C. Hou, H. Fujiwara, and K. Zhang, “Structural origin of coercivity enhancement and exchange-bias field in double antiferromagnet/ferromagnet bilayers”, *Appl. Phys. Lett.* **76**, 3974 (2000).
- [136] P. J. van der Zaag, Y. Ijiri, J. A. Borchers, L. F. Feiner, R. M. Wolf, J. M. Gaines, R. W. Erwin, and M. A. Verheijen, “Difference between Blocking and Néel Temperatures in the Exchange Biased Fe₃O₄/CoO System”, *Phys. Rev. Lett.* **84**, 6102 (2000).
- [137] C. Leighton, M. Song, J. Nogués, M. C. Cyrille, and I. K. Schuller, “Using magnetoresistance to probe reversal asymmetry in exchange biased bilayers”, *J. Appl. Phys.* **88**, 344 (2000).
- [138] G. Ju, L. Chen, A. V. Nurmikko, R. F. C. Farrow, R. F. Marks, M. J. Carey, and B. A. Gurney, “Coherent magnetization rotation induced by optical modulation in ferromagnetic/antiferromagnetic exchange-coupled bilayers”, *Phys. Rev. B* **62**, 1171 (2000).
- [139] J. van Driel, F. R. de Boer, K.-M. H. Lenssen, and R. Coehoorn, “Exchange biasing by Ir₁₉Mn₈₁: Dependence on temperature, microstructure and antiferromagnetic layer thickness”, *J. Appl. Phys.* **88**, 975 (2000).
- [140] H. Matsuyama, C. Haginoya, and K. Koike, “Microscopic Imaging of Fe Magnetic Domains Exchange Coupled with Those in a NiO(001) Surface”, *Phys. Rev. Lett.* **85**, 646 (2000).
- [141] J. S. Jiang, G. P. Felcher, A. Inomata, R. Goyette, C. S. Nelson, and S. D. Bader, “Exchange bias in Fe/Cr double superlattices”, *J. Vac. Sci. Technol. A* **18**, 1264 (2000).
- [142] G. Li, T. Yang, Q. Yu, and W. Lai, “Exchange coupling in NiFe/FeMn films studied by pseudo-Hall effect”, *Appl. Phys. Lett.* **77**, 1032 (2000).
- [143] Y. J. Tang, X. Zhou, X. Chen, B. Q. Lang, and W. S. Zhan, “Exchange anisotropy of epitaxial Fe/MnPd bilayers”, *J. Appl. Phys.* **88**, 2054 (2000).
- [144] A. Ercole, W. S. Lew, G. Lauhoff, E. T. M. Kernohan, J. Lee, and J. A. C. Bland, “Temperature-dependent spin-wave behavior in Co/CoO bilayers studied by Brillouin light scattering”, *Phys. Rev. B* **62**, 6429 (2000).

- [145] F. Y. Yang and C. L. Chien, “Spiraling Spin Structure in an Exchange-Coupled Antiferromagnetic Layer”, *Phys. Rev. Lett.* **85**, 2597 (2000).
- [146] Y. J. Tang, B. F. P. Roos, T. Mewes, A. R. Frank, M. Rickart, M. Bauer, S. O. Demokritov, B. Hillebrands, X. Zhou, B. Q. Liang, X. Chen, and W. S. Zhan, “Structure and magnetic properties of exchange-biased polycrystalline Fe/MnPd bilayers”, *Phys. Rev. B* **62**, 8654 (2000).
- [147] S. G. E. te Velthuis, J. S. Jiang, and G. P. Felcher, “Switching of the exchange bias in Fe/Cr(211) double-superlattice structures”, *Appl. Phys. Lett.* **77**, 2222 (2000).
- [148] J. Wang, W. N. Wang, X. Chen, H. W. Zhao, J. G. Zhao, and W. S. Zhan, “Asymmetry of coercivity dependence on temperature in exchange-biased FeMn/Co bilayers”, *Appl. Phys. Lett.* **77**, 2731 (2000).
- [149] M. Gruyters and D. Riegel, “Optimized exchange biasing by controlled in situ oxidation”, *J. Appl. Phys.* **88**, 6610 (2000).
- [150] M. Fraune, U. Rüdiger, G. Güntherodt, S. Cardoso, and P. Freitas, “Size dependence of the exchange bias field in NiO/Ni nanostructures”, *Appl. Phys. Lett.* **77**, 3815 (2000).
- [151] J. A. Borchers, Y. Ijiri, D. M. Lind, P. G. Ivanov, R. W. Erwin, A. Qasba, S. H. Lee, K. V. O’Donovan, and D. C. Dender, “Detection of field-dependent antiferromagnetic domains in exchange-biased Fe₃O₄/NiO superlattices”, *Appl. Phys. Lett.* **77**, 4187 (2000).
- [152] M. Gruyters and D. Riegel, “Strong exchange bias by a single layer of independent antiferromagnetic grains: The CoO/Co model system”, *Phys. Rev. B* **63**, 052401 (2001).
- [153] C. Hou, H. Fujiwara, K. Zhang, A. Tanaka, and Y. Shimizu, “Temperature dependence of the exchange-bias field of ferromagnetic layers coupled with antiferromagnetic layers”, *Phys. Rev. B* **63**, 024411 (2001).
- [154] L. Smardz, “Exchange Biasing Effect in NiO/Co Thin Films”, *Phys. Status Solidi A* **181**, R7 (2000).
- [155] M. Rubinstein, P. Lubitz, and S.-F. Cheng, “Comparison of parallel and perpendicular ferromagnetic resonance in an exchange-biased bilayer”, *J. Magn. Mater.* **210**, 329 (2000).
- [156] K. Liu, S. M. Baker, M. Tuominen, T. P. Russell, and I. K. Schuller, “Tailoring exchange bias with magnetic nanostructures”, *Phys. Rev. B* **63**, 060403(R) (2001).
- [157] A. Mougin, T. Mewes, M. Jung, D. Engel, A. Ehresmann, H. Schmoranzler, J. Fassbender, and B. Hillebrands, “Local manipulation and reversal of the exchange bias field by ion irradiation in FeNi/FeMn double layers”, *Phys. Rev. B* **63**, 060409(R) (2001).
- [158] M.-T. Lin, C. H. Ho, C.-R. Chang, and Y. D. Yao, “Thermally assisted oscillatory interlayer exchange bias coupling”, *Phys. Rev. B* **63**, 100404 (2001).
- [159] S. M. Zhou and C. L. Chien, “Dependence of exchange coupling on magnetization in Co-Ni/FeMn bilayers”, *Phys. Rev. B* **63**, 104406 (2001).
- [160] J.-W. Cai, S. Okamoto, O. Kitakami, and Y. Shimida, “Large coercivity and surface anisotropy in MgO/Co multilayer films”, *Phys. Rev. B* **63**, 104418 (2001).

- [161] G. H. Yu, C. L. Chai, F. W. Zhu, J. M. Xiao, and W. Y. Lai, “Interface reaction of NiO/NiFe and its influence on magnetic properties”, *Appl. Phys. Lett.* **78**, 1706 (2001).
- [162] H. Ohldag, A. Scholl, F. Nolting, S. Anders, F. U. Hillebrecht, and J. Stöhr, “Spin Reorientation at the Antiferromagnetic NiO(001) Surface in Response to an Adjacent Ferromagnet”, *Phys. Rev. Lett.* **86**, 2878 (2001).
- [163] J. Wang, W. N. Wang, X. Chen, H. W. Zhao, J. G. Zhao, and W. S. Zhan, “Effect of an antiferromagnetic layer on the temperature dependence of coercivity in biased FeMn/Co systems”, *J. Appl. Phys.* **89**, 3897 (2001).
- [164] C. Leighton and I. K. Schuller, “Magnetic viscosity measurements reveal reversal asymmetry in exchange-biased bilayers”, *Phys. Rev. B* **63**, 174419 (2001).
- [165] N. J. Gökemeijer, R. L. Penn, D. R. Veblen, and C. L. Chien, “Exchange coupling in epitaxial CoO/NiFe bilayers with compensated and uncompensated interfacial spin structures”, *Phys. Rev. B* **63**, 174422 (2001).
- [166] C. Leighton, M. R. Fitzsimmons, P. Yashar, A. Hoffmann, J. Nogués, J. Dura, C. F. Majkrzak, and I. K. Schuller, “Two-Stage Magnetization Reversal in Exchange Biased Bilayers”, *Phys. Rev. Lett.* **86**, 4394 (2001).
- [167] S. M. Rezende, A. Azevedo, M. A. Lucena, and F. M. de Aguiar, “Anomalous spin-wave damping in exchange-biased films”, *Phys. Rev. B* **63**, 214418 (2001).
- [168] B. Warot, E. Snoeck, P. Baulès, J.-C. Ousset, M.-J. Casanove, S. Dubourg, and J. F. Bobo, “Growth and stress relaxation of Co/NiO bilayers on MgO(001)”, *J. Appl. Phys.* **89**, 5414 (2001).
- [169] M. J. Carey, N. Smith, B. A. Gurney, J. R. Childress, and T. Lin, “Thermally assisted decay of pinning in polycrystalline exchange biased systems (invited)”, *J. Appl. Phys.* **89**, 6579 (2001).
- [170] J. Camarero, Y. Pennec, M. Bonfim, J. Vogel, S. Pizzini, A. Fontaine, M. Cartier, F. Fettar, and B. Dieny, “Magnetization reversal dynamics in exchange-coupled NiO-Co bilayers”, *J. Appl. Phys.* **89**, 6585 (2001).
- [171] T. Pokhil, E. Linville, and S. Mao, “Exchange anisotropy and micromagnetic properties of PtMn/NiFe bilayers”, *J. Appl. Phys.* **89**, 6588 (2001).
- [172] T. Hughes, H. Laider, K. O’Grady, A. K. Petford-Long, S. Mao, M. Kief, and E. Linville, “Magnetization reversal in the pinned layer of PtMnCr/NiFe exchange biased bilayers”, *J. Appl. Phys.* **89**, 6591 (2001).
- [173] C.-H. Lai, W. C. Lien, F. R. Chen, J. J. Kai, and S. Mao, “Effects of phase transformation and interdiffusion on the exchange bias of NiFe/NiMn”, *J. Appl. Phys.* **89**, 6600 (2001).
- [174] Y.-H. Wang, C.-H. Lai, C.-R. Chang, J.-S. Yang, and C. K. Lo, “Uniaxial anisotropy induced by field annealing in (001) NiMn/Co films”, *J. Appl. Phys.* **89**, 6603 (2001).
- [175] K. Yagami, M. Tsunoda, and M. Takahashi, “Enhancement of exchange bias in Mn-Ir/Co-Fe based spin valves with an ultrathin Cu underlayer and *in situ* Mn-Ir surface modification”, *J. Appl. Phys.* **89**, 6609 (2001).

- [176] D. Spenato, J. B. Youssef, H. L. Gall, and J. Ostoréro, “From ferromagnetic-ferromagnetic to ferromagnetic-antiferromagnetic exchange coupling in NiFe/MnNi bilayers”, *J. Appl. Phys.* **89**, 6898 (2001).
- [177] P. Lubitz, M. Rubinstein, J. J. Krebs, and S.-F. Cheng, “Frequency and temperature dependence of ferromagnetic linewidth in exchange biased Permalloy”, *J. Appl. Phys.* **89**, 6901 (2001).
- [178] K. Zhang, T. Zhao, and H. Fujiwara, “Training effect of exchange biased iron-oxide/ferromagnet systems”, *J. Appl. Phys.* **89**, 6910 (2001).
- [179] A. Scholl, F. Nolting, J. Stöhr, T. Regan, J. Lüning, J. W. Seo, J.-P. Locquet, J. Fompeyrine, S. Anders, H. Ohldag, and H. A. Padmore, “Exploring the microscopic origin of exchange bias with photoelectron emission microscopy (invited)”, *J. Appl. Phys.* **89**, 7266 (2001).
- [180] Y.-J. Wang and C.-H. Lai, “Size and shape effects on exchange field of patterned NiO/NiFe films”, *J. Appl. Phys.* **89**, 7537 (2001).
- [181] M.-T. Lin, C. H. Ho, C.-R. Chang, and Y. D. Yao, “Temperature-dependence of interlayer exchange bias coupling in NiO/Cu/NiFe”, *J. Appl. Phys.* **89**, 7540 (2001).
- [182] H. Brown, E. D. Dahlberg, and C. Hou, “Exchange bias measurements of CoFe/IrMn”, *J. Appl. Phys.* **89**, 7543 (2001).
- [183] K. Zhang, T. Kai, T. Zhao, H. Fujiwara, C. Hou, and M. T. Kief, “Rotational hysteresis of torque curves in polycrystalline ferro/antiferromagnetic systems”, *J. Appl. Phys.* **89**, 7546 (2001).
- [184] T. Zhao, K. Zhang, and H. Fujiwara, “Angular dependence of remanence of exchange-coupled CoFe/NiO bilayers”, *J. Appl. Phys.* **89**, 7549 (2001).
- [185] L. Wee, R. L. Stamps, Z. Celinski, and D. Skrzypek, “Exchange bias in Fe/KNiF₃ bilayers”, *J. Appl. Phys.* **89**, 7555 (2001).
- [186] W. Zhu, L. Seve, R. Sears, B. Sinkovic, and S. S. P. Parkin, “Field Cooling Induced Changes in the Antiferromagnetic Structure in NiO Films”, *Phys. Rev. Lett.* **86**, 5389 (2001).
- [187] S. Dubourg, J. F. Bobo, B. Warot, E. Snoeck, and J. C. Ousset, “Exchange-biased Co layers on self-organized faceted NiO epitaxially grown on MgO(110)”, *Phys. Rev. B* **64**, 054416 (2001).
- [188] C. Liu, J. Du, J. A. Bernard, and G. J. Mankey, “Study of exchange anisotropy for Ni₈₀Fe₂₀/Fe₆₀Mn₄₀ (111) epitaxial films”, *J. Vac. Sci. Technol. A* **19**, 1213 (2001).
- [189] Z. Q. Lu, G. Pan, and W. Y. Lai, “Planar Hall effect in NiFe/NiMn bilayers”, *J. Appl. Phys.* **90**, 1414 (2001).
- [190] T. P. A. Hase, B. D. Fulthorpe, S. B. Wilkins, B. K. Tanner, C. H. Marrows, and B. J. Hickey, “Weak magnetic moment on IrMn exchange bias pinning layers”, *Appl. Phys. Lett.* **79**, 895 (2001).
- [191] C.-H. Lai, Y.-H. Wang, C.-R. Chang, J.-S. Yang, and Y. D. Yao, “Exchange-bias-induced double-shifted magnetization curves in Co biaxial films”, *Phys. Rev. B* **64**, 094420 (2001).

- [192] N. Moutis, C. Christides, I. Panagiotopoulos, and D. Niarchos, “Exchange-coupling properties of $\text{La}_{1-x}\text{Ca}_x\text{MnO}_3$ ferromagnetic/antiferromagnetic multilayers”, *Phys. Rev. B* **64**, 094429 (2001).
- [193] M. Gruyters, M. Gierlings, and D. Riegel, “Rapid suppression of exchange bias across thin Au spacer layers”, *Phys. Rev. B* **64**, 132401 (2001).
- [194] S. Maat, K. Takano, S. S. P. Parkin, and E. E. Fullerton, “Perpendicular Exchange Bias of Co/Pt Multilayers”, *Phys. Rev. Lett.* **87**, 087202 (2001).
- [195] M. R. Fitzsimmons, C. Leighton, A. Hoffmann, P. C. Yashar, J. Nogués, K. Liu, C. F. Majkrzak, J. A. Dura, H. Fritzsche, and I. K. Schuller, “Influence of interfacial disorder and temperature on magnetization reversal in exchange-coupled bilayers”, *Phys. Rev. B* **64**, 104415 (2001).
- [196] J. Camarero, Y. Pennec, J. Vogel, M. Bonfim, S. Pizzini, M. Cartier, F. Ernult, F. Fettar, and B. Dieny, “Dynamical properties of magnetization reversal in exchange-coupled NiO/Co bilayers”, *Phys. Rev. B* **64**, 172402 (2001).
- [197] G. H. Yu, L. R. Zeng, F. W. Zhu, C. L. Chai, and W. Y. Lai, “Magnetic properties and x-ray photoelectron spectroscopy study of NiO/NiFe films prepared by magnetron sputtering”, *J. Appl. Phys.* **90**, 4039 (2001).
- [198] A. Punnoose, H. Magnone, M. S. Seehra, and J. Bonevich, “Bulk to nanoscale magnetism and exchange bias in CuO nanoparticles”, *Phys. Rev. B* **64**, 174420 (2001).
- [199] H. Xi, R. M. White, S. Mao, Z. Gao, Z. Yang, and E. S. Murdock, “Low-frequency dynamic hysteresis in exchange-coupled $\text{Ni}_{81}\text{Fe}_{19}/\text{Ir}_{22}\text{Mn}_{78}$ bilayers”, *Phys. Rev. B* **64**, 184416 (2001).
- [200] L. Sun, Y. Ding, C. L. Chien, and P. C. Searson, “Exchange coupling in nanostructured CoO/NiFe networks”, *Phys. Rev. B* **64**, 184430 (2001).
- [201] H. Ohldag, T. J. Regan, J. Stöhr, A. Scholl, F. Nolting, J. Lüning, C. Stamm, S. Anders, and R. L. White, “Spectroscopic Identification and Direct Imaging of Interfacial Magnetic Spins”, *Phys. Rev. Lett.* **87**, 247201 (2001).
- [202] X. Chen, C. Binek, A. Hochstrat, and W. Kleemann, “Dilution-induced enhancement of the blocking temperature in exchange-bias heterosystems”, *Phys. Rev. B* **65**, 012415 (2001).
- [203] T. Zhao, H. Fujiwara, K. Zhang, C. Hou, and T. Kai, “Enhanced uniaxial anisotropy and two-step magnetization process along the hard axis of polycrystalline NiFe/NiO bilayers”, *Phys. Rev. B* **65**, 014431 (2001).
- [204] L. Lazar, J. S. Jiang, G. P. Felcher, A. Inomata, and S. D. Bader, “Oscillatory exchange bias in Fe/Cr double superlattices”, *J. Magn. Magn. Mater.* **223**, 299 (2001).
- [205] M. Cartier, S. Auffret, Y. Samson, P. Bayle-Guillemaud, and B. Dieny, “Magnetic domain configurations in exchange-coupled NiO/Co bilayer films”, *J. Magn. Magn. Mater.* **223**, 63 (2001).
- [206] T. Hughes, K. O’Grady, H. Laidler, and R. W. Chantrell, “Thermal activation in exchange biased bilayers”, *J. Magn. Magn. Mater.* **235**, 329 (2001).

- [207] M. Xu, T. Yang, G. Luo, Z. Lu, C. Liu, N. Yang, Z. Mai, W. Lai, Z. Wu, and J. Wang, “Study of Ni₈₀Fe₂₀/Fe₅₀Mn₅₀ superlattice microstructures by transmission electron microscopy and x-ray diffraction”, *J. Phys.: Condens. Matter* **13**, 2891 (2001).
- [208] Q. Y. Xu, G. Ni, H. Sang, and Y. W. Du, “The exchange coupling of a NiO/FeNi bilayer with interdiffused interface”, *J. Phys.: Condens. Matter* **13**, 5047 (2001).
- [209] J. P. King, J. N. Chapman, M. F. Gillies, and J. C. S. Kools, “Magnetization reversal of NiFe films exchange-biased by IrMn and FeMn”, *J. Phys. D: Appl. Phys.* **34**, 528 (2001).
- [210] J. M. González, C. Prados, A. Salcedo, E. Pina, F. J. Palomares, F. Cebollada, and A. Hernando, “Some open problems related to the link between structure, morphology and extrinsic magnetic properties in layered nanostructures”, *Physica B* **299**, 270 (2001).
- [211] A. Berger, M. J. Pechan, R. Compton, J. S. Jiang, J. E. Pearson, and S. D. Bader, “Disorder-tuning of hysteresis-loop properties in Co/CoO-film structures”, *Physica B* **306**, 235 (2001).
- [212] C. Leighton, M. R. Fitzsimmons, A. Hoffmann, J. Dura, C. F. Majkrzak, M. S. Lund, and I. K. Schuller, “Thickness-dependent coercive mechanisms in exchange-biased bilayers”, *Phys. Rev. B* **65**, 064403 (2002).
- [213] M. J. Pechan, D. Bennett, N. Teng, C. Leighton, J. Nogués, and I. K. Schuller, “Induced anisotropy and positive exchange bias: A temperature, angular, and cooling field study by ferromagnetic resonance”, *Phys. Rev. B* **65**, 064410 (2002).
- [214] J. H. Lee, H. D. Jeong, C. S. Yoon, C. K. Kim, B. G. Park, and T. D. Lee, “Interdiffusion in antiferromagnet/ferromagnetic exchange coupled NiFe/IrMn/CoFe multilayer”, *J. Appl. Phys.* **91**, 1431 (2002).
- [215] M. Cartier, S. Auffret, P. Bayle-Guillemaud, F. Ernult, F. Fettar, and B. Dieny, “Influence of deposition angle on the properties of NiO spin-valves”, *J. Appl. Phys.* **91**, 1436 (2002).
- [216] I. N. Krivorotov, C. Leighton, J. Nogués, I. K. Schuller, and E. D. Dahlberg, “Relation between exchange anisotropy and magnetization reversal asymmetry in Fe/MnF₂ bilayers”, *Phys. Rev. B* **65**, 100402(R) (2002).
- [217] M. Gierlings, M. J. Prandolini, H. Fritzsche, M. Gruyters, and D. Riegel, “Change and asymmetry of magnetization reversal for a Co/CoO exchange-bias system”, *Phys. Rev. B* **65**, 092407 (2002).
- [218] S. Soeya, “Exchange coupling mechanism of polycrystalline Co/CrMnPt films”, *J. Appl. Phys.* **91**, 2197 (2002).
- [219] H. Y. Li, L. Y. Chen, and S. M. Zhou, “Thermal stability of exchange coupling in permalloy/FeMn bilayers and its dependence on the antiferromagnet layer thickness”, *J. Appl. Phys.* **91**, 2243 (2002).
- [220] I. Panagiotopoulos, N. Moutis, and C. Christides, “Asymmetry of the magnetization reversal mechanism probed by relaxation measurements in La-Ca-Mn-O ferromagnetic/antiferromagnetic multilayers”, *Phys. Rev. B* **65**, 132407 (2002).

- [221] G. Li, T. Yang, Q. Hu, H. Jiang, and W. Lai, “Ferromagnetic domain structure and hysteresis of exchange bias in NiFe/NiMn bilayers”, *Phys. Rev. B* **65**, 134421 (2002).
- [222] M. R. Fitzsimmons, C. Leighton, J. Nogués, A. Hoffmann, K. Liu, C. F. Majkrzak, J. A. Dura, J. R. Groves, R. W. Springer, P. N. Arendt, V. Leiner, H. Lauter, and I. K. Schuller, “Influence of in-plane crystalline quality of an antiferromagnet on perpendicular exchange coupling and exchange bias”, *Phys. Rev. B* **65**, 134436 (2002).
- [223] W. Kuch, X. Gao, and J. Kirschner, “Competition between in-plane and out-of-plane magnetization in exchange-coupled magnetic films”, *Phys. Rev. B* **65**, 064406 (2002).
- [224] T. Pokhil, D. Song, and E. Linville, “Magnetic force microscope study of antiferromagnet-ferromagnet exchange coupled films”, *J. Appl. Phys.* **91**, 6887 (2002).
- [225] T. Zhao, K. Zhang, and H. Fujiwara, “Magnetization reversal of exchange coupled CoFe/IrMn bilayers”, *J. Appl. Phys.* **91**, 6890 (2002).
- [226] H.-W. Zhao, W. N. Wang, Y. J. Wang, W. S. Zhao, and J. Q. Xiao, “Investigation of exchange bias in FeMnC/FeMn bilayers”, *J. Appl. Phys.* **91**, 6893 (2002).
- [227] J. Juraszek, J. Fassbender, S. Poppe, T. Mewes, B. Hillebrands, D. Engel, A. Kronenberger, A. Ehresmann, and H. Schmoranzler, “Tuning exchange bias and coercive fields in ferromagnet/antiferromagnet bilayers with ion irradiation”, *J. Appl. Phys.* **91**, 6896 (2002).
- [228] H. S. Jung, W. D. Doyle, H. Fujiwara, J. E. Wittig, J. F. Al-Sharab, J. Bentley, and N. D. Evans, “Exchange coupling in FeTaN/IrMn/FeTaN and NiFe/IrMn/NiFe trilayer films”, *J. Appl. Phys.* **91**, 6899 (2002).
- [229] K. Zhang, T. Zhao, and H. Fujiwara, “Training effect in ferro (F)/antiferromagnetic (AF) exchange coupled systems: Dependence on AF thickness”, *J. Appl. Phys.* **91**, 6902 (2002).
- [230] F. Garcia, G. Casali, S. Auffret, B. Rodmacq, and B. Dieny, “Exchange bias in $(\text{Pt}/\text{Co}_{0.9}\text{Fe}_{0.1})_n/\text{FeMn}$ multilayers with perpendicular magnetic anisotropy”, *J. Appl. Phys.* **91**, 6905 (2002).
- [231] K.-U. Barholz and E. Mattheis, “Determination of the distribution of both exchange bias field strength and direction in ferromagnet/antiferromagnet systems”, *J. Appl. Phys.* **91**, 7224 (2002).
- [232] Y. F. Li, J. Q. Xiao, and D. V. Dimitrov, “Exchange bias in standard spin valves after different thermal processes”, *J. Appl. Phys.* **91**, 7227 (2002).
- [233] C. C. Yu, J. C. A. Huang, and Y. D. Yao, “Step surface induced unidirectional exchange anisotropy in PtMn/Ni₈₀Fe₂₀ on Mo(001)”, *J. Appl. Phys.* **91**, 7230 (2002).
- [234] J. van Lierop, L. H. Lewis, K. E. Williams, and R. J. Gambino, “Magnetic exchange effects in a nanocomposite Ni/NiO film”, *J. Appl. Phys.* **91**, 7233 (2002).
- [235] J. Wang, W. N. Wang, X. Chen, H. W. Zhao, J. G. Zhao, and W. S. Zhan, “The effect of the interlayer on the exchange bias in FeMn/Cu/Co system”, *J. Appl. Phys.* **91**, 7236 (2002).

- [236] J. B. Youssef, D. Spenato, H. L. Gall, and J. Ostoréro, “Large exchange bias in interdiffused NiFe/Mn bilayers”, *J. Appl. Phys.* **91**, 7239 (2002).
- [237] L. Malkinski, N. Cramer, A. Hutchinson, R. Camley, Z. Celinski, and D. Skrzypek, “Temperature dependence of anisotropy in exchange biased Fe/KCoF₃ system”, *J. Appl. Phys.* **91**, 7242 (2002).
- [238] D. Magnoux, D. Hrabovsky, P. Baulès, M. J. Casanove, E. Snoeck, A. R. Fert, and J. F. Bobo, “Sputter growth and magnetic properties of exchange-biased La_{1/4}Ca_{3/4}MnO₃-La_{2/3}Sr_{1/3}MnO₃”, *J. Appl. Phys.* **91**, 7730 (2002).
- [239] A. Kirilyuk, T. Rasing, H. Jaffrès, D. Lacour, and F. N. V. Dau, “Domain structures during magnetization reversal in exchange-biased layers”, *J. Appl. Phys.* **91**, 7745 (2002).
- [240] A. Paetzold and K. Röhl, “Thermally activated self-alignment of exchange coupling in NiO/NiFe bilayers”, *J. Appl. Phys.* **91**, 7748 (2002).
- [241] C.-H. Lai, T. Ming, R. Erwin, and J. Borchers, “Exchange anisotropy between single twin domain NiO and NiFe”, *J. Appl. Phys.* **91**, 7751 (2002).
- [242] A. E. P. de Araújo, F. L. A. Machado, A. R. Rodrigues, A. Azevedo, F. M. de Aguiar, J. R. L. de Almeida, S. M. Rezende, and W. F. Egelhoff, Jr., “Spin-glass and random-field effects in exchange-biased NiFe film on a NiO single-crystal substrate”, *J. Appl. Phys.* **91**, 7754 (2002).
- [243] S. Dubourg, J. F. Bobo, J. C. Ousset, B. Warot, and E. Snoeck, “Correlations between coercivity and exchange bias in epitaxial NiO-Co(110) bilayers”, *J. Appl. Phys.* **91**, 7757 (2002).
- [244] T. Gredig, I. N. Krivorotov, and E. D. Dahlberg, “Magnetization reversal in exchange biased Co/CoO probed with anisotropic magnetoresistance”, *J. Appl. Phys.* **91**, 7760 (2002).
- [245] H. Shi, D. Lederman, and E. E. Fullerton, “Exchange bias in Fe_xZn_{1-x}F₂/Co bilayers”, *J. Appl. Phys.* **91**, 7763 (2002).
- [246] A. Punnoose and M. S. Seehra, “Hysteresis anomalies and exchange bias in 6.6 nm CuO nanoparticles”, *J. Appl. Phys.* **91**, 7766 (2002).
- [247] W. M. Liu, B. Wu, X. Zhou, D. K. Campbell, S. T. Chui, and Q. Niu, “Interacting domain walls in an easy-plane ferromagnet”, *Phys. Rev. B* **65**, 172416 (2002).
- [248] T. Mewes, H. Nembach, M. Rickart, S. O. Demokritov, J. Fassbender, and B. Hillebrands, “Angular dependence and phase diagrams of exchange-coupled epitaxial Ni₈₁Fe₁₉/Fe₅₀Mn₅₀(001) bilayers”, *Phys. Rev. B* **65**, 224423 (2002).
- [249] T. L. Kirk, O. Hellwig, and E. E. Fullerton, “Coercivity mechanisms in positive exchange-biased Co films and Co/Pt multilayers”, *Phys. Rev. B* **65**, 224426 (2002).
- [250] J. Keller, P. Miltényi, B. Beschoten, G. Güntherodt, U. Nowak, and K. D. Usadel, “Domain state model for exchange bias. II. Experiments”, *Phys. Rev. B* **66**, 014431 (2002).
- [251] C. H. Marrows, S. Langridge, M. Ali, A. T. Hindmarch, D. T. Dekadjevi, S. Foster, and B. J. Hickey, “Mapping domain disorder in exchange-biased magnetic multilayers”, *Phys. Rev. B* **66**, 024437 (2002).

- [252] T. Gredig, I. N. Krivorotov, P. Eames, and E. D. Dahlberg, “Unidirectional coercivity enhancement in exchange-biased Co/CoO”, *Phys. Rev. Lett.* **81**, 1270 (2002).
- [253] P. Steadman, M. Ali, A. T. Hindmarch, C. H. Marrows, B. J. Hickey, S. Langridge, R. M. Dalgliesh, and S. Foster, “Exchange Bias in Spin-Engineered Double Superlattices”, *Phys. Rev. Lett.* **89**, 077201 (2002).
- [254] M. Xu, Z. Lu, T. Yang, C. Liu, S. Cui, Z. Mai, W. Lai, Q. Jia, and W. Zheng, “Relation between microstructures and magnetic properties upon annealing in Fe₅₀Mn₅₀/Ni₈₀Mn₂₀ films”, *J. Appl. Phys.* **92**, 2052 (2002).
- [255] R. L. Compton, M. J. Pechan, S. Maat, and E. E. Fullerton, “Probing the magnetic transitions in exchange-biased FePt₃/Fe bilayers”, *Phys. Rev. B* **66**, 054411 (2002).
- [256] M. S. Lund, W. A. A. Macedo, K. Liu, J. Nogués, I. K. Schuller, and C. Leighton, “Effect of anisotropy on the critical antiferromagnet thickness in exchanged-biased bilayers”, *Phys. Rev. B* **66**, 054422 (2002).
- [257] B. Beschoten, J. Keller, P. Miltényi, and G. Güntherodt, “Domain state model for exchange bias: thickness dependence of diluted antiferromagnetic Co_{1-y}O on exchange bias in Co/CoO”, *J. Magn. Magn. Mater.* **240**, 248 (2002).
- [258] F. Radu, M. Etzkorn, T. Schmitte, R. Siebrecht, A. Schreyer, K. Westerholt, and H. Zabel, “Asymmetric magnetization reversal on exchange biased CoO/Co bilayers”, *J. Magn. Magn. Mater.* **240**, 251 (2002).
- [259] D. Spenato, J. B. Youssef, and H. L. Gall, “Spin dynamics in exchange-biased F/AF bilayers”, *J. Magn. Magn. Mater.* **240**, 254 (2002).
- [260] C. Binek, X. Chen, A. Hochstrat, and W. Kleemann, “Exchange bias in Fe_{0.6}Zn_{0.4}F₂/Fe heterostructures”, *J. Magn. Magn. Mater.* **240**, 257 (2002).
- [261] L. Malkinski, N. Cramer, A. Hutchison, R. Camley, Z. Celinski, D. Skrzypek, and R. B. Goldfarb, “Exchange bias and anisotropy in the Fe/KCoF₃ structure”, *J. Magn. Magn. Mater.* **240**, 261 (2002).
- [262] Y.-J. Lee, C.-R. Chang, T.-M. Hong, C. H. Ho, and M.-T. Lin, “Long-range exchange bias through a metal spacer”, *J. Magn. Magn. Mater.* **240**, 264 (2002).
- [263] L. Wee, R. L. Stamps, Z. Celinski, L. Malkinski, and D. Skrzypek, “Ferromagnetic resonance study of interface anisotropies in exchange-biased Fe(001)/KNiF₃ bilayers”, *J. Magn. Magn. Mater.* **240**, 270 (2002).
- [264] L. Smardz, “Exchange coupling effects in NiO/Co and NiO/permalloy bilayers”, *J. Magn. Magn. Mater.* **240**, 273 (2002).
- [265] T. Sato, M. Tsunoda, and M. Takahashi, “Correlation between the exchange bias and the degree of ordering of antiferromagnetic layer in PtMn/Co-Fe bilayers”, *J. Magn. Magn. Mater.* **240**, 277 (2002).
- [266] M. Gierlings, M. J. Prandolini, M. Gruyters, W. D. Brewer, and D. Riegel, “On the possibility of detecting asymmetric magnetization reversal processes in exchange bias systems by low temperature nuclear orientation”, *J. Magn. Magn. Mater.* **240**, 280 (2002).
- [267] F. Micheli, J. Degauque, P. Baulès, J. P. Peyrade, J. L. Gauffier, and J. F. Bobo, “Epitaxial growth and magnetic properties of permalloy thin films on MgO(001)”, *J. Magn. Magn. Mater.* **242-245**, 173 (2002).

- [268] F. Ernult, B. Dieny, and J. R. Regnard, “Experimental study of the coupling between two ferromagnetic layers through an antiferromagnetic spacer”, *J. Magn. Magn. Mater.* **242-245**, 515 (2002).
- [269] Z. Q. Lu, G. Pan, W. Y. Lai, D. J. Mapps, and W. W. Clegg, “Exchange anisotropy in NiFe/FeMn bilayers studied by planar Hall effect”, *J. Magn. Magn. Mater.* **242-245**, 525 (2002).
- [270] B. Negulescu, L. Thomas, Y. Dumont, M. Tessier, N. Keller, and M. Guyot, “Exchange biasing in NiO/NiFe₂O₄ bilayers”, *J. Magn. Magn. Mater.* **242-245**, 529 (2002).
- [271] N. Moutis, C. Christides, I. Panagiotopoulos, and D. Niarchos, “On the temperature dependence of coercivity and exchange biasing field in La-Ca-Mn-O ferromagnetic/antiferromagnetic multilayers”, *J. Magn. Magn. Mater.* **242-245**, 544 (2002).
- [272] N. M. Hong, N. H. Dan, and N. X. Phue, “Large unidirectional anisotropy in Nd₆₀Fe₃₀Al₁₀ bulk amorphous alloys”, *J. Magn. Magn. Mater.* **242-245**, 847 (2002).
- [273] W. J. A. Jr, T. Hughes, H. Laider, P. J. Doherty, and A. Johnston, “XMCD measurements of exchange biased PtMn/Co bilayers”, *J. Magn. Magn. Mater.* **242-245**, 961 (2002).
- [274] T. Hughes, W. J. A. Jr, H. Laider, K. O’Grady, and M. T. Kief, “Thermally activated reversal of the antiferromagnet in exchange biased IrMn/CoFe bilayers”, *J. Magn. Magn. Mater.* **242-245**, 1070 (2002).
- [275] Y. G. Wang, A. K. Petford-Long, T. Hughes, H. Laider, K. O’Grady, and M. T. Kief, “Magnetization reversal of the ferromagnetic layer in IrMn/CoFe bilayer films”, *J. Magn. Magn. Mater.* **242-245**, 1081 (2002).
- [276] Y. W. Lee, C. G. Kim, C. O. Kim, and Y. T. Park, “AC characteristics of Hall voltage in NiO/NiFe bilayer”, *J. Magn. Magn. Mater.* **242-245**, 1175 (2002).
- [277] V. S. Gornakov, V. I. Nikitenko, A. J. Shapiro, R. D. Shull, J. S. Jiang, and S. D. Bader, “Direct experimental study of the exchange spring formation process”, *J. Magn. Magn. Mater.* **246**, 80 (2002).
- [278] L. Ritchie, X. Liu, S. Ingvarsson, G. Xiao, J. Du, and J. Q. Xiao, “Magnetic exchange bias enhancement through seed layer variation in FeMn/NiFe layered structures”, *J. Magn. Magn. Mater.* **247**, 187 (2002).
- [279] H. Sang, Q. Y. Xu, K. Yu-Zhang, and Y. W. Du, “Exchange coupling and enhanced coercivity in Fe₅₀Mn₅₀/permalloy bilayers”, *J. Phys.: Condens. Matter* **14**, 507 (2002).
- [280] J. Fassbender, S. Poppe, T. Mewes, A. Mougin, B. Hillebrands, D. Engel, M. Jung, A. Ehresmann, H. Schmoranzler, G. Faini, K. J. Kirk, and J. N. Chapman, “Magnetization Reversal of Exchange Bias Double Layers Magnetically Patterned by Ion Irradiation”, *Phys. Status Solidi A* **189**, 439 (2002).
- [281] M. Tsunoda, M. Konoto, and M. Takahashi, “Magnetic Anisotropy of Antiferromagnet in Exchange Coupled Ni–Fe/Mn– Epitaxial Bilayers”, *Phys. Status Solidi A* **189**, 449 (2002).
- [282] B. K. Charkrabarti and M. Acharyya, “Dynamic transitions and hysteresis”, *Rev. Mod. Phys.* **71**, 847 (1999).

- [283] R. D. McMichael, M. D. Stiles, P. J. Chen, and W. F. Egelhoff, Jr., “Ferromagnetic resonance studies of NiO-coupled thin films of $\text{Ni}_{80}\text{Fe}_{20}$ ”, *Phys. Rev. B* **58**, 8605 (1998).
- [284] L. Wee, R. L. Stamps, L. Malkinski, and Z. Celinski (unpublished).
- [285] J. S. Kouvel, “A ferromagnetic-antiferromagnetic model for copper-manganese and related alloys”, *J. Phys. Chem. Solids* **24**, 795 (1963).
- [286] L. Néel, “Etude théorique du couplage ferro-antiferromagnétique dans les couches minces”, *Ann. Phys. (Paris)* **2**, 61 (1967).
- [287] E. Fulcomer and S. H. Charap, “Thermal fluctuation aftereffect model for some systems with ferromagnetic-antiferromagnetic coupling”, *J. Appl. Phys.* **43**, 4190 (1972).
- [288] L. L. Hinchey and D. L. Mills, “Magnetic properties of superlattices formed from ferromagnetic and antiferromagnetic materials”, *Phys. Rev. B* **33**, 3329 (1986).
- [289] L. L. Hinchey and D. L. Mills, “Magnetic properties of ferromagnet-antiferromagnet superlattice structures with mixed-spin antiferromagnetic sheets”, *Phys. Rev. B* **34**, 1689 (1986).
- [290] D. Mauri, H. C. Siegmann, P. S. Bagus, and E. Kay, “Simple model for thin ferromagnetic films exchange coupled to an antiferromagnetic substrate”, *J. Appl. Phys.* **62**, 3047 (1987).
- [291] A. P. Malozemoff, “Random-field model of exchange anisotropy at rough ferromagnetic-antiferromagnetic interfaces”, *Phys. Rev. B* **35**, 3679 (1987).
- [292] A. P. Malozemoff, “Mechanisms of exchange anisotropy (invited)”, *J. Appl. Phys.* **63**, 3874 (1988).
- [293] A. P. Malozemoff, “Heisenberg-to-Ising crossover in a random-field model with uniaxial anisotropy”, *Phys. Rev. B* **37**, 7673 (1988).
- [294] M. Labruno and J. Miltat, “Wall structures in ferro / antiferromagnetic exchange-coupled bilayers: a numerical micromagnetic approach”, *J. Magn. Magn. Mater.* **151**, 231 (1995).
- [295] R. L. Stamps, R. E. Camley, and R. J. Hicken, “Influence of exchange-coupled anisotropies on spin-wave frequencies in magnetic layered systems: Application to Co/CoO”, *Phys. Rev. B* **54**, 4159 (1996).
- [296] J.-G. Zhu, Y. Zhang, and Z. Lin, “Micromagnetics of small size patterned exchange biased Permalloy film elements”, *J. Appl. Phys.* **81**, 4336 (1997).
- [297] N. C. Koon, “Calculations of Exchange Bias in Thin Films with Ferromagnetic / Antiferromagnetic Interfaces”, *Phys. Rev. Lett.* **78**, 4865 (1997).
- [298] A. F. Khapikov, “Theory of the Magnetization Reversal of Ultrathin Fe Films on a Cr Substrate”, *Phys. Rev. Lett.* **80**, 2209 (1998).
- [299] T. M. Hong, “Simple mechanism for a positive exchange bias”, *Phys. Rev. B* **58**, 97 (1998).
- [300] H. Suhl and I. K. Schuller, “Spin-wave theory of exchange-induced anisotropy”, *Phys. Rev. B* **58**, 258 (1998).

- [301] V. D. Levchenko, Y. S. Sigov, A. I. Morozov, and A. S. Sigov, ““Unusual” domain walls in multilayer systems: ferromagnet + layered antiferromagnet”, *JETP* **87**, 985 (1998).
- [302] T. C. Schulthess and W. H. Butler, “Consequences of Spin-Flop Coupling in Exchange Biased Films”, *Phys. Rev. Lett.* **81**, 4516 (1998).
- [303] O. K. Dudko and A. S. Kovalev, “Magnetic ordering at the stepped ferro/antiferromagnetic interface”, *Low Temp. Phys.* **25**, 18 (1999).
- [304] M. D. Stiles and R. D. McMichael, “Model for exchange bias in polycrystalline ferromagnet-antiferromagnet bilayers”, *Phys. Rev. B* **59**, 3722 (1999).
- [305] H. Fujiwara and M. Sun, “Spin fanning configurations in antiferromagnetic layers with a uniaxial anisotropy and torque transfer characteristics from top to bottom spins”, *J. Appl. Phys.* **85**, 4940 (1999).
- [306] T. C. Schulthess and W. H. Butler, “Coupling mechanisms in exchange biased films (invited)”, *J. Appl. Phys.* **85**, 5510 (1999).
- [307] R. E. Camley, B. V. McGrath, R. J. Aсталos, R. L. Stamps, J.-V. Kim, and L. Wee, “Magnetization dynamics: A study of the ferromagnet/antiferromagnet interface and exchange biasing”, *J. Vac. Sci. Technol. A* **17**, 1335 (1999).
- [308] J.-V. Kim, L. Wee, R. L. Stamps, and R. Street, “Exchange Bias: Interface Imperfection and Temperature Dependence”, *IEEE Trans. Magn.* **35**, 2994 (1999).
- [309] M. D. Stiles and R. D. McMichael, “Temperature dependence of exchange bias in polycrystalline ferromagnet-antiferromagnet bilayers”, *Phys. Rev. B* **60**, 12950 (1999).
- [310] M. Kiwi, J. Mejía-López, R. D. Portugal, and R. Ramírez, “Exchange bias model for Fe/FeF₂: Role of domains in the ferromagnet”, *Europhys. Lett.* **48**, 573 (1999).
- [311] M. Kiwi, J. Mejía-López, R. D. Portugal, and R. Ramírez, “Exchange-bias systems with compensated interfaces”, *Appl. Phys. Lett.* **75**, 3995 (1999).
- [312] R. E. Camley and R. J. Aсталos, “Probing the ferromagnet/antiferromagnet interface with spin waves”, *J. Magn. Magn. Mater.* **198-199**, 402 (1999).
- [313] A. L. Dantas and A. S. Carriço, “Domain wall pinning at an interface step defect”, *J. Phys.: Condens. Matter* **11**, 2707 (1999).
- [314] H. Xi and R. M. White, “Antiferromagnetic thickness dependence of exchange biasing”, *Phys. Rev. B* **61**, 80 (2000).
- [315] A. Layadi, “Resonance modes of cubic single crystal thin film with exchange anisotropy: A theoretical study”, *J. Appl. Phys.* **87**, 1429 (2000).
- [316] V. D. Levchenko, A. I. Morosov, and A. S. Sigov, “Phase Diagram of a Thin Ferromagnetic Film on the Surface of an Antiferromagnet”, *JETP Lett.* **71**, 373 (2000).
- [317] B. Dieny, M. Li, S. H. Liao, C. Horng, and K. Ju, “Quantitative interpretation of the magnetoresistive response (amplitude and shape) of spin valves with synthetic antiferromagnetic pinned layers”, *J. Appl. Phys.* **87**, 3415 (2000).
- [318] J.-V. Kim, R. L. Stamps, B. V. McGrath, and R. E. Camley, “Angular dependence and interfacial roughness in exchange-biased ferromagnetic/antiferromagnetic bilayers”, *Phys. Rev. B* **61**, 8888 (2000).

- [319] A. G. Grechnev and A. S. Kovalev, “Surface spin waves near a ferromagnet-antiferromagnet interface”, *Low Temp. Phys.* **26**, 334 (2000).
- [320] R. L. Stamps, “Dynamic magnetic hysteresis and anomalous viscosity in exchange bias systems”, *Phys. Rev. B* **61**, 12174 (2000).
- [321] B. V. McGrath, R. E. Camley, L. Wee, J.-V. Kim, and R. L. Stamps, “Temperature dependence of exchange biased thin films”, *J. Appl. Phys.* **87**, 6430 (2000).
- [322] Z. Li and S. Zhang, “Coercive mechanisms in ferromagnetic-antiferromagnetic bilayers”, *Phys. Rev. B* **61**, R14897 (2000).
- [323] H. Xi and R. M. White, “Coupling between two ferromagnetic layers separated by an antiferromagnetic layer”, *Phys. Rev. B* **62**, 3933 (2000).
- [324] J. Geshev, “Analytical solutions for exchange bias and coercivity in ferromagnetic/antiferromagnetic bilayers”, *Phys. Rev. B* **62**, 5627 (2000).
- [325] R. L. Stamps and L. Wee, “Stability of Exchange Bias and Thermally Activated Processes”, *IEEE Trans. Magn.* **36**, 3170 (2000).
- [326] A. L. Dantas, A. S. Carriço, and R. L. Stamps, “Local modes of thin magnetic films”, *Phys. Rev. B* **62**, 8650 (2000).
- [327] A. Layadi, “A method for the determination of exchange and magnetocrystalline anisotropies in exchange-coupled thin films”, *J. Magn. Magn. Mater.* **219**, 294 (2000).
- [328] M. Kiwi, J. Mejía-López, R. D. Portugal, and R. Ramírez, “Positive exchange bias model: Fe/FeF₂ and Fe/MnF₂ bilayers”, *Solid State Comm.* **116**, 315 (2000).
- [329] N. Cramer and R. E. Camley, “Influence of interface coupling on spin-flop critical fields in ferromagnet-antiferromagnet coupled systems”, *Phys. Rev. B* **63**, 060404(R) (2001).
- [330] M. D. Stiles and R. D. McMichael, “Coercivity in exchange-bias bilayers”, *Phys. Rev. B* **63**, 064405 (2001).
- [331] L. Wee, R. L. Stamps, and R. E. Camley, “Temperature dependence of domain-wall bias and coercivity”, *J. Appl. Phys.* **89**, 6913 (2001).
- [332] R. L. Stamps, “High frequency spin dynamics in magnetic heterostructures (invited)”, *J. Appl. Phys.* **89**, 7101 (2001).
- [333] U. Nowak, A. Misra, and K. D. Usadel, “Domain state model for exchange bias”, *J. Appl. Phys.* **89**, 7269 (2001).
- [334] Z. Li and S. Zhang, “On the exchange bias in single and polycrystalline ferro/antiferromagnetic bilayers”, *J. Appl. Phys.* **89**, 7272 (2001).
- [335] O. Heinonen, “Monte Carlo simulations of ferromagnetic-antiferromagnetic grains”, *J. Appl. Phys.* **89**, 7552 (2001).
- [336] J.-V. Kim and R. L. Stamps, “Theory of long-wavelength spin waves in exchange biased bilayers”, *J. Appl. Phys.* **89**, 7651 (2001).
- [337] J. Geshev, L. G. Pereira, and J. E. Schmidt, “Angular dependence of the exchange bias obtained from magnetization and ferromagnetic resonance measurements in exchange-coupled bilayers”, *Phys. Rev. B* **64**, 184411 (2001).

- [338] J.-V. Kim and R. L. Stamps, “Defect-modified exchange bias”, *Appl. Phys. Lett.* **79**, 2785 (2001).
- [339] A. Layadi, “Investigation of off-aligned exchange coupling by torque curve and ferromagnetic resonance”, *J. Appl. Phys.* **90**, 4651 (2001).
- [340] K. Nakamura, A. J. Freeman, D.-S. Wang, L. Zhong, and J. F. de Castro, “Magnetic structures at the ferromagnetic NiFe and antiferromagnetic NiMn interface in exchange-biased films: Role of noncollinear magnetism and roughness”, *Phys. Rev. B* **65**, 012402 (2001).
- [341] P. Weinberger, “Exchange bias due to configurational magnetic rearrangements”, *Phys. Rev. B* **65**, 014430 (2001).
- [342] S. Zhang and Z. Li, “Size dependence of exchange bias in ferromagnetic/antiferromagnetic bilayers”, *Phys. Rev. B* **65**, 054406 (2001).
- [343] D. V. Dimitrov, A. Mack, and S. Gangopadhyay, “A study of the induced anisotropy in a ferromagnetic grain from an exchange coupled antiferromagnetic grain with uniaxial anisotropy”, *J. Magn. Magn. Mater.* **225**, 403 (2001).
- [344] A. L. Dantas and A. S. Carrico, “Magnetic excitations of interface pinned domains”, *J. Magn. Magn. Mater.* **231**, 246 (2001).
- [345] M. Weissmann, A. M. Llois, and M. Kiwi, “Calculation of the interface exchange coupling constants between Fe and FeF₂ fluorides”, *J. Magn. Magn. Mater.* **234**, 19 (2001).
- [346] C. Binek, A. Hochstrat, and W. Kleemann, “Exchange bias in a generalized Meiklejohn-Bean approach”, *J. Magn. Magn. Mater.* **234**, 353 (2001).
- [347] J.-G. Hu, G.-J. Jin, and Y.-Q. Ma, “Exchange bias in ferromagnetic/antiferromagnetic bilayers”, *Mod. Phys. Lett. B* **15**, 1087 (2001).
- [348] J. R. L. de Almeida and S. M. Rezende, “Microscopic model for exchange anisotropy”, *Phys. Rev. B* **65**, 092412 (2002).
- [349] J.-G. Hu, G.-J. Jin, and Y.-Q. Ma, “Ferromagnetic resonance and exchange anisotropy in ferromagnetic/antiferromagnetic bilayers”, *J. Appl. Phys.* **91**, 2180 (2002).
- [350] D. S. Deng, X. F. Jin, and R. Tao, “Antiferromagnetic domains in a two-dimensional Heisenberg square lattice”, *Phys. Rev. B* **65**, 132406 (2002).
- [351] S.-H. Tsai, D. P. Landau, and T. C. Schulthess, “Monte Carlo simulations of ordering in ferromagnetic-antiferromagnetic bilayers”, *J. Appl. Phys.* **91**, 6884 (2002).
- [352] U. Nowak, K. D. Usadel, J. Keller, P. Miltényi, B. Beschoten, and G. Güntherodt, “Domain state model for exchange bias. I. Theory”, *Phys. Rev. B* **66**, 014430 (2002).
- [353] U. Nowak, A. Misra, and K. D. Usadel, “Modeling exchange bias microscopically”, *J. Magn. Magn. Mater.* **240**, 243 (2002).
- [354] J.-V. Kim and R. E. Camley, “Probing antiferromagnetic order with heat capacity in exchange-biased structures”, *J. Magn. Magn. Mater.* **240**, 267 (2002).
- [355] O. K. Dudko and A. S. Kovalev, “Effect of roughness on the magnetic structure of ferro/ antiferromagnetic interface”, *J. Magn. Magn. Mater.* **240**, 321 (2002).

- [356] J. Mejía-López, R. Ramírez, and M. Kiwi, “Analytic treatment of the incomplete ferromagnetic domain-wall model for exchange bias”, *J. Magn. Magn. Mater.* **241**, 364 (2002).
- [357] R. L. Stamps, “Mechanisms of exchange bias: partial wall pinning, and fluctuations”, *J. Magn. Magn. Mater.* **242-245**, 139 (2002).
- [358] A. I. Morosov and A. S. Sigov, “Interface roughness and unidirectional anisotropy of thin ferromagnetic film on uncompensated surface of antiferromagnet”, *J. Magn. Magn. Mater.* **242-245**, 1012 (2002).
- [359] Y. Imry and S.-K. Ma, “Random-Field Instability of the Ordered State of Continuous Symmetry”, *Phys. Rev. Lett.* **35**, 1399 (1975).
- [360] H.-B. Braun, J. Kryiakidis, and D. Loss, “Macroscopic quantum tunneling of ferromagnetic domain walls”, *Phys. Rev. B* **56**, 8129 (1997).
- [361] N. Papanicolaou, “Antiferromagnetic domain walls”, *Phys. Rev. B* **51**, 15062 (1995).
- [362] J. C. Slonczewski, “Fluctuation Mechanism for Biquadratic Exchange Coupling in Magnetic Multilayers”, *Phys. Rev. Lett.* **67**, 3172 (1991).
- [363] C. Herring and C. Kittel, “On the Theory of Spin Waves in Ferromagnetic Media”, *Phys. Rev.* **81**, 869 (1951).
- [364] M. Sparks, *Ferromagnetic relaxation theory* (McGraw-Hill, New York, 1964).
- [365] J. Chen and J. L. Erskine, “Surface-Step-Induced Magnetic Anisotropy in Thin Epitaxial Fe Films on W(001)”, *Phys. Rev. Lett.* **68**, 1212 (1992).
- [366] R. K. Kawakami, E. J. Escorcia-Aparicio, and Z. Q. Qiu, “Symmetry-Induced Magnetic Anisotropy in Fe Films Grown on Stepped Ag(001)”, *Phys. Rev. Lett.* **77**, 2570 (1996).
- [367] H. J. Choi, Z. Q. Qiu, J. Pearson, J. S. Jiang, D. Li, and S. D. Bader, “Magnetic anisotropy of epitaxial Fe films grown on curved W(001) with a graded step density”, *Phys. Rev. B* **57**, R12713 (1998).
- [368] H. J. Choi, R. K. Kawakami, E. J. Escorcia-Aparicio, Z. Q. Qiu, J. Pearson, J. S. Jiang, D. Li, and S. D. Bader, “Curie Temperature Enhancement and Induced Pd Magnetic Moments for Ultrathin Fe Films Grown on Stepped Pd(001)”, *Phys. Rev. Lett.* **82**, 1947 (1999).
- [369] B. Hillebrands, P. Baumgart, and G. Güntherodt, “*In situ* Brillouin scattering from surface-anisotropy-dominated Damon-Eshbach modes in ultrathin epitaxial Fe(110) layers”, *Phys. Rev. B* **36**, 2450 (1987).
- [370] A. Moschel, R. A. Hyman, A. Zangwill, and M. D. Stiles, “Magnetization Reversal in Ultrathin Films with Monolayer-Scale Surface Roughness”, *Phys. Rev. Lett.* **77**, 3653 (1996).
- [371] R. A. Hyman, M. D. Stiles, L.-H. Tang, and A. Zangwill, “Coercivity of ultrathin films with in-plane magnetization”, *J. Appl. Phys.* **81**, 3911 (1997).
- [372] R. A. Hyman, A. Zangwill, and M. D. Stiles, “Magnetic reversal on vicinal surfaces”, *Phys. Rev. B* **58**, 9276 (1998).
- [373] P. Gaunt, “Ferromagnetic domain wall pinning by a random array of inhomogeneities”, *Philos. Mag. B* **48**, 261 (1983).

- [374] P. Gaunt, “Magnetic viscosity and thermal activation energy”, *J. Appl. Phys.* **59**, 4129 (1986).
- [375] X. Chen and P. Gaunt, “The pinning force between a Bloch wall and a planar pinning site in MnAlC”, *J. Appl. Phys.* **67**, 2540 (1990).
- [376] X. Chen and P. Gaunt, “Domain wall pinning by magnetic inhomogeneities in Sm(CoNi)_{2.5}”, *J. Appl. Phys.* **67**, 4592 (1990).
- [377] D. Ng and P. Gaunt, “Domain wall pinning transition in an iron-rich FeCu alloy”, *J. Appl. Phys.* **67**, 4598 (1990).
- [378] P. Bruno, G. Bayreuther, P. Beauvillain, C. Chappert, G. Lugert, D. Renard, J. P. Renard, and J. Seiden, “Hysteresis properties of ultrathin ferromagnetic films”, *J. Appl. Phys.* **68**, 5759 (1990).
- [379] S. Lemerle, J. Ferré, C. Chappert, V. Mathet, T. Giamarchi, and P. L. Doussal, “Domain Wall Creep in an Ising Ultrathin Magnetic Film”, *Phys. Rev. Lett.* **80**, 849 (1998).
- [380] S. Zapperi, P. Cizeau, G. Durin, and H. E. Stanley, “Dynamics of a ferromagnetic domain wall: Avalanches, depinning transition, and the Barkhausen effect”, *Phys. Rev. B* **58**, 6353 (1998).
- [381] R. P. Cowburn, J. Ferré, S. J. Gray, and J. A. C. Bland, “Domain-wall dynamics, pinning, and nucleation in ultrathin epitaxial Fe films”, *Phys. Rev. B* **58**, 11507 (1998).
- [382] T. Shibauchi, L. Krusin-Elbaum, V. M. Vinokur, B. Argyle, D. Weller, and B. D. Terris, “Deroughening of a 1D Domain Wall in an Ultrathin Magnetic Film by a Correlated Defect”, *Phys. Rev. Lett.* **87**, 267201 (2001).
- [383] G. Vértesy, I. Tomás, and Z. Vértesy, “On the temperature dependence of domain wall pinning field in soft, uniaxial magnetic materials”, *J. Phys. D: Appl. Phys.* **35**, 625 (2002).
- [384] L. Néel, “Anisotropie magnétique superficielle et surstructures d’orientation”, *J. Phys. Radium* **15**, 225 (1954).
- [385] J. G. Gay and R. Richter, “Spin Anisotropy of Ferromagnetic Films”, *Phys. Rev. Lett.* **56**, 2728 (1986).
- [386] P. Bruno, “Magnetic surface anisotropy of cobalt and surface roughness effects within Néel’s model”, *J. Phys. F: Met. Phys.* **18**, 1291 (1988).
- [387] C. H. Lee, H. He, F. J. Lamelas, W. Vavra, C. Uher, and R. Clarke, “Magnetic anisotropy in epitaxial Co superlattices”, *Phys. Rev. B* **42**, 1066 (1990).
- [388] D. L. Mills, “Surface Effects in Magnetic Crystals near the Ordering Temperature”, *Phys. Rev. B* **3**, 3887 (1971).
- [389] F. Bloch, “Zur Theorie des Ferromagnetismus”, *Z. Phys.* **61**, 206 (1930).
- [390] E. N. Abarra, K. Takano, F. Hellman, and A. E. Berkowitz, “Thermodynamic Measurements of Magnetic Ordering in Antiferromagnetic Superlattices”, *Phys. Rev. Lett.* **77**, 3451 (1996).
- [391] R. E. Camley, “Heat capacity as a probe of surface phase transitions in thin anti-ferromagnetic films”, *Phys. Rev. B* **56**, 2336 (1997).

- [392] A. Layadi, “Effect of biquadratic coupling and in-plane anisotropy on the resonance modes of a trilayer system”, *Phys. Rev. B* **65**, 104422 (2002).
- [393] R. P. Erickson and D. L. Mills, “Microscopic theory of spin arrangements and spin waves in very thin ferromagnetic films”, *Phys. Rev. B* **43**, 10715 (1991).
- [394] F. C. Nörtemann, R. L. Stamps, and R. E. Camley, “Microscopic calculation of spin waves in antiferromagnetically coupled multilayers: Nonreciprocity and finite-size effects”, *Phys. Rev. B* **47**, 11910 (1993).
- [395] R. L. Stamps, R. E. Camley, F. C. Nörtemann, and D. R. Tilley, “Dynamic susceptibilities for magnetic layered structures”, *Phys. Rev. B* **48**, 15740 (1993).
- [396] R. E. Camley and R. L. Stamps, “Magnetic multilayers: spin configurations, excitations and giant magnetoresistance”, *J. Phys.: Condes. Matter* **5**, 3727 (1993).
- [397] R. L. Stamps, “Spin configurations and spin-wave excitations in exchange-coupled bilayers”, *Phys. Rev. B* **49**, 339 (1994).
- [398] R. W. Wang and D. L. Mills, “Magnetic properties of finite antiferromagnetic superlattices: Statics, dynamics, and the surface spin-flop phase”, *Phys. Rev. B* **50**, 3931 (1994).
- [399] N. Papanicolaou, “Low-frequency dynamics in an antiferromagnetic superlattice”, *J. Phys.: Condes. Matter* **11**, 59 (1999).
- [400] R. P. Erickson and D. L. Mills, “Thermodynamics of thin ferromagnetic films in the presence of anisotropy and dipolar coupling”, *Phys. Rev. B* **44**, 11825 (1991).
- [401] B. Friedman, *Principles and Techniques of Applied Mathematics* (John Wiley & Sons, New York, 1956).
- [402] A. S. Carriço, R. E. Camley, and R. L. Stamps, “Phase diagram of thin antiferromagnetic films in strong magnetic fields”, *Phys. Rev. B* **50**, 13453 (1994).
- [403] R. W. Wang, D. L. Mills, E. E. Fullerton, J. E. Mattson, and S. D. Bader, “Surface Spin-Flop Transition in Fe/Cr(211) Superlattices: Experiment and Theory”, *Phys. Rev. Lett.* **72**, 920 (1994).
- [404] F. Boutron, “Facteur de transmission d’une paroi de Bloch pour des ondes de spin de vecteur d’onde normal à la paroi”, *Compt. Rend.* **252**, 3955 (1961).
- [405] J. M. Winter, “Bloch Wall Excitation. Application to Nuclear Resonance in a Bloch Wall”, *Phys. Rev.* **124**, 452 (1961).
- [406] D. I. Paul, “Interaction of Antiferromagnetic Spin Waves with a Bloch Wall”, *Phys. Rev.* **126**, 78 (1962).
- [407] D. I. Paul, “Nuclear Magnetic Resonance within an Antiferromagnetic Bloch Wall”, *Phys. Rev.* **127**, 455 (1962).
- [408] D. I. Paul, “Spin Waves and Nuclear Magnetic Resonance Enhancement in NiF₂ Domain Walls”, *Phys. Rev.* **131**, 178 (1963).
- [409] J. F. Janak, “Quantum Theory of Domain-Wall Motion”, *Phys. Rev.* **134**, A411 (1964).
- [410] J. Smit and H. G. Beljers, “Ferromagnetic resonance absorption in BaFe₁₂O₁₉, a highly anisotropic crystal”, *Philips Res. Rep.* **10**, 113 (1955).

- [411] M. T. Weiss and P. W. Anderson, “Ferromagnetic Resonance in Ferroxdure”, *Phys. Rev.* **98**, 925 (1955).
- [412] M. Sparks, “Ferromagnetic Resonance in Thin Films I: Theory of Normal-Mode Frequencies”, *Phys. Rev. B* **1**, 3831 (1970).
- [413] R. L. Stamps, R. E. Camley, B. Hillebrands, and G. Güntherodt, “Spin-wave propagation on imperfect ultrathin ferromagnetic films”, *Phys. Rev. B* **47**, 5072 (1993).
- [414] M. Grimsditch, R. E. Camley, E. E. Fullerton, S. Jiang, S. D. Bader, and C. H. Sowers, “Exchange-spring systems: Coupling of hard and soft ferromagnets as measured by magnetization and Brillouin light scattering (invited)”, *J. Appl. Phys.* **85**, 5901 (1999).
- [415] A. Hubert and R. Schäfer, *Magnetic domains: The analysis of magnetic microstructures* (Springer-Verlag, Berlin, 1998).
- [416] T. Moriya, *Spin Fluctuations in Itinerant Electron Magnetism* (Springer-Verlag, Berlin, 1985).
- [417] A. Lyberatos, D. V. Berkov, and R. W. Chantrell, “A method for the numerical simulation of the thermal magnetization fluctuations in micromagnetics”, *J. Phys.: Condens. Matter* **5**, 8911 (1993).
- [418] M. A. Wongsam, J. D. Hannay, G. W. Roberts, and R. W. Chantrell, “Recent studies in thermal activation and spin waves”, *J. Magn. Magn. Mater.* **200**, 649 (1999).
- [419] U. Nowak, R. W. Chantrell, and E. C. Kennedy, “Monte Carlo Simulation with Time Step Quantification in Terms of Langevin Dynamics”, *Phys. Rev. Lett.* **84**, 163 (2000).
- [420] O. Chubykako, J. D. Hannay, M. Wongsam, R. W. Chantrell, and J. M. González, “Langevin dynamic simulation of spin waves in a micromagnetic model”, *Phys. Rev. B* **65**, 184428 (2002).
- [421] C. Chappert, H. Bernas, J. Ferré, V. Kottler, J.-P. Jamet, Y. Chen, E. Cambril, T. Devolder, F. Rousseaux, V. Mathet, and H. Launois, “Planar Patterned Magnetic Media Obtained by Ion Irradiation”, *Science* **280**, 1919 (1998).
- [422] B. D. Terris, L. Folks, D. Weller, J. E. E. Baglin, and A. J. Kellock, “Ion-beam patterning of magnetic films using stencil masks”, *Appl. Phys. Lett.* **75**, 403 (1999).
- [423] T. Devolder, C. Chappert, Y. Chen, E. Cambril, H. Bernas, J. P. Jamet, and J. Ferré, “Sub-50 nm planar magnetic nanostructures fabricated by ion irradiation”, *Appl. Phys. Lett.* **74**, 3383 (1999).
- [424] M. Cai, T. Veres, S. Roorda, R. W. Cochrane, R. Abdouche, and M. Sutton, “MeV ion irradiation of Co/Cu multilayers”, *J. Appl. Phys.* **81**, 5200 (1997).
- [425] J. Ferré, C. Chappert, H. Bernas, J.-P. Jamet, P. Meyer, O. Kaitasov, S. Lemerle, V. Mathet, F. Rousseaux, and H. Launois, “Irradiation induced effects on magnetic properties of Pt/Co/Pt ultrathin films”, *J. Magn. Magn. Mater.* **198-199**, 191 (1999).
- [426] D. Weller, J. E. E. Baglin, A. J. Kellock, K. A. Hannibal, M. F. Toney, G. Kusinski, S. Lang, L. Folks, M. E. Best, and B. D. Terris, “Ion induced magnetization reorientation in Co/Pt multilayers for patterned media”, *J. Appl. Phys.* **87**, 5768 (2000).

- [427] R. E. Camley, T. S. Rahman, and D. L. Mills, “Theory of light scattering by the spin-wave interactions of thin ferromagnetic films”, *Phys. Rev. B* **23**, 1226 (1981).
- [428] G. N. Coverdale, R. W. Chantrell, A. Hart, and D. Parker, “A computer simulation of the microstructure of a particulate dispersion”, *J. Appl. Phys.* **75**, 5574 (1994).
- [429] M. El-Hilo, R. W. Chantrell, and K. O’Grady, “A model of interaction effects in granular magnetic solids”, *J. Appl. Phys.* **84**, 5114 (1998).
- [430] N. S. Walmsley and R. W. Chantrell, “Simulations of the magnetic properties of thin film media with low coercivity grains”, *J. Appl. Phys.* **85**, 6154 (1999).
- [431] R. W. Chantrell, D. Weller, T. J. Klemmer, S. Sun, and E. E. Fullerton, “Model of the magnetic properties of FePt granular media”, *J. Appl. Phys.* **91**, 6866 (2002).
- [432] D. Süß, *Micromagnetic simulation of antiferro- and ferromagnetic structures for magnetic recording*, Ph.D. thesis, Technische Universität Wien, 2002.
- [433] D. P. Landau and K. Binder, *A Guide to Monte Carlo Simulations in Statistical Physics* (Cambridge University Press, Cambridge, 2000).
- [434] D. P. Landau and M. Krech, “Spin dynamics simulations of classical ferro- and antiferromagnetic model systems: comparison with theory and experiment”, *J. Phys.: Condens. Matter* **11**, R179 (1999).
- [435] R. L. Burden and J. D. Faires, *Numerical Analysis* (Brooks/Cole, Pacific Grove, CA, 2001).
- [436] D. Cohen and A. C. Hindmarsh, *CVODE User Guide*, 1994.
- [437] D. Cohen and A. C. Hindmarsh, “CVODE, A Stiff/Nonstiff ODE Solver in C”, *Comput. Phys.* **10**, 138 (1996).
- [438] H. Benson and D. L. Mills, “Spin Waves in Thin Films: Dipolar Effects”, *Phys. Rev.* **178**, 839 (1969).

Bibliography

- [B1] *Surface Excitations*, edited by V. M. Agranovich and R. Loudon (North-Holland, New York, 1984).
- [B2] *Ultrathin Magnetic Structures I*, edited by J. A. C. Bland and B. Heinrich (Springer-Verlag, Berlin, 1994).
- [B3] *Ultrathin Magnetic Structures II*, edited by J. A. C. Bland and B. Heinrich (Springer-Verlag, Berlin, 1994).
- [B4] P. M. Chaikin and T. C. Lubensky, *Principles of Condensed Matter Physics* (Cambridge University Press, Cambridge, 1995).
- [B5] M. G. Cottam and A. A. Maradudin, in *Surface Excitations*, edited by V. M. Agranovich and R. Loudon (North-Holland, New York, 1984), pp. 1–194. See Ref. [B1].
- [B6] A. G. Gurevich and G. A. Melkov, *Magnetization Oscillations and Waves* (CRC Press, Boca Raton, 1996).
- [B7] A. Hubert, *Theorie der Domänenwände in geordneten Medien* (Springer-Verlag, Berlin, 1974).
- [B8] I. S. Jacobs and C. P. Bean, in *Magnetism*, edited by G. T. Rado and H. Suhl (Academic Press, New York, 1963), Vol. 3, pp. 271–350. See Ref. [B21].
- [B9] F. Keffer, in *Ferromagnetismus*, Vol. XVIII/2 of *Handbuch der Physik*, edited by H. P. J. Wijn (Springer-Verlag, Berlin, 1966), pp. 1–273. See Ref. [B24].
- [B10] C. Kittel, *Introduction to Solid State Physics*, 7th ed. (John Wiley & Sons, New York, 1996).
- [B11] C. Kittel, *Quantum Theory of Solids* (John Wiley & Sons, New York, 1963).
- [B12] L.-P. Lévy, *Magnetism and Superconductivity* (Springer-Verlag, Berlin, 2000).
- [B13] A. P. Malozemoff and J. C. Slonczewski, *Magnetic Domain Walls in Bubble Materials* (Academic Press, New York, 1979).
- [B14] D. C. Mattis, *The Theory of Magnetism I* (Springer-Verlag, Berlin, YEAR).
- [B15] T. Mewes, *Das epitaktische NiFe/FeMn-Austausch-Bias-Schichtsystem: Herstellung und magnetische Charakterisierung*, Diplomarbeit, Universität Kaiserslautern, 1998.
- [B16] D. L. Mills, in *Surface Excitations*, edited by V. M. Agranovich and R. Loudon (North-Holland, New York, 1984), pp. 397–439. See Ref. [B1].

- [B17] P. Miltényi, *Mikroskopischer Ursprung der Austauschkopplung in ferromagnetischen/antiferromagnetischen Schichten*, Ph.D. thesis, RWTH Aachen, 2000.
- [B18] *Spectroscopy and Theory*, Vol. 2 of *Handbook of Nanostructured Materials and Nanotechnology*, edited by H. S. Nalwa (Academic Press, San Diego, California, 2000).
- [B19] *Magnetic Nanostructures*, edited by H. S. Nalwa (American Scientific, Los Angeles, 2002).
- [B20] K. Ounadjela and R. L. Stamps, in *Spectroscopy and Theory*, Vol. 2 of *Handbook of Nanostructured Materials and Nanotechnology*, edited by H. S. Nalwa (Academic Press, San Diego, California, 2000), pp. 429–474. See Ref. [B18].
- [B21] *Magnetism*, edited by G. T. Rado and H. Suhl (Academic Press, New York, 1963), Vol. 3.
- [B22] R. L. Stamps, in *Magnetic Nanostructures*, edited by H. S. Nalwa (American Scientific, Los Angeles, 2002). See Ref. [B19].
- [B23] R. M. White, *Quantum Theory of Magnetism*, 2nd ed. (Springer-Verlag, Berlin, 1983).
- [B24] *Ferromagnetismus*, Vol. XVIII/2 of *Handbuch der Physik*, edited by H. P. J. Wijn (Springer-Verlag, Berlin, 1966).
- [B25] K. Yosida, *Theory of Magnetism* (Springer-Verlag, Berlin, 1996).

Selected Publications

- [P1] R. E. Camley, B. V. McGrath, R. J. Astalos, R. L. Stamps, Joo-Von Kim, and Leonard Wee, “Magnetization dynamics: A study of the ferromagnet/antiferromagnet interface and exchange biasing”, *J. Vac. Sci. Technol. A* **17**, 1335 (1999).
- [P2] J.-V. Kim, L. Wee, R. L. Stamps, and R. Street, “Exchange Bias: Interface Imperfection and Temperature Dependence”, *IEEE Trans. Magn.* **35**, 2994 (1999).
- [P3] Joo-Von Kim, R. L. Stamps, B. V. McGrath, and R. E. Camley, “Angular dependence and interfacial roughness in exchange-biased ferromagnetic/antiferromagnetic bilayers”, *Phys. Rev. B* **61**, 8888 (2000).
- [P4] B. V. McGrath, R. E. Camley, Leonard Wee, Joo-Von Kim, and R. L. Stamps, “Temperature dependence of exchange biased thin films”, *J. Appl. Phys.* **87**, 6430 (2000).
- [P5] Joo-Von Kim and R. L. Stamps, “Theory of long-wavelength spin waves in exchange biased bilayers”, *J. Appl. Phys.* **89**, 7651 (2001).
- [P6] Joo-Von Kim and R. L. Stamps, “Defect-modified exchange bias”, *Appl. Phys. Lett.* **79**, 2785 (2001).
- [P7] Joo-Von Kim and R. E. Camley, “Probing antiferromagnetic order with heat capacity in exchange-biased structures”, *J. Magn. Magn. Mater.* **240**, 267 (2002).
- [P8] T. Mewes, H. Nembach, J. Fassbender, B. Hillebrands, J.-V. Kim, and R. L. Stamps, “Phase diagrams and energy barriers of exchange biased bilayers with additional anisotropies in the ferromagnet”, submitted to *Phys. Rev. B*.
- [P9] D. Suess, T. Schrefl, R. L. Stamps, J.-V. Kim, and J. Fidler, “Exchange bias of polycrystalline antiferromagnets with perfectly compensated interface”, (unpublished).
- [P10] Joo-Von Kim, L. Wee, R. L. Stamps, and R. E. Camley, “Hysteresis from antiferromagnet domain-wall processes in exchange-biased systems: Magnetic defects and thermal effects”, (unpublished).

